# Probing and controlling ultracold polar molecules in a quantum gas microscope

Jason Scott Rosenberg

A Dissertation
Presented to the Faculty
of Princeton University
in Candidacy for the Degree
of Doctor of Philosophy

Recommended for Acceptance
by the Department of
Physics
Adviser: Professor Waseem S. Bakr

May 2025

# Abstract

Ultracold polar molecules are of great interest for the quantum simulation of many-body physics due to their strong dipolar interactions, large set of internal states, and favorable coherence to interaction time ratios. They have been proposed, for example, as a platform to realize quantum spin liquids and to explore the phase diagrams of quantum magnets. However, the complexity of molecules that lends them many appealing features for studying many-body physics also makes them challenging to probe and control. In this thesis, we present our work advancing the capabilities of the molecular quantum simulation platform by developing single lattice site detection of polar molecules and working to combine that technology with high phase-space density molecular gases. We first discuss the creation of a quantum gas microscope for sodium-rubidium (NaRb) molecules, enabling for the first time the measurement of site-resolved correlations between individual molecules in an optical lattice. As an initial demonstration, we observe Hanbury Brown-Twiss correlations between non-interacting molecules arising from their quantum statistics. The microscope allows for the measurement of a high visibility interference pattern despite a correlation peak width of less than one lattice site. In a second experiment, we transfer the molecules to their absolute ground state to probe correlation dynamics in lattice spin models. We show the flexibility of our platform by tuning both the spatial and spin anisotropy of the Hamiltonian, the latter representing the first application of Floquet engineering to polar molecules. In the second part of the thesis, we describe current efforts toward achieving a high phase-space density gas of polar NaRb molecules in our microscope apparatus. This has necessitated the implementation of collisional shielding mechanisms to address universal loss at short intermolecular distances as well as the exploration of protocols to increase our molecule number. Together with rapid advances by other groups in the field, this work holds promise for creating close to unity filling optical lattices of polar molecules in the near future.

# Acknowledgements

I would first like to thank my adviser Waseem Bakr. I am always amazed at how quickly he can come up with creative solutions for problems we encounter in lab, and his enthusiasm for the research is infectious. Waseem has been a wonderful mentor during graduate school, and I am greatly appreciative of the amount of time he spends each day with us discussing both the experiment and broader progress in the field.

For the majority of my PhD I have had the privilege of working with Lysander Christakis on the experiment. His vast knowledge of the field and forward-thinking ideas were a large factor behind our achievements in those years. Despite the challenges that we often faced in setting up the experiment, I always looked forward to working with him in the molecule lab.

I was fortunate to have two great postdocs during my time at Princeton. Zoe Yan joined the lab while we were in the middle of difficulties with our vacuum chamber. Thanks to her keen insights and enthusiasm the experiment soon progressed to taking data. In the last couple of years I worked with Youssef Aziz Alaoui on the experiment, whose strong work ethic and knowledge of physics enabled a thorough exploration of different protocols to increase our molecule number and shield the molecules from collisions.

I would additionally like to thank the other members past and present of the molecule experiment. It was a pleasure working with Ravin Raj, who was instrumental in the study of site-resolved correlations of polar molecules and in our first attempts at Förster resonance shielding. Sanjay Kumar Keshava, Sungjae Chi, Pascal Weckesser, and many others also helped to move the research forward. The experiment is now in the very capable hands of Jongheum Jung and Laura Futamura, and I look forward to hearing about their exciting results in the coming years.

I am also indebted to the rest of the Bakr lab as well as to other members of the Princeton AMO community. In particular I would like to thank Ben Spar, Max

Prichard, Elmer Guardado-Sanchez, Peter Brown, Zengli Ba, Fred Shi, Junlan Jin, Connor Holland, and Yukai Lu.

I am grateful for the guidance throughout graduate school of the other members of my thesis committee, Lawrence Cheuk and David Huse. I would also like to thank Mike Romalis for his careful reading of this thesis.

The Princeton physics department is lucky to have many wonderful staff members. Steve Lowe's expertise in the machine shop has been vital in the construction of the molecular quantum gas microscope. Ted Lewis and Lauren Callahan have always been helpful when purchasing equipment, and Darryl Johnson, along with Corbe Pale, have ensured that we receive all of these items in a timely manner. I am also grateful for the assistance of Julio Lopez and Geoff Gettelfinger.

Last but not least, I would like to thank my family for their constant support throughout these years.

*To my family.*

# Contents

# List of Figures

# List of Tables

# Chapter 1

# Introduction

"At each level of complexity entirely new properties appear," writes Anderson in his seminal article "More Is Different" [1]. In the case of ultracold polar molecules, the emergent properties that distinguish them from their constituent atoms have motivated wide-ranging research in the fields of quantum sensing and metrology [2], ultracold chemistry [3–7], and quantum simulation and computing [5,8–10]. Since the first production of ultracold polar molecules in 2008 [11], experiments have tracked quantum coherence from reactants to products in a bimolecular reaction [12], demonstrated second-scale entanglement of pairs of molecules [13], and created quantum degenerate gases of fermionic and bosonic polar molecules [14–16], to cite but a few examples. The complexity that molecules possess as compared to neutral atoms has nevertheless also proved to be a challenge, and much of the theoretical and experimental work in the field has been devoted to better understanding and controlling their additional degrees of freedom [4, 17].

Ultracold polar molecules, unlike neutral atoms, have rotational and vibrational structure. Together with electronic and hyperfine structure, the rovibrational states form part of a vast hierarchy of molecular energy levels. This complex structure presents complications for cooling even the simplest molecules, namely diatomic

molecules, to ultracold temperatures. Laser cooling, the workhorse technique for producing ultracold atomic gases, relies upon the ability of atoms to repeatedly absorb and emit photons by transitioning between two states. For most molecules, however, these so-called closed optical cycling transitions do not exist. Instead, after absorbing a photon a molecule can readily decay into states other than the original state, halting the laser cooling process. This challenge has led to two different approaches in the field: indirect and direct production of ultracold molecules [9,17]. The indirect route begins with ultracold alkali atoms and associates them into diatomic molecules [4,18], while the direct method makes use of a special class of molecules that are able to be laser-cooled to the ultracold regime [19,20].

The indirect approach was historically the first to be implemented [11], taking advantage of well-established techniques for laser cooling alkali atoms. In this method, the formation of bialkali molecules in their electronic, vibrational, and rotational ground state is generally performed as follows. First, two species of alkali atoms are cooled to ultracold temperatures before being associated into weakly-bound molecules through a process known as magnetoassociation [21,22]. Magnetoassociation consists of ramping a magnetic field across a particular value called a Feshbach resonance at which the energy of two free atoms matches that of a bound state of a molecular potential. The resulting weakly-bound molecules, or Feshbach molecules, are then coherently transferred to the electronic and rovibrational ground state via stimulated Raman adiabatic passage (STIRAP) [23]. Depending on the STIRAP pathway, the molecules may or may not be in the hyperfine ground state, but two-photon microwave transitions can subsequently be employed to transfer molecules between different hyperfine levels [24–27].

In the indirect method of forming ultracold diatomic molecules, there is a further distinction to be made with regard to the optical trap in which the atoms are associated. Most commonly, degenerate or near-degenerate 3D bulk gases of ultracold

atoms are held in optical dipole traps before and during the association process. Alternatively, the molecule formation can occur in tightly confining optical tweezers, with one atom of each species in a given tweezer prior to association [28–31]. A third method, which is the one adopted throughout the majority of this thesis, begins by forming dual Mott insulators (or a band insulator and a Mott insulator in the case of $^{40}$K$^{87}$Rb) of the two atomic species in an optical lattice [32–35]. On lattice sites containing one atom of each species, the atoms can then be associated into molecules with high efficiency through magnetoassociation and STIRAP. Of these three platforms, so far only the first, bulk association, has produced polar molecules in the quantum degenerate regime [14–16].

Direct formation of ultracold molecules, in contrast to the indirect approach, is not compatible with bialkali molecules due to their lack of optical cycling transitions needed for laser cooling. Instead, certain types of molecules are used, such as SrF [36], CaF [37, 38], and YO [39], in which a photon absorption and emission process leaves the molecule in its original vibrational level with high probability [19, 20, 40]. With the addition of only a few more lasers to close the cycling transition, these molecules are able to be laser cooled to ultracold temperatures. At this point the molecules can be loaded into optical tweezer arrays [41–43] and even prepared in their motional ground state with the use of Raman sideband cooling [44, 45]. One benefit of the molecules' cycling transition is that they can be not only directly cooled but also directly imaged by driving an optical transition and capturing the fluorescence. This is in contrast with bialkali molecules produced by the indirect formation method, which must generally be transferred back into their Feshbach state or fully dissociated for imaging (an exception to this is the direct imaging scheme demonstrated in ref. [46]). An additional feature of direct cooling is that it can be applied to polyatomic molecules, whose additional degrees of freedom compared to

diatomic molecules are particularly intriguing in the context of precision measurement [47–49].

Whether formed by the direct or indirect approach, once the molecules are in their electronic and rovibrational ground state they possess a significant body-frame electric dipole moment of up to several Debye depending on the species. For molecules in identical rotational states in the absence of an applied electric field, however, the lab-frame dipole moment is zero since the dipole operator can only couple states of opposite parity (classically, the dipoles do not have a well-defined orientation). Nevertheless, microwaves or DC electric fields can be used to engineer dipole-dipole interactions by creating superpositions of opposite parity rotational states [9,10]. The resulting dipole-dipole interaction $V_{ij}^{dd}$ between two molecules at positions $\mathbf{r}_i$ and $\mathbf{r}_j$ with dipole moments $\mathbf{d}_i$ and $\mathbf{d}_j$ takes the form:

$$V_{ij}^{dd} = \frac{1}{4\pi\epsilon_0} \frac{\mathbf{d}_i \cdot \mathbf{d}_j - 3(\mathbf{d}_i \cdot \hat{\mathbf{r}}_{ij})(\mathbf{d}_j \cdot \hat{\mathbf{r}}_{ij})}{|\mathbf{r}_i - \mathbf{r}_j|^3} \tag{1.1}$$

where $\hat{\mathbf{r}}_{ij} = \frac{\mathbf{r}_i - \mathbf{r}_j}{|\mathbf{r}_i - \mathbf{r}_j|}$ is a unit vector in the direction of the displacement between the molecules. The $1/r^3$ distance-dependence of the interaction is of particular importance because it signifies that the interaction is long-range compared to the typical contact interactions of neutral atoms. Moreover, we can express equation 1.1 in a more intuitive form by taking the dipoles to both point along a particular lab-frame quantization axis:

$$V_{ij}^{dd} = \frac{d_i d_j}{4\pi\epsilon_0} \frac{1 - 3\cos^2\theta}{|\mathbf{r}_i - \mathbf{r}_j|^3} \tag{1.2}$$

where $\theta$ is the angle between the quantization axis and the dipole-dipole displacement $\mathbf{r}_{ij}$. The dependence of $V_{ij}^{dd}$ on $\theta$ reveals that the dipole-dipole interaction is anisotropic, changing sign as $\theta$ goes from 0 to $\pi/2$. The long-range and anisotropic nature of the dipole-dipole interaction, together with the molecules' rovibrational

structure, make ultracold polar molecules an appealing platform for the quantum simulation of many-body physics.

Quantum simulation, proposed by Feynman in 1981 [50], is the use of a well-controlled quantum system in order to study the behavior of a model quantum Hamiltonian [51–53]. This offers a distinct advantage over simulation on classical computers when studying systems with large numbers of particles. The computational resources required to numerically evaluate these models on a classical computer grow exponentially with system size, but by using an inherently quantum platform for the simulation we can simply let particles interact under the target many-body Hamiltonian and read out the results by performing measurements on the system. Today, numerous quantum simulation platforms exist including ultracold neutral atoms [54, 55], Rydberg atom arrays [56], superconducting circuits [57], photons [58], trapped ions [59,60], and ultracold molecules [5, 10].

The different platforms each have certain classes of Hamiltonians that are best-suited for them. In the case of ultracold polar molecules, Hamiltonians with $1/r^3$ interactions such as dipolar spin and extended-Hubbard models are most naturally implemented [10]. Molecules in optical tweezers or frozen in deep optical lattices can be used to simulate spin-exchange models of quantum magnetism, in which the spin is encoded in different rotational states [8, 9, 61, 62]. For instance, experiments have realized the dipolar spin-1/2 $XY$ Hamiltonian in optical lattices [35, 63]:

$$\begin{aligned} H_{XY} &= J \sum_{i>j} \frac{1-3\cos^2\theta_{ij}}{|\mathbf{r}_i - \mathbf{r}_j|^3} \left(S_i^X S_j^X + S_i^Y S_j^Y\right) \\ &= \frac{J}{2} \sum_{i>j} \frac{1-3\cos^2\theta_{ij}}{|\mathbf{r}_i - \mathbf{r}_j|^3} \left(S_i^+ S_j^- + S_i^- S_j^+\right) \end{aligned} \tag{1.3}$$

where $J$ characterizes the strength of the spin-exchange interaction, $\mathbf{r}_i$ is the position of molecule $i$ in units of the lattice constant, $\theta_{ij}$ is the angle between the quantization axis and the displacement $\mathbf{r}_{ij} = \mathbf{r}_i - \mathbf{r}_j$, and $S_i^X, S_i^Y, S_i^+, S_i^-$ are the spin-1/2

operators for molecule $i$. Dipolar spin-exchange has also been demonstrated in optical tweezers [13, 64–66]. Additionally, lattice experiments have used either Floquet engineering via repeated microwave pulses or a DC electric field to implement the $XXZ$ Hamiltonian, which differs from the $XY$ Hamiltonian by an Ising term [35, 67]. Further Hamiltonians can be realized by allowing the molecules to tunnel in an optical lattice. For example, $t$-$J$-$V$-$W$ models have been experimentally studied [68], and extended Hubbard models containing fractional Mott insulator and supersolid phases have been proposed for itinerant molecules in a 2D lattice [69]. Recently, spin-exchange, Floquet engineering, and tunneling have all been combined in one experiment to realize an $XYZ$ model exhibiting two-axis twisting dynamics [67].

One important feature of the ultracold polar molecule platform is that long coherence times have now been demonstrated relative to the timescale set by molecules' dipolar interaction energies. Typical dipolar interaction strengths between molecules are on the order of hundreds of Hz to kHz [10]. By comparison, state-of-the-art rotational [13, 70] and nuclear spin [71–73] coherence times are now on the second-scale. Several other groups have demonstrated rotational coherence times of tens of milliseconds without spin echo pulses [35, 74]. For optically trapped molecules, these coherence times are often limited by spatially varying differential AC Stark shifts between rotational levels [17, 75–77]. A variety of different strategies have been used in order to mitigate this source of decoherence, including tuning the polarization and intensity of the trapping light [64, 65, 74, 76, 78–80] (in some cases in conjunction with an applied DC electric field [81]), utilizing magic wavelength traps [13, 70], and choosing magnetic field angles and strengths at which hyperfine couplings lead to states that are less sensitive to differential light shifts [35]. Furthermore, the use of spin echo and dynamical decoupling sequences can dramatically extend molecular coherence times [35, 63–65, 67, 68, 70, 74, 80, 82].

Other ultracold gas platforms exist for the quantum simulation of dipolar systems, in particular Rydberg atom arrays and strongly magnetic atoms. All of these platforms have certain strengths and weaknesses and can therefore be viewed as complementary to one another. Furthermore, in areas of overlap they are able to serve as cross-validations of each other's results. Rydberg atom arrays consist of neutral atoms held in optical tweezers with strong interactions generated by promoting atoms to highly excited Rydberg states. Dipolar interactions occur for pairs of atoms in opposite parity Rydberg states [56], enabling studies of, for example, bosonic Su-Schrieffer-Heeger [83], $XY$ [84, 85], $XXZ$ [86], and $t$-$J$-$V$ [87] models. These dipolar interactions are typically on the MHz scale [56], much larger than those in polar molecule experiments. However, the coherence times in Rydberg atom arrays are much shorter than for polar molecules, fundamentally limited by typical Rydberg state lifetimes of tens to hundreds of microseconds [56]. Platforms making use of circular Rydberg states [88–92] and Rydberg dressing [56, 93–95] in conjunction with cryogenic environments [89, 96, 97] are now being developed to address this issue, promising large ratios of coherence to interaction times in the coming years. Strongly magnetic atoms, on the other hand, have long coherence times but dipolar interactions that are smaller than those of both Rydberg atoms and polar molecules (typically tens of Hz). Quantum simulation experiments with this platform include studies of dipolar $XXZ$ spin-exchange dynamics [98, 99] as well as the realization of extended Bose-Hubbard models [100] in which a stripe phase was recently observed [101].

Quantum simulation of many-body physics with ultracold atoms and molecules is greatly enhanced by the ability to probe the system at the single-particle level. One way in which this can be accomplished is through the use of optical tweezer arrays [102]. For lattice platforms, however, a different tool is needed: the quantum gas microscope. Quantum gas microscopy is a technique developed in 2009 to study large numbers of atoms in optical lattices with single-site resolution [103–105].

This is accomplished by simultaneously cooling the atoms and collecting the fluorescence through a high numerical aperture objective. Many research groups around the world have since constructed quantum gas microscopes for neutral atoms, enabling site-resolved imaging of bosonic Mott insulator shells [104, 106], measurements of antiferromagnetic spin correlations between individual fermions in Fermi-Hubbard systems [107–110], and the observation of Kardar-Parisi-Zhang hydrodynamics [111], among countless other landmark studies. Moreover, dipolar systems of strongly magnetic erbium atoms can now be studied with a quantum gas microscope, which has been used to measure density-density correlations in the extended Hubbard model [101]. Prior to the work described in this thesis as well as in the thesis of Lysander Christakis [112], however, site-resolved detection of ultracold polar molecules in optical lattices had never been demonstrated.

The development of the first quantum gas microscope for ultracold polar molecules is the subject of chapters 2 and 3 of this thesis. We study ultracold bosonic $^{23}$Na$^{87}$Rb, which was first produced in its absolute ground state by the Wang group in 2016 [113]. It was chosen for its large dipole moment of 3.2 D [113] as well as its known pathway for ground state formation, allowing us to focus on the novel aspects of the quantum gas microscope rather than on the time-consuming spectroscopy required to find a suitable STIRAP pathway. The first results from our development of a molecular quantum gas microscope are discussed in chapter 2, in which we use the single-site resolution to observe the Hanbury Brown-Twiss effect with non-interacting Feshbach molecules. Chapter 3 then describes the transfer of the molecules to their rovibrational ground state, enabling measurements of site-resolved correlations in spin models of lattice-confined polar molecules.

Following our development of a molecular quantum gas microscope, we desired to increase the lattice filling fraction by evaporatively cooling the molecules to increase their phase-space density. This required us to confront a critical challenge

in the field of ultracold polar molecules, namely collisional loss. The first ultracold molecule prepared in its absolute ground state, $^{40}K^{87}Rb$, can undergo an exothermic chemical reaction in which two KRb molecules produce one $K_2$ molecule and one $Rb_2$ molecule with an accompanying release of energy that ejects the molecules from the trap [114]. This implies that once two KRb molecules come sufficiently close to each other to undergo such a reaction, they are lost with close to unity probability. Consequently, the two-body loss rate can be determined with only the knowledge of the long-range intermolecular potential; the complicated short-range chemistry can simply be replaced by the assumption that molecules are lost once they are below a critical intermolecular separation. This regime is termed "universal loss" [115].

In 2010, ref. [114] experimentally observed the loss rates of KRb in two cases: indistinguishable particles (all KRb molecules prepared in the same hyperfine state) and distinguishable particles (molecules prepared in a mixture of two hyperfine states). In the absence of an applied electric field, ultracold molecules collide primarily in their lowest allowed partial wave. Since $^{40}K^{87}Rb$ is fermionic, indistinguishable molecules cannot collide in the s-wave channel. Instead, the long-range intermolecular potential is characterized by a p-wave barrier that the molecules need to tunnel through in order to reach short range. Distinguishable KRb molecules, on the other hand, do not experience this barrier and should undergo faster loss. In ref. [114], measured loss rates were in agreement with predictions based on universal loss, confirming that the indistinguishable molecules had significantly longer lifetimes.

Since identical bosonic molecules, as with distinguishable molecules, are not protected by a p-wave collisional barrier, these experiments motivated a search for molecules that do not experience short-range loss. A study investigating which species of bialkali dimers could be classified as reactive (undergo exothermic reactions) versus nonreactive (endothermic reactions) concluded, "All the heteronuclear Li dimers and KRb will be subject to reactive trap loss, but all the remainder should be stable

with respect to atom exchange collisions in their ground rovibronic state" [116]. Surprisingly, however, later experiments observed that these nonreactive molecules also experience near-universal loss [113, 117–120]. To explain this fast loss of nonreactive molecules, it was proposed [121] that during "sticky collisions," long-lived intermediate complexes could be excited by the trapping light resulting in loss [7, 122–124]. Indeed, nonreactive RbCs molecules were found to agree with the theory of photoexcitation of intermediate complexes [125], but experiments with NaK and NaRb found no effect of the trapping light on the loss rates [126, 127]. This discrepancy remains an area of active research [7, 124].

To mitigate two-body loss in both reactive and nonreactive diatomic molecules, collisional shielding techniques that raise a large barrier in the long-range intermolecular potential have been proposed and experimentally demonstrated. Different methods have been developed to accomplish this. In a 2D geometry, a static electric field perpendicular to the plane of confinement can be applied so that pairs of molecules have strictly repulsive dipole-dipole interactions, preventing them from reaching short range [128–132]. This technique has been used to evaporatively cool KRb molecules to Fermi degeneracy [132]. For shielding in three dimensions, circularly polarized microwaves blue-detuned relative to the ground to first excited rotational state transition [16, 133–143] have enabled the evaporation of NaK below the Fermi temperature [138] as well as the production of the first Bose-Einstein condensate of polar molecules with NaCs [16]. Microwaves and static electric fields can also be combined to realize three dimensional shielding [144, 145]. In addition, by preparing the molecules in their first excited rotational state, one can take advantage of a Förster-like resonance at a particular DC electric field to generate a large barrier in the intermolecular potential [146–154].

The collisional shielding of polar diatomic molecules is discussed in greater depth in chapter 4 of this thesis. This is followed by a description in chapter 5 of our efforts

toward the production of a high phase-space density gas of polar molecules in our quantum gas microscope apparatus. Finally, chapter 6 will present an outlook on future applications of the quantum gas microscope for high-filling lattices of ultracold polar molecules.

# Chapter 2

# Observation of the Hanbury Brown-Twiss effect with a molecular quantum gas microscope

Portions of this chapter are based on work previously published as

> Rosenberg, J. S., Christakis, L., Guardado-Sanchez, E., Yan, Z. Z. & Bakr, W. S. Observation of the Hanbury Brown–Twiss effect with ultracold molecules. *Nat. Phys.* **18**, 1062–1066 (2022).

This work was also presented publicly in the following talk: [155].

The construction of the molecular quantum gas microscope took place over several years, but by 2021 we were able to capture site-resolved images of Feshbach molecules in an optical lattice. This represented a milestone in the ability to probe large systems of ultracold molecules, enabling the simultaneous detection of over one hundred individual molecules prepared in the same internal and motional state with near-unity efficiency. Although the Feshbach molecules were non-interacting, we could already take advantage of the quantum gas microscope to measure correlations arising from their quantum statistics. In particular, more than 60 years after its landmark demon-

stration with photons, we observed for the first time the Hanbury Brown-Twiss effect with ultracold molecules.

## 2.1 The Hanbury Brown-Twiss effect

The Hanbury Brown-Twiss (HBT) effect has had a remarkable impact on physics since its first observation in the 1950s. What began as an experiment to improve measurements of the diameters of stars [156–158] within a decade had prompted the development of modern quantum optics [159–161]. Moreover, the HBT effect has been realized not only with its original platform of photons but also with electrons [162, 163], neutrons [164], phonons [165, 166], and ultracold atoms [167–178]. It has additionally become an important tool for studying particle collisions in high-energy physics [179, 180]. To provide context for our HBT experiment with molecules described later in this chapter, we begin by presenting an overview of the history and theory of this important effect.

### 2.1.1 The intensity interferometer

Efforts in astronomy to determine the angular diameters of stars date back centuries to Galileo [181]. Despite this long history, by the beginning of the 1950s the diameters of fewer than ten stars were known with any reasonable accuracy [182]. The established technology at the time for making these measurements was the Michelson stellar interferometer, a diagram of which is shown in Fig. 2.1. In the Michelson interferometer, light from a distant star is collected by two mirrors, labeled M1 and M2, separated by a distance $d$ (this detector separation is often referred to as the "baseline" following the nomenclature of radio astronomy). An imaging system then brings the two beams of light to a focus at the common point P. For coherent light,

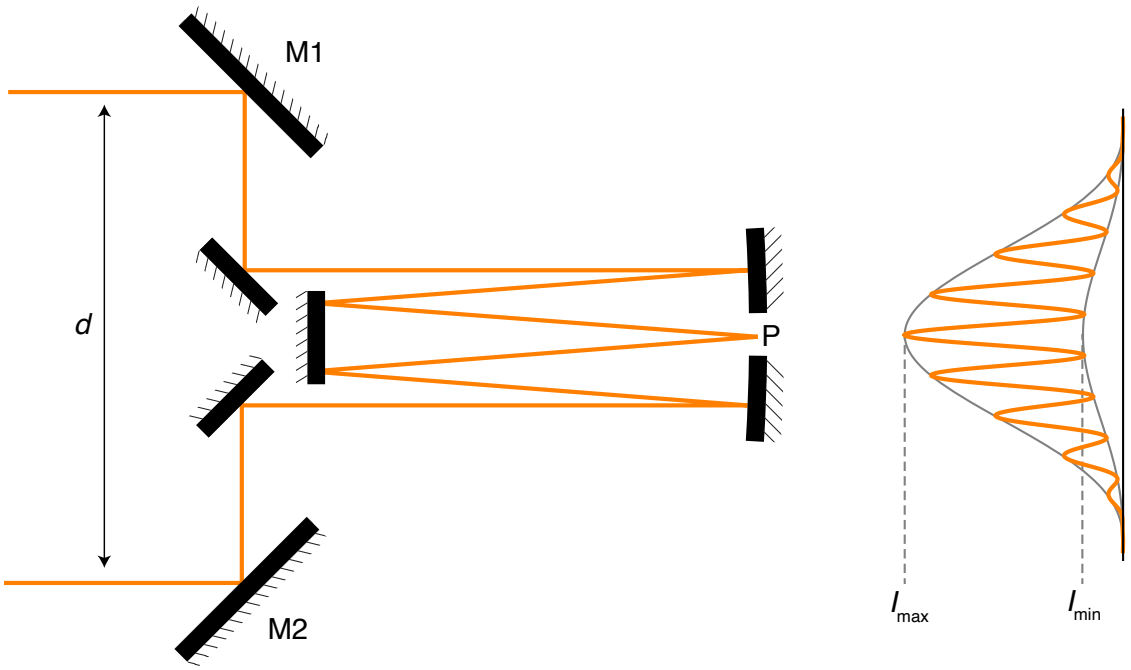


**Figure 2.1: The Michelson stellar interferometer.** Light from a star is collected on two separated mirrors and focused to a common point P. For coherent light, the superimposed beams form an interference pattern. Adapted from ref. [181].

the superimposed beams form an interference pattern consisting of light and dark fringes.

The visibility $V(d)$ of the fringes at detector separation $d$ is defined as

$$V(d) = \frac{I_{\max} - I_{\min}}{I_{\max} + I_{\min}} \tag{2.1}$$

where $I_{\max}$ and $I_{\min}$ are the maximum and minimum intensities in the central region of the interference pattern, respectively [183]. The visibility ranges from $V = 0$ for $I_{\max} = I_{\min}$ to $V = 1$ for $I_{\min} = 0$. It can be shown that the visibility is given by the absolute value of the normalized Fourier transform of the intensity distribution of the

light source [181, 183]:

$$V(d) = \left| \frac{\iint I(x,y) e^{\frac{-2\pi i d x}{\lambda D}} \, \mathrm{d}x \, \mathrm{d}y}{\iint I(x,y) \, \mathrm{d}x \, \mathrm{d}y} \right| \tag{2.2}$$

where $D$ is the distance from the interferometer to the source, $x$ and $y$ are coordinates on the source in a plane normal to the interferometer-source displacement (with $x$ parallel to the detector baseline), $I(x,y)$ is the intensity distribution of the source, and $\lambda$ is the wavelength (assuming for simplicity a monochromatic source).* For example, if we model a star as a disk of uniform intensity $I_0$ and radius $\rho$, then equation 2.2 becomes

$$\begin{aligned} V(d) &= \left| \frac{I_0 \int_0^{2\pi} \int_0^{\rho} e^{\frac{-2\pi i d r \cos\phi}{\lambda D}} r \, \mathrm{d}r \, \mathrm{d}\phi}{I_0 \int_0^{2\pi} \int_0^{\rho} r \, \mathrm{d}r \, \mathrm{d}\phi} \right| \\ &= \left| \frac{2 J_1(\frac{2\pi\rho d}{\lambda D})}{\frac{2\pi\rho d}{\lambda D}} \right| \end{aligned} \tag{2.3}$$

where $J_1(z)$ is the Bessel function of the first kind and where we have written the source coordinates in the polar form $x = r\cos\phi$. For $D \gg \rho$ the angular diameter of the star is given by $\theta = 2\rho/D$. With this substitution, we have

$$V(d) = \left| \frac{2 J_1(\frac{\pi\theta d}{\lambda})}{\frac{\pi\theta d}{\lambda}} \right|. \tag{2.4}$$

The Bessel function $J_1(z)$ has its first zero at $z \approx 1.22\pi$, so we see that the visibility equals zero at a detector separation of

$$d = \frac{1.22\lambda}{\theta}. \tag{2.5}$$

Therefore, one can determine the angular diameter $\theta$ of a star by finding the mirror separation at which the interference fringes first disappear.

*Equation 2.2 is a form of the van Cittert-Zernike theorem [183].

In practice, however, the Michelson stellar interferometer presents several challenges [181]. For example, the fringe pattern will shift to one side if the difference in path lengths of the two beams changes on the order of a wavelength. If the path lengths are changing rapidly, such as from vibrations of the mirrors, then the interference pattern will become blurred. Moreover, the interference pattern is sensitive not only to relative changes in the path lengths but also to the absolute difference between the two paths. If the absolute difference is greater than the coherence length of the light then the interference pattern will not be visible. These two considerations require the interferometer structure to be extremely stable and rigid, which becomes increasingly difficult as the mirror separation becomes larger. From equation 2.5, it is apparent that the smaller the diameter of a star, the larger the required mirror separation in order to resolve it, and so limitations on the Michelson interferometer's size set a bound on the stellar diameters it can measure. An additional consideration is that atmospheric turbulence can reduce fringe visibility by causing fluctuating path length differences between the light collected at the two mirrors.

The difficulty in extending detector baselines also hindered measurements of the angular diameters of celestial radio sources with Michelson-type interferometers [156], prompting the British radio astronomer Robert Hanbury Brown in 1949 to conceive of a different approach: the intensity interferometer [181]. The sensitivity of the Michelson interferometer to path length differences fundamentally results from the visibility being related to the product of two electric fields [183]. Hanbury Brown's great insight was to instead form an interferometer based on the product of two intensities. More specifically, he realized that from the correlation between intensity fluctuations recorded by two spatially separated detectors, one can extract the angular diameter of the source with minimal sensitivity to path length differences.

To see how this works, let us consider the following example from ref. [181] depicted in Fig. 2.2. Electromagnetic radiation from a distant source impinges on an intensity

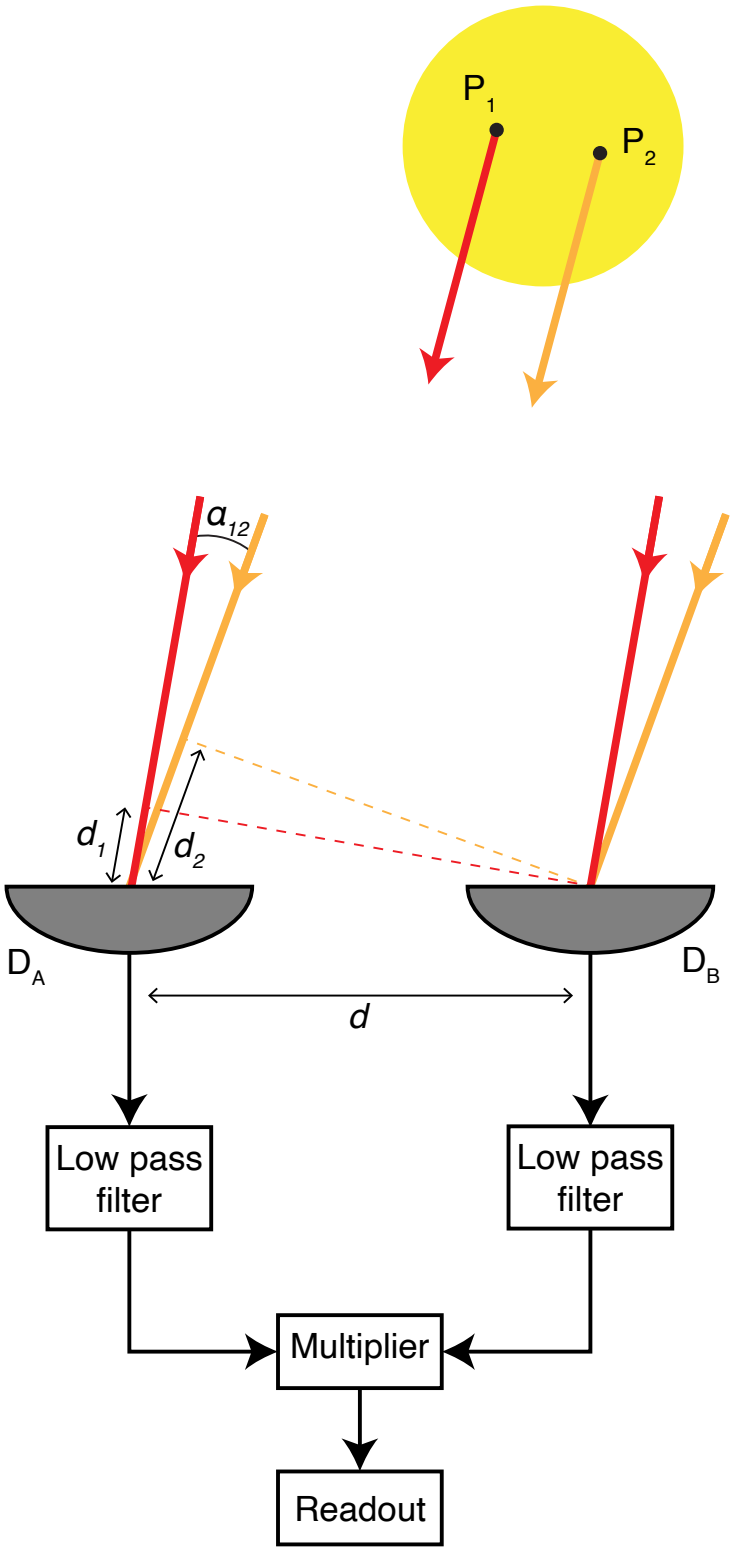


**Figure 2.2: Model of the intensity interferometer.** To understand the principles of the intensity interferometer, we examine the case of two emitters on a distant source. Adapted from ref. [181].

interferometer consisting of two detectors $\mathrm{D_A}$ and $\mathrm{D_B}$ separated by distance $d$. The detectors record intensities $\mathrm{I_{A(B)}}$ and convert them to proportional electrical currents $i_{\mathrm{A(B)}}$. For now, we restrict ourselves to considering two points on the source $\mathrm{P_1}$ and $\mathrm{P_2}$ emitting independent electric fields $E_1(t) = E_1 \sin(\omega_1 t + \phi_1)$ and $E_2(t) = E_2 \sin(\omega_2 t + \phi_2)$, and for simplicity let us take both electric fields to have identical linear polarizations. We can then express the current generated by detector $\mathrm{D_A}$ due to $E_1(t)$ and $E_2(t)$ as

$$i_{\mathrm{A}} = K_{\mathrm{A}} \left[E_1 \sin(\omega_1 t + \phi_1) + E_2 \sin(\omega_2 t + \phi_2)\right]^2 \tag{2.6}$$

where $\mathrm{K_A}$ is a proportionality constant related to the detector's conversion from intensity to current. Likewise, detector $\mathrm{D_B}$ produces a current

$$i_{\mathrm{B}} = K_{\mathrm{B}} \left[E_1 \sin(\omega_1 (t + d_1/c) + \phi_1) + E_2 \sin(\omega_2 (t + d_2/c) + \phi_2)\right]^2 \tag{2.7}$$

where the distances $d_1$ and $d_2$, defined in Fig. 2.2, represent the additional path length that the light must take to reach $\mathrm{D_A}$. Expanding these equations:

$$\begin{aligned} i_{\mathrm{A}} = \frac{1}{2} K_{\mathrm{A}} \Big\{ & (E_1^2 + E_2^2) - \left[E_1^2 \cos\left[2(\omega_1 t + \phi_1)\right] + E_2^2 \cos\left[2(\omega_2 t + \phi_2)\right]\right] \\ & - 2E_1 E_2 \cos\left[(\omega_1 + \omega_2)t + (\phi_1 + \phi_2)\right] \\ & + 2E_1 E_2 \cos\left[(\omega_1 - \omega_2)t + (\phi_1 - \phi_2)\right] \Big\} \end{aligned} \tag{2.8}$$

$$\begin{aligned} i_{\mathrm{B}} = \frac{1}{2} K_{\mathrm{B}} \Big\{ & (E_1^2 + E_2^2) - \left[E_1^2 \cos\left[2(\omega_1 (t + d_1/c) + \phi_1)\right]\right. \\ & \left. + E_2^2 \cos\left[2(\omega_2 (t + d_2/c) + \phi_2)\right]\right] \\ & - 2E_1 E_2 \cos\left[(\omega_1 + \omega_2)t + \omega_1 d_1/c + \omega_2 d_2/c + (\phi_1 + \phi_2)\right] \\ & + 2E_1 E_2 \cos\left[(\omega_1 - \omega_2)t + \omega_1 d_1/c - \omega_2 d_2/c + (\phi_1 - \phi_2)\right] \Big\}. \end{aligned} \tag{2.9}$$

The second and third terms in each equation oscillate rapidly compared to the first terms (which are the DC currents) and the last terms (which oscillate at the difference

frequency $\omega_1 - \omega_2$). Therefore, by employing low pass filters we can discard the second and third terms. After filtering, we can multiply the signals together to construct the time-averaged correlation

$$\langle i_{\mathrm{A}} i_{\mathrm{B}} \rangle = \frac{1}{4} K_{\mathrm{A}} K_{\mathrm{B}} \left( (E_1^2 + E_2^2)^2 + 2E_1^2 E_2^2 \cos(\omega_1 d_1/c - \omega_2 d_2/c) \right). \tag{2.10}$$

If the frequencies emitted at positions $\mathrm{P}_1$ and $\mathrm{P}_2$ are contained within a narrow bandwidth (this can be ensured by placing optical band-pass filters in front of the detectors), then $\omega_1 \approx \omega_2 \equiv \omega = 2\pi c/\lambda$. In addition, by examining Fig. 2.2 we can express the quantity $d_1 - d_2$ as $d\alpha_{12}$ where $d$ is the detector baseline and $\alpha_{12}$ is the angular separation of $\mathrm{P}_1$ and $\mathrm{P}_2$ (recall that we have assumed a distant source). With these substitutions, equation 2.10 becomes

$$\langle i_{\mathrm{A}} i_{\mathrm{B}} \rangle = \frac{1}{4} K_{\mathrm{A}} K_{\mathrm{B}} \left( (E_1^2 + E_2^2)^2 + 2E_1^2 E_2^2 \cos(2\pi d\alpha_{12}/\lambda) \right). \tag{2.11}$$

We can also obtain the time-average of the individual currents:

$$\begin{aligned} \langle i_{\mathrm{A}} \rangle &= \frac{1}{2} K_{\mathrm{A}} \left( E_1^2 + E_2^2 \right) \\ \langle i_{\mathrm{B}} \rangle &= \frac{1}{2} K_{\mathrm{B}} \left( E_1^2 + E_2^2 \right). \end{aligned} \tag{2.12}$$

From equations 2.11 and 2.12 we can at last construct the normalized time-averaged correlation of the intensities, which we call $g^{(2)}(d)$ anticipating the formalism of coherence orders introduced later in this section:

$$g^{(2)}(d) = \frac{\langle i_{\mathrm{A}} i_{\mathrm{B}} \rangle}{\langle i_{\mathrm{A}} \rangle \langle i_{\mathrm{B}} \rangle} = 1 + \frac{2E_1^2 E_2^2 \cos(2\pi d\alpha_{12}/\lambda)}{(E_1^2 + E_2^2)^2}. \tag{2.13}$$

It is worth pausing here to consider the implications of this result. By superimposing two intensities (in the form of electrical currents) rather than two electric fields, we have obtained a measurable quantity that reveals the angular separation $\alpha_{12}$

of the two emitters at $P_1$ and $P_2$. The derivation of equation 2.13 illuminates some of the key advantages of Hanbury Brown's intensity interferometer compared to the Michelson interferometer. As we discussed previously, the Michelson interferometer is sensitive to changes in path lengths on the order of a wavelength. By contrast, the correlated fluctuations that the intensity interferometer detects are related to the difference frequency $\omega_1 - \omega_2$, which is bounded by the cutoff frequency of the low pass filters. Therefore, path length differences in the intensity interferometer only need to be small with respect to the shortest wavelength within the filter bandwidth. Since each filter's cutoff frequency is many orders of magnitude lower than the original frequencies $\omega_{1(2)}$, this requirement is relatively easy to fulfill. For example, Hanbury Brown found that path length differences within 30 cm were acceptable for an optical source and a 100 MHz filter bandwidth [181]. The detector separations in an intensity interferometer can consequently be made much larger without the same demands on the rigidity of the instrument, leading to a significant improvement in angular resolution. Moreover, this insensitivity to path length differences extends to those caused by atmospheric turbulence, solving one of the critical issues of the Michelson interferometer.

We can gain further insight by generalizing equation 2.13 to the case of a disk-shaped source of uniform average intensity such as we considered for the Michelson interferometer. First, we set the electric field amplitude of each emitter to be the same such that $E_1 = E_2 \equiv E$. Equation 2.11 then simplifies to

$$\langle i_A i_B \rangle = K_A K_B E^4 \left(1 + \frac{1}{2}\cos(2\pi d\alpha_{12}/\lambda)\right). \tag{2.14}$$

Let us now consider how this equation is modified when we go from having $N = 2$ emitters on the source to a general number $N$. The first term in equation 2.14 results from the DC current terms in equations 2.8 and 2.9, which in turn represent the total

average intensity received by each detector. For $N$ emitters, this average intensity is proportional to $NE^2/2$, so the first term in equation 2.14 becomes $K_\mathrm{A}K_\mathrm{B}(NE^2/2)^2$. We can likewise rewrite equation 2.12 as

$$\begin{aligned}\langle i_\mathrm{A}\rangle &= \frac{1}{2}K_\mathrm{A}NE^2 \\ \langle i_\mathrm{B}\rangle &= \frac{1}{2}K_\mathrm{B}NE^2.\end{aligned} \tag{2.15}$$

The second term in equation 2.14 results from the pairwise difference frequency terms in equations 2.8 and 2.9. If we allow each of the $N$ emitters to have individual frequencies $\omega_i$, then there will be $\binom{N}{2}$ terms. Defining $\alpha_{ij}$ to be the angular separation of emitters $i$ and $j$ in each of those terms, equation 2.14 becomes

$$\langle i_\mathrm{A}i_\mathrm{B}\rangle = K_\mathrm{A}K_\mathrm{B}E^4\left(\left(\frac{N}{2}\right)^2 + \sum_{i>j}\frac{1}{2}\cos(2\pi d\alpha_{ij}/\lambda)\right). \tag{2.16}$$

As in our derivation of the Michelson interferometer visibility, we can define coordinates $x$ and $y$ on the source with $x$ parallel to the detector baseline such that $\alpha_{ij} = (x_i - x_j)/D$ where $D$ is the distance to the source and $x_{i(j)}$ is the position of emitter $i(j)$ on the $x$-axis. With this substitution, we can combine equations 2.15 and 2.16 to form the correlation

$$g^{(2)}(d) = \frac{\langle i_\mathrm{A}i_\mathrm{B}\rangle}{\langle i_\mathrm{A}\rangle\langle i_\mathrm{B}\rangle} = \frac{K_\mathrm{A}K_\mathrm{B}E^4\left(\left(\frac{N}{2}\right)^2 + \sum_{i>j}\frac{1}{2}\cos\left(2\pi d(x_i - x_j)/(\lambda D)\right)\right)}{K_\mathrm{A}K_\mathrm{B}E^4\left(\frac{N}{2}\right)^2}. \tag{2.17}$$

We next integrate $\langle i_{\mathrm{A}} i_{\mathrm{B}} \rangle$ and $\langle i_{\mathrm{A}} \rangle \langle i_{\mathrm{B}} \rangle$ over all emitter pair positions in a uniform disk of radius $\rho$:

$$g^{(2)}(d) = \left\{ \int_0^{2\pi} \mathrm{d}\phi_i \int_0^{2\pi} \mathrm{d}\phi_j \int_0^{\rho} \mathrm{d}r_i \int_0^{\rho} \mathrm{d}r_j K_{\mathrm{A}} K_{\mathrm{B}} E^4 r_i r_j \left[ \left(\frac{N}{2}\right)^2 + \sum_{i>j} \frac{1}{2} \cos\Big(2\pi d (r_i \cos\phi_i - r_j \cos\phi_j)/(\lambda D)\Big) \right] \right\} \Bigg/ \left\{ \int_0^{2\pi} \mathrm{d}\phi_i \int_0^{2\pi} \mathrm{d}\phi_j \int_0^{\rho} \mathrm{d}r_i \int_0^{\rho} \mathrm{d}r_j K_{\mathrm{A}} K_{\mathrm{B}} E^4 r_i r_j \left(\frac{N}{2}\right)^2 \right\}. \tag{2.18}$$

Evaluating the integrals, we obtain:

$$\begin{aligned} g^{(2)}(d) &= 1 + \sum_{i>j} \frac{2}{N^2} \left( \frac{2J_1\left(\frac{2\pi\rho d}{\lambda D}\right)}{\frac{2\pi\rho d}{\lambda D}} \right)^2 \\ &= 1 + \binom{N}{2} \frac{2}{N^2} \left( \frac{2J_1\left(\frac{2\pi\rho d}{\lambda D}\right)}{\frac{2\pi\rho d}{\lambda D}} \right)^2 \\ &= 1 + \frac{N-1}{N} \left( \frac{2J_1\left(\frac{2\pi\rho d}{\lambda D}\right)}{\frac{2\pi\rho d}{\lambda D}} \right)^2 . \end{aligned} \tag{2.19}$$

Finally, taking the limit $N \to \infty$ and labeling the angular diameter of the source as $\theta = 2\rho/D$, we have

$$g^{(2)}(d) = 1 + \left( \frac{2J_1\left(\frac{\pi\theta d}{\lambda}\right)}{\frac{\pi\theta d}{\lambda}} \right)^2 . \tag{2.20}$$

A plot of equation 2.20 is shown in Fig. 2.3. The correlation decays as a function of detector separation from its maximal value of $g^{(2)}(0) = 2$ to $g^{(2)}(d \gg L_c) = 1$, where $L_c$ is the coherence length of the light. Comparing equation 2.20 with equation 2.4, we see that

$$g^{(2)}(d) = 1 + V^2. \tag{2.21}$$

In fact, this relationship between $g^{(2)}$ and the visibility is general for what is known as chaotic light. Chaotic light is defined as having partial coherence, such that fringes will appear with nonzero visibility in a Michelson-type experiment if the detector

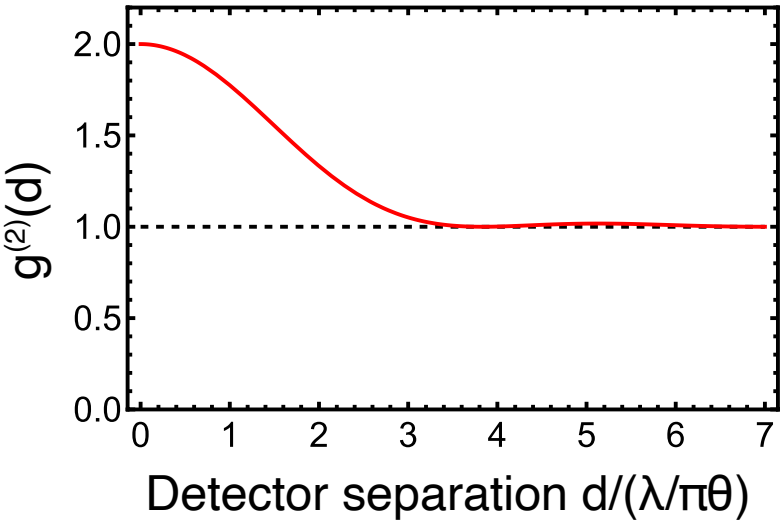


**Figure 2.3: $g^{(2)}$ correlation for a uniform circular source.** The correlation is plotted as a function of the detector separation according to equation 2.20.

separation is small but vanish at separations beyond $L_c$ (or after coherence time $\tau_c$ if we are referring to temporal rather than spatial coherence) [160]. Perfectly coherent light, on the other hand, has a fixed value of $V = 1$ (i.e. $L_c = \tau_c = \infty$) and equation 2.21 does not apply. (As we will see in section 2.1.2, the concept of coherence is actually more subtle than this, and the visibility only determines what is known as first-order coherence.) An additional relationship regarding $g^{(2)}$ for chaotic light may be obtained by recalling that the visibility is proportional to the absolute value of the Fourier transform of the intensity distribution of the light source (equation 2.2). Therefore, we see from equation 2.21 that $g^{(2)} - 1$ is proportional to the absolute square of the Fourier transform of the source's intensity distribution.

Hanbury Brown first put these ideas into practice in 1952, constructing an intensity interferometer and successfully measuring the angular diameters of two radio sources [184]. He then collaborated with fellow astronomer Richard Twiss in 1954 to work out the mathematical details of the radio-frequency intensity interferometer [156]. However, a debate soon began in the scientific community as to whether

this theory of intensity correlations was also valid at the optical frequencies required to measure the angular diameter of stars [181]. One article even suggested, "It would appear to the authors... that if such a correlation did exist, it would call for a major revision of some fundamental concepts in quantum mechanics" [185]. In fact, Hanbury Brown and Twiss themselves concluded their 1954 paper by writing, "A preliminary examination of this question... suggests that the technique cannot be applied to optical wavelengths" [156].

To settle the matter, Hanbury Brown and Twiss performed a landmark experiment in 1956 in which they simulated a star with a mercury arc lamp as depicted in Fig. 2.4 [157]. This light was sent through a small aperture before being divided into two paths by a beamsplitter and finally detected by separate photomultiplier tubes. One of the photomultiplier tubes was placed on a translation stage, serving as a means to vary the detector separation $d$ of Fig. 2.2. When the photomultiplier tubes were in identical spatial positions as viewed from the light source ($d = 0$), positive correlations in the intensity fluctuations at the two positions were observed. Then, as the variable-position photomultiplier tube was translated to increase the effective separation $d$, the correlations correspondingly decayed to zero in agreement with theory [186]. Following this proof-of-principle experiment, that same year Hanbury Brown and Twiss used an intensity interferometer designed for optical wavelengths to successfully measure the angular diameter of the star Sirius [158]. A much larger intensity interferometer was subsequently constructed in Australia, and by 1972 it had been used to measure the angular diameters of 32 stars [181].

Today, the correlation of intensity fluctuations between light measured on separate detectors, now referred to as the HBT effect, is most well known in the field of quantum optics rather than in astronomy. Thanks to the development of the laser, improved optical detectors, and vastly increased computational power, automated path-length correction has rendered Michelson-type interferometry once again the

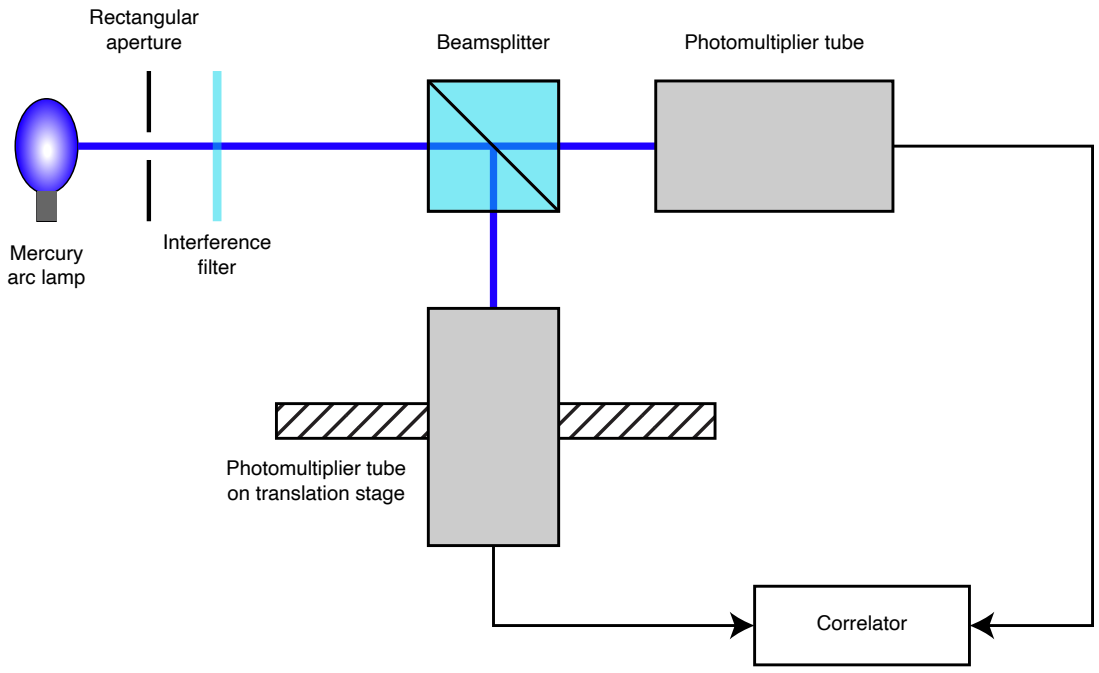


**Figure 2.4: Schematic of the Hanbury Brown and Twiss tabletop experiment.** A simplified diagram of the landmark experiment from ref. [157] illustrates the measurement of intensity fluctuations with a chaotic source of light.

leading method to measure the angular diameters of stars [187]. On the other hand, subsequent interpretations of the HBT effect in the language of quantum mechanics have profoundly changed our understanding of light.

### 2.1.2 A quantum picture of the HBT effect

In a famous 1963 paper, Roy Glauber redefined the meaning of optical coherence [159]. Prior to the 1950s, the coherence of light was thought of in terms of the visibility of interference fringes. In other words, it measured the correlation between two electric fields, a quantity quadratic in electric field strength. However, the experiments of Hanbury Brown and Twiss described in the previous section showed that this definition does not capture all of the possible correlations in a beam of light. Namely,

the HBT effect is a correlation of two intensities, which is quartic in electric field strength. In order to modify the definition of coherence to include more general correlations between light, Glauber introduced the concept of orders of coherence. The previous notion of coherence in this formulation is called first-order coherence and is defined as [161]:

$$g^{(1)}(\mathbf{r}_1, \mathbf{r}_2; \tau) = \frac{\langle E^*(\mathbf{r}_1, t) E(\mathbf{r}_2, t+\tau) \rangle}{\langle E^*(\mathbf{r}_1, t) E(\mathbf{r}_1, t) \rangle^{\frac{1}{2}} \langle E^*(\mathbf{r}_2, t+\tau) E(\mathbf{r}_2, t+\tau) \rangle^{\frac{1}{2}}}, \tag{2.22}$$

where $\langle \cdot \rangle$ is an ensemble average (for stationary fields this is simply an average over long times) [188]. The intensity correlations in the HBT effect are an example of second-order coherence:

$$g^{(2)}(\mathbf{r}_1, \mathbf{r}_2; \tau) = \frac{\langle E^*(\mathbf{r}_1, t) E^*(\mathbf{r}_2, t+\tau) E(\mathbf{r}_2, t+\tau) E(\mathbf{r}_1, t) \rangle}{\langle E^*(\mathbf{r}_1, t) E(\mathbf{r}_1, t) \rangle \langle E^*(\mathbf{r}_2, t+\tau) E(\mathbf{r}_2, t+\tau) \rangle}. \tag{2.23}$$

For parallel plane waves we can express the temporal second-order coherence in the simpler form:

$$g^{(2)}(\tau) = \frac{\langle I(t) I(t+\tau) \rangle}{\langle I(t) \rangle \langle I(t+\tau) \rangle}. \tag{2.24}$$

These equations can be extended to any arbitrary order $n$ so that we may refer to light as having $n$th order coherence $g^{(n)}$.

Equation 2.22 enables us to find a simple relationship between $g^{(1)}$ and the visibility of an interference pattern. Following ref. [160], let us consider the interference of a plane wave of constant average intensity $I_0$ with a time-delayed version of itself. The total electric field amplitude can be written as:

$$E_{\text{tot}}(t) = E(t) + E(t+\tau). \tag{2.25}$$

The time-averaged intensity of $E_{\text{tot}}(t)$ is

$$\begin{aligned} I(\tau) &\propto \langle E^*_{\text{tot}}(t) E_{\text{tot}}(t) \rangle \\ &\propto \langle E^*(t)E(t)\rangle + \langle E^*(t+\tau)E(t+\tau)\rangle + \langle E^*(t)E(t+\tau)\rangle + \langle E(t)E^*(t+\tau)\rangle \\ &\propto 2\langle |E(t)|^2 \rangle + 2\text{Re}[\langle E^*(t)E(t+\tau)\rangle] \end{aligned} \tag{2.26}$$

Since $E(t)$ is a plane wave of constant average intensity, the first-order coherence function is

$$g^{(1)}(\tau) = \frac{\langle E^*(t)E(t+\tau)\rangle}{\langle |E(t)|^2 \rangle}. \tag{2.27}$$

Substituting $g^{(1)}(\tau)$ into equation 2.26, we have

$$\begin{aligned} I(\tau) &\propto 2\langle |E(t)|^2 \rangle \left(1 + \text{Re}[g^{(1)}(\tau)]\right) \\ &= 2I_0 \left(1 + \text{Re}[g^{(1)}(\tau)]\right). \end{aligned} \tag{2.28}$$

Since the maximum value of $\text{Re}[g^{(1)}(\tau)]$ is $|g^{(1)}(\tau)|$ and the minimum value is $-|g^{(1)}(\tau)|$, we can write the maximum and minimum values of the intensity as

$$I_{\text{max/min}} = 2I_0 \left(1 \pm \left|g^{(1)}(\tau)\right|\right). \tag{2.29}$$

Finally, substituting this equation into equation 2.1, we see that the visibility of interference fringes can be expressed as

$$V = \left|g^{(1)}(\tau)\right|. \tag{2.30}$$

Therefore, the formation of interference fringes with unity visibility corresponds to $\left|g^{(1)}\right| = 1$, which can now be taken as the definition of first-order coherent light. However, in Glauber's formulation this is not a sufficient condition to determine if

light is perfectly coherent. Perfectly coherent light, such as an ideal laser beam*, requires coherence to all orders such that $\left|g^{(1)}\right| = \left|g^{(2)}\right| = \ldots = \left|g^{(n)}\right| = 1$ [159, 189].

For chaotic light, such as we encountered in the previous section, we can also relate $g^{(1)}$ and $g^{(2)}$. By combining equations 2.21 and 2.30, we have

$$g^{(2)}(\tau) = 1 + \left|g^{(1)}(\tau)\right|^2. \tag{2.31}$$

Since the visibility ranges from $V = 0$ to $V = 1$, we see that $g^{(2)}(\tau) \geq 1$ for chaotic light. We saw an example of this behavior in Fig. 2.3 for the case of a star modeled as a disk of uniform average intensity.

Armed with this new language of orders of coherence, we can return to the 1956 tabletop experiment of Hanbury Brown and Twiss and reexamine it in the quantum picture of light consisting of discrete photons (Fig. 2.5). Now, instead of having detectors that measure continuous optical intensities, the detectors consist of single-photon counters. We will consider temporal rather than spatial coherence in this example, so that we observe detection events with time delay $\tau$ rather than separation distance $d$. The analog of correlations between the intensities $I_1(t)$ and $I_2(t + \tau)$ measured at two detectors is correlations in the photon detection events separated by time $\tau$. In particular, $\tau = 0$ corresponds to the case of simultaneous detection events by detectors $D_1$ and $D_2$. We now need to develop a quantum formulation of the second-order coherence $g^{(2)}(\tau)$ to describe this. Following ref. [188], let us consider an electromagnetic field in an initial state $|\psi_i\rangle$. If we detect a photon in this field, then the absorption of a photon by the detector removes one photon from $|\psi_i\rangle$. We can express this using creation and annihilation operators $\hat{a}^\dagger$ and $\hat{a}$, such that a detection event is represented by $\hat{a}|\psi_i\rangle$. Restricting ourselves to the simultaneous detection case $g^{(2)}(0)$, we see that two detections correspond to $\hat{a}\hat{a}|\psi_i\rangle$. The electromagnetic

*It was in fact the invention of the maser in the 1950s, together with the HBT experiments, that prompted Glauber's development of orders of coherence.

field after the detection events can be described by a complete set of final states $|\psi_f\rangle$. The correlation $g^{(2)}(0)$ is related to the joint detection probability, which itself is related to the transition rate from $|\psi_i\rangle$ to the final states $|\psi_f\rangle$. The transition rate is proportional to

$$\sum_{\text{all } f} |\langle\psi_f|\hat{a}\hat{a}|\psi_i\rangle|^2 = \sum_{\text{all } f} \langle\psi_i|\hat{a}^\dagger\hat{a}^\dagger|\psi_f\rangle\langle\psi_f|\hat{a}\hat{a}|\psi_i\rangle = \langle\psi_i|\hat{a}^\dagger\hat{a}^\dagger\hat{a}\hat{a}|\psi_i\rangle. \tag{2.32}$$

The expectation value of a single detection event is simply given by the number operator $\langle\hat{n}\rangle = \langle\hat{a}^\dagger\hat{a}\rangle$. From this, it follows that the quantum formulation of equation 2.24 for $\tau = 0$ is:

$$g^{(2)}(0) = \frac{\langle\hat{a}^\dagger\hat{a}^\dagger\hat{a}\hat{a}\rangle}{\langle\hat{a}^\dagger\hat{a}\rangle\langle\hat{a}^\dagger\hat{a}\rangle}. \tag{2.33}$$

Note that the detection process has naturally placed the operators in normal order.

It will be useful to express equation 2.33 in terms of number operators [160]. Using the commutation relation $[\hat{a}, \hat{a}^\dagger] = 1$, we have

$$g^{(2)}(0) = \frac{\langle\hat{a}^\dagger(\hat{a}\hat{a}^\dagger - 1)\hat{a}\rangle}{\langle\hat{a}^\dagger\hat{a}\rangle\langle\hat{a}^\dagger\hat{a}\rangle} = \frac{\langle\hat{a}^\dagger\hat{a}\hat{a}^\dagger\hat{a}\rangle - \langle\hat{a}^\dagger\hat{a}\rangle}{\langle\hat{a}^\dagger\hat{a}\rangle\langle\hat{a}^\dagger\hat{a}\rangle} = \frac{\langle\hat{n}^2\rangle - \langle\hat{n}\rangle}{\langle\hat{n}\rangle^2}. \tag{2.34}$$

The variance $(\Delta n)^2 = \langle\hat{n}^2\rangle - \langle\hat{n}\rangle^2$, so

$$g^{(2)}(0) = 1 + \frac{(\Delta n)^2 - \langle\hat{n}\rangle}{\langle\hat{n}\rangle^2}. \tag{2.35}$$

The value of $g^{(2)}(0)$ enables us to classify the distribution of photons emitted by the source [160]. As we have seen before, the HBT effect with a chaotic source of light (such as a mercury arc lamp or a star) produces a value of $g^{(2)}(0) > 1$ with $g^{(2)}(0) > g^{(2)}(\tau > 0)$. In the photon picture, this indicates that the expectation value of coincident detections is greater than that for independent events, so photons emitted by the source tend to arrive at the detectors in pairs. This is known as bunched light, since it implies that the photon stream has a clustered distribution. If

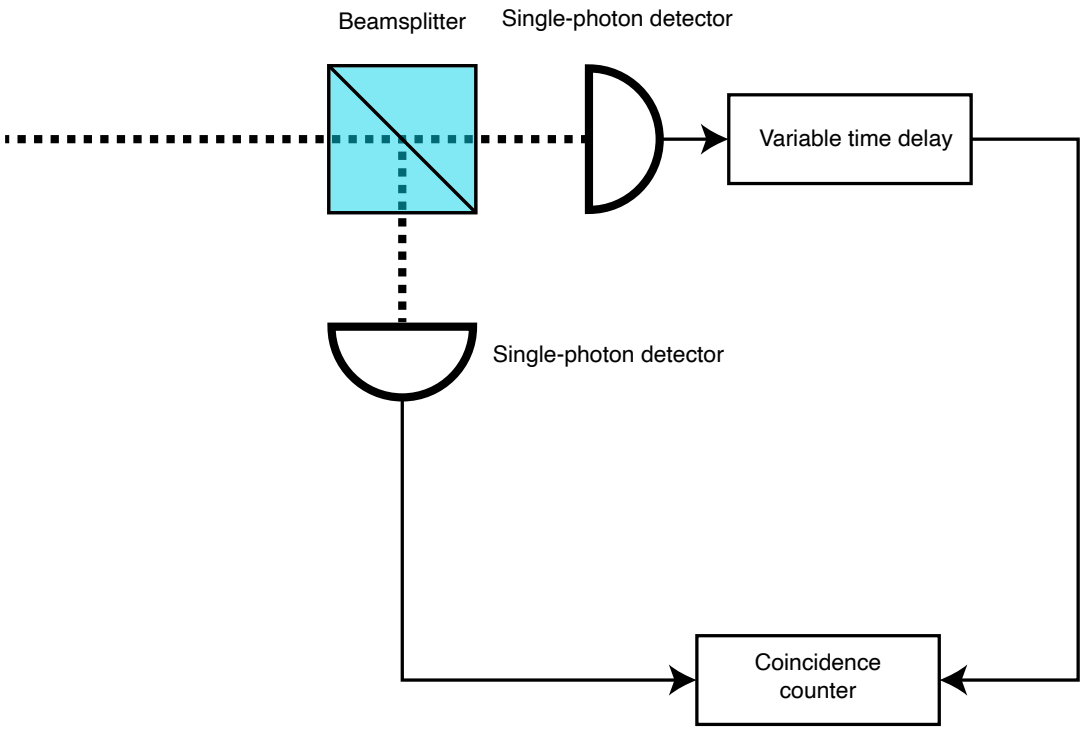


**Figure 2.5: Photon interpretation of the Hanbury Brown and Twiss experiment.** We reconsider the Hanbury Brown and Twiss tabletop experiment in the photon picture. A variable time delay is used to look at temporal rather than spatial correlations in this setup. Figure adapted from refs. [160, 190].

we instead have a coherent source of light, such as a laser, then by definition $g^{(2)}(0) = 1$. From equation 2.35, this implies that the variance $(\Delta n)^2 = \langle n \rangle$, which is a property of a Poissonian distribution. Indeed, it can be shown that the distribution of photons in a coherent beam of light obeys Poissonian statistics [160, 189]. The Poissonian number fluctuations are also referred to as shot noise. Since we have just seen that the photons emitted from a chaotic source are bunched, $(\Delta n)_{\text{chaotic}} > (\Delta n)_{\text{coherent}}$ and we can describe the bunched light as obeying super-Poissonian statistics. Classically, perfectly coherent light has the lowest intensity noise of any source. However, it is clear from the photon picture that we could imagine spacing the photons more regularly, or even perfectly regularly. This is referred to as antibunching, which

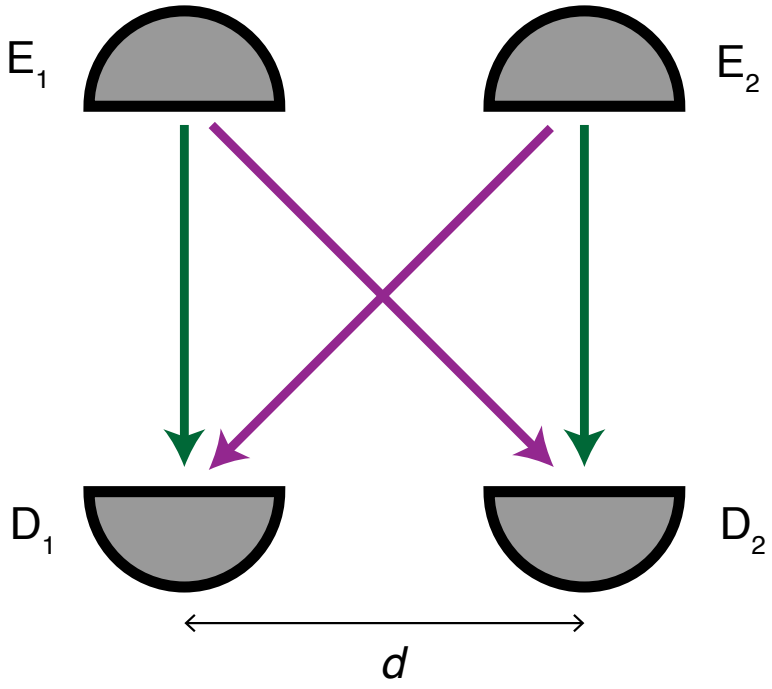


**Figure 2.6: Toy model of the HBT effect.** The quantum mechanical amplitudes associated with the two-particle trajectories shown in green and purple interfere, leading to an oscillating joint detection probability as a function of detector separation $d$. For $d = 0$, bosons exhibit bunching due to constructive interference.

generally corresponds to sub-Poissonian light*. Antibunched light satisfies $g^{(2)}(0) < 1$ and $g^{(2)}(0) < g^{(2)}(\tau > 0)$, and it represents a purely quantum effect. Photon antibunching was first observed in 1977 by ref. [193] using a sub-Poissonian source of light in an HBT experiment.

In the preceding discussion, we have described *how* the value of $g^{(2)}(\tau)$ measured in an HBT experiment reveals the distribution of photons in a beam of light, but what we have not yet given is an intuitive picture for *why* this bunching and antibunching occurs. Some intuition can be gained by a toy model of the HBT effect proposed by Fano in 1961 and shown in Fig. 2.6 [194]. As in the example of Fig. 2.2, we again have

*There are some situations in which sub-Poissonian light can actually exhibit photon bunching rather than antibunching [191], as well as where super-Poissonian light exhibits antibunching [192]. In the main text, we will use the terms sub-Poissonian and antibunching interchangeably (and similarly for super-Poissonian and bunching) since both properties will be simultaneously satisfied for all of the cases that we consider.

two emitters of light and two detectors; however, we now treat the light as consisting of discrete photons rather than classical waves. Photons originating from emitters $E_1$ and $E_2$ can arrive at detectors $D_1$ and $D_2$ in two different ways ($E_1 \to D_1$, $E_2 \to D_2$ and $E_1 \to D_2$, $E_2 \to D_1$). If the two paths are indistinguishable, then their quantum mechanical amplitudes interfere. For detectors at zero separation, the amplitudes interfere constructively, resulting in both detectors registering photon counts ($g^{(2)}(d = 0) > 1$). Although this photon bunching can be explained classically, the toy model can also capture the phenomenon of antibunching. For instance, if there is only one emitter instead of two, then coincident detection of multiple photons is impossible and we will measure $g^{(2)}(d = 0) < 1$. Moreover, if we have two emitters but replace the bosonic photons with fermions, then the constructive interference of indistinguishable photon paths becomes destructive interference. The HBT experiment with fermionic particles, therefore, will result in $g^{(2)}(d = 0) < 1$. This was first observed in refs. [162, 163] with electrons.

## 2.2 The HBT effect with ultracold atoms in an optical lattice

As we mentioned at the start of section 2.1, the HBT effect has been observed with many different platforms, but the one with the most relevance for the work presented in this thesis is that of ultracold bosonic atoms in an optical lattice [168, 195–198]. An HBT experiment with this platform proceeds as follows (Fig. 2.7). The atoms are initially confined in an optical lattice, and their density distribution is the analog of the source's intensity distribution in the optical HBT effect. The atoms are then released from the optical lattice and after a certain time of flight are detected by an imaging system. Whereas in the previous section we considered the case of two detectors separated by a displacement $\mathbf{d}$, here we acquire a two-dimensional image

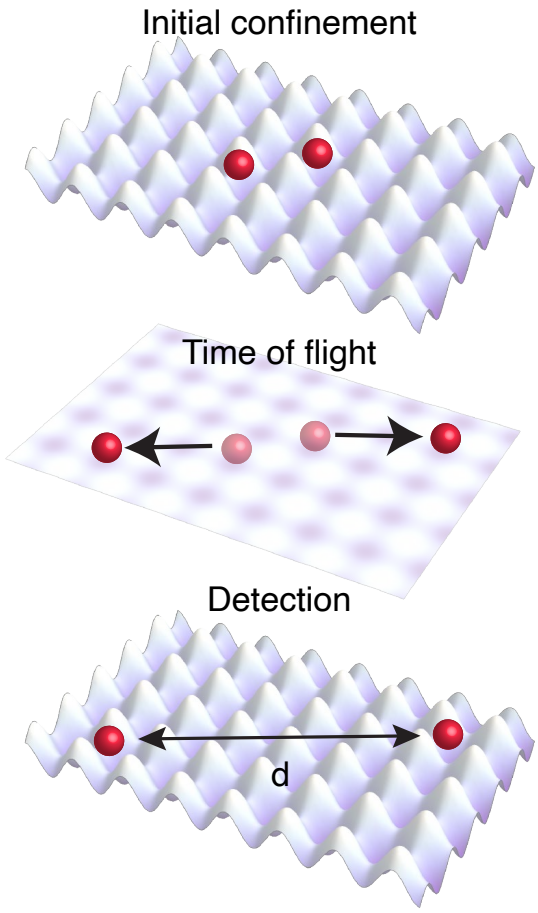


**Figure 2.7: The HBT effect in an optical lattice experiment.** Particles initially confined in an optical lattice are released in time of flight. For bulk experiments, detection occurs by a comparatively fast absorption imaging process, while for the slower process of quantum gas microscopy (the case shown here), the lattice needs to turn back on to pin the distribution prior to imaging.

of the atoms after time of flight. The density-density correlation proportional to $\langle \hat{n}(\mathbf{x})\hat{n}(\mathbf{x}+\mathbf{d})\rangle$ is therefore determined by integrating over all positions $\mathbf{x}$ in the image.

The phase coherence of the atomic wavefunctions prior to time of flight determines the measured $g^{(2)}(\mathbf{d})$ correlation in an HBT experiment. For example, a superfluid in a weak lattice potential possesses global phase coherence and corresponds to the coherent light source described in section 2.1.2. Accordingly, it has first-order coherence and forms an interference pattern in time of flight [199]. Since a perfectly

coherent source is coherent to all orders, $g^{(2)}(\mathbf{d}) = 1$ for the superfluid and a plot of the density-density correlation appears featureless (the denominator of $g^{(2)}$ normalizes away the density structure of the superfluid's interference pattern [200]). Let us now consider bosonic atoms initially pinned in a deep optical lattice, as would be the case for a Mott insulator. Since there is no phase coherence in this situation between atoms on different sites, no interference pattern forms after time of flight. However, the detected atom distribution *does* contain density-density correlations. In particular, an HBT experiment reveals bunching correlations with $g^{(2)} > 1$.

We can now derive the detailed form of $g^{(2)}(\mathbf{d})$ for bosonic atoms initially localized in a deep optical lattice. This derivation also holds for the case of non-interacting bosonic molecules, so it will be of use for the experiment described in section 2.4. The key result will be that $g^{(2)}(\mathbf{d}) - 1$ is proportional to the absolute square of the Fourier transform of the initial atomic distribution. In the process we will see what the requirements are on the time of flight for this relation to apply. The following derivation closely follows that of ref. [198], which the reader is directed to for more details.

We begin by considering bosonic atoms confined in a deep two-dimensional optical lattice. The ground state of an atom localized to a lattice site is well approximated by a Gaussian wavefunction. If we release that atom in time of flight, then the time evolution of the wavefunction is given by:

$$\psi(\mathbf{x}, t) = W(\mathbf{x}, t) e^{\frac{i\hbar t \mathbf{x}^2}{2m\sigma_0^2 \sigma(t)^2}} \tag{2.36}$$

where $m$ is the mass of the atom, $\sigma_0$ is the width of the Gaussian wavefunction at time $t = 0$, W($\mathbf{x}$,t) is the Gaussian envelope

$$W(\mathbf{x}, t) = \frac{1}{(2\pi\sigma(t)^2)^{3/4}} e^{-\frac{\mathbf{x}^2}{2\sigma(t)^2}}, \tag{2.37}$$

and $\sigma(t)$ is the width of the Gaussian envelope:

$$\sigma(t) = \sqrt{\sigma_0^2 + \frac{\hbar^2 t^2}{\sigma_0^2 m^2}}. \tag{2.38}$$

If the time of flight $t$ satisfies $t \gg m\sigma_0^2/\hbar$, then we have

$$\sigma(t) = \frac{\hbar t}{\sigma_0 m}. \tag{2.39}$$

Note that $\sigma_0$ for the ground state of a harmonic oscillator with trap frequency $\omega$ is $\sqrt{\hbar/m\omega}$, so the long time of flight condition can be written as

$$t \gg \frac{1}{\omega_{\text{latt}}} \tag{2.40}$$

where $\omega_{\text{latt}}$ refers to the on-site trap frequency of the optical lattice (here taken to be isotropic for simplicity). Substituting equation 2.39 into equation 2.36, we have

$$\psi(\mathbf{x}, t) = W(\mathbf{x}, t) e^{\frac{im\mathbf{x}^2}{2\hbar t}}. \tag{2.41}$$

We can now define the bosonic field operator $\hat{a}(\mathbf{x}, t)$ as

$$\hat{a}(\mathbf{x}, t) = \sum_j \psi(\mathbf{x} - \mathbf{x}_j, t)\hat{a}_j \tag{2.42}$$

where $\hat{a}_j$ is the bosonic annihilation operator at lattice site $j$ with position $\mathbf{x}_j$ and the sum is over all lattice sites. The number operator is then given by

$$\begin{aligned}\hat{n}(\mathbf{x},t) &= \hat{a}^\dagger(\mathbf{x},t)\hat{a}(\mathbf{x},t) \\ &= \sum_{j,k} \psi^*(\mathbf{x}-\mathbf{x}_j,t)\psi(\mathbf{x}-\mathbf{x}_k,t)\hat{a}_j^\dagger\hat{a}_k \\ &= \sum_{j,k} W^*(\mathbf{x}-\mathbf{x}_j,t)W(\mathbf{x}-\mathbf{x}_k,t)e^{\frac{im}{2\hbar t}(-(\mathbf{x}-\mathbf{x}_j)^2+(\mathbf{x}-\mathbf{x}_k)^2)}\hat{a}_j^\dagger\hat{a}_k \\ &= \sum_{j,k} W^*(\mathbf{x}-\mathbf{x}_j,t)W(\mathbf{x}-\mathbf{x}_k,t)e^{\frac{im}{2\hbar t}((\mathbf{x}_k^2-\mathbf{x}_j^2)+2\mathbf{x}\cdot(\mathbf{x}_j-\mathbf{x}_k))}\hat{a}_j^\dagger\hat{a}_k.\end{aligned} \tag{2.43}$$

For a sufficiently long time of flight, the Gaussian envelope is approximately uniform over the initial positions of the atoms and we can express it simply as $W(\mathbf{x},t)$. Specifically, this requires that $\sigma(t) \gg s_0$ where $s_0$ characterizes the width of the initial atomic distribution. Using equation 2.39 and $\sigma_0 = \sqrt{\hbar/m\omega_{\text{latt}}}$, we see that this simplification of the Gaussian envelope requires

$$t \gg s_0\sqrt{\frac{m}{\hbar\omega_{\text{latt}}}}. \tag{2.44}$$

We can now write equation 2.43 as

$$\hat{n}(\mathbf{x},t) = \sum_{j,k} |W(\mathbf{x},t)|^2 e^{\frac{im}{2\hbar t}((\mathbf{x}_k^2-\mathbf{x}_j^2)+2\mathbf{x}\cdot(\mathbf{x}_j-\mathbf{x}_k))}\hat{a}_j^\dagger\hat{a}_k. \tag{2.45}$$

For the density-density correlation, we need to consider the product

$$\hat{n}(\mathbf{x},t)\hat{n}(\mathbf{x}',t) = \hat{a}^\dagger(\mathbf{x},t)\hat{a}(\mathbf{x},t)\hat{a}^\dagger(\mathbf{x}',t)\hat{a}(\mathbf{x}',t). \tag{2.46}$$

Using the commutation relation $[\hat{a}(\mathbf{x},t),\hat{a}^\dagger(\mathbf{x}',t)]=\delta(\mathbf{x}-\mathbf{x}')$, we can place the operators in normal order:

$$\hat{a}^\dagger(\mathbf{x},t)\hat{a}(\mathbf{x},t)\hat{a}^\dagger(\mathbf{x}',t)\hat{a}(\mathbf{x}',t)=\hat{a}^\dagger(\mathbf{x},t)\hat{a}^\dagger(\mathbf{x}',t)\hat{a}(\mathbf{x},t)\hat{a}(\mathbf{x}',t)+\delta(\mathbf{x}-\mathbf{x}')\hat{a}^\dagger(\mathbf{x},t)\hat{a}(\mathbf{x}',t). \tag{2.47}$$

The second term produces an autocorrelation peak at $\mathbf{d}=0$ in $g^{(2)}(\mathbf{d})$. We will be interested in the structure of the density-density correlation at $\mathbf{d}\neq 0$, so we will omit this term going forward. Making the substitution $\mathbf{x}'\rightarrow\mathbf{x}+\mathbf{d}$, the density-density correlation can be expressed as

$$\hat{n}(\mathbf{x},t)\hat{n}(\mathbf{x}+\mathbf{d},t)= \\ \sum_{j,k,l,m}|W(\mathbf{x},t)|^2|W(\mathbf{x}+\mathbf{d},t)|^2 e^{\frac{im}{2\hbar t}((\mathbf{x}_k^2-\mathbf{x}_j^2+\mathbf{x}_m^2-\mathbf{x}_l^2)+2\mathbf{x}\cdot(\mathbf{x}_j-\mathbf{x}_k+\mathbf{x}_l-\mathbf{x}_m)+2\mathbf{d}\cdot(\mathbf{x}_l-\mathbf{x}_m))}\hat{a}_j^\dagger\hat{a}_l^\dagger\hat{a}_k\hat{a}_m. \tag{2.48}$$

Atoms localized in a deep optical lattice can be described by the Fock state $|n_1,n_2,\ldots,n_j,\ldots\rangle$ where $n_j$ is the occupation number of lattice site $j$. To evaluate the expectation value of $\hat{a}_j^\dagger\hat{a}_l^\dagger\hat{a}_k\hat{a}_m$ in this basis, we can consider three cases that will produce a nonzero value:

$$\langle\hat{a}_j^\dagger\hat{a}_l^\dagger\hat{a}_k\hat{a}_m\rangle=\begin{cases} n_j(n_j-1) & \text{for } j=k=l=m \\ n_jn_l & \text{for } j=k,l=m,j\neq l \\ n_jn_l & \text{for } j=m,l=k,j\neq l \end{cases} \tag{2.49}$$

This can be expressed as

$$\begin{aligned}\langle\hat{a}_j^\dagger\hat{a}_l^\dagger\hat{a}_k\hat{a}_m\rangle &= n_j(n_j-1)\delta_{jk}\delta_{jl}\delta_{jm}+(n_jn_l\delta_{jk}\delta_{lm}-n_j^2\delta_{jk}\delta_{jl}\delta_{jm}) \\ &\quad +(n_jn_l\delta_{jm}\delta_{lk}-n_j^2\delta_{jk}\delta_{jl}\delta_{jm}) \\ &= n_jn_l\delta_{jk}\delta_{lm}+n_jn_l\delta_{jm}\delta_{lk}-(n_j^2+n_j)\delta_{jk}\delta_{jl}\delta_{jm}.\end{aligned} \tag{2.50}$$

If the lattice sites are only occupied by zero or one atom, then $(n_j^2 + n_j) = 2n_j$. Using this simplification, we have

$$\langle \hat{a}_j^\dagger \hat{a}_l^\dagger \hat{a}_k \hat{a}_m \rangle = n_j n_l \delta_{jk} \delta_{lm} + n_j n_l \delta_{jm} \delta_{lk} - 2n_j \delta_{jk} \delta_{jl} \delta_{jm}. \tag{2.51}$$

The expectation value of equation 2.48 is therefore

$$\langle \hat{n}(\mathbf{x}, t) \hat{n}(\mathbf{x}+\mathbf{d}, t) \rangle = |W(\mathbf{x}, t)|^2 |W(\mathbf{x}+\mathbf{d}, t)|^2 \Big( N^2 - 2N + \sum_{j,l} e^{\frac{im}{\hbar t} \mathbf{d} \cdot (\mathbf{x}_l - \mathbf{x}_j)} n_j n_l \Big) \tag{2.52}$$

where $N$ is the total number of atoms. We can also evaluate the expectation value of equation 2.45 for positions $\mathbf{x}$ and $\mathbf{x} + \mathbf{d}$:

$$\begin{aligned} \langle \hat{n}(\mathbf{x}, t) \rangle &= N |W(\mathbf{x}, t)|^2 \\ \langle \hat{n}(\mathbf{x} + \mathbf{d}, t) \rangle &= N |W(\mathbf{x} + \mathbf{d}, t)|^2. \end{aligned} \tag{2.53}$$

So, for a given time of flight that satisfies equations 2.40 and 2.44, we can write the density-density correlation function as*

$$g^{(2)}(\mathbf{d}) = \frac{\int \langle \hat{n}(\mathbf{x}) \hat{n}(\mathbf{x} + \mathbf{d}) \rangle \, \mathrm{d}^2\mathbf{x}}{\int \langle \hat{n}(\mathbf{x}) \rangle \langle \hat{n}(\mathbf{x} + \mathbf{d}) \rangle \, \mathrm{d}^2\mathbf{x}} = 1 - \frac{2}{N} + \frac{1}{N^2} \sum_{j,l} e^{\frac{im}{\hbar t} \mathbf{d} \cdot (\mathbf{x}_l - \mathbf{x}_j)} n_j n_l \tag{2.54}$$

where we have integrated the numerator and denominator of $g^{(2)}(\mathbf{d})$ over all positions $\mathbf{x}$ in the detected 2D image. For large $N$, the second term can be ignored:

$$g^{(2)}(\mathbf{d}) = 1 + \frac{1}{N^2} \sum_{j,l} e^{\frac{im}{\hbar t} \mathbf{d} \cdot (\mathbf{x}_l - \mathbf{x}_j)} n_j n_l = 1 + \frac{1}{N^2} \left| \sum_j e^{\frac{im}{\hbar t} \mathbf{d} \cdot \mathbf{x}_j} n_j \right|^2. \tag{2.55}$$

We see that $g^{(2)}(\mathbf{d}) - 1$ is proportional to the absolute square of the Fourier transform of the initial atomic distribution. This implies that $g^{(2)}(\mathbf{d})$ will have a

*Note that the numerator is *not* in normal order in this formulation of $g^{(2)}$ as a density-density correlation, in contrast to equation 2.33. This results in the autocorrelation peak discussed in the context of equation 2.47.

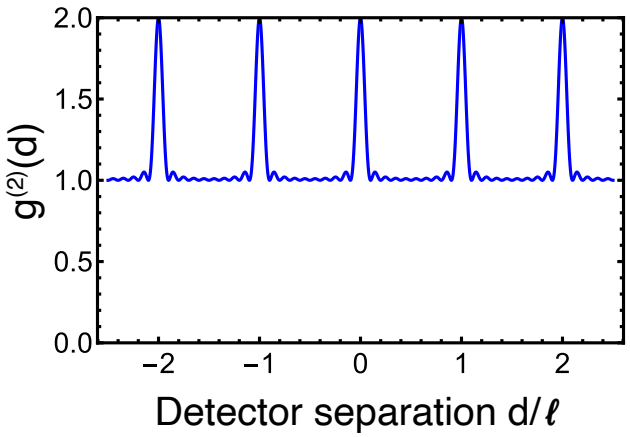


**Figure 2.8: $g^{(2)}$ correlation for a 1D distribution.** The source distribution consists of a uniformly filled 1D array with 10 lattice sites and one particle per site.

periodic structure reflecting the distribution's underlying lattice spacing. To find an expression for the periodicity of $g^{(2)}(\mathbf{d})$, for simplicity we consider a one-dimensional source distribution. The lattice site position can be written as $x_j = ja$ where $a$ is the lattice constant, so we have

$$g^{(2)}(d) = 1 + \frac{1}{N^2}\left|\sum_j e^{\frac{imjad}{\hbar t}} n_j\right|^2. \tag{2.56}$$

Labeling the period $\ell$ and setting $2\pi = ma\ell/\hbar t$, we see that

$$\ell = \frac{ht}{ma}. \tag{2.57}$$

As an example, Fig. 2.8 shows a plot of $g^{(2)}(d)$ for an initial atomic distribution consisting of a uniformly filled 1D array with 10 lattice sites and $n_j = 1$ on each site. The value of $g^{(2)}(d)$ ranges from 1 to 2, with the peaks separated by $\ell$ in agreement with equation 2.57.

We will be most interested in the case of an initial Gaussian distribution of particles in the optical lattice. For this distribution, we can find a simple expression for the

width of the peaks in $g^{(2)}(d)$. Rewriting $n_j$ as the Gaussian function $f(x_j) = Ae^{-bx_j^2}$, the finite sum in equation 2.56 can be expressed as

$$\sum_j e^{-\frac{imx_j d}{\hbar t}} f(x_j). \tag{2.58}$$

If the width of the initial Gaussian distribution spans many lattice sites, then we can treat $j$ as a continuous variable and make the replacement:

$$\sum_{j=-\infty}^{\infty} \sim \int_{-\infty}^{\infty} \mathrm{d}j = \frac{1}{a}\int_{-\infty}^{\infty} \mathrm{d}x \tag{2.59}$$

where we have used $x = ja$. So, equation 2.58 becomes

$$\frac{1}{a}\int_{-\infty}^{\infty} \mathrm{d}x f(x) e^{-\frac{imxd}{\hbar t}}. \tag{2.60}$$

This now has the form of a continuous Fourier transform

$$\tilde{f}(\xi) = \int_{-\infty}^{\infty} \mathrm{d}x f(x) e^{-2\pi i \xi x} \tag{2.61}$$

with the identification

$$\xi = \frac{md}{ht}. \tag{2.62}$$

Recall that the Fourier transform of a Gaussian function $f(x) = Ae^{-bx^2}$ is given by

$$\int_{-\infty}^{\infty} \mathrm{d}x f(x) e^{-2\pi i \xi x} = A\sqrt{\frac{\pi}{b}} e^{-\frac{\pi^2 \xi^2}{b}}. \tag{2.63}$$

Using equation 2.62, we see that the exponential on the right hand side of equation 2.63 is

$$e^{-\frac{\pi^2 m^2 d^2}{b\hbar^2 t^2}}. \tag{2.64}$$

If the width of the initial Gaussian distribution is $s_0$, then $b = 1/(2s_0^2)$ and the exponential becomes

$$e^{-\frac{2s_0^2\pi^2m^2d^2}{\hbar^2t^2}}. \tag{2.65}$$

Since $g^{(2)}(d) - 1$ is proportional to the absolute square of the Fourier transform, we see that

$$g^{(2)}(d) - 1 \propto e^{-\frac{4s_0^2\pi^2m^2d^2}{\hbar^2t^2}} \equiv e^{-\frac{d^2}{\delta^2}}. \tag{2.66}$$

Therefore, for an initial Gaussian distribution of half-width $s_0$ (at $e^{-\frac{1}{2}}$ of the maximum), the half-width $\delta$ of the correlation peaks at $e^{-1}$ of the maximum is given by

$$\delta = \frac{\hbar t}{ms_0}. \tag{2.67}$$

Before concluding this section, it is worth remarking on one assumption on the time of flight that we did *not* make. In conventional measurements of the density distribution $\langle\hat{n}(\mathbf{x})\rangle$ after time of flight it is generally the external harmonic confinement that sets the minimum time of flight to reach the "far-field" regime, defined as when the density distribution corresponds to the momentum distribution prior to time of flight [201]. However, when measuring the density-density correlation in an HBT experiment it is primarily the on-site confinement that sets the far-field condition (the requirement of equation 2.40 is more important to satisfy than that of equation 2.44). For the density distribution in time of flight to map to the initial momentum distribution, it must be proportional to the Fourier transform of the initial source distribution:

$$\langle\hat{n}(\mathbf{x})\rangle \propto \sum_{j,k} e^{\frac{im}{\hbar t}\mathbf{x}\cdot(\mathbf{x}_j-\mathbf{x}_k)}\langle\hat{a}_j^\dagger\hat{a}_k\rangle. \tag{2.68}$$

When a cloud is released from a lattice in time of flight, assuming $t$ is much greater than the inverse on-site trap frequency, its density distribution is given by (see equa-

tion 2.45):

$$\langle \hat{n}(\mathbf{x}) \rangle \propto \sum_{j,k} e^{\frac{im}{\hbar t}\mathbf{x}\cdot(\mathbf{x}_j - \mathbf{x}_k) - \frac{im}{2\hbar t}(\mathbf{x}_j^2 - \mathbf{x}_k^2)} \langle \hat{a}_j^\dagger \hat{a}_k \rangle. \tag{2.69}$$

The second term of the exponent, representing a quadratic phase factor, must be small compared to the first term of the exponent to recover the far-field distribution given by equation 2.68. In the case of a condensate of size $s_0$, for example, this condition implies that $t \gg ms_0^2/\hbar \sim 1/\omega_{\text{ext}}$ where $\omega_{\text{ext}}$ is the trap frequency due to the external harmonic confinement. By contrast, in deriving the density-density correlation we have seen that the quadratic phase factors cancel without any need for the assumption $t \gg 1/\omega_{\text{ext}}$ (this cancellation occurs between equations 2.48 and 2.52). Therefore, the condition to reach the far-field in an HBT measurement is simply $t \gg 1/\omega_{\text{latt}}$.

## 2.3 The molecular quantum gas microscope

Conventional absorption imaging has been used previously to observe the HBT effect with bosonic atoms [168, 196]. However, in our experiment with Feshbach molecules, a quantum gas microscope was critical for detecting the density-density correlations. To understand why, let us first characterize the strength of the HBT signal by the integrated value of $g^{(2)}(\mathbf{d}) - 1$ over one period of the correlation. For the case of a 2D source distribution with 2D detection, we can express this signal $S$ as [200]:

$$S = \int_{\ell^2} \left( g^{(2)}(\mathbf{d}) - 1 \right) \mathrm{d}^2\mathbf{d} = \frac{\ell^2}{N^2} \sum_j n_j^2 \tag{2.70}$$

where we have used equation 2.55 and Parseval's theorem to evaluate the integral. If we make the simplification of a uniformly filled lattice with occupation per site $n$ and number of occupied sites $N_{\text{occ}}$, then

$$\sum_j n_j^2 = \sum_j n^2 = n^2 N_{\text{occ}} = \frac{nN}{N_{\text{occ}}} N_{\text{occ}} = nN. \tag{2.71}$$

So, in the uniform filling case we have

$$S = \frac{\ell^2 n}{N}. \tag{2.72}$$

Therefore, we see that the integrated value of $g^{(2)}(\mathbf{d})-1$ over one period scales linearly with the density. For HBT experiments with Mott insulators of ultracold bosons, this density can be close to unity. However, achieving high-filling optical lattices of molecules is a long-standing challenge in the field (our group's efforts toward this goal are in fact the subject of chapter 5). As we will see shortly, in our experiment measuring the HBT effect with Feshbach molecules, the peak filling was 15%, resulting in a significant reduction of $S$ for fixed $\ell, N$.

By writing equation 2.72 as $S = \ell^2/N_{\mathrm{occ}}$, we can equivalently understand the signal strength to be related to the size of the source for fixed $\ell$. One must therefore compromise at a given lattice filling between having enough particles to acquire the HBT signal within a reasonable number of experimental repetitions and having a small enough source size so that the signal is reasonably strong. In our case, the low molecule filling led us to adopt experimental parameters such that the predicted peak width (equation 2.67) of the density-density correlation was less than one lattice site. This brings us to an additional consideration for detecting the HBT effect. Although theoretical correlation peak widths can be infinitesimally narrow while preserving a peak height of $g^{(2)} = 2$, in practice the correlation peak is integrated over a certain detection bin size. For absorption imaging, this bin size is given by the effective point spread function [198], while for microscopy the bin size corresponds to one lattice site. If the bin size is much larger than the width of the correlation peak, then the measured correlation in that bin averages in the background value of $g^{(2)}$, reducing the height of the peak. The narrow peak widths for the molecular HBT signal would

have therefore led to dramatically smaller values of $g^{(2)}$ with absorption imaging, while our quantum gas microscope enabled us to measure a large value of $g^{(2)} \sim 1.6$.

Here, we present a brief overview of the NaRb molecular quantum gas microscope as well as the experimental sequence for producing and detecting individual Feshbach molecules. A detailed description can be found in the thesis of Lysander Christakis [112]. The transfer of the Feshbach molecules to the ground state is described in chapter 3. Later changes to the apparatus in order to achieve higher molecular phase-space densities are discussed in detail in chapter 5.

Our experiment begins by loading a dual-species magneto-optical trap (MOT) with typically $8 \times 10^8$ Na atoms and $3 \times 10^6$ Rb atoms from two separate 2D-MOTs in 8 s. We deliberately load fewer Rb atoms than Na because we use the Na as a sympathetic coolant for the Rb during forced evaporative cooling. For Na, we employ a dark-spot MOT to increase its initial phase-space density. We then cool the Na atoms in an optical molasses, at the end of which the temperature of the Na atoms is $\sim$140 $\mu$K. The $|F = 1, m_F = -1\rangle$ atoms are loaded into a magnetic quadrupole trap by ramping a magnetic field gradient to 174 G/cm. The temperature of the mixture after loading the magnetic trap is $\sim$160 $\mu$K. We perform forced microwave evaporation of the Na atoms by flipping atoms in $|1, -1\rangle$ to $|2, -2\rangle$. The Rb atoms are sympathetically cooled. In order to minimize atom loss near the center of the trap where the magnetic field goes to zero, we plug the trap with a repulsive laser beam using 10 W of 532 nm light focused to a 45 $\mu$m waist.

The evaporation in the magnetic trap lasts for 20 s. Halfway through the evaporation, a crossed optical dipole trap (XODT) is ramped up to 18 W. The dipole trap is created using a single beam at 1064 nm folded into a 90° bowtie configuration, with the two intersecting arms orthogonally polarized. The waist at the atoms is 105 $\mu$m. At the end of the evaporation in the quadrupole trap, the magnetic field is ramped down and the atoms are transferred to the optical trap. At this point, the atom

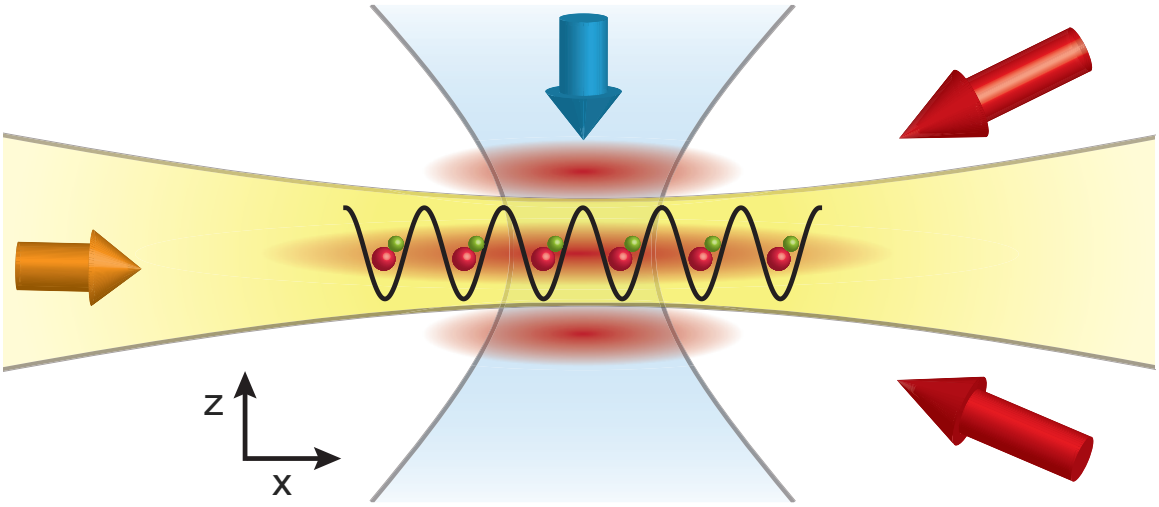


**Figure 2.9: Schematic of relevant optical potentials.** The yellow beam depicts the 1064 nm light sheet, and the red beams represent the vertical lattice formed by a 16° intersection of two 1064 nm beams. Two overlapping dimple beams with wavelengths 840 nm and 640 nm (shown in blue) help load a small, reproducible number of Rb and Na atoms on every experimental cycle. The 2D lattice at 1064 nm forms an in-plane sinusoidal potential.

number is $2.3 \times 10^6$ ($6 \times 10^5$) for Na (Rb) and the temperature of the mixture is 10 $\mu$K. We perform an optical evaporation by lowering the depth of the optical trap exponentially to 340 mW over 4 s. A bias magnetic field of 8 G is applied during the optical evaporation to suppress spin-changing collisions. To avoid differential gravitational sag between the Na and Rb atoms, we turn on an 80 mW 1064 nm light sheet beam (waists $w_z = 14\,\mu$m, $w_r = 235\,\mu$m) during the XODT evaporation.

At the end of the evaporation, we achieve a dual BEC with $2 \times 10^5$ atoms of each species. We perform an RF Landau-Zener transfer of the atoms in both species to the $|1, 1\rangle$ state, the entrance channel for the Feshbach resonance we use. To prepare a 2D system, we increase the depth of the light sheet to 2 W to reduce the vertical size of the clouds and transfer the atoms into a single layer of a vertical lattice. The vertical lattice is created by two 1064 nm beams intersecting at 16°, resulting in a lattice spacing of 3.8 $\mu$m (Fig. 2.9).

Our approach to forming Feshbach molecules is to perform the association of atoms in an optical lattice. On lattice sites containing one Na atom and one Rb atom, molecules can be produced by ramping the magnetic field through a Feshbach resonance. Therefore, the central density of the Na and Rb clouds needs to be approximately one atom per site for efficient association. Given our trap parameters, this requires the ability to reproducibly generate small condensates on the order of one hundred atoms. Preparing such gases by evaporation in the XODT is unrealistic because of its very weak confinement. Instead, we achieve this by performing a second stage of evaporative cooling in a tightly focused bichromatic dimple trap, which allows for independent adjustment of the atom number in each species [202].

The dimple trap is formed by two overlapping beams at 840 nm and 640 nm, each focused through the microscope objective to a waist of 8 $\mu$m. Vertical confinement of the atoms continues to be provided by the vertical lattice. We use a 14 G/cm magnetic field gradient to spill atoms from the reservoir. At the end of the evaporation we lower the dimple depths to zero to load the atoms back into the vertical lattice. By tuning the relative laser powers in the 840 nm versus 640 nm dimples (both on the order of 100 $\mu$W), we can independently control the number of Na and Rb atoms that remain after the evaporation. An example histogram of the molecule number achieved in this way is shown in Fig. 2.10.

Near zero magnetic field, the Na and Rb BECs are immiscible. To increase the overlap of the spatial distributions prior to magnetoassociation, we tune the interspecies scattering length using an $s$-wave Feshbach resonance at 347.6 G [203–205] to bring the clouds into a miscible regime [206]. We quickly ramp the field above the resonance to 415.9 G, then slowly decrease the field to the zero crossing of the interspecies scattering length at 351.9 G in 20 ms. The 2D mixture is then loaded into an in-plane square lattice with spacing $a = 752$ nm created by the fourfold interference of a single 1064 nm beam (105 $\mu$m waist) in a bowtie configuration [207]. The

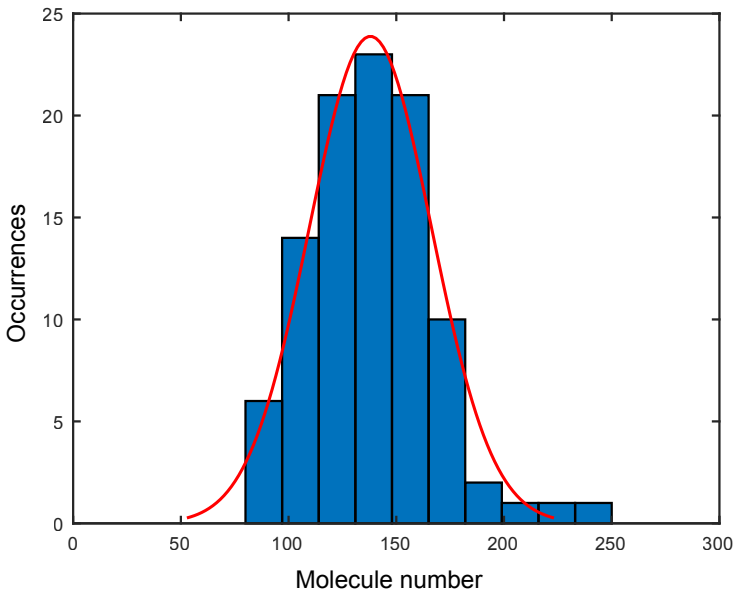


**Figure 2.10: Molecule number distribution with bichromatic dimple trap.** Here, the average number of molecules is 138 with a standard deviation of 28. The red line is a Gaussian fit to the data.

in-plane lattice depth is then ramped to $36\,E_{\mathrm{r,Na}}$ (where $E_{\mathrm{r,Na}} = h^2/8m_{\mathrm{Na}}a^2$ is the recoil energy for Na), crossing the superfluid to Mott insulator transition and freezing tunneling for both species. We associate the atoms into molecules by adiabatically ramping the magnetic field across the resonance at a rate of $2.5\,\mathrm{G/ms}$, changing the scattering length from attractive to repulsive.

For lattice sites containing one atom of each species, the theoretical conversion efficiency is close to unity. The probability of forming a molecule after the ramp through the Feshbach resonance is given by the Landau-Zener formula $p = 1 - e^{-2\pi\delta_{\mathrm{LZ}}}$, where $\delta_{\mathrm{LZ}} = \frac{hn_2}{\mu}\left|\frac{a_{\mathrm{bg}}\Delta}{\dot{B}}\right|$ [22,29]. Here, $\mu$ is the reduced mass of the two atoms, $a_{\mathrm{bg}} = 76.33\,a_0$ is the interspecies background scattering length [205], $\Delta = 4.255\,\mathrm{G}$ is the width of the resonance, $\dot{B} = 2.5\,\mathrm{G/ms}$ is the field ramp rate, and $n_2 = \int\int n_{\mathrm{Na}}(\mathbf{r})n_{\mathrm{Rb}}(\mathbf{r})d\mathbf{r}$ is the pair density on a site. The wavefunctions of the non-interacting atoms in the ground state of a site of a deep lattice can be approximated by the ground state of an anisotropic harmonic oscillator with trap frequencies $\omega_{r,\mathrm{Na}} = 2\pi \times 35.3\,\mathrm{kHz}$ and

$\omega_{z,\mathrm{Na}} = 2\pi \times 2.4\,\mathrm{kHz}$ ($\omega_{\mathrm{Rb}} = 0.88\,\omega_{\mathrm{Na}}$), which gives $n_2 = 2.3 \times 10^{19}\,\mathrm{m}^{-3}$. We therefore expect $p \approx 1$ for our experimental parameters.

Remaining free Na and Rb atoms are then selectively removed by transferring them to $|2,2\rangle$ with a microwave Landau-Zener sweep at a field of ∼346.6 G (molecule binding energy $E_\mathrm{b}/h \approx 0.7\,\mathrm{MHz}$) and applying resonant light on the $|2,2\rangle$ to $|3,3\rangle$ optical cycling transition. The transfer and removal is repeated four times for both species to achieve high efficiency. Each pulse is 50 $\mu$s in duration at $1\,\mathrm{mW/cm^2}$. The molecule lifetime in the presence of the Na optical removal light is 1710(120) $\mu$s, and the lifetime is 5720(360) $\mu$s in the presence of the Rb light. From these lifetimes, we estimate that the free atom removal pulses lead to a loss of 14% of the molecules.

To realize a quantum gas microscope for molecules, we employ a three-step process to extract site-resolved positions, as shown in Fig. 2.11a. We first ramp the magnetic field back to the attractive side of the Feshbach resonance, increasing the Franck-Condon overlap between the bound and free states of atoms on a site. We note that a confinement-induced weakly-bound state exists here due to the lattice [22, 208–211], so an adiabatic ramp across the resonance does not break apart the molecules. The confinement-induced molecules are then dissociated by addressing Na with another series of microwave transfers and optical removal pulses. The remaining Rb atoms serve as markers for the Feshbach molecule locations.

When multiple atoms are confined to the same site of a lattice, light-assisted collisions can cause pairs of atoms to be ejected from the trap during illumination with resonant light [102, 212]. Therefore, it is important to determine if light-assisted collisions during the Na optical removal pulses can also remove the Rb atoms that tag the molecule positions. We estimate that this process is negligible in our case. To understand why this is so, it is helpful to compare light-assisted collisions for Na-Rb versus the example of Rb-Rb. For homonuclear light-assisted collisions, the atoms experience an attractive potential that scales with the internuclear distance

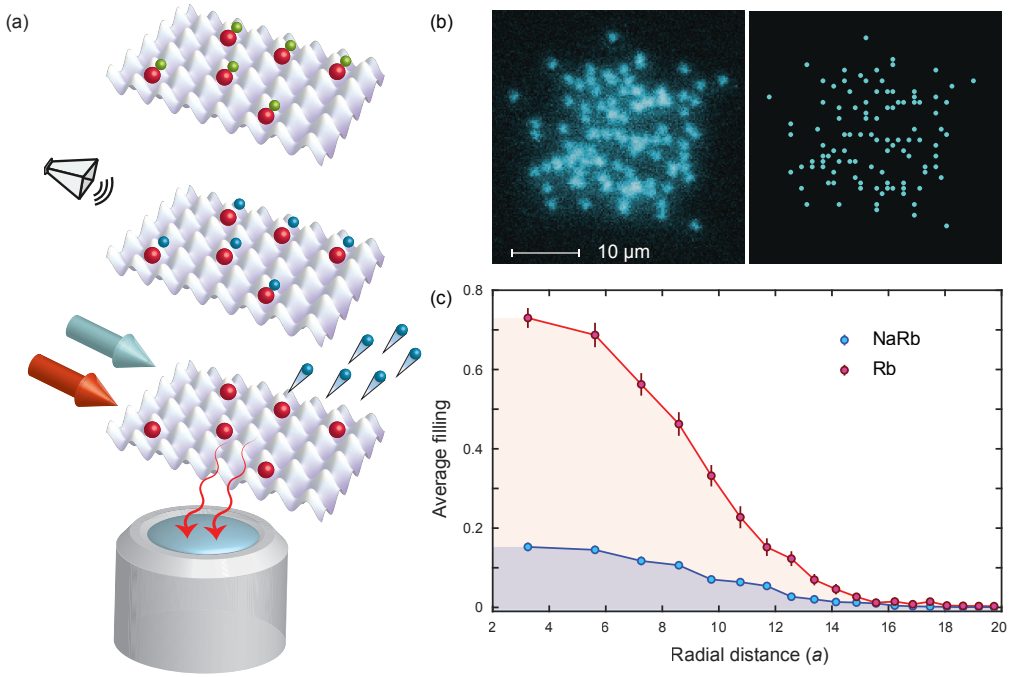


**Figure 2.11: Microscopy of molecules in an optical lattice. a)** Three-step process for detecting the molecules. An array of NaRb molecules is prepared in a lattice (top). A microwave Landau–Zener sweep flips the Na atoms from the $|1,1\rangle$ to $|2,2\rangle$ state, breaking apart the molecules into unbound Rb (red) and Na (blue) atoms (middle). A pulse of resonant light (blue beam) removes the Na atoms from the lattice (bottom). The remaining Rb atoms are laser cooled (red beam) and the fluorescence photons are collected with an objective, revealing the original positions of the molecules with single-site resolution. **b)** A sample fluorescence image of Rb atoms tagging the positions of molecules in the lattice (left). Molecule occupancy of the lattice for the fluorescence image (right). **c)** Radially averaged density profile of the NaRb molecules (blue) as well as Rb atoms (red) before associating the atoms into molecules. We observe peak fillings of 0.73(2) for the Rb atoms and 0.15(1) for the molecules. Both density profiles are averaged over 30 experimental repetitions. The error bars are standard error of the mean (s.e.m.).

$R$ as $1/R^3$ while for heteronuclear collisions the interaction potential scales as $1/R^6$. This means that a heteronuclear atom pair gains significantly less energy during each scattering event as compared to a homonuclear pair. Using known values for the $C_3$ and $C_6$ coefficients [213, 214], we estimate the energy gained by the atoms using a classical toy model in the center-of-mass frame with reduced mass $\mu$. We assume that the atoms are initially at rest with a separation of approximately 100 nm on a lattice site and that the time spent in the excited state is given by $\tau = 1/\Gamma$, where $\Gamma = 2\pi \times 10\,\mathrm{MHz}$ ($2\pi \times 6\,\mathrm{MHz}$) is the decay rate for Na (Rb). We then numerically integrate Newton's equation $d^2R/dt^2 = -3C_3/\mu R^4$ for the case of two Rb atoms, or $d^2R/dt^2 = -6C_6/\mu R^7$ for the case of one Rb and one Na atom, to determine the change in the internuclear separation during the excited state lifetime and hence the energy gained per scattering event. We estimate that the energy gained per photon from a light-assisted collision is about fourteen orders of magnitude smaller for Na-Rb pairs than for Rb-Rb pairs.

After breaking apart the molecules and removing the residual Na atoms, the magnetic field is ramped to zero in preparation for laser cooling. The 2D lattice is ramped to a depth of 6000 $E_{\mathrm{r,Rb}}$ to suppress hopping of the Rb atoms during fluorescence imaging. The light sheet potential is then pinned to a depth of 140 $\mu$K after which the vertical lattice depth is ramped down to zero.

We image the Rb atoms in the lattice by applying optical molasses cooling beams and collecting a portion of the scattered photons. We send two beams each with a 500 $\mu$m waist containing 30 $\mu$W of cooling and 6 $\mu$W of repump light through the side of the vacuum chamber, intersecting at a 90° angle in the horizontal plane to produce the requisite polarization gradients. We find that by tilting one of the molasses beams at 8° with respect to the horizontal we are able to provide sufficient cooling along the vertical direction. The cooling light is 30 MHz red-detuned from the $F = 2 \rightarrow F' = 3$ free-space transition, and the repump light is 42 MHz blue-detuned from the $F =$

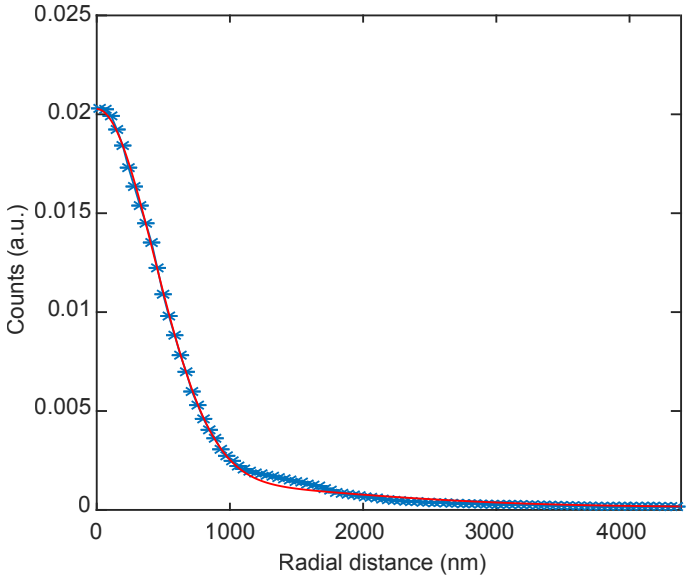


**Figure 2.12: Point spread function.** The point spread function of the quantum gas microscope with radial averaging (blue stars) and a double Gaussian fit (red line).

$1 \rightarrow F' = 2$ transition. The molasses beams are retroreflected with mirrors mounted on piezo chips oscillating at 300-400 Hz to smooth out interference patterns in the cooling beams during the exposure time. We use a custom microscope objective with NA = 0.5 (Special Optics 54-25-25) mounted directly above the vacuum chamber to collect $\sim 10^4$ photons/atom/second on an Andor Zyla 4.2 sCMOS camera* with 30x magnification and a 0.5 s exposure time. The full-width at half-maximum of the point spread function is 1010(15) nm (Fig. 2.12), which allows us to extract the positions of the Rb atoms with single-site resolution using a reconstruction algorithm [104].

Fig. 2.11b shows an example image of an *in-situ* cloud of 103 molecules. A radially-averaged density profile, averaged over 30 experimental repetitions, is shown in Fig. 2.11c. We measure a central molecule filling of 0.15(1), compared to the Rb parity-projected central filling of 0.73(2). The Rb filling may be limited by low val-

*We measure a background-subtracted value of 11,700 counts/atom/s during our 0.5 s exposure time. The sensitivity of the Andor Zyla 4.2 sCMOS camera is 0.53 electrons/count for a readout rate of 200 MHz and the "low noise and high well capacity" gain setting. The quantum efficiency of the camera at 780 nm is 0.54 electrons/photon. We therefore obtain a value of 11,500 collected photons/atom/s.

ues of $U/T$ at the superfluid to Mott insulator transition, where $U$ is the Hubbard interaction strength and $T$ is the temperature [106]. In particular, the weak confinement of the 3.8 $\mu$m spacing vertical lattice reduces the on-site interaction strength. It is difficult to characterize the Na filling in the lattice due to low signal-to-noise in absorption imaging. The molecule filling likely suffers from the additional effect of imperfect spatial overlap between the Na and Rb clouds. Our later efforts to address these issues are discussed in chapter 5.

A high molecule detection fidelity is essential for obtaining high contrast HBT interference as well as for future applications of the molecule microscope. Possible limitations on the molecule detection fidelity include imperfect atom-tagging of sites that had molecules as well as site-to-site hopping and loss of the Rb tag atoms during fluorescence imaging. We first measure the false negative molecule detection rate due to imperfect tagging. After performing the tagging protocol consisting of dissociating the molecules and optically removing Na, we ramp the field to the repulsive side of the Feshbach resonance and remove the Rb tag atoms. The false negative rate of 1.2(1)% is obtained by repeating the tagging protocol prior to fluorescence imaging to identify failures from the first attempt. During our 0.5 s imaging exposure time, we measure site-to-site hopping of 0.1(1)% and 1.7(3)% loss. The latter is consistent with the measured atom lifetime limited by background gas collisions. We additionally measure the false positive rate due to Rb atoms that did not associate into molecules and were not removed before imaging. This rate is measured by forming a molecular gas, removing stray atoms, and then reducing the magnetic field to zero without dissociating the molecules. We measure the number of Rb atoms detected and compare it to an equivalent sequence in which we dissociate the molecules before imaging. After 100 repetitions of each sequence, we find that 0.34 (5)% of the Rb tag atoms in the molecule detection sequence are also present in the sequence in which we do not deliberately detect the molecules.

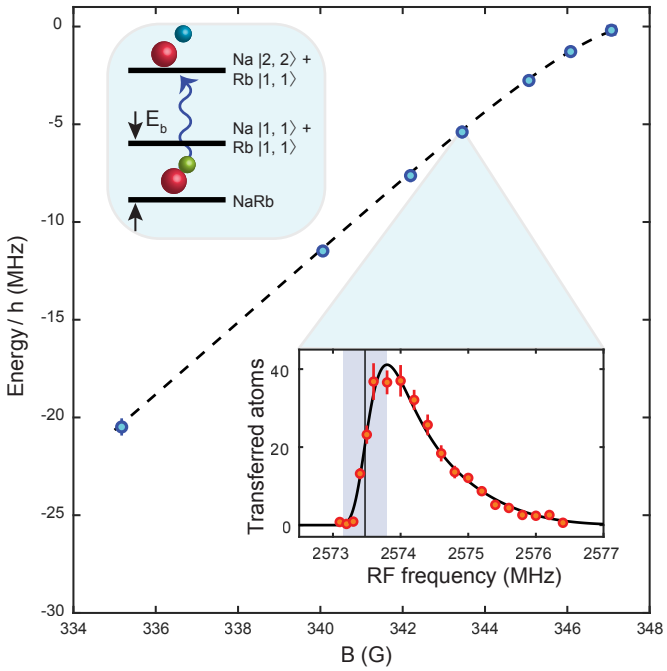


**Figure 2.13: Molecular binding energy versus magnetic field $B$.** For each field, we drive the $|1,1\rangle \rightarrow |2,2\rangle$ transition in Na to break apart the molecules (upper-left inset) and measure the resulting dissociation spectrum. We extract the bound-free transition frequency from the onset of the spectrum. We also measure the free atomic transition frequency at each field. The difference between the atomic and molecular transition frequencies gives the binding energy (blue circles). The black dashed line is the predicted binding energy from a coupled-channel calculation. The lower-right inset shows an example molecular dissociation spectrum at 343.4 G (red circles) fit to an asymmetric Gaussian (solid black line). The error bars in the inset are the s.e.m. The error on the binding energies is taken as the half-width of the shaded region of the spectrum.

We further confirm that the detected particles are molecules by measuring their binding energy as a function of magnetic field using dissociation spectroscopy (Fig. 2.13). Driving the Na $|1,1\rangle \rightarrow |2,2\rangle$ transition yields the molecular dissociation spectrum, showing a sharp onset at a microwave frequency shifted by the binding energy $E_\mathrm{b}$ from the atomic transition. Molecules that are not dissociated are not detected in the fluorescence imaging. More specifically, for each point in the dissociation spectrum (see representative example in lower-right inset of Fig. 2.13), we fix the microwave frequency and scan the magnetic field by $\sim 130\,\mathrm{mG}$, corresponding to a $\sim 300\,\mathrm{kHz}$ Landau-Zener sweep. The molecular binding energies are extracted by fitting the dissociation curves to a phenomenological function $N(\omega)$, where $N$ is the number of Na atoms transferred from the molecular state to the free $|2,2\rangle$ state:

$$\begin{aligned} N(\omega) &= \frac{p_1}{f(\omega)} e^{-8\log(2)((x-p_2)/f(\omega))^2} \\ f(\omega) &= \frac{2p_3}{1+e^{p_4(\omega-p_2)}}. \end{aligned} \tag{2.73}$$

Here, $p_i$ are free fitting parameters. The binding energy is taken to be the frequency at which the transfer $N(\omega)$ is half the peak of the fitted lineshape. We find close agreement between our measured binding energies and a coupled-channel calculation using the BOUND package [215] based on the parameters in ref. [205]. Confinement effects are ignored since they are smaller than the resolution of the measurement.

We also measure the lifetime of the NaRb molecules as a function of lattice depth and magnetic field. As shown in Fig. 2.14a, performed at our typical 2D lattice intensity of $12.5\,\mathrm{kW/cm^2}$, the molecule lifetime in the lattice is sufficiently long at all magnetic fields studied that loss can be ignored for the experiments presented in this paper. Following the removal of residual unassociated atoms at 346.6 G, we ramp the magnetic field to the target value and hold for a variable length of time. We

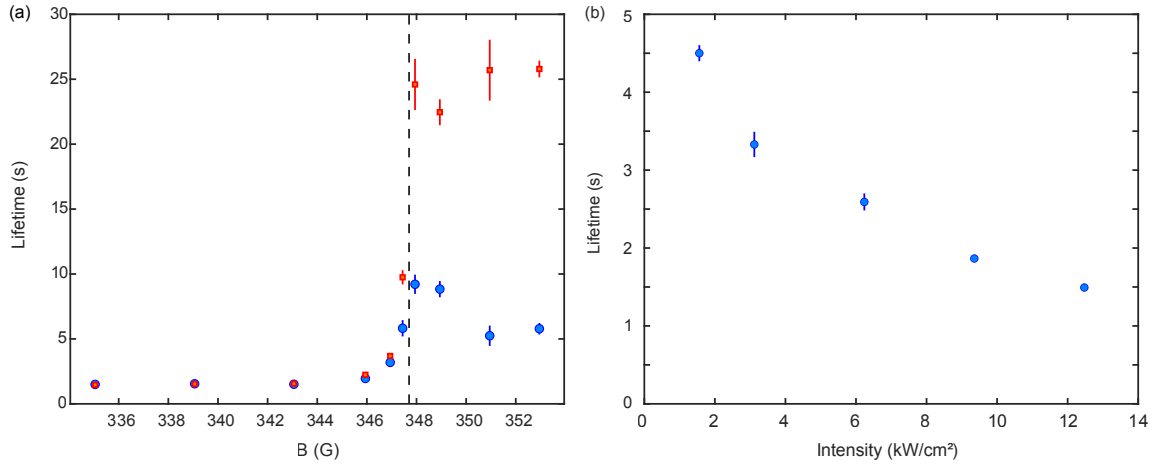


**Figure 2.14: Molecule lifetime in an optical lattice. a)** Molecule lifetime versus magnetic field for a lattice intensity of 12.5 kW/cm$^2$. Blue circles indicate the pure molecular lifetime where free atoms are removed both before and after the hold time, while the red squares do not include the second free atom removal. **b)** Lifetime versus 2D lattice depth at 335.1 G. Error bars are s.e.m.

then return the magnetic field to 346.6 G and repeat the removal of free atoms before dissociating and imaging the surviving molecules (blue circles).

On the repulsive side of the Feshbach resonance, the molecule lifetime initially decreases with decreasing magnetic field before saturating at ∼1.5 s. This follows the magnetic field dependence of the closed channel fraction of the Feshbach molecules. As has been previously observed, larger closed channel fractions increase the wavefunction overlap with electronically excited molecular states, enhancing molecule loss due to off-resonant excitation by the lattice beams [216, 217]. Interestingly, we find that the lifetime of the molecules also decreases above the Feshbach resonance. Since the molecules are only weakly bound due to confinement effects above the resonance [208, 210], we explore whether at these fields the molecule lifetime is limited by a mechanism that breaks apart the molecules but does not eject the remaining atoms from the trap, such as noise in the magnetic field. We therefore repeat this measurement without the final removal of stray atoms (red squares). The molecule lifetimes show the same behavior as before on the repulsive side of the resonance,

but on the attractive side we now see long lifetimes consistent with background gas-limited atomic lifetimes. This indicates that dissociation of the molecules does in fact occur in our system when holding the weakly bound molecules above the Feshbach resonance.

To examine the role of the light scattering on these lifetimes, we additionally measure the lifetimes at a fixed field of 335.1 G for five different lattice intensities (Fig. 2.14b). We see that the lifetime increases for shallower lattice depths, consistent with reduced off-resonant excitation of the molecules by the lattice. For much shallower lattice depths (not shown), molecule tunneling occurs and a single-body loss rate is no longer appropriate due to inelastic collisions between the molecules.

## 2.4 Observation of the HBT effect with ultracold molecules

Having established our molecule detection procedure, we now observe the HBT effect by measuring the density-density correlation function $g^{(2)}(\mathbf{d})$ after a time of flight (TOF). The correlation function is defined as

$$g^{(2)}(\mathbf{d}) = \frac{\int \langle \hat{n}(\mathbf{x})\hat{n}(\mathbf{x}+\mathbf{d})\rangle \, \mathrm{d}^2\mathbf{x}}{\int \langle \hat{n}(\mathbf{x})\rangle\langle \hat{n}(\mathbf{x}+\mathbf{d})\rangle \, \mathrm{d}^2\mathbf{x}} \tag{2.74}$$

where $\hat{n}(\mathbf{x})$ is the number operator at detection position $\mathbf{x}$, and $\mathbf{d}$ is the displacement between the detection positions. As can be seen in Fig. 2.15a,b, the density distribution after time of flight does not reveal any visually discernible structure, reflecting the lack of first-order coherence for particles confined in a deep lattice. The presence of second-order coherence, however, is clearly visible in the density-density correlations given by $g^{(2)}(\mathbf{d})$ (Fig. 2.15c-f).

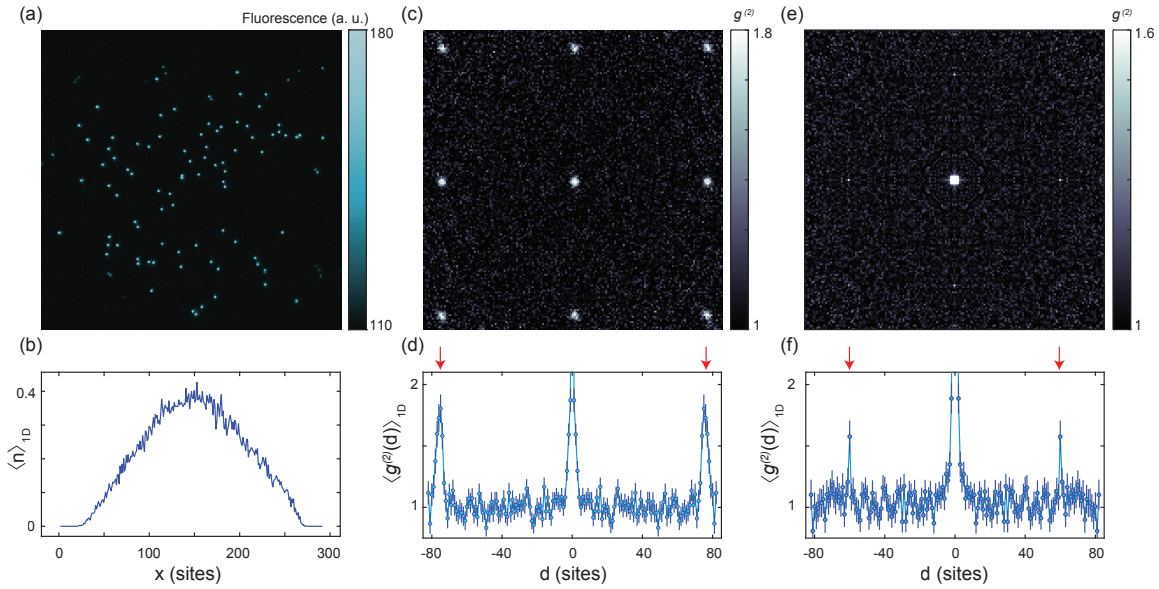


**Figure 2.15: Observation of the HBT effect with molecules. a)** Typical fluorescence image obtained after molecule TOF. **b)** Integrated density profile after TOF, averaged over 764 images. **c)** HBT correlations for Rb atoms, post-selected for images that yielded between 130 and 300 atoms. **d)** Profile of the Rb HBT correlations, taken as the average of 1D cuts along the horizontal and vertical axes of the 2D correlations. The red arrows indicate the predicted position of the interference peaks, corresponding to the reciprocal lattice spacing. **e)** HBT correlations for molecules averaged across the lattice symmetries. Images with fewer than 20 molecules were excluded from the analysis. **f)** Profile of the NaRb HBT correlations, taken as the average of 1D cuts along the horizontal and vertical axes of the 2D correlations. The red arrows indicate the predicted position of the interference peaks. The error bars are the s.e.m.

As discussed at the beginning of section 2.3, a larger signal-to-noise ratio for the HBT correlations can be achieved for higher *in-situ* lattice filling fractions. Since we achieve higher fillings with atoms than with molecules, we first benchmark the interferometry protocol with Rb atoms. We prepare a gas with 189(20) Rb atoms frozen in a 2D optical lattice (66 $E_{\mathrm{r,Rb}}$ depth), with a peak filling of 0.86(2) and an average source size $s_0 = 7(1)$ sites. We abruptly turn off the 2D lattice to initiate a 9.4(1) ms TOF in the vertical lattice. The vertical lattice confinement is set to $\omega_{\mathrm{Rb}} = 2\pi \times (3, 4, 1000)$ Hz, providing negligible radial confinement. The TOF satisfies the far-field detection condition $t \gg 2\pi/\omega_r$ (see equation 2.40), where $\omega_r = 2\pi \times 14$ kHz

is the on-site radial trap frequency of the 2D lattice for Rb. Following the TOF, we turn on the 2D lattice to pin the distribution for imaging.

The observed atomic HBT correlations are shown in Fig. 2.15c. We observe a high contrast interference pattern with average correlation peak amplitudes of 1.80(12) and an average background value of 0.999(6). The measured peak separation and width from the 1D cut in Fig. 2.15d are $\ell = 75.9(4)$ and $\delta = 2.4(2)$ sites respectively, close to the theoretically expected spacing of $\ell = 76.2(8)$ and $\delta = 1.7(3)$ sites (see equations 2.57 and 2.67). The recapture of the atoms in the 2D pinning lattice may contribute to the observed broadening of the peak width [218]. The symmetric pattern verifies that the 2D lattice axes are orthogonal and the lattice spacings along both axes are identical to better than 0.5%. This implies that $g^{(2)}(\mathbf{d})$ is invariant for $\mathbf{d}$ reflected across the $x = 0$, $y = 0$, $x = y$, and $x = -y$ symmetry axes, justifying averaging of the weaker molecular correlations across the lattice symmetries to reduce noise.

We repeat the HBT interferometry with 56(13) molecules and a mean source size $s_0 \approx 17$ sites, which is expected to produce interference peaks whose widths are on the order of the lattice spacing. The protocol is the same as that used for atoms, with the molecules released from the 2D lattice at a magnetic field of 335.1 G (with binding energy $E_\mathrm{b}/h \approx 20\,\mathrm{MHz}$). Fig. 2.15e,f show the observed molecular correlations averaged across the lattice symmetries. Since the TOF is the same as that used in the Rb atom correlation measurement, the smaller correlation peak spacing for the molecules is a direct result of their increased mass. The measured spacing is $\ell = 60.0(5)$ sites, consistent with the theoretical expectation of $\ell = 60.3(6)$ sites. While the correlation peaks are narrower than for Rb ($\delta < 1$ site), the peak amplitude remains large at 1.58(13). The average baseline is 1.04(1), with the deviation from unity caused by correlations at all distances due to shot-to-shot molecule number fluctuations. The interference contrast is sensitive to the preparation of the molecules in the same in-

ternal state and the same motional state of the vertical lattice, since these quantum numbers can provide which-path information during the free expansion; therefore, the measured contrast of 54(13)% indicates a high degree of indistinguishability of the molecules.

The primary cause of the imperfect contrast for the molecules is estimated to be due to the narrow peak width of the correlation. As mentioned in section 2.3, if the correlation peak width is smaller than the detector size of one lattice site, then the correlation peak is averaged together with baseline noise. This is the case for the molecular correlations, where the predicted correlation peak width is $\delta = 0.56(13)$ sites. Averaging over one lattice site reduces the correlations to 62(15)% of full contrast. Using the 80(12)% contrast of the Rb HBT correlations as a reference, the expected contrast of the molecular correlations is 50(14)%, consistent within error with the experimentally observed contrast of 54(13)%.

Reductions in the contrast due to hopping and loss of Rb during imaging are estimated to be negligible compared to this effect. Although we measure a hopping rate per exposure of 0.1 (1)% and a loss rate of 1.7 (3)% for the *in-situ* cloud of Rb atoms pinned near the center of the beam waists forming the 2D lattice, in the HBT experiment the distribution of the pinned atoms is much wider due to the 9.4(1) ms TOF. For a broader distribution of atoms ($\sigma = 57$ sites, where $\sigma$ is the half-width at $e^{-1/2}$ of maximum), within $1\sigma$ the hopping rate per 0.5 s exposure averages to 0.28(4)% and the average loss rate is 2.0(1)%. Beyond $1\sigma$, the average hopping and loss rates are 1.8(1)% and 7.9(2)%, respectively. The reduced microscopy fidelity is caused by an effective detuning of the molasses beams away from the optimal values since the 2D lattice beam intensity decreases with distance from the trap center. The higher loss rate increases the noise in the $g^{(2)}$ correlation measurement but does not affect the height of the correlation peaks. The higher hopping rate away from the trap center can in principle broaden the correlation peaks and reduce their amplitude,

although our simulations indicate that at $< 2\%$ this should be a negligible effect for our system.

# Chapter 3

# Quantum gas microscopy of polar molecules

Portions of this chapter are based on work previously published as

> Christakis, L., Rosenberg, J. S., Raj, R., Chi, S., Morningstar, A., Huse, D. A., Yan, Z. Z. & Bakr, W. S. Probing site-resolved correlations in a spin system of ultracold molecules. *Nature* **614**, 64-69 (2023).

This work was also presented publicly in the following talks: [219, 220].

Following our development of a molecular quantum gas microscope and its demonstration with non-interacting Feshbach molecules to measure the HBT effect, we proceeded to transfer the molecules to their absolute ground state. NaRb molecules in this state possess a large body-frame electric dipole moment, enabling their use to study dipolar physics. In this chapter, we present an overview of the structure of diatomic molecules, followed by a brief description of our stimulated Raman adiabatic passage (STIRAP) procedure for producing NaRb in the rovibrational ground state. Finally, we discuss our results using the quantum gas microscope to measure site-resolved correlations of lattice-confined polar molecules. Further details on our STIRAP setup and on our correlation measurements can be found in ref. [112].

## 3.1 Structure of diatomic molecules

In chapter 1, we discussed how the rich internal structure of diatomic molecules presents both an opportunity and a challenge in the study of quantum physics at ultracold temperatures. Here, we will talk about each component of the hierarchy of internal energy levels in turn, progressing to increasingly finer corrections. This section follows and largely adopts the notation of ref. [221].

### 3.1.1 The Born-Oppenheimer approximation and electronic structure

We begin our discussion by considering the largest contribution to the total molecular Hamiltonian, namely the electron-electron, electron-nucleus, and nucleus-nucleus Coulomb interactions. The potential energy for this interaction can be expressed as [221]:

$$\begin{aligned} V(\mathbf{R};\mathbf{r}_1,\ldots,\mathbf{r}_N) = &-\sum_{i=1}^{N}\left(\frac{Z_\mathrm{A}e^2}{4\pi\epsilon_0|\mathbf{r}_i-\mathbf{R}_\mathrm{A}|}+\frac{Z_\mathrm{B}e^2}{4\pi\epsilon_0|\mathbf{r}_i-\mathbf{R}_\mathrm{B}|}\right) \\ &+\sum_{i<j}^{N}\frac{e^2}{4\pi\epsilon_0|\mathbf{r}_i-\mathbf{r}_j|}+\frac{Z_\mathrm{A}Z_\mathrm{B}e^2}{4\pi\epsilon_0 R}, \end{aligned} \tag{3.1}$$

where the two nuclei A and B have charges $Z_\mathrm{A}e$ and $Z_\mathrm{B}e$ as well as positions $\mathbf{R}_\mathrm{A}$ and $\mathbf{R}_\mathrm{B}$, respectively. The $N$ electrons have charge $-e$, with the $i$th electron at position $\mathbf{r}_i$. $\mathbf{R}$ represents the internuclear displacement with magnitude $R$. The Schrödinger equation for this potential is quite daunting to solve, but a great simplification can often be made known as the Born-Oppenheimer approximation. It relies on the fact that the electron mass is far less than the nuclear mass, so classically in response to the same force the electronic motion is much faster than the nuclear motion [221]. Crucially, since the heavier nuclei in a diatomic molecule move a negligible amount on the timescale of the electronic motion, the positions of the nuclei may be treated

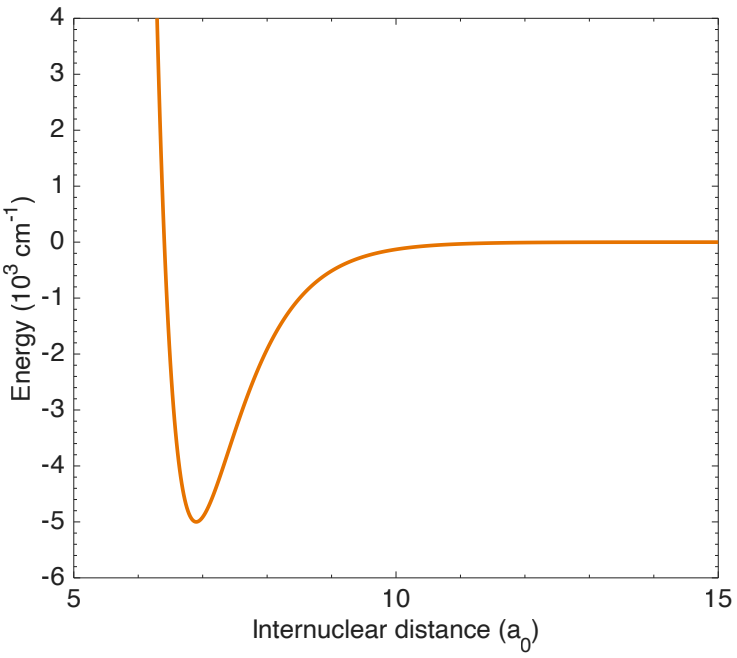


**Figure 3.1: The Morse potential.** The energy at long range is that of two isolated atoms. Due to the increasing delocalization of the electronic wavefunction as the atoms move closer together, the potential energy initially decreases. Below a certain distance the Coulomb repulsion between the nuclei causes a steep increase in the energy. The Morse potential is given by equation 3.8, and here we have used the parameters $V_0 = 5 \times 10^3\,\mathrm{cm}^{-1}$, $a = 1.4\,a_0^{-1}$, and $R_0 = 6.9\,a_0$ where $a_0$ is the Bohr radius.

as fixed when solving the electronic Schrödinger equation. This allows us to factor the total molecular wavefunction $\Psi(\mathbf{R}; \mathbf{r}_1, \ldots, \mathbf{r}_N)$ into the product of a nuclear wavefunction $F_s(\mathbf{R})$ and an electronic wavefunction $\Phi_s(\mathbf{R}; \mathbf{r}_1, \ldots, \mathbf{r}_N)$ where the $s$ subscript indexes the particular electronic state. We can then separate the molecular Schrödinger equation into an electronic wave equation and a nuclear wave equation, solving each individually.

The electronic wave equation is $H_e\Phi_s(\mathbf{R}; \mathbf{r}_1, \ldots, \mathbf{r}_N) = E_s\Phi_s(\mathbf{R}; \mathbf{r}_1, \ldots, \mathbf{r}_N)$ where the electronic Hamiltonian $H_e$ is the sum of the kinetic energy of the electrons and the potential energy of equation 3.1 with the internuclear separation taken to be a fixed parameter. We then repeatedly solve the electronic wave equation for different internuclear separations to construct the electronic eigenstates and eigenenergies as a

function of $R$. This results in electronic potential energy curves of the form plotted in Fig. 3.1, which depicts a simplified analytic model known as the Morse potential. We can understand its shape as follows. For large internuclear distances, the electronic energy asymptotically approaches that of two isolated atoms. As the atoms come closer together, the electronic energy decreases. This can be thought of as resulting from the ability of the electronic wavefunction to delocalize over a greater region (from the volume of an isolated atom to the volume of the diatomic molecule), similar to the lowering of the eigenenergy of a particle in a box as the box width increases [222]. As the internuclear separation approaches zero the electronic energy again rises (steeply) due to the Coulomb repulsion between the nuclei. For a sufficiently deep potential well, one or more bound states exist corresponding to stable molecules.

We now consider the electronic potential energy curves of NaRb depicted in Fig. 3.2 [223, 224]. We see that there are two lower energy electronic states that asymptotically connect to a Na atom and a Rb atom both in the $^2S_{1/2}$ state. The multiple higher energy curves correspond at large internuclear distance to a Na atom in the $^2S_{1/2}$ state and a Rb atom either in the excited $^2P_{1/2}$ or $^2P_{3/2}$ state. States at higher energy (for example corresponding to an excited Na atom) are outside of the range of the plot. The labels for the potential energy curves are known as molecular term symbols and for heteronuclear molecules take the form [221]:

$$^{2S+1}\Lambda^{+/-} \tag{3.2}$$

$\Lambda$ refers to the projection of the electronic orbital angular momentum along the internuclear axis, which is a good quantum number ($[H_e, L_{\bar{z}}] = 0$, where $\bar{z}$ denotes the internuclear axis) for the states that we shall consider in this section*. $\Lambda$ takes on the values $0, 1, 2, \ldots$, which are denoted $\Sigma, \Pi, \Delta, \ldots$, respectively. Note that unlike with

*The two lower energy states at small internuclear separation are classified as Hund's case (b). The higher energy states at small internuclear separation are Hund's case (a). See, for example, refs. [221, 225, 226].

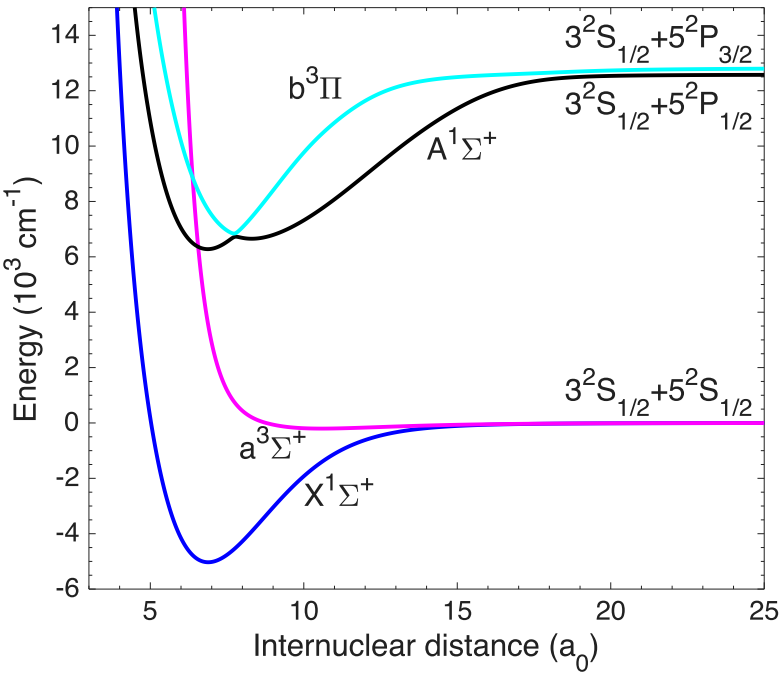


**Figure 3.2: Electronic potential energy curves for NaRb.** Only the states referred to in this thesis are depicted here. The potential energy curves are based on refs. [203, 223, 224, 227, 228].

atoms, $\mathbf{L}^2$ (where $\mathbf{L}$ is the total electronic orbital angular momentum operator) does *not* commute with the electronic Hamiltonian, as diatomic molecules have cylindrical but not spherical symmetry.

The $+/-$ label in the term symbol denotes the symmetry of the electronic wavefunction under reflections about a plane containing the internuclear axis. Looking at Fig. 3.2, one may observe that the $\Sigma$ states use this label but the $\Pi$ states do not. To see why, we follow ref. [221] in considering an operator $A_{\bar{y}}$ that reflects the position of each electron about the $\bar{x}\bar{z}$ plane, where $\bar{x}, \bar{z}$ refer to the molecular coordinate system and as before, $\bar{z}$ labels the internuclear axis. For simplicity we will just examine the effect of the operators $A_{\bar{y}}$ and $L_{\bar{z}}$ on the wavefunction of a single electron labeled

$\psi_i(\bar{x}_i, \bar{y}_i, \bar{z}_i)$. We observe that

$$\begin{aligned} A_{\bar{y}} L_{\bar{z}} \psi_i(\bar{x}_i, \bar{y}_i, \bar{z}_i) &= A_{\bar{y}} \left( -i\hbar \left( \bar{x} \frac{\partial}{\partial \bar{y}} - \bar{y} \frac{\partial}{\partial \bar{x}} \right) \right) \psi_i(\bar{x}_i, \bar{y}_i, \bar{z}_i) \\ &= -i\hbar \left( \bar{x} \frac{\partial}{\partial(-\bar{y})} - (-\bar{y}) \frac{\partial}{\partial \bar{x}} \right) \psi_i(\bar{x}_i, -\bar{y}_i, \bar{z}_i) \\ &= -L_{\bar{z}} \psi_i(\bar{x}_i, -\bar{y}_i, \bar{z}_i) \\ &= -L_{\bar{z}} A_{\bar{y}} \psi_i(\bar{x}_i, \bar{y}_i, \bar{z}_i), \end{aligned} \tag{3.3}$$

so $A_{\bar{y}} L_{\bar{z}} = -L_{\bar{z}} A_{\bar{y}}$. Using $L_{\bar{z}} \psi_i = \Lambda\hbar\psi_i$, we have $L_{\bar{z}}(A_{\bar{y}}\psi_i) = -A_{\bar{y}} L_{\bar{z}} \psi_i = -\Lambda\hbar(A_{\bar{y}}\psi_i)$. Since $A_{\bar{y}}$ commutes with the electronic Hamiltonian, we therefore see that the state $\psi_i$ corresponding to eigenvalue $\Lambda\hbar$ of $L_{\bar{z}}$ has the same energy as the state $(A_{\bar{y}}\psi_i)$ with eigenvalue $-\Lambda\hbar$. This implies that states with nonzero $\Lambda$ are doubly degenerate, and consequently the $\pm 1$ eigenvalues of $A_{\bar{y}}$ ($A_{\bar{y}}^2 = 1$) are not needed in the term symbol to label the state. On the other hand, there is no degeneracy for the $\Sigma$ states with $\Lambda = 0$, so the $+/-$ label is meaningful and is included in the term symbol.

The final part of the term symbol, namely the $2S + 1$ label, denotes the electron spin multiplicity as with atomic term symbols. States with the same spin multiplicity as the ground electronic state are additionally labeled by a capital letter for easy identification (see Fig. 3.2). The letters A,B,C,... are used in order of increasing energy with the exception of the ground state which is labeled X. States of a different multiplicity are labeled by lowercase letters.

The two lowest energy states $X^1\Sigma^+$ and $a^3\Sigma^+$ are of particular importance for our experiment, as the electronic state of the Feshbach molecules discussed in the previous chapter is primarily $a^3\Sigma^+$ [224] and the electronic state of the polar molecules discussed in the remainder of this thesis is $X^1\Sigma^+$. The fact that the singlet electronic state is lower in energy than the triplet can easily be understood by recalling that the total spatial and spin electronic wavefunction must be antisymmetric. Therefore,

the antisymmetric spin singlet state has a symmetric spatial wavefunction, enabling the delocalization of the electrons and the lowering of the potential energy.

### 3.1.2 Vibrational and rotational structure

In the previous section, we saw that the Born-Oppenheimer approximation allows us to separate the electronic and nuclear wave equations by treating the internuclear distance as a fixed parameter each time the electronic wave equation is solved. After having explored the electronic structure of diatomic molecules, this section will address the internal structure arising from the motion of the nuclei. The nuclear wave equation in the Born-Oppenheimer approximation is solved by choosing a particular electronic state $\Phi_s(\mathbf{R}; \mathbf{r}_1, \ldots, \mathbf{r}_N)$ and using the corresponding eigenenergy curve (i.e. the electronic energy curves plotted in the previous section) as an effective potential $V_s(R)$. In addition, the nuclear wave equation can be further simplified by factoring the nuclear wavefunction $F_s(\mathbf{R})$ into a radial wavefunction $\chi(R)$ and an angular wavefunction, which in the case of $\Lambda = 0$ is given by the spherical harmonics $Y_{N,m_N}(\theta, \phi)$ [221]. This leads to the radial wave equation:

$$\left(-\frac{\hbar^2}{2\mu}\left(\frac{d^2}{dR^2} - \frac{J(J+1)}{R^2}\right) + V_s(R)\right)\chi(R) = E\chi(R) \tag{3.4}$$

where $J$ is the total angular momentum quantum number, $\mu$ is the reduced mass of the nuclei, and $E$ is the total energy.

From equation 3.4, we can immediately obtain the rotational energy levels of the molecule in the rigid rotor approximation. Here, the internuclear separation $R$ of the diatomic molecule is treated as fixed at the equilibrium distance $R_0$, corresponding to the minimum of the associated electronic potential energy curve [229]. The derivative

term then cancels, and defining the rotational energy $E_{\text{rot}}$ as $E - V_s(R_0)$ we have:

$$E_{\text{rot}} = \frac{\hbar^2}{2\mu R_0^2} J(J+1) \equiv BJ(J+1) \tag{3.5}$$

where $B$ is known as the rotational constant. For electronic ground state NaRb molecules, the value of $B/h \approx 2.1\,\text{GHz}$ [27]. Note that in the electronic ground state the total angular momentum quantum number $J$ is equal to the rotational angular momentum quantum number $N$, which we will often use to label the rotational states.

Electronic and vibrational ground state NaRb molecules have a permanent body-frame electric dipole moment of $d = 3.2\,\text{D}$ [113]. External electric fields can therefore be used to couple opposite parity rotational states and induce a lab-frame dipole moment. The rotational transitions must satisfy the $\Lambda = 0$ selection rules $\Delta N = \pm 1$ and $\Delta m_N = 0, \pm 1$, where $m_N$ is the projection onto the quantization axis [221]. For a static electric field $\boldsymbol{E}$ pointing along the lab-frame $z$ axis, the coupling of two rotational states $|N, m_N\rangle$ is given by the matrix element [230]:

$$\begin{aligned}
&\langle N, m_N | H_{\text{DC}} | N', m_N' \rangle = \langle N, m_N | - \boldsymbol{d} \cdot \boldsymbol{E} | N', m_N' \rangle \\
&= -dE \sqrt{(2N+1)(2N'+1)} (-1)^{m_N} \begin{pmatrix} N & 1 & N' \\ -m_N & 0 & m_N' \end{pmatrix} \begin{pmatrix} N & 1 & N' \\ 0 & 0 & 0 \end{pmatrix}.
\end{aligned} \tag{3.6}$$

Together with the rotational matrix elements $BN(N+1)\delta_{N,N'}\delta_{m_N,m_N'}$, we can plot the energy levels and induced dipole moments of $\tilde{N} = 0$ and $\tilde{N} = 1$ NaRb molecules in a static electric field (Fig. 3.3). Since the bare rotational states are mixed by the electric field, the label $\tilde{N}$ is used to denote the field-dressed rotational states that adiabatically connect to the zero-field states $N$.

Returning to the radial wave equation 3.4, we will now examine the vibrational structure of diatomic molecules. The vibrational energy scale is much larger than the characteristic energy set by the rotational constant $B$, so we will make the approx-

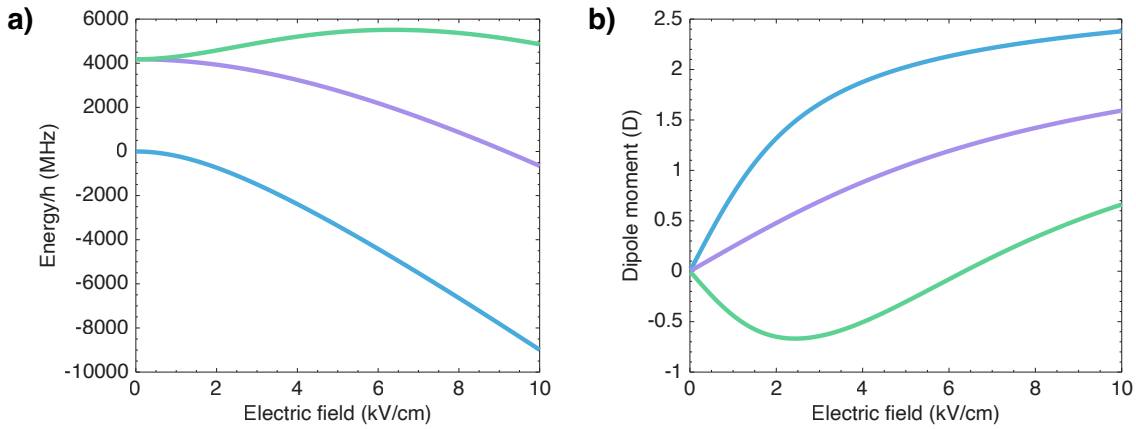


**Figure 3.3: Stark shift and induced dipole moment of NaRb.** **a)** Energy of NaRb molecules in the electronic and vibrational ground state as a function of electric field. Three field-dressed rotational states are plotted: $|0,0\rangle$ (blue), $|1,\pm1\rangle$ (purple), and $|1,0\rangle$ (green). **b)** The corresponding induced dipole moments versus electric field.

imation that the vibrational and rotational energies are decoupled and neglect the rotational term:

$$\left(-\frac{\hbar^2}{2\mu}\frac{d^2}{dR^2} + V_s(R)\right)\chi(R) = E\chi(R). \tag{3.7}$$

This is a 1D Schrödinger equation that in general must be solved numerically to find the vibrational energies. However, we will first examine an effective electronic potential that has an analytic solution. In particular, we use the idealized Morse potential of section 3.1.1 and now give its explicit form [231]:

$$V_{\text{Morse}}(R) = V_0 e^{-2a(R-R_0)} - 2V_0 e^{-a(R-R_0)}. \tag{3.8}$$

Setting $V_s(R) = V_{\text{Morse}}(R)$ in equation 3.4, we can solve for the vibrational energy levels [231]:

$$E_v = -\frac{a^2\hbar^2}{2\mu}(v_D - v)^2, \tag{3.9}$$

where

$$v_D = \frac{\sqrt{2\mu V_0}}{a\hbar} - \frac{1}{2}, \tag{3.10}$$

and where the vibrational quantum number $v = 0, 1, 2, \ldots, v_{\max} \leq v_D$. These energy levels along with the Morse potential are plotted as blue lines in Fig. 3.4. Many numerical methods exist to solve the 1D radial Schrödinger equation. Here, as an example we employ the sine representation of the mapped Fourier grid method from ref. [231]. Fourier grid methods work by dividing the distance $R$ (in our case the internuclear distance) into $q$ points, leading to a size $q \times q$ Hamiltonian for a single potential energy channel. In the mapped Fourier grid method, the points take on variable spacings based on the local de Broglie wavelength at a given position to improve the computational efficiency [231, 232]. The vibrational eigenenergies for the Morse potential calculated using this technique are shown as red lines in Fig. 3.4, which are indistinguishable from the analytic solution on the scale of the plot.

### 3.1.3 Hyperfine structure and Zeeman shift

Up to this point, we have ignored the nuclear spins since their interactions are small compared to the rotational structure. Nevertheless, the resulting hyperfine structure plays an important role in experiments with ultracold polar molecules. For molecules in the vibrational and electronic ground state, the hyperfine Hamiltonian can be written as [223, 233]:

$$H_{\text{hf}} = \sum_{i=1}^{2} c_i \mathbf{N} \cdot \mathbf{I}_i + c_3 \mathbf{I}_1 \cdot \tilde{T} \cdot \mathbf{I}_2 + c_4 \mathbf{I}_1 \cdot \mathbf{I}_2 + \sum_{i=1}^{2} \mathbf{V}_i \cdot \mathbf{Q}_i, \tag{3.11}$$

where the $i$ index labels the nucleus. A useful basis for studying the hyperfine structure is the uncoupled basis $|I_1, m_{I_1}, I_2, m_{I_2}, N, m_N\rangle$.

The first term in equation 3.11 corresponds to the rotation-nuclear spin interaction, with $c_{\text{Na}} = 60.7\,\text{Hz}$ and $c_{\text{Rb}} = 983.8\,\text{Hz}$ for NaRb [27]. The second and third terms represent the nuclear spin-nuclear spin interaction. This interaction is divided into two types known as direct and indirect, which are not the same as the divi-

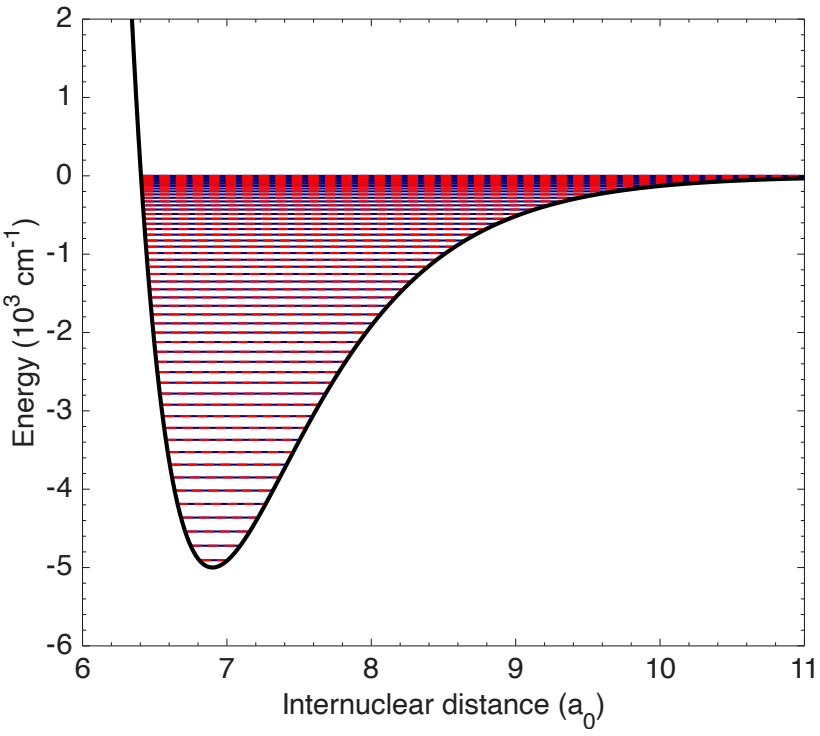


**Figure 3.4: Vibrational levels in the Morse potential.** The analytic solution of equation 3.9 is plotted in blue, while the numerical solution using the sine representation of the mapped Fourier grid method from ref. [231] is shown in red. The agreement is excellent, and the lines are indistinguishable on the scale of this plot. Here, the Morse potential parameters are $V_0 = 5 \times 10^3\,\mathrm{cm}^{-1}$, $a = 1.4\,a_0^{-1}$, and $R_0 = 6.9\,a_0$ where $a_0$ is the Bohr radius.

sion into the $c_3$ term and the $c_4$ term [233, 234]. The direct interaction represents the standard dipole-dipole interaction and is included as part of the $c_3$ tensor term. The indirect contribution is due to the electron spins mediating the interaction between the nuclear spins, and contributes to both the scalar $c_4$ term and the tensor $c_3$ term. As ref. [233] notes, $^1\Sigma$ electronic states still possess this electron-mediated interaction, and in fact the $c_4$ term is typically the largest hyperfine contribution for $N = 0$ molecules. For NaRb, $c_3 = 259.3\,\mathrm{Hz}$ and $c_4 = 6.56\,\mathrm{kHz}$ [27]. The last term in equation 3.11 is the interaction between the electric quadrupole moment of the nuclei (for nuclei with $I \geq 1$) with the electric field gradient due to the electrons [225]. This term is zero for $N = 0$ molecules but is the dominant hyperfine interaction for

higher rotational states. It is characterized by the coupling constants $(eqQ)_i$, which for NaRb are $(eqQ)_{\mathrm{Na}} = -0.139\,\mathrm{MHz}$ and $(eqQ)_{\mathrm{Rb}} = -3.048\,\mathrm{MHz}$ [27].

In the presence of a magnetic field, there is also a Zeeman shift with nuclear spin and (much smaller) rotational terms. The Hamiltonian can be expressed as [223,233]:

$$H_Z = -g_r \mu_N \mathbf{N} \cdot \mathbf{B} - \sum_{i=1}^{2} g_i (1 - \sigma_i) \mu_N \mathbf{I}_i \cdot \mathbf{B}, \tag{3.12}$$

where for NaRb $g_r = 0.001$, $g_{\mathrm{Na}}(1-\sigma_{\mathrm{Na}}) = 1.484$, and $g_{\mathrm{Rb}}(1-\sigma_{\mathrm{Rb}}) = 1.832$ [27]. Note that since the molecules are in the electronic ground state, the Zeeman interaction scales with the nuclear magneton $\mu_N$ rather than the Bohr magneton $\mu_B$, where $\mu_N = (5 \times 10^{-4})\mu_B$.

## 3.2 Transfer to the absolute ground state

Chapter 2 discussed the formation of non-interacting NaRb Feshbach molecules via magnetoassociation in our apparatus. The closed channel fraction of these molecules occupies a vibrational level near the dissociation threshold of the $a^3\Sigma^+$ state. To study dipolar physics, we need to transfer these weakly-bound molecules to the ground vibrational level of the $X^1\Sigma^+$ state. Fortunately, a highly efficient process known as stimulated Raman adiabatic passage (STIRAP) can be used to perform this transfer, coherently removing an energy (divided by the Boltzmann constant) corresponding to thousands of kelvin. The production of ultracold polar molecules via STIRAP was first demonstrated in ref. [11].

We can understand the basic principles of STIRAP by considering the three level system in Fig. 3.5a. The level labeled $|F\rangle$ corresponds to the Feshbach state, $|G\rangle$ corresponds to the target ground state, and $|I\rangle$ is a higher energy intermediate state. The levels are coupled by two lasers. The up leg, also known as the pump beam, connects $|F\rangle$ to $|I\rangle$ with a Rabi coupling $\Omega_P$. The down leg, often called the Stokes

beam, connects $|I\rangle$ to $|G\rangle$ and has a Rabi frequency $\Omega_S$. Since the ground state is lower in energy than the Feshbach state, the down leg laser uses a shorter wavelength than the up leg laser. We will consider the situation in which the lasers are at the one- and two-photon resonance, which is what we use in the NaRb experiment, although efficient STIRAP can also be achieved with nonzero detuning from the intermediate state [30]. The time-dependent Schrödinger equation for the three-level system can then be written in the rotating wave approximation as [23]:

$$i\hbar\frac{d}{dt}\begin{pmatrix} c_F(t) \\ c_I(t) \\ c_G(t) \end{pmatrix} = H(t)\begin{pmatrix} c_F(t) \\ c_I(t) \\ c_G(t) \end{pmatrix} = \frac{\hbar}{2}\begin{pmatrix} 0 & \Omega_P(t) & 0 \\ \Omega_P(t) & 0 & \Omega_S(t) \\ 0 & \Omega_S(t) & 0 \end{pmatrix}\begin{pmatrix} c_F(t) \\ c_I(t) \\ c_G(t) \end{pmatrix}. \tag{3.13}$$

One of the eigenstates of the Hamiltonian has zero intermediate state component. This state is referred to as a dark state and can be expressed as [23]:

$$|0\rangle = \cos(\theta(t))|F\rangle - \sin(\theta(t))|G\rangle, \tag{3.14}$$

where the mixing angle $\theta$ is defined as

$$\tan(\theta(t)) = \frac{\Omega_P(t)}{\Omega_S(t)}. \tag{3.15}$$

We see that if the pump laser is initially off ($\Omega_P(t=0)=0$) and the Stokes laser is on, then the dark state corresponds to the initial Feshbach state $|F\rangle$. By adiabatically and simultaneously ramping down the power in the Stokes beam and ramping up the power in the pump beam, the mixing angle goes from $\theta = 0$ to $\theta = \pi/2$ and the dark state switches character to the ground state without ever populating the intermediate state. An example of such a pulse sequence is given in Fig. 3.5b. In reality, inefficiencies can be introduced through such mechanisms as finite intermediate state lifetimes, non-adiabatic ramps, magnetic field noise, and laser frequency noise [223].

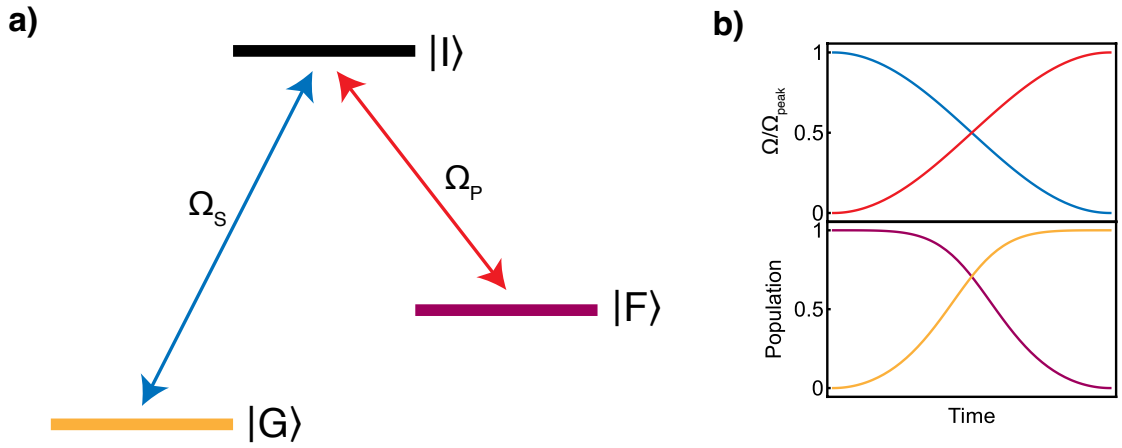


**Figure 3.5: Fundamentals of STIRAP. a)** Three-level system with states $|F\rangle$, $|I\rangle$, and $|G\rangle$. STIRAP is able to efficiently convert particles in state $|F\rangle$ to state $|G\rangle$ without populating a lossy intermediate state. **b)** Upper panel, Stokes (blue) and pump (red) Rabi frequencies during the STIRAP sequence. Lower panel, population of state $|F\rangle$ (purple) and $|G\rangle$ (yellow) during STIRAP.

We follow the STIRAP pathway first demonstrated for NaRb by the Wang group [113]. The chief difficulty in determining a STIRAP pathway is to find a suitable intermediate state, which requires extensive spectroscopy. The intermediate state must satisfy several criteria [223]. First, since the transitions between spin singlet and spin triplet states are forbidden, the intermediate state must have a mixed singlet-triplet character to connect the triplet Feshbach state to the singlet ground state. Second, there must be favorable Franck-Condon factors between the Feshbach and intermediate states and between the ground and intermediate states, where the Franck-Condon factor describes the overlap of the vibrational wavefunctions. Finally, the intermediate state must be sufficiently isolated in energy from other nearby states so that the three-level system approximation is accurate. Following extensive spectroscopy [223], the Wang group found that the mixed $A^1\Sigma^+/b^3\Pi$ $|v = 55, J = 1\rangle$ state meets all of these criteria. Since the Feshbach state is $m_F = 2$, the intermediate state is $m_F = 2$, and the $|N, m_N, m_{I,\mathrm{Na}}, m_{I,\mathrm{Rb}}\rangle = |0, 0, 3/2, 3/2\rangle$ ground state is $m_F = 3$, where $m_F = m_{I,\mathrm{Na}} + m_{I,\mathrm{Rb}} + m_J$, the up leg must have $\pi$ polarization while the down leg must be $\sigma^-$ [223].

A detailed description of the STIRAP setup in our experiment is given in ref. [112]. Briefly, the STIRAP light is generated by two Toptica DL Pro external-cavity diode lasers (ECDL) at 1248 nm for the up leg and 770 nm for the down leg. To achieve narrow linewidths necessary for high efficiency STIRAP, we lock both lasers to a dual-wavelength ultra-low expansion (ULE) cavity (Stable Laser Systems) with a finesse of 43,000 at 1248 nm and 34,000 at 770 nm. The cavity is temperature-stabilized to the zero-crossing of the ULE spacer's coefficient of thermal expansion to minimize drift. Each wavelength light sent to the cavity passes through a fiber electro-optic modulator (EOSpace) that is used both to generate sidebands for Pound-Drever-Hall (PDH) locking as well as to offset the laser frequency within the 1.5 GHz free spectral range of the cavity. We servo the laser current with a Toptica FALC 110 locking module for fast PID control, and we also use the FALC to correct slow drifts by feeding back on the ECDL piezo voltage. The extracted laser linewidths are $\lesssim 2$ kHz. In addition, for the light sent to the experiment we use two acousto-optic modulators (IntraAction) to dynamically control the optical power.

Due to its much lower Franck-Condon factor, the up leg requires a higher intensity than the down leg to achieve the same Rabi frequency. The maximum power of our 1248 nm light at the molecules is $< 30$ mW, so we focus the beam to a smaller waist ($w = 45\,\mu$m) than the 770 nm down leg beam ($w = 150\,\mu$m). This setup gives us peak Rabi frequencies of $\Omega_P = 2\pi \times 0.70(4)$ MHz and $\Omega_S = 2\pi \times 0.9(1)$ MHz. Since the 335 G magnetic field setting the quantization axis points along the vertical direction, the 1248 nm beam is vertically polarized to drive the required $\pi$ transition (note that later experiments use a magnetic field closer to the 347.6 G Feshbach resonance, as discussed in chapter 5). The 770 nm laser is horizontally polarized, enabling it to drive both $\sigma^+$ and the desired $\sigma^-$ transitions. The duration of amplitude overlap for the STIRAP pulses is $\sim$100 $\mu$s. With this setup, we achieve a one-way STIRAP efficiency

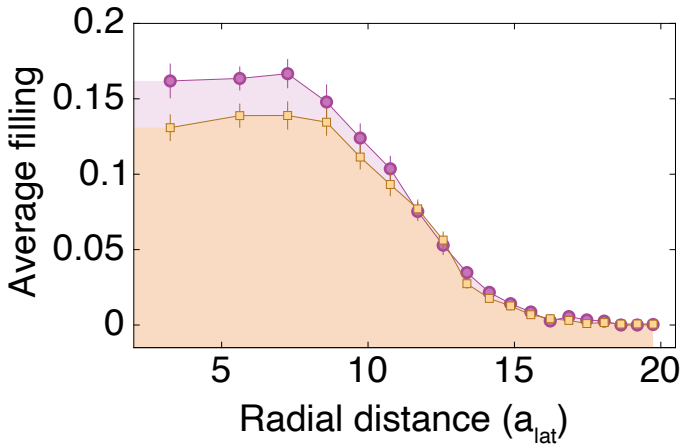


**Figure 3.6: Molecule lattice filling fraction.** Average density profile of a cloud of Feshbach molecules (purple circles) and the corresponding profile of detected molecules after round-trip STIRAP (orange squares) versus radial distance from the center of the molecular gas. Error bars represent standard error of the mean (s.e.m.).

of 93.9(3) %, resulting in a peak ground state lattice filling of 15(1)% (taking into account the detection efficiency of 92.0(3)%) with order $10^2$ molecules (Fig. 3.6).

In later work with larger numbers of molecules (see chapter 5), we measure lower STIRAP efficiencies typically between 75% and 85%. This may be due to the small waist of the 1248 nm beam leading to lower intensities and therefore lower STIRAP efficiencies outside of the central region for larger cloud sizes. An examination of the STIRAP efficiency as a function of distance from the beam center would be required to confirm this hypothesis. We briefly attempted to increase our STIRAP efficiency by using a booster optical amplifier (Thorlabs BOA1250P) to achieve a higher optical power in the 1248 nm beam. Despite increasing the maximum 1248 nm power at the molecules by a factor of three, we measured a lower STIRAP efficiency of 57%. This may be due to a broadening of the laser linewidth caused by the BOA. A tapered amplifier may be used in the future to increase the power in the 1248 nm beam if higher STIRAP efficiencies are required [223].

## 3.3 Microscopy of dipolar spin models

With the successful transfer of NaRb Feshbach molecules to the absolute ground state, we realized the first quantum gas microscope for polar molecules. At the time, the only quantum simulation experiments that had been performed with polar molecules were those of the Ye group studying the dipolar spin-exchange model with KRb molecules [63, 235]. As these studies used absorption imaging to probe the many-body system, we sought to build on this work by using the quantum gas microscope to measure site-resolved correlations between individual interacting polar molecules.

As previously demonstrated in refs. [63, 79, 235], a spin-1/2 can be encoded in the ground (labeled $|\uparrow\rangle$) and first rotational ($|\downarrow\rangle$) states of the molecules, which gives rise to dipolar interactions from a resonant exchange of rotational quanta between pairs of molecules. With the NaRb molecules pinned in the 2D lattice, this realizes the quantum $XY$ spin-exchange Hamiltonian:

$$H_{XY} = \sum_{i>j} V(\mathbf{r}_i - \mathbf{r}_j)(S_i^X S_j^X + S_i^Y S_j^Y), \tag{3.16}$$

where $V(\mathbf{a}) = J\langle(1-3\cos^2\theta)/|\mathbf{a}|^3\rangle$, $J$ characterizes the strength of the spin-exchange interaction, $S_i^{X(Y)} = \sigma_i^{X(Y)}/2$ are spin-1/2 operators for molecule $i$, $\mathbf{r}_i$ is the position of molecule $i$ in units of the lattice constant $a_{\text{lat}}$, and $\theta$ is the angle between the quantization axis and the vector $\mathbf{a}$. The quantum average $\langle\cdot\rangle$ accounts for the finite size of the molecule center-of-mass wavefunctions.

One complication in this spin-1/2 encoding is that the AC polarizability of the first excited rotational state in general differs from that of the ground state [74–76, 78, 81, 236]. Therefore, the overall Gaussian intensity profile of the 2D lattice leads to spatially varying transition frequencies between the two states, representing a source of rotational decoherence. Various methods have been developed to extend the rotational coherence times of polar molecules, as outlined in chapter 1. Here, we

mitigate the decoherence by relying on the mixing of rotational states with different $m_N$ at weak magnetic fields due to hyperfine couplings. The relative admixture of these states varies with the magnetic field. Since the polarizability can differ in sign and strength between the $m_N$ states, we can find a magnetic field and $|\downarrow\rangle$ hyperfine level for a given lattice polarization and intensity that minimizes the differential polarizability $\Delta\alpha = \alpha_{|\uparrow\rangle} - \alpha_{|\downarrow\rangle}$. In the following experiments, we use one of two different $|\downarrow\rangle$ states depending on whether the magnetic field orientation is vertical or horizontal. For the vertical orientation, we work at 60 G and use the $|\downarrow\rangle$ state

$$|\downarrow\rangle \approx 0.688|1,-1,3/2,3/2\rangle - 0.569|1,0,3/2,1/2\rangle + 0.448|1,1,3/2,-1/2\rangle, \quad (3.17)$$

where the states are labeled $|N, m_N, m_{I,\mathrm{Na}}, m_{I,\mathrm{Rb}}\rangle$. For the horizontal orientation, the magnetic field strength that we can reach is limited by our coil setup (see appendix A). Consequently, we work at an in-plane magnetic field of 4.1 G and use the $|\downarrow\rangle$ state

$$|\downarrow\rangle \approx 0.715|1,-1,3/2,3/2\rangle - 0.562|1,0,3/2,1/2\rangle + 0.413|1,1,3/2,-1/2\rangle. \quad (3.18)$$

With this choice of magnetic fields and $|\downarrow\rangle$ states, the $|\uparrow\rangle$ to $|\downarrow\rangle$ transition frequency varies by less than 20 Hz over the extent of the cloud.

In order to drive the ground to first excited rotational state transition, we use the following setup. An analog signal generator (Agilent E8257C) provides a carrier signal at 4.13 GHz, which is then mixed with an arbitrary waveform generator (Keysight 33621A with option MEM) operating in the vicinity of 50 MHz. The two frequency generators share a common 10 MHz clock. The signal after the frequency mixer is passed through an amplifier (Mini-Circuits ZHL-5W-63-S+) and then sent to a home-built four-turn helical antenna with a pitch angle of 13° (Fig. 3.7). A brass reflector is used to increase its directivity. The microwave polarization is not pure at the location of the molecules, allowing us to drive $\sigma^+$, $\pi$, and $\sigma^-$ transitions.

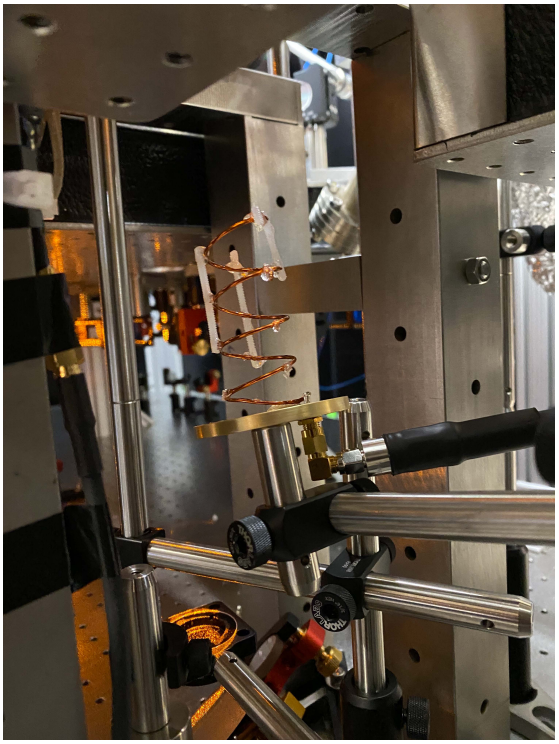

**Figure 3.7: Helical antenna.** The helical antenna used to drive rotational state transitions is located underneath the science chamber. Since large Rabi frequencies were not needed in these experiments, we placed it approximately 20 cm away from the molecules to aid optical access.

We begin by benchmarking the rotational coherence of our system using the Ramsey sequence shown in Fig. 3.8. The molecules are initially prepared in $|\uparrow\rangle$ at a dilute peak filling of 1.0(2)% to reduce dipolar interactions. A $(\pi/2)_Y$ pulse transfers the molecules to the equator of the Bloch sphere, producing a superposition of $|\uparrow\rangle$ and $|\downarrow\rangle$. After a precession time $T$, a second $\pi/2$ pulse is performed with a phase $\phi$ relative to the first pulse. The number of detected molecules $N_\uparrow$ as a function of $\phi$ can then be fit to $N_\uparrow = A\cos(\phi + \phi_0) + B$, from which we extract the contrast $A/B$ for a given precession time (note that $|\downarrow\rangle$ molecules are not detected since STIRAP is rotational state-selective). We observe a $1/e$ decay time of 56(2) ms, already highlighting the efficacy of our technique to minimize the differential polarizability. To suppress residual light shifts (but not dipolar interactions), we repeat the Ramsey experiment with

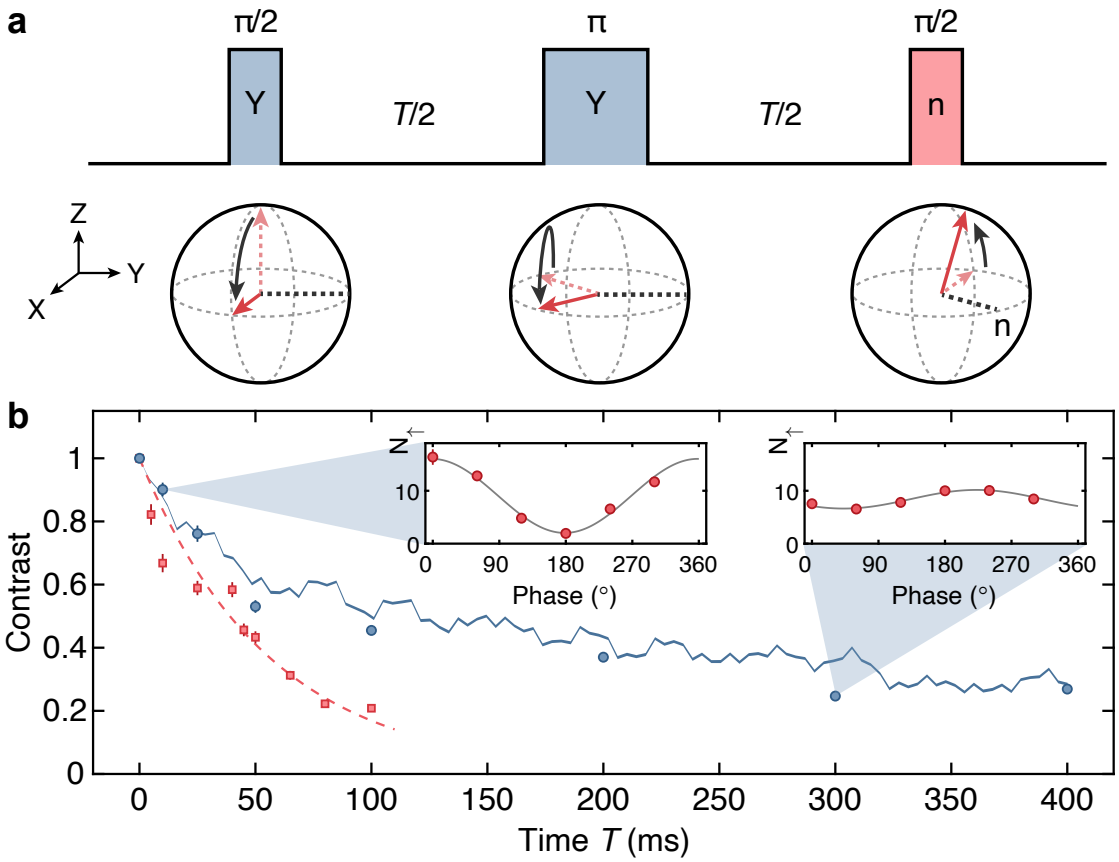


**Figure 3.8: Rotational state coherence.** **a)** Microwave pulse sequence for the Ramsey coherence measurement including the spin echo $\pi$ pulse. **b)** Ramsey fringe contrast versus total precession time, with (blue circles) and without (red squares) the spin echo pulse in the middle of the precession time, for a sample with a peak filling of 1.0(2)%. The blue line shows the predicted dynamics from exact diagonalization, and the red dashed line is an exponential decay fit for the Ramsey contrast data without a spin echo. Inset: representative Ramsey fringes from 10 ms and 300 ms precession times with a spin echo. Error bars represent s.e.m.

a spin echo $(\pi)_Y$ pulse inserted halfway through the precession time. The resulting slow contrast decay is consistent with a numerical simulation of the dipolar $XY$ spin-exchange model out to 400 ms. Moreover, the time over which the contrast decays is long compared to the millisecond-scale nearest-neighbor interactions, representing a favorable regime for the quantum simulation of many-body dynamics.

This extended rotational coherence time now enables us to probe the dipolar interactions of the molecules using our quantum gas microscope. For these experiments,

we use a higher peak filling of 5.4(4)%. This filling is deliberately diluted from the maximum filling in Fig. 3.6 in order to slow down the thermalization timescale compared to that of the nearest-neighbor dynamics. The magnetic field, which sets the quantization axis, is perpendicular to the plane of the molecules so that the interactions are isotropic. We again perform a spin echo Ramsey sequence*, but this time the phase of the final $\pi/2$ pulse is fixed at 180° so that in the absence of dipolar interactions no molecules will be observed. Fig. 3.9a shows the fraction of detected molecules versus precession time. We see that the number of $|\uparrow\rangle$ molecules gradually rises, revealing the thermalization of the system due to many-body interactions. However, this increase is not monotonic; instead, the molecule number oscillates in agreement with the theoretically expected frequency of $|V(\mathbf{e})|/2h = 241\,\mathrm{Hz}$ for nearest-neighbor molecules, where $\mathbf{e} = (1, 0)$.

These dipolar oscillations were originally observed in ref. [63]. Now, however, we can take advantage of the quantum gas microscope to measure the dynamics of site-resolved correlations between the interacting molecules. We study the lattice-averaged density correlation

$$C(\mathbf{a}, T) = \frac{\mathcal{N}}{N_s} \sum_{\mathbf{r}} (\langle n_{\mathbf{r}}^{\uparrow} n_{\mathbf{r}+\mathbf{a}}^{\uparrow} \rangle - \langle n_{\mathbf{r}}^{\uparrow} \rangle \langle n_{\mathbf{r}+\mathbf{a}}^{\uparrow} \rangle), \tag{3.19}$$

where $\langle \cdot \rangle$ denotes averaging over the quantum state of the many-body spin system as well as classical realizations of the dilute lattice filling, and $N_s$ is the number of sites in the region used to evaluate the correlator. The normalization factor, which will be discussed below, is $\mathcal{N} = (\langle \rho^2 \rangle_{\mathrm{lat}})^{-1}$ with $\langle \rho^2 \rangle_{\mathrm{lat}}$ defined as the average of the square of the filling fraction.

Fig. 3.9b,c shows the dynamics of these correlations as a function of time. The nearest-neighbor, next-nearest neighbor, and next-next-nearest neighbor correlations

*To be precise, odd integer multiples of spin echo pulses are used in order to reduce single-particle rotational decoherence.

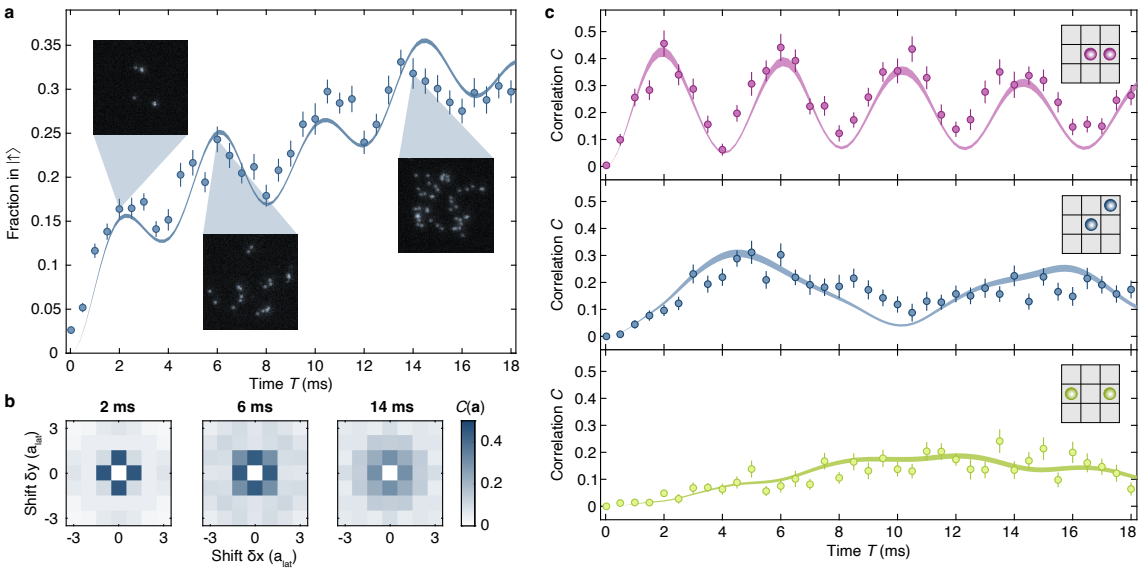


**Figure 3.9: Correlation dynamics in an $XY$ spin model. a)** Fraction of molecules in $|\uparrow\rangle$ versus time. Insets show representative fluorescence images from 2 ms (left), 6 ms (middle) and 14 ms (right). **b)** Representative correlation matrices corresponding to the precession times for the inset images in **a)**. All correlations are averaged along the lattice symmetry axes. **c)** Line plots showing the correlations versus precession time for the specific displacements shown in the inset lattice diagrams. Top: nearest-neighbor correlations. Middle: next-nearest-neighbor correlations. Bottom: next-next-nearest-neighbor correlations. Fifty images were collected for each precession time. The correlations were averaged along the lattice symmetry axes. All shaded bands are theory predictions of the dynamics from exact diagonalization of the dipolar $XY$ model. The theoretical predictions for the correlations were scaled vertically to best fit the experimental data for the shown displacements simultaneously. Error bars represent s.e.m.

are observed to oscillate at different frequencies. To understand this behavior, let us first consider how the initial state $|\uparrow\uparrow\rangle$ of an isolated pair of molecules evolves throughout the Ramsey sequence. The first $(\pi/2)_Y$ pulse prepares each molecule in the state $|{+}X\rangle = (|\uparrow\rangle + |\downarrow\rangle)/\sqrt{2}$, so we have the pair state

$$|{+}X\rangle|{+}X\rangle = \frac{1}{2}(|\uparrow\uparrow\rangle + |\uparrow\downarrow\rangle + |\downarrow\uparrow\rangle + |\downarrow\downarrow\rangle). \tag{3.20}$$

In the two-molecule basis $\{|\uparrow\uparrow\rangle, |\uparrow\downarrow\rangle, |\downarrow\uparrow\rangle, |\downarrow\downarrow\rangle\}$, the $XY$ Hamiltonian of equation 3.16 is given by

$$H_{XY} = \begin{pmatrix} 0 & 0 & 0 & 0 \\ 0 & 0 & \frac{V(\mathbf{a})}{2} & 0 \\ 0 & \frac{V(\mathbf{a})}{2} & 0 & 0 \\ 0 & 0 & 0 & 0 \end{pmatrix}. \tag{3.21}$$

The eigenvectors of this Hamiltonian are $\psi_0 = |\uparrow\uparrow\rangle$ with eigenvalue 0, $\psi_1 = |\downarrow\downarrow\rangle$ with eigenvalue 0, $\psi_2 = (|\uparrow\downarrow\rangle + |\downarrow\uparrow\rangle)/\sqrt{2}$ with eigenvalue $V(\mathbf{a})/2$, and $\psi_3 = (|\uparrow\downarrow\rangle - |\downarrow\uparrow\rangle)/\sqrt{2}$ with eigenvalue $-V(\mathbf{a})/2$. The pair state $|+X\rangle|+X\rangle$ of equation 3.20 can be expressed in terms of these eigenvectors as $(\psi_0 + \psi_1 + \sqrt{2}\psi_2)/2$. Following the Ramsey precession time $T$, the pair wavefunction is

$$\begin{aligned} &\frac{1}{2}\left(\psi_0 + \psi_1 + \sqrt{2}e^{-iV(\mathbf{a})T/2\hbar}\psi_2\right) \\ &= \frac{1}{2}\left(|\uparrow\uparrow\rangle + |\downarrow\downarrow\rangle + e^{-iV(\mathbf{a})T/2\hbar}(|\uparrow\downarrow\rangle + |\downarrow\uparrow\rangle)\right) \\ &= \frac{1}{2}\big(|+Z\rangle|+Z\rangle + |-Z\rangle|-Z\rangle \\ &+ e^{-iV(\mathbf{a})T/2\hbar}(2|+X\rangle|+X\rangle - |+Z\rangle|+Z\rangle - |-Z\rangle|-Z\rangle)\big). \end{aligned} \tag{3.22}$$

The spin echo $(\pi)_Y$ pulse in the middle of the precession time has the effect of sending $|\pm Z\rangle \to |\mp Z\rangle$ and $|\pm X\rangle \to |\mp X\rangle$:

$$\frac{1}{2}\left(|-Z\rangle|-Z\rangle + |+Z\rangle|+Z\rangle + e^{-iV(\mathbf{a})T/2\hbar}(2|-X\rangle|-X\rangle - |-Z\rangle|-Z\rangle - |+Z\rangle|+Z\rangle)\right). \tag{3.23}$$

After the final $(\pi/2)_{-Y}$ pulse we have the pair state:

$$\frac{1}{2}\left(|+X\rangle|+X\rangle + |-X\rangle|-X\rangle + e^{-iV(\mathbf{a})T/2\hbar}(2|-Z\rangle|-Z\rangle - |+X\rangle|+X\rangle - |-X\rangle|-X\rangle)\right). \tag{3.24}$$

This simplifies to:

$$e^{-iV(\mathbf{a})T/4\hbar}\left(i\sin\left(\frac{V(\mathbf{a})T}{4\hbar}\right)|\uparrow\uparrow\rangle+\cos\left(\frac{V(\mathbf{a})T}{4\hbar}\right)|\downarrow\downarrow\rangle\right). \tag{3.25}$$

Therefore, the probability of detecting the molecule pair in state $|\uparrow\uparrow\rangle$ after Ramsey evolution time $T$ is $P_{\uparrow\uparrow}(T)=\sin^2(V(\mathbf{a})T/4\hbar)$. When generalizing to larger systems of molecules, owing to the low filling fractions used in the Ramsey experiments we can approximate our system as consisting of single molecules and isolated pairs. In addition, at the end of our Ramsey sequence, single molecules that do not experience many-body interactions are in $|\downarrow\rangle$, so they do not contribute to the correlation function of equation 3.19. Consequently, both $\langle n_{\mathbf{r}}^{\uparrow}n_{\mathbf{r}+\mathbf{a}}^{\uparrow}\rangle$ and $\langle n_{\mathbf{r}}^{\uparrow}\rangle$ scale as the probability $\rho^2$ of a molecule being in a pair, where $\rho$ is the lattice filling fraction. The lattice-averaged correlation function before the density normalization is then $C(\mathbf{a},T)=\langle\rho^2\rangle_{\text{lat}}\sin^2(V(\mathbf{a})T/4\hbar)-\langle\rho^2\rangle_{\text{lat}}^2\sin^4(V(\mathbf{a})T/4\hbar)$. For low fillings the second term can be neglected, so as mentioned previously we normalize the correlation function by multiplying it by $(\langle\rho^2\rangle_{\text{lat}})^{-1}$.

Due to the presence of $V(\mathbf{a})$ in the argument of $\sin^2$ in $C(\mathbf{a},T)$, we therefore see that the oscillation frequency of the correlations directly reveals the geometric dependence of the dipole-dipole interaction. It is now clear that the different oscillation frequencies we observed in the nearest-neighbor, next-nearest-neighbor, and next-next-nearest neighbor correlations in Fig. 3.9b,c result from the $1/r^3$ dependence of the dipolar interaction on distance.

So far, we have studied the case of isotropic interactions, but by changing the quantization axis set by the magnetic field to lie within the plane of the molecules (tilted 9° with respect to the lattice axes $x$ and $y$) we can probe the effect of an anisotropic interaction potential on the many-body dynamics [237]. The measured correlations in this configuration are shown in Fig. 3.10 together with the isotropic

correlations from Fig. 3.9 for comparison. In our analysis, we now separate the correlations along each lattice axis to reveal the anisotropy. For the case of the in-plane magnetic field, we see that the nearest-neighbor correlations along $x$ oscillate at almost twice the frequency as those along $y$, which can be attributed to the factor of $\sim$2 difference in the interaction strength between the two lattice axes. Moreover, since the angle $\theta = 54.7°$ for which the dipolar interaction is zero lies almost exactly along one of the diagonals of the lattice axes, we observe that the correlations are strongly suppressed in the $y = x$ direction.

As a final experiment, we go beyond the natural $XY$ model of the dipolar system by using Floquet engineering [86, 238, 239] to realize an effective $XXZ$ Hamiltonian. Namely, we periodically drive the Hamiltonian fast compared to the interaction timescale such that the molecules experience a time-averaged Hamiltonian. Using the Floquet cycle shown in Fig. 3.11a, the molecules spend an equal time undergoing $XY$ and $XZ$ dynamics, averaging to

$$H_{XYY} = \sum_{i>j} V(\mathbf{r}_i - \mathbf{r}_j) \left( S_i^X S_j^X + \frac{1}{2}(S_i^Y S_j^Y + S_i^Z S_j^Z) \right), \tag{3.26}$$

which is equivalent to the $XXZ$ model with a permutation of the axis labels. Due to the Hamiltonian's symmetry under rotations about the $X$ axis, magnetization along $X$ should be conserved while that along $Y$ and $Z$ should not. To test this, we prepare three separate initial states ($|+X\rangle$, $|+Y\rangle$, and $|+Z\rangle$) and measure the fraction of molecules in $|\uparrow\rangle$ as a function of evolution time under the Floquet Hamiltonian (Fig. 3.11b). The magnetization is once again in the vertical direction such that the interactions are spatially isotropic. We see that the magnetization of the molecules starting in $|+X\rangle$ is nearly conserved while significantly greater demagnetization occurs for the $|+Y\rangle$ and $|+Z\rangle$ initial states. We can also examine the site-resolved correlation dynamics in the $XXZ$ model (Fig. 3.11c). In comparison with Fig. 3.9c, the

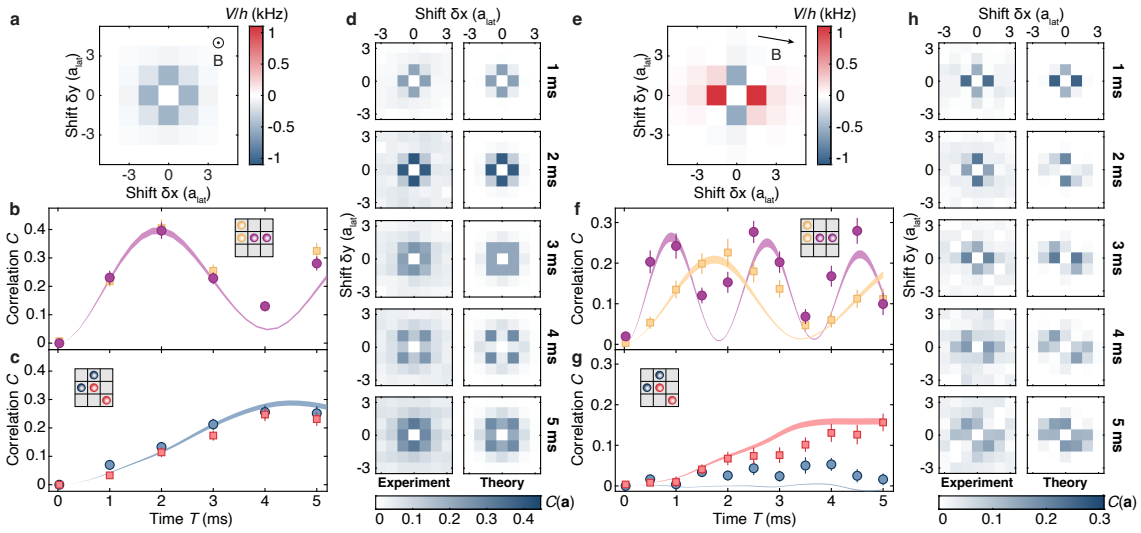


**Figure 3.10: Tunable spatial anisotropy of the dipolar interactions.** **a)** Interaction potential ($V/h$), where $h$ is Planck's constant, between the molecules when the magnetic field $B$ is perpendicular to the 2D lattice plane. **b)** Nearest-neighbor correlations along the vertical (yellow squares) and horizontal (purple circles) lattice axes for different evolution times for the isotropic configuration. **c)** Next-nearest-neighbor correlations along $y = x$ (blue circles) and $y = -x$ (red squares) for different evolution times for the isotropic configuration. **d)** Full correlation matrices obtained from 200 experimental iterations for each evolution time (left) compared to theory predictions from exact diagonalization (right). **e)** Interaction potential between the molecules when the magnetic field is in the 2D lattice plane and oriented 9° from the lattice axes. **f)** Nearest-neighbor correlations along the vertical (yellow squares) and horizontal (purple circles) lattice axes for different evolution times for the anisotropic configuration. **g)** Next-nearest-neighbor correlations along $y = x$ (blue circles) and $y = -x$ (red squares) for different evolution times for the spatially anisotropic configuration. **h)** Full correlation matrices obtained from 50 experimental iterations for each evolution time (left) compared to theory predictions from exact diagonalization (right). All shaded bands are theory predictions from exact diagonalization of the dipolar $XY$ model. Inset lattice diagrams show the specific site displacements used to calculate the correlations. The theoretical predictions for the correlations were scaled vertically to best fit the experimental data for the shown displacements simultaneously. Error bars represent s.e.m.

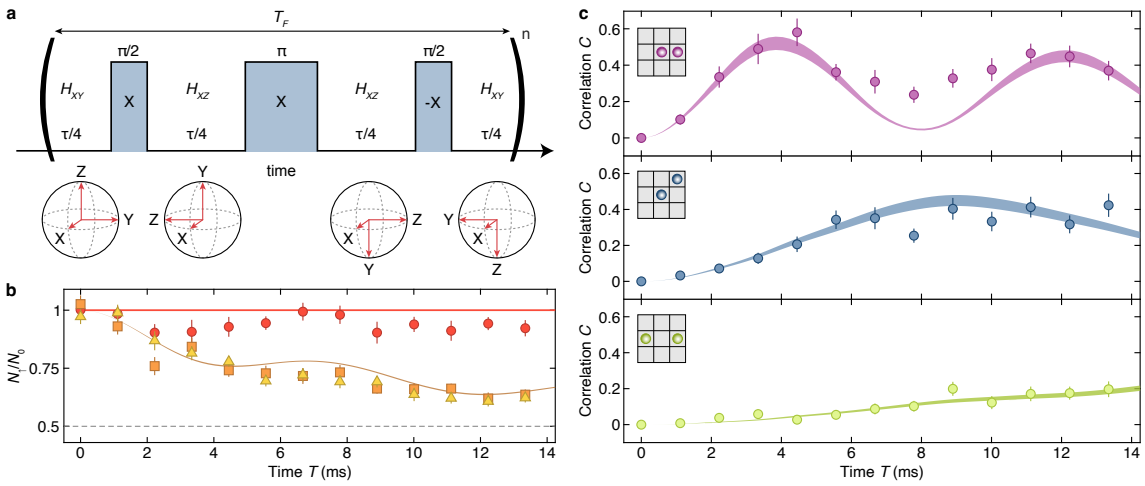


**Figure 3.11: Floquet engineering of an anisotropic Heisenberg model.** **a)** Pulse sequence used for an individual Floquet cycle, which is repeated $n$ times. Each microwave pulse separates an equal time segment $\tau/4$, where $\tau = 1\,\text{ms}$, the $\pi$-pulse duration is $56.2\,\mu\text{s}$ and the total Floquet cycle time $T_\text{F} = 1.1124\,\text{ms}$. **b)** Magnetization dynamics for three different initial states. Red circles: $|{+}X\rangle$ initial state. Orange squares: $|{+}Y\rangle$ initial state. Yellow triangles: $|{+}Z\rangle$ initial state. The dashed line indicates the demagnetized value with $N_\uparrow = N_0/2$. **c)** Correlation dynamics for a $|{+}Z\rangle$ initial state. Top: nearest-neighbor correlations. Middle: next-nearest-neighbor correlations. Bottom: next-next-nearest-neighbor correlations. All shaded bands are theory predictions of the dynamics from exact diagonalization of the $XYY$ Hamiltonian. Inset lattice diagrams show the specific site displacements used to calculate the correlations. The theoretical predictions for the correlations were scaled vertically to best fit the experimental data for the shown displacements simultaneously. Error bars represent s.e.m.

nearest-neighbor oscillation frequency is reduced by a factor of $\sim$2, in agreement with numerical simulations shown by the shaded bands. We have therefore demonstrated control over and detection of both the spin and spatial anisotropy of the dipolar interactions, highlighting the utility of a quantum gas microscope for studying many-body physics with polar molecules.

# Chapter 4

# Collisional shielding methods for polar molecules

As discussed in chapter 1, both chemically reactive and nonreactive ultracold polar molecules experience universal two-body loss at short range. Despite lingering questions on the exact mechanism of this loss, mitigation strategies collectively known as collisional shielding have proven enormously successful, enabling the evaporation of Fermi [132,138] and Bose [16] gases of polar molecules to quantum degeneracy. These techniques work by putting up a large barrier in the intermolecular potential so that the molecules cannot approach close enough together to experience lossy dynamics. In this chapter, we will present an overview of several collisional shielding mechanisms making use of static as well as microwave electric fields. We will also examine in the last section shielding techniques that are effective against both two-body and three-body loss, which has proven to be necessary for the evaporation of Bose gases to high phase-space densities [16,142,240].

## 4.1 Static electric field shielding in a 2D geometry

Perhaps the most intuitive collisional shielding mechanism is that of applying a static electric field perpendicular to a 2D plane of molecules [128–131]. This technique was employed in the first demonstration of evaporative cooling of fermionic molecules to degeneracy [132]. Treating the molecules as classical dipoles, the DC field orients them all in the same direction, which we will take to be the $+z$ axis. If two molecules approach each other side-to-side, then the dipole-dipole interaction of equation 1.2 is repulsive and naturally prevents the molecules from reaching short range. On the other hand, if the molecules approach head-to-tail, then the dipole-dipole interaction is attractive and they will experience universal loss.

The essence of this collisional shielding technique is to geometrically confine the molecules to a 2D plane so that only repulsive side-to-side interactions are possible. This can be done through the use of a 1D optical lattice, with the layers orthogonal to the electric field along $z$ and the temperature of the molecules satisfying the quasi-2D condition $k_B T < \hbar\omega_z$. The interaction potential between two molecules with induced dipole moment $d$ within a vertical lattice layer is given by the sum of the dipole-dipole interaction and the vertical harmonic confinement [128]:

$$V(\mathbf{r}) = \frac{d^2(r^2 - 3z^2)}{4\pi\epsilon_0 r^5} + \frac{1}{2}\mu\omega_z^2 z^2, \tag{4.1}$$

where $\mu$ is the reduced mass of the two molecules and $r = \sqrt{\rho^2 + z^2}$ is the distance between the molecules with radial component $\rho$ and vertical component $z$. The interaction potential is plotted in Fig. 4.1 for the example of NaRb with $\omega_z = 2\pi \times 50\,\mathrm{kHz}$ and an induced dipole moment of 2.2 D. This dipole moment is the largest that we can achieve in our experiment for NaRb molecules in their rotational ground state at our maximum electric field of 7 kV/cm. We see that for two molecules approaching side-to-side, a potential barrier separates them from short range. The two green dots

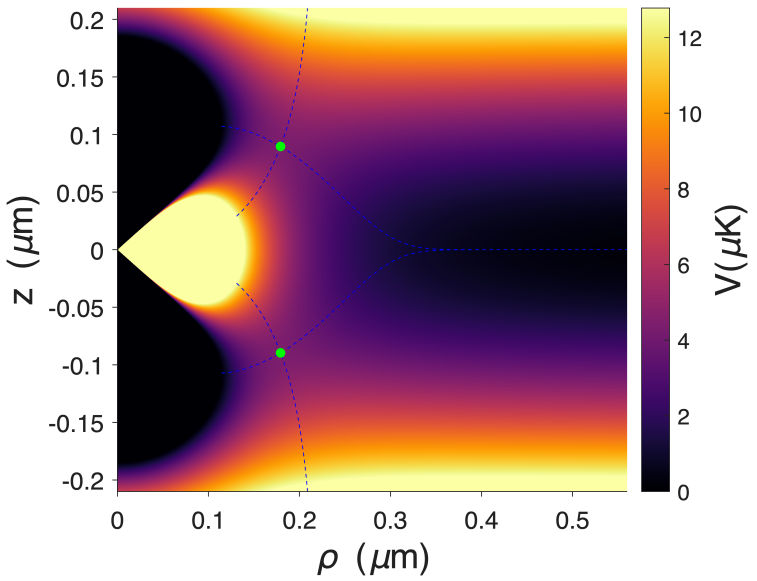


**Figure 4.1: Static electric field shielding in quasi-2D.** For $|0,0\rangle$ NaRb molecules at 7 kV/cm in a vertical lattice with $\omega_z = 2\pi \times 50$ kHz, a barrier exists in the interaction potential. At the saddle points, marked as green dots, the barrier is $V = 4\,\mu$K. $\rho$ is the radial in-plane intermolecular distance and $z$ is the vertical distance. Figure modeled on ref. [128].

in the plot denote saddle points in the intermolecular potential representing a barrier $V_s \propto d^{4/5}\omega_z^{6/5}$. For the chosen NaRb parameters, the potential barrier at the saddle point is $V_s = 4\,\mu$K.

Out of all of the shielding methods presented in this chapter, this is the only one in which the induced dipole moment of the molecules can approach the full permanent dipole moment (for sufficiently large electric fields). This makes it a particularly appealing technique for the study of dipolar physics with large interactions. Moreover, our molecular quantum gas microscope is already best-suited for the study of 2D systems, so the restriction to a quasi-2D geometry does not pose a limitation on the lattice physics we are interested in studying. For example, this shielding method could be used to implement a hardcore Bose-Hubbard model with polar molecules [69], enabling the realization of fractional Mott insulator phases such as were observed with dipolar atoms [101].

## 4.2 Förster resonance collisional shielding

Another technique that uses static electric fields is Förster resonance shielding [146–149, 152–154], which unlike the previous method is able to mitigate two-body loss in 3D systems. Here, one takes advantage of the Stark shifts of the molecular $|N = 0, m_N = 0\rangle$, $|1, 0\rangle$, and $|2, 0\rangle$ rotational states to engineer a repulsive barrier along all approach angles of two colliding molecules. To see how this works, let us consider a pair of molecules that has been prepared in the field-dressed $|1, 0\rangle$ state. At a certain electric field, the total energy of the pair state $|1, 0\rangle|1, 0\rangle$ comes into resonance with that of $|0, 0\rangle|2, 0\rangle$. As shown in Fig. 4.2, for NaRb this crossing occurs at $\sim$4.2 kV/cm, which is labeled the Förster resonance. In general, the Förster resonance is located at approximately $3.25B/d$ where $B$ is the rotational constant and $d$ is the permanent dipole moment [149]. The dipolar interaction between the two colliding molecules opens up an avoided crossing at the Förster resonance. Since the dipolar interaction becomes stronger for decreasing intermolecular separation, as the molecules approach closer together the energy gap becomes larger. If the $|1, 0\rangle|1, 0\rangle$ molecules are at an electric field slightly above the Förster resonance, then their total energy is increased by this widening energy gap. That is to say, the interaction potential above the Förster resonance for a pair of molecules in the $|1, 0\rangle$ state features a barrier at short range.

We can gain further intuition by considering the simplified model of ref. [152]. Here, we reduce a complicated coupled-channels problem into a two-level calculation by only considering the two resonant pair states $|1, 0\rangle|1, 0\rangle$ and $|0, 0\rangle|2, 0\rangle$. (The $|0, 0\rangle|2, 0\rangle$ state is implicitly taken to represent the symmetrized state $(|0, 0\rangle|2, 0\rangle + |2, 0\rangle|0, 0\rangle)/\sqrt{2}$.) Although depending on the molecular species and the electric field the accuracy of this simplification can vary, it highlights the underlying physical mechanism present in the full calculation. In Fig. 4.3, adapted from ref. [152], we plot the energies of these two pair states as a function of intermolecular distance for NaRb

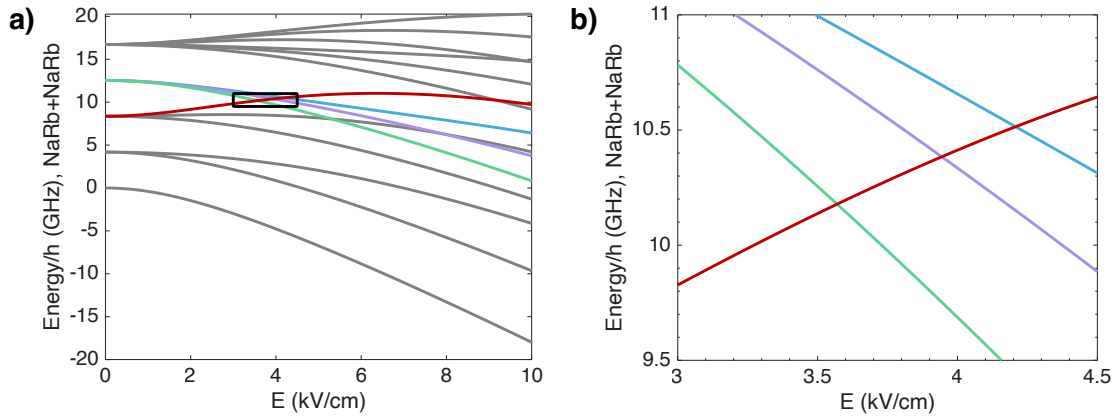


**Figure 4.2: Förster resonance for two $|1,0\rangle$ NaRb molecules.** **a)** NaRb pair energies for the rotational states $|1,0\rangle|1,0\rangle$ (red), $|0,0\rangle|2,0\rangle$ (blue), $|0,0\rangle|2,\pm1\rangle$ (purple), and $|0,0\rangle|2,\pm2\rangle$ (green). At $\sim$4.2 kV/cm, the $|1,0\rangle|1,0\rangle$ pair energy crosses that of $|0,0\rangle|2,0\rangle$. **b)** Magnified view of the region marked by a black rectangle in **a)**.

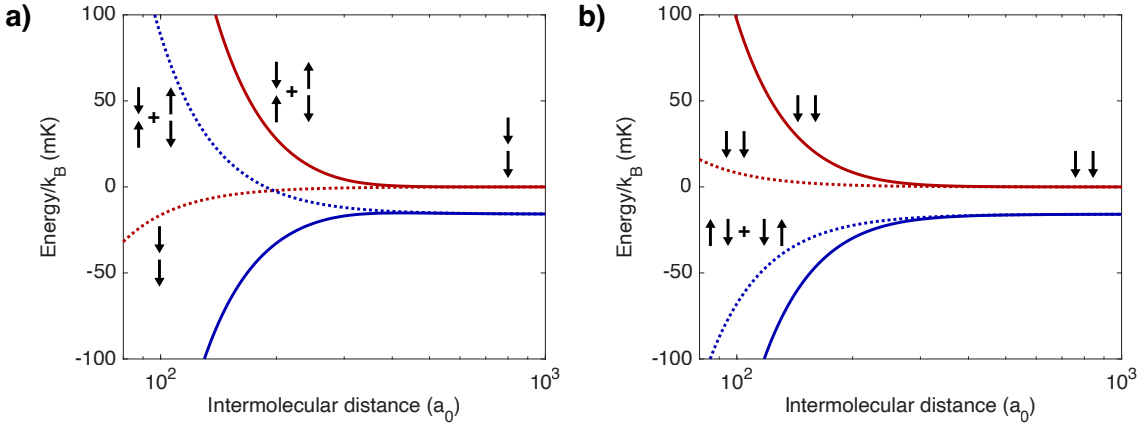


**Figure 4.3: Simplified two-level model of Förster resonance shielding.** For two NaRb molecules at 4.5 kV/cm (above the Förster resonance), we plot the diabatic (dotted lines) and adiabatic (solid lines) interaction potentials as a function of intermolecular distance. The $|1,0\rangle|1,0\rangle$ entrance channel (red) is the higher energy state at large intermolecular distances. We consider its coupling near the Förster resonance to the $|0,0\rangle|2,0\rangle$ state (blue). **a)** Interaction potentials for a collision angle of $\theta = 0°$. The $|1,0\rangle|1,0\rangle$ state initially experiences an attractive potential, but due to the coupling with $|0,0\rangle|2,0\rangle$, its state composition changes leading to a repulsive barrier below a certain intermolecular distance. **b)** For a collision angle of $\theta = 90°$, the $|1,0\rangle|1,0\rangle$ state experiences repulsive interactions at all distances. The simplified model is of limited quantitative accuracy for NaRb, but it is helpful for gaining intuition on the shielding mechanism. Adapted from ref. [152].

at 4.5 kV/cm. For isolated molecules at this shielding field, the $|1,0\rangle|1,0\rangle$ pair state (shown in red) has a higher energy than $|0,0\rangle|2,0\rangle$ (blue). The left panel considers the case of two molecules approaching each other vertically with fixed $\theta = 0°$, where $\theta$ is defined as the angle between the quantization axis (i.e. the electric field, taken to point in the $+z$ direction) and the displacement of the two molecules. At fields just above the Förster resonance, the $|1,0\rangle$ molecules have a negative dipole moment so isolated molecules are anti-aligned with respect to the electric field. Since the dipoles are oriented in the same direction, this represents an attractive head-to-tail collision as illustrated by the dotted diabatic energy curve in the plot. The $|0,0\rangle$ and $|2,0\rangle$ states making up the (symmetrized) pair state $|0,0\rangle|2,0\rangle$, on the other hand, have opposite dipole moments and consequently undergo repulsive head-to-head/tail-to-tail collisions for $\theta = 0°$ (shown as the dotted blue diabatic potential). Note the crossing between the two diabatic energies at $\sim 200\, a_0$, where $a_0$ is the Bohr radius. If we now turn on the dipolar coupling between the pair states and plot the adiabatic energies (solid lines), we see that this becomes an avoided crossing leading to a repulsive energy barrier for the upper adiabat. The physical picture is that two colliding $|1,0\rangle$ molecules change from an attractive head-to-tail orientation to a repulsive superposition of head-to-head and tail-to-tail orientations as they take on the character of the $|0,0\rangle|2,0\rangle$ pair state. The orthogonal collision axis of $\theta = 90°$ is shown in the right panel. Here, the $|1,0\rangle|1,0\rangle$ pair state represents a side-to-side approach of two identically oriented dipoles and correspondingly has repulsive diabatic and adiabatic potentials. We therefore see that above the Förster resonance, $|1,0\rangle$ molecules experience a 3D repulsive collisional barrier.

A full coupled-channels calculation is required to compute quantitatively accurate collision rates. The basis set consists of the states $|N_1, m_{N_1}\rangle|N_2, m_{N_2}\rangle|\ell, m_\ell\rangle$, which are then adapted to respect the bosonic exchange symmetry. Here, $\ell$ is the partial wave and $m_\ell$ is its projection onto the quantization axis. The rotational states

$|N, m_N\rangle$ are implicitly field-dressed rotational states, as the electric field mixes the rotational quanta. More bare rotational states must be included in the calculation for higher electric fields. The basis is restricted to states for which the total projection $M = m_{N_1} + m_{N_2} + m_\ell$ is conserved, and only even values of $\ell$ are included for bosonic molecules. The hyperfine structure of the molecules can be safely ignored as long as the magnetic field is greater than $\sim$100 G [135].

The coupled-channels calculation has been performed for NaRb in, for example, ref. [154]. For effective collisional shielding, and especially for performing evaporative cooling of collisionally shielded molecules, we want a large ratio $\gamma$ of the elastic collision rate to the total two-body loss rate. This loss rate can be divided into two types: inelastic and short-range loss. For the inelastic case, the molecules transition to a lower-energy channel than the entrance channel, resulting in loss due to the acquired kinetic energy. Short-range loss corresponds to the case in which the molecules tunnel through the potential barrier. The calculated collision rates of ref. [154] show that above the NaRb Förster resonance at 4.2 kV/cm, $\gamma > 10^5$ over a broad range of electric fields approximately 0.5 kV/cm in width. This makes Förster resonance shielding of NaRb robust to moderate amounts of electric field noise and drift, easing technical requirements on the electric field control system.

This shielding method was first experimentally demonstrated in ref. [150] in a quasi-2D system of KRb molecules. It was later extended to a 3D geometry in ref. [151], confirming that a potential barrier exists for all collisional approach angles. In contrast to the 2D shielding method of section 4.1, however, the induced dipole moment is much lower. NaRb molecules in the $|1, 0\rangle$ state at 4.5 kV/cm have an induced dipole moment of $-0.4$ D, and in general $d_{\text{ind}} = -0.13d$ for a shielding electric field $E = 3.4B/d$ [149].

## 4.3 Microwave shielding

Perhaps the most versatile technique to mitigate two-body loss is microwave shielding [133–135, 137, 139, 143, 145], which uses blue-detuned circularly polarized microwaves addressing the $N = 0 \rightarrow 1$ transition to engineer a repulsive 3D interaction potential. Its demands on the microwave polarization, Rabi frequency, and phase noise were initially seen as difficult to meet, prompting studies of shielding in the presence of microwave imperfections [135] and of ways to ease the requirements by combining the microwaves with static electric fields [145]. Nevertheless, rapid experimental progress has shown that this shielding technique is indeed feasible, with its first demonstration in ref. [136] using CaF molecules. Since then, microwave shielding has enabled such advances as evaporatively cooling fermionic [138] and bosonic [16] polar molecules to degeneracy as well as associating two molecules into a tetramer state [241] through a field-linked resonance [242]. Microwave shielding has also been used to evaporatively cool NaRb molecules in ref. [141].

As with Förster resonance shielding, microwave shielding ultimately relies on a reorientation of two approaching polar molecules to maintain a repulsive barrier at all collision angles. We can begin to understand its mechanism by considering two molecules initially in their ground rotational state $|0, 0\rangle$. For this shielding mechanism, we must now include a label in our basis denoting the number of $\sigma^+$ photons $\mathcal{N}$ with respect to the (very large) reference number of photons $\mathcal{N}_0$ in the microwave field [133, 135, 137]. We take the microwaves to propagate along the lab-frame $z$ axis. For pure $\sigma^+$ polarization the total projection $M = m_{N_1} + m_{N_2} + m_\ell + \mathcal{N}$ onto the $z$ axis is conserved. If the $\sigma^+$ Rabi frequency $\Omega$ is comparable to or greater than the detuning $\Delta$ from the $N = 0 \rightarrow 1$ transition, then a coupling is introduced between the field-dressed ground rotational state $|N, m_N, \mathcal{N}\rangle = |0, 0, 0\rangle$ and the state $|1, 1, -1\rangle$.

The resulting eigenstates are [137]:

$$\begin{aligned} |+\rangle &= \cos\varphi|0,0,0\rangle + \sin\varphi|1,1,-1\rangle \\ |-\rangle &= -\sin\varphi|0,0,0\rangle + \cos\varphi|1,1,-1\rangle. \end{aligned} \tag{4.2}$$

Here, $\varphi = \arctan((\Delta + \sqrt{\Omega^2 + \Delta^2})/\Omega)$, and the $|+\rangle$ state lies $\hbar\sqrt{\Omega^2 + \Delta^2}$ above the $|-\rangle$ state with $\sqrt{\Omega^2 + \Delta^2}$ being the generalized Rabi frequency. If we adiabatically ramp on blue detuned ($\Delta > 0$) microwaves, then molecules initially in the ground rotational state connect to the higher energy state $|+\rangle$. Therefore, two colliding molecules occupy the uppermost entrance channel $|++\rangle$. Other states in the $N = 1$ manifold with $m_N = 0, -1$ are not coupled to $N = 0$ by the $\sigma^+$ polarized microwaves, and we label these spectator states $|0\rangle$.

There are therefore six asymptotic collision channels corresponding to the symmetrized pair states $|++\rangle, |+0\rangle, |+-\rangle, |00\rangle, |-0\rangle$, and $|--\rangle$, as can be seen in Fig. 4.4a [133, 138]. This plot shows the adiabatic potentials as a function of intermolecular distance for a pair of NaRb molecules with $\Omega = \Delta = 2\pi \times 10\,\text{MHz}$. The $|++\rangle$ entrance channel corresponds to the red line. At large separations, the orientation of the isolated molecules' dipole moments is set by the circularly polarized microwaves, with an effective time-averaged dipole moment $d_{\text{eff}} = d/\sqrt{12(1 + (\Delta/\Omega)^2)}$ [137]. Consequently, the molecules can be visualized as rotating parallel to the $xy$ plane at the microwave frequency (Fig. 4.4b). For two molecules approaching vertically ($\theta = 0°$), the synchronously rotating molecules experience a repulsive dipole-dipole interaction and are prevented from reaching short range (in the rotating frame, it simply looks like the repulsive side-to-side interaction of the previous sections). Note that this is opposite to the conventional dipole-dipole interaction in a static field (or with $\pi$ polarized microwaves) in which $\theta = 0°$ corresponds to an attractive interaction.

For a collision angle of $\theta = 90°$, the time-averaged dipolar interaction is attractive (see inset of Fig. 4.4a). Fortunately, the next-highest energy collision channel has a

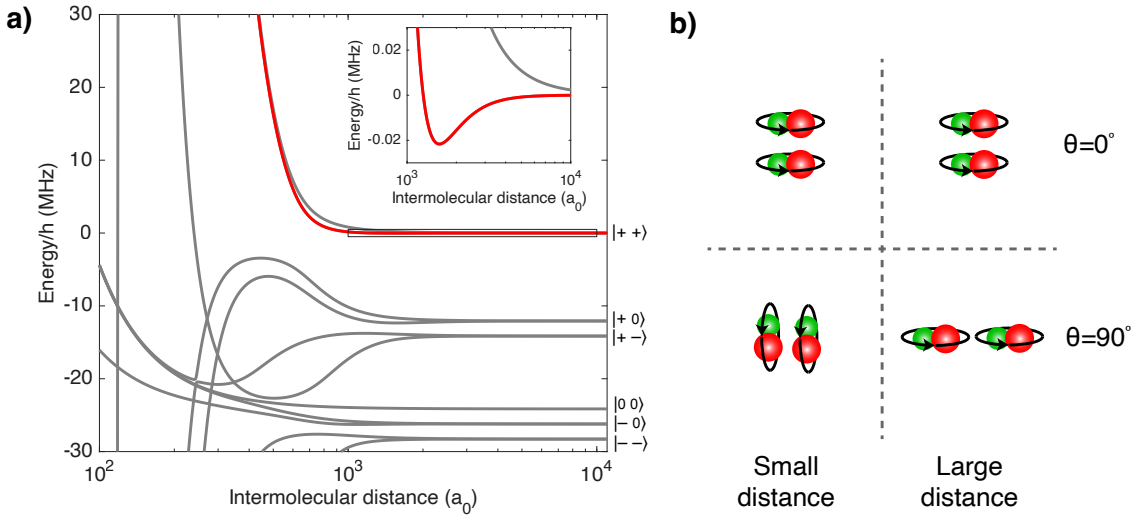


**Figure 4.4: Microwave shielding.** **a)** NaRb adiabatic potentials in the presence of microwave shielding for $\Omega = \Delta = 2\pi \times 10\,\mathrm{MHz}$. For visual simplicity, we restrict the basis set to $N_{\mathrm{max}} = 1$, $\ell = 0, 2$, and $\mathcal{N} = 0, -1, -2$. The eigenstates at large separation in the presence of the microwaves are labeled on the right side of the plot. The inset shows that an attractive well exists due to dipolar interactions. Note that these adiabats are calculated taking into account all collision angles rather than restricting to a fixed value of $\theta$. **b)** In microwave shielding, molecules at a collision angle of $\theta = 90°$ initially experience attractive interactions, but reorient at small distances due to the strong intermolecular interaction energy, providing a repulsive barrier. Molecules at a collision angle of $\theta = 0°$ have repulsive interactions at all distances. Adapted from ref. [138].

repulsive dipolar interaction, so the diabatic energies (not shown in the plot) cross at what is known as the Condon point. This crossing is avoided by $\hbar\Omega$ due to the resonant dipolar exchange of rotational quanta, resulting in a potential barrier in the upper adiabat (the $|{+}{+}\rangle$ entrance channel) [135, 137]. One can view this barrier as a reorientation of the molecules' rotational angular momentum along the intermolecular axis that occurs when the interaction energy between two nearby molecules overwhelms the energy associated with the microwave Rabi frequency (Fig. 4.4b).

The loss processes associated with microwave shielding are divided into two categories. The first process, reaching short range, refers to molecules tunneling through the shielding barrier and experiencing loss with unity probability. Inelastic loss, on the

other hand, results from transitions to lower-lying states. This second process is often labeled microwave-induced loss. Ref. [143] calculated that for $\Delta = \Omega = 2\pi \times 10\,\mathrm{MHz}$ the ratio $\gamma$ of the elastic collision rate to the two-body loss rate is greater than $10^3$, which is a favorable regime for evaporative cooling.

## 4.4 Suppressing three-body loss

The first experimental efforts to evaporatively cool bosonic NaCs [140] and NaRb [141] molecules in the presence of microwave shielding were able to increase the phase-space density (PSD) by about an order of magnitude, with an initial evaporation efficiency $-d\ln(\mathrm{PSD})/d\ln(N)$ of 1.0 and 1.7, respectively (here $N$ is the number of molecules). However, the phase-space density was found to saturate prior to the onset of degeneracy, and a further reduction in trap depth only resulted in a decrease of the molecule number. It is now believed that losses from three-body recombination limited these evaporation attempts [16, 240]. As seen in the inset of Fig. 4.4a, the upper (entrance channel) adiabat for microwave shielding contains a potential well resulting from the long-range attractive dipolar interaction at collision angles approaching $\theta = 90°$. For values of $\Omega$ and $\Delta$ that are effective for two-body collisional shielding, this potential well generally supports one or more bound states that can lead to loss if a third molecule interacts with the collision complex. This source of loss is not limited to microwave shielding. Depending on the molecular species, the interaction potential for Förster resonance collisional shielding may support bound states, again leading to three-body recombination [154]. In the case of NaRb, for example, coupled-channel calculations in ref. [154] found that a bound state exists at 4.5 kV/cm with a weak binding energy of 50 Hz.

The importance of mitigating three-body loss was already realized in early theoretical studies on collisions of ultracold polar molecules [144, 243]. It was proposed

that two external electric fields could be combined to cancel the first-order dipolar interaction responsible for the potential well, leaving behind a repulsive $1/r^6$ van der Waals interaction. Specifically, as we saw in the previous section, the time-averaged interaction of two dipoles induced by circularly polarized microwaves is opposite in sign to the dipolar interaction induced by static electric fields or by $\pi$ polarized microwaves. By combining these fields in the appropriate ratio, we can therefore cancel the $1/r^3$ dipole-dipole interaction, resulting in a purely repulsive barrier at all collision angles *and* intermolecular distances. The absence of a potential well also implies that the s-wave scattering length is strictly repulsive ($a_s > 0$) [142, 154]. Moreover, if the dipole-dipole interaction is kept finite but too weak to support a bound state, then the sign and strength of both the dipolar interaction and the scattering length can be tuned while preserving two- and three-body collisional shielding [142].

As originally envisioned, the cancellation of the first-order dipolar interaction was accomplished using a combination of a static electric field and circularly polarized microwaves [144, 243]. The evaluation of the two-body elastic and inelastic collision rates in this method was later refined in ref. [133]. However, the scheme first experimentally demonstrated employs both $\pi$ and $\sigma^+$ polarized microwave fields at zero DC electric field to bring the dipolar interaction close to zero [16, 142, 244]. Using this double microwave shielding, evaporative cooling of NaCs was able to push past the earlier three-body loss limit, enabling the formation of a BEC of polar molecules [16].

# Chapter 5

# Toward high phase-space density polar molecules in a quantum gas microscope

This work was presented publicly in the following talks: [245, 246].

In our previous work described in chapter 3 with polar molecules, the lattice filling was limited to 15%. Although this was sufficient to observe correlation dynamics in $XY$ and $XXZ$ spin models, many interesting applications of the molecular quantum gas microscope require higher filling fractions (see chapter 6). A natural approach in our apparatus to obtain higher fillings is to transfer the molecules from the 2D lattice to a bulk harmonic trap, evaporate the molecules to achieve a high phase-space density (ideally forming a BEC), and finally load the molecules back into a 2D lattice for quantum gas microscopy. Due to the large on-site interactions that can be engineered with polar molecules, the last step should form a near-unity filling Mott insulator. However, there are two upgrades to our apparatus that are required to implement this scheme. First, the pre-evaporation molecule number needs to be higher so that

we can remove the most energetic molecules during the evaporation and still end up with at least $\sim 10^2$ molecules for quantum gas microscopy. Our efforts on this front are discussed in sections 5.2 and 5.4 of this chapter. Furthermore, as discussed in chapters 1 and 4, ultracold molecules suffer from collisional loss in bulk traps. We therefore need to implement a collisional shielding scheme to enable evaporation to high phase-space densities. This work is the subject of sections 5.1 and 5.3.

## 5.1 Förster resonance shielding

In 2022, after our experiments measuring site-resolved correlations of polar molecules were completed, we considered which of the collisional shielding mechanisms described in chapter 4 we should set up. At the time, we did not have an antenna that could provide large Rabi frequencies with a highly circular polarization needed for the microwave shielding scheme discussed in section 4.3. However, we already had in-vacuum electrodes and high voltage amplifiers to produce large DC electric fields. Since our maximum vertical lattice confinement was too shallow for DC electric field shielding in a 2D layer (see section 4.1), it was natural for us to adopt the Förster resonance approach of section 4.2. Here, we will first describe the electrode geometry and high voltage control system before presenting our results on collisional shielding of polar NaRb molecules. Details on the design and installation of the electrodes can be found in ref. [112].

### 5.1.1 Electric field control system

Our electrodes consist of eight in-vacuum 316 stainless steel rods (1.5 mm diameter) arranged in an octagon (Fig. 5.1). The rods are held in place with two custom-machined Macor holders on either end of the science chamber. These are designed to maximize the distance along the surface of the holders between adjacent rods and

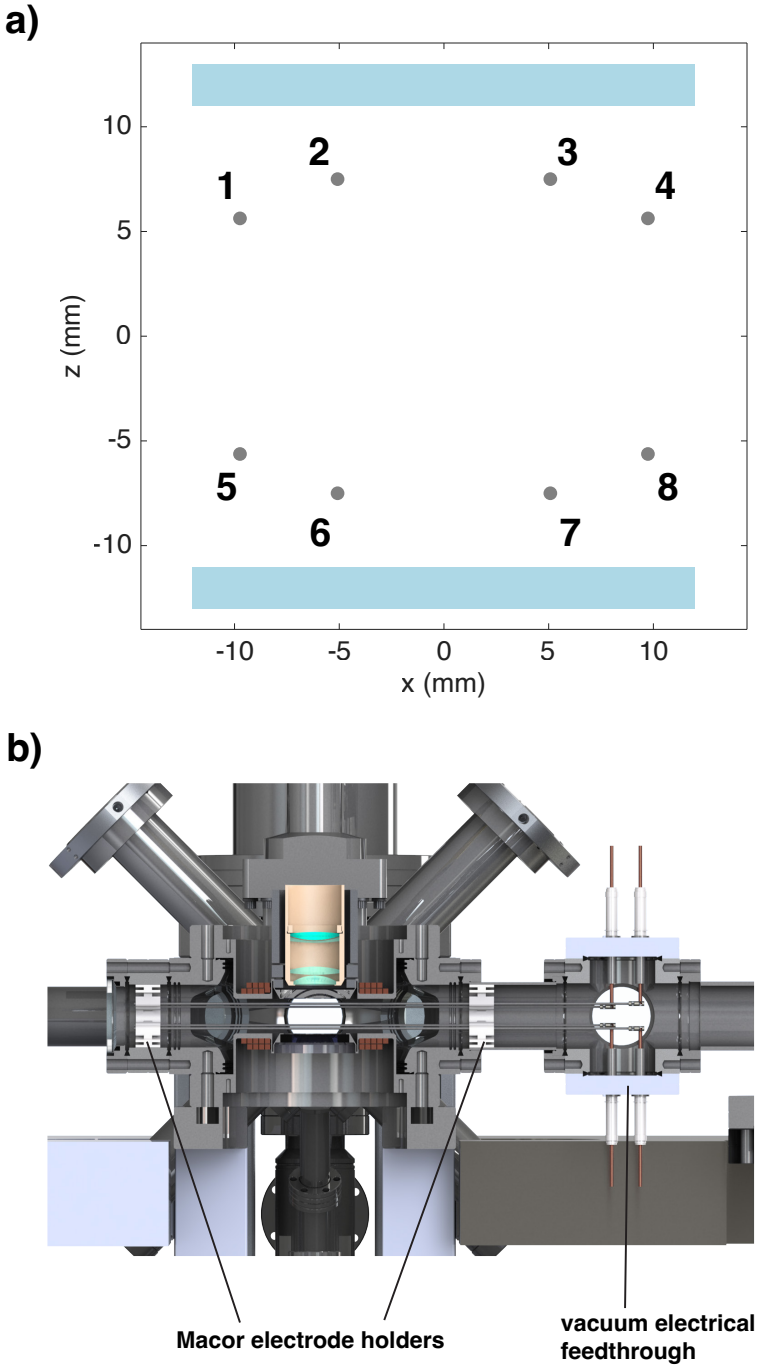


**Figure 5.1: Electrode geometry.** **a)** Schematic of the eight in-vacuum electrodes including our rod numbering convention. The bucket windows are shown in blue. The positions of the rods are dimensionally accurate, but the thickness of the rods and bucket windows is not to scale. **b)** Cross-section of the science chamber, showing the Macor electrode holders and vacuum electrical feedthrough.

between the rods and the vacuum chamber in order to avoid surface tracking at high voltage. At one end of each rod a connection is made to a 20 kV rated vacuum feedthrough (Solid Sealing Technology FA14101). The electrode geometry is compatible with the high numerical aperture (NA) imaging required for quantum gas microscopy. Specifically, we use an NA = 0.5 objective, so the spacing of the rods is chosen to be just large enough to accommodate this. The resulting dimensions are shown in Fig. 5.1. This eight-electrode geometry gives us the capability of nulling gradients and curvatures of the electric field in the plane perpendicular to the symmetry axis by adjusting the voltage ratios on the rods. Furthermore, uniform electric fields can be produced in both the horizontal and vertical directions (see ref. [112] for details on the Ansys Maxwell simulations used to design the electrode geometry). For the orthogonal electric field component (parallel to the rods), we rely on the symmetry of the electrodes and vacuum chamber to obtain low electric field gradients at the position of the molecules. With a maximum applied voltage of ±10 kV, the electrodes can produce a uniform electric field of ∼7 kV/cm at the center of the science chamber. At this electric field, NaRb molecules in the dressed $|N = 0, m_N = 0\rangle$ state have an induced electric dipole moment of 2.2 D (Fig. 3.3). (Unless otherwise noted, in this chapter rotational state labels at nonzero electric fields refer to dressed states.)

An important concern with high voltage electrode systems is the buildup of charge on nearby glass windows, resulting in drifting electric fields between experimental cycles [223, 230, 247]. In our case, the closest windows to the electrodes are the top and bottom bucket windows of the science chamber with less than 3 mm glass-to-rod separation (Fig. 5.1). Since our electrodes are inside the vacuum chamber, however, this issue could be avoided by coating the inner surfaces of the bucket windows with a 10 nm conductive layer of indium tin oxide (ITO). This ITO coating is electrically connected to our grounded science chamber by the use of a clamping system involving stainless steel springs in contact with the edges of the windows [112]. A 5 mm diameter

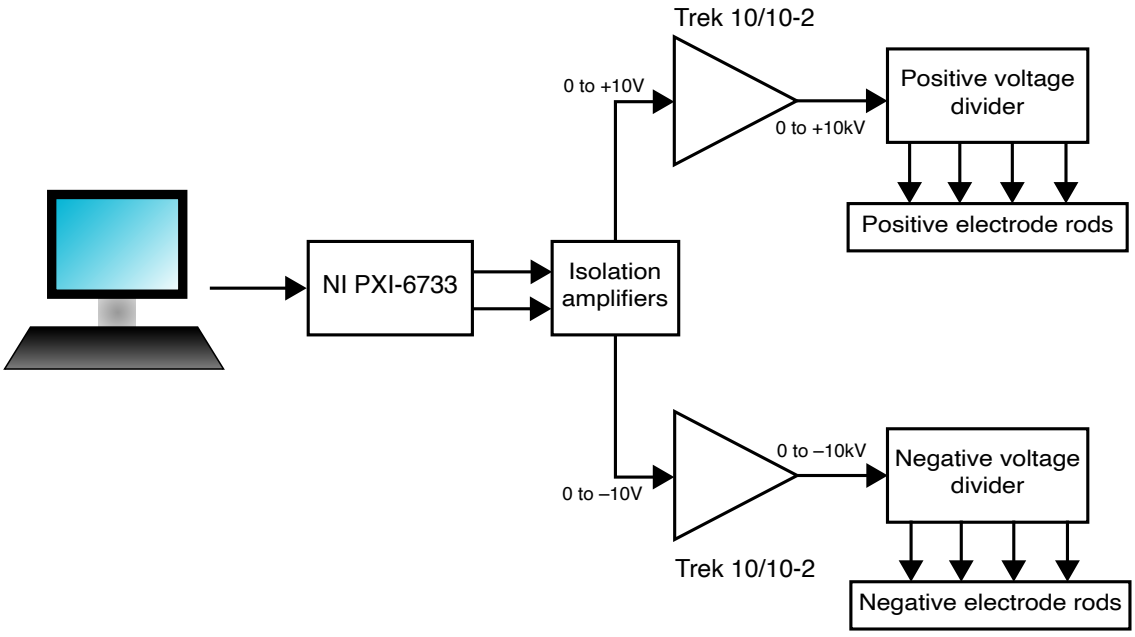


**Figure 5.2: Block diagram of electric field control system.** Computer-controlled voltage setpoints for the positive and negative high voltage amplifiers are converted into isolated analog voltages and sent to two high voltage amplifiers. The output of the positive amplifier ranges from 0 to +10 kV while the output of the negative amplifier ranges from 0 to −10 kV. The outputs are then sent to custom voltage divider boxes as described in the text, which are connected to the electrode rods in the science chamber.

region in the center of both the top and bottom bucket windows is not coated with ITO in order to prevent damage to the coating from high power optical potentials sent vertically through the science chamber. With this setup, we have never experienced any issues with stray charge buildup on the bucket windows.

We will now describe our electric field control system in detail. The first version of the control system that we used is shown in Fig. 5.2. This setup is open-loop, relying on the stability of the amplifier gain and voltage division ratios to avoid drift of the electric field strength. Since in our initial collisional shielding studies all of the electric field ramps took place with molecules frozen in an optical lattice, limitations on the electric field bandwidth due to the resistance of the voltage dividers and the capacitance of the rods and wires were not a concern. Upgrades to the system to

allow for higher bandwidths, as well as improved noise and stability, will be described later. Setpoint voltages from $-10\,\mathrm{V}$ to $10\,\mathrm{V}$ are generated in the same manner as all of the other computer-controlled analog setpoints in the experiment. In brief, our experimental sequence is programmed and run using the Cicero Word Generator control system [248]. For outputting analog voltages, the software interfaces with an 8-channel, 16-bit National Instruments PXI-6733 analog output card. Since the voltage distribution on the electrodes for uniform field configurations involves four of the electrodes being set to positive voltages and the other four to negative voltages, we use one analog output channel as the setpoint for the four positive rods and a second channel as the setpoint for the negative rods. We then pass the signals through an analog isolator based on the Analog Devices AD215AY isolation amplifier to prevent ground loops.

The setpoint voltages are next sent to the inputs of two Trek 10/10-2 high speed, high voltage amplifiers. These amplifiers can produce a maximum voltage of $\pm 10\,\mathrm{kV}$ at a current of $\pm 10\,\mathrm{mA}$ ($\pm 15\,\mathrm{mA}$ peak). Although they have bipolar outputs, in our setup we use one for positive voltages and the other for negative voltages. The amplifiers have a gain of $1000\,\mathrm{V/V}$, so a $10\,\mathrm{V}(-10\,\mathrm{V})$ input corresponds to a $10\,\mathrm{kV}(-10\,\mathrm{kV})$ output. The amplifiers' outputs are then sent to two voltage divider boxes using $20\,\mathrm{kV}$ rated connectors (TE Connectivity LGH series 5-861610-3 and 5-862197-3) and 22 AWG, $30\,\mathrm{kV}$ wire (Alpha Wire 392275). As with the amplifiers, one voltage divider is used for positive voltages and the other for negative voltages. For a given polarity, the voltage divider splits the amplifier output into four different voltages corresponding to the four electrodes of that polarity, with the voltage ratios described in section 5.1.2.

Fig. 5.3 shows the construction of one of the voltage divider boxes. The complicated structure results from adhering to conservative electrical clearance and creepage distances. Clearance refers to the point-to-point distance through air between two locations at different potentials, while creepage refers to the distance across the surface

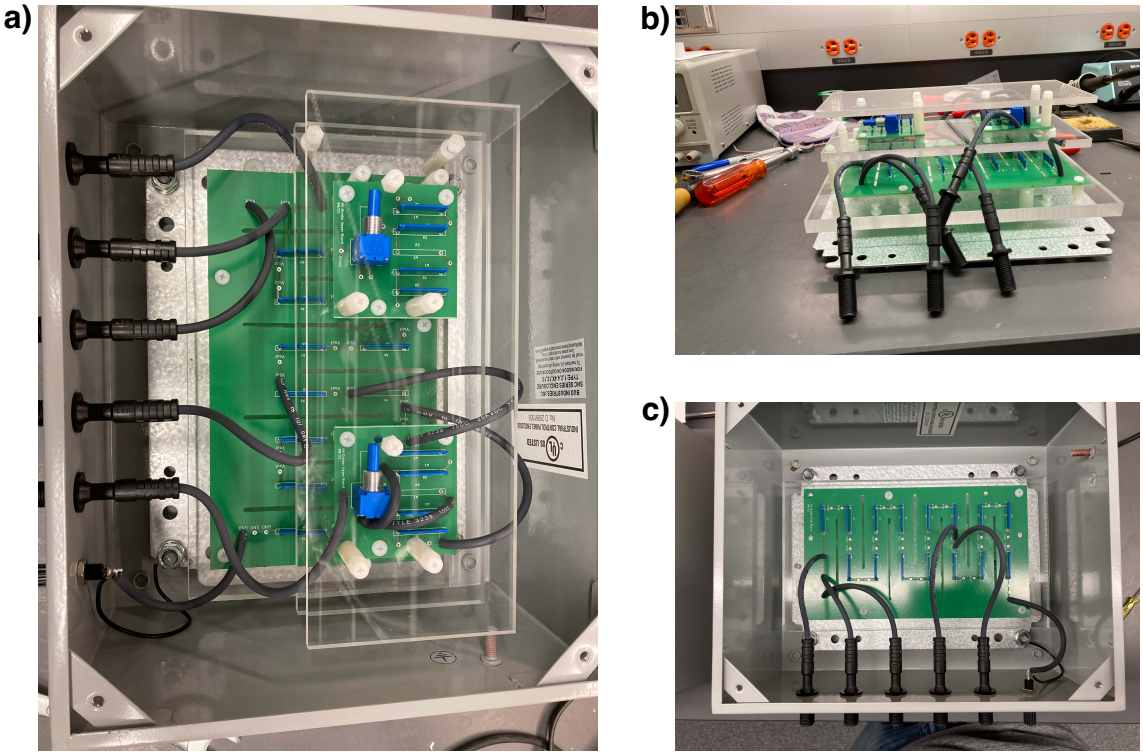


**Figure 5.3: Electrode voltage divider.** **a)** Top view of the electrode voltage divider, showing the upper boards containing 1 MΩ resistors and potentiometers, as well as the lower board containing 5 MΩ resistors. **b)** Side view showing the multilayer construction. Acrylic sheets are used to prevent arcing. **c)** The lower board of the electrode divider. Slots are used to increase the electrical creepage distance.

of a material. As an example, slots cut into a printed circuit board (PCB) can increase the creepage distance while they do not affect the clearance. We maintain $> 50$ mm clearance and $> 125$ mm creepage across 10 kV voltage differences. Although the use of potting compounds could ease these requirements, we avoided them so that we could easily make changes to the circuit boards. The steel enclosure and the ground of the voltage divider are tied to Earth ground for safety, as are the load returns of the high voltage amplifiers. Ground loops in high voltage applications are difficult to avoid due to the necessity of Earth grounding the system, although a few mitigation strategies such as using large ground conductors can be employed to reduce noise pickup [249].

The voltage divider consists of a "lower" circuit board and two "upper" boards. Acrylic sheets are placed between the circuit boards as well as between the boards and the outer steel enclosure for clearance distance considerations. The lower board nominally consists of fifteen 5 MΩ resistors (Ohmite SM104035004FE) connected in series between the amplifier output voltage and ground. For our initial testing of the electric fields on the molecules, the 25 ppm/°C temperature coefficient of these resistors was sufficient. The voltage can then be tapped off between individual resistors and sent to one of the four electrodes matching that voltage divider's polarity. By adjusting the voltage ratios between the electrodes, we can minimize electric field gradients at the molecules (see section 5.1.2). The magnitude of the resulting uniform field can then be varied in the experimental sequence by programming the setpoint voltages for the high voltage amplifier inputs. Although tuning the ratios was a time-consuming process (the amplifiers must be turned off and wires must be re-soldered to new positions on the voltage divider for each ratio change), this only needed to be performed once for a given vertical or horizontal electric field configuration. Furthermore, predicted ratios based on Ansys Maxwell electric field simulations provided good starting parameters (see ref. [112]).

However, we found that adjustments of the electrode voltage ratios in steps of $V_{\text{in}}/15$, where $V_{\text{in}}$ is the input voltage to the divider, did not give us the precision necessary to null electric field gradients at the molecules. We therefore installed two "upper" boards per voltage divider box, each of which nominally consists of five 1 MΩ resistors (Ohmite SM104031004FE) placed in series. We can obtain a finer voltage division ratio by removing one of the 5 MΩ resistors and wiring one of the upper boards in its place, thereby giving us four intermediate voltage divider positions. In turn, for final adjustments of the voltage ratios, we can remove one of the 1 MΩ resistors on the upper board and replace it with a 1 MΩ potentiometer (Bourns 93R1A-R22-A25L), enabling virtually continuous tuning of the voltage ratio within its range. The eight

output voltages of the two voltage dividers (four per divider) are then connected to the eight electrodes via high voltage plugs (Solid Sealing Technologies FP10883-02) and the previously mentioned vacuum feedthroughs.

Although we do not have a way of continuously reading out the voltages on individual electrodes in this setup, we are able to monitor the input to the voltage dividers via the 1000:1 voltage monitor output ports of the Trek high voltage amplifiers (for greater stability of the monitored ratio as well as closed-loop operation, we later constructed our own monitor divider as described in section 5.1.4). During initial testing, we observed spikes on this monitored voltage corresponding to 60 Hz noise from the AC mains. To mitigate this issue, we synchronize the electric field portion of the experimental sequence to the 60 Hz mains voltage. In particular, we generate a trigger signal for the sequence to advance when the mains voltage crosses zero on a falling edge (circuit diagram shown in appendix B).

### 5.1.2 Electric field calibration and gradient nulling

We perform STIRAP at zero electric field, which produces lattice-confined ground state molecules in their $|0,0\rangle$ rotational state. To calibrate the electric field and for certain measurements of electric field gradients (as well as for Förster resonance collisional shielding), we need to transfer the molecules from $N = 0$ to $N = 1$. We perform this transfer using a microwave flip with the same helical antenna used in the experiments of section 3.3. A carrier frequency typically between 3 and 6 GHz depending on the transition and the electric field is produced by a low phase noise signal generator (Agilent E8257C with option UNR). For frequency and amplitude control, we mix this signal with that of an arbitrary waveform generator (Keysight 33621A with option MEM) using a double balanced mixer (Mini-Circuits ZMX-7GR). The output of the mixer goes to two switches connected in series (Mini-Circuits ZYSWA-2-50DR and Mini-Circuits ZASWA-2-50DR), which are used to quickly turn

the RF power on and off. The signal is then sent through a 5 W amplifier (Mini-Circuits ZHL-5W-63-S+) before going to the helical antenna. The antenna consists of four turns of copper wire at an approximately 13° pitch angle with a center frequency of ∼4.2 GHz. A metal reflector is located at its base, and impedance matching is performed by adjusting the distance between the reflector and the wire in the first turn. Since high Rabi frequencies were not needed initially, the helical antenna was placed relatively far from the center of the science chamber (∼20 cm) so as not to impede optical access and to make the installation simpler.

We first obtained a calibration between the electric field at the molecules and the programmed voltage setpoints of the amplifiers by using microwave spectroscopy (Fig. 5.4a). Throughout the remainder of this section, we will assume a vertically oriented electric field unless otherwise stated. The calibration was performed with a magnetic field of 335 G pointing in the same direction as the electric field. For lower values of the electric field, we transfer the molecules from $|0,0\rangle$ to $|1,\pm1\rangle$ using a 2 MHz Landau-Zener sweep. Since we can only drive transitions within a certain bandwidth set by the RF electronics and the antenna, this transition is chosen instead of $|0,0\rangle$ to $|1,0\rangle$ as it has a reduced sensitivity to electric fields (see Fig. 3.3). The STIRAP pulse used to dissociate the molecules for imaging is state-selective, so we observe a loss of molecules when we successfully drive this transition. The hyperfine splitting of the $|1,1\rangle$ and $|1,-1\rangle$ states is unresolved since it is smaller than the Landau-Zener sweep range. Once we find the transition frequency at a given amplifier voltage setpoint, it can then be converted to an electric field based on the molecular constants determined in refs. [27, 113].

One complication is that if the electric field gradients are not sufficiently close to zero (such as with initial electric field calibrations performed prior to nulling the gradient), then the $|0,0\rangle$ molecules with a strong induced dipole moment may not be held in the trap at the highest electric fields. The upper values of the electric field

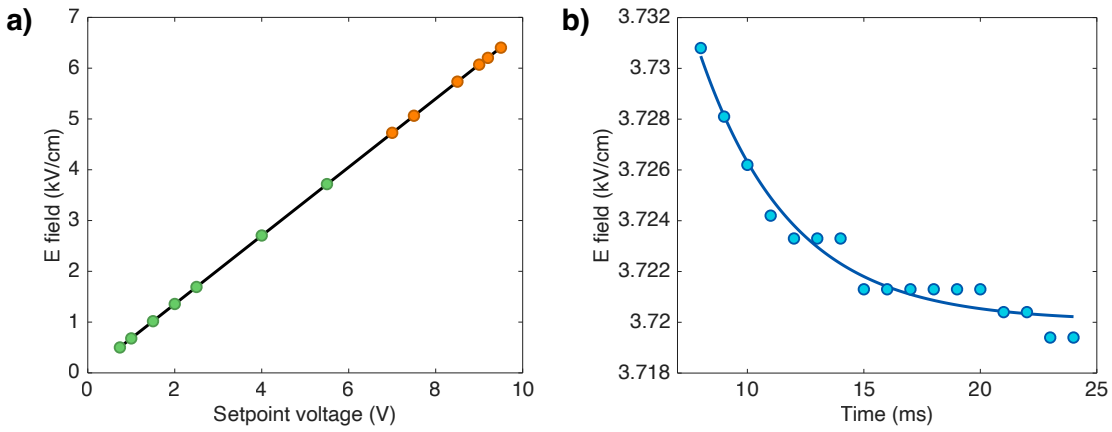


**Figure 5.4: Electric field calibration. a)** Calibration of the programmed voltage setpoint in our computer control system to the electric field at the molecules. For lower electric fields, we determine the electric field by driving a rotational state transition from the field-dressed $|0,0\rangle$ state to $|1,\pm1\rangle$ (green). At higher electric fields, we instead drive the $|1,0\rangle$ to $|1,\pm1\rangle$ transition (orange). **b)** In one of our first calibration measurements, we observed a 4 ms $1/e$ settling time of the electric field due to the low-pass effect of the resistance of the voltage dividers and the capacitance of the wires and electrode rods.

calibration plot in Fig. 5.4a are therefore determined via a different method, taking advantage of the lower induced dipole moment of NaRb in the $N = 1$ state. We first transfer the molecules from $|0,0\rangle$ to $|1,0\rangle$ at a lower electric field before raising the field to the target spectroscopy value. We next perform a Landau-Zener sweep attempting to drive the $|1,0\rangle$ to $|1,\pm1\rangle$ transition. Finally, we go back to the lower electric field value and transfer molecules remaining in $|1,0\rangle$ to $|0,0\rangle$, which can then be detected. If the $|1,0\rangle$ to $|1,\pm1\rangle$ transition is successful, then as before we observe a loss of molecules at the end of the sequence. Note that we are able to drive the $|1,0\rangle$ to $|1,\pm1\rangle$ transition despite the $\Delta N = \pm1$ selection rule because these are dressed states; at high electric fields they contain significant admixtures of other bare rotational levels.

The electric field is recalibrated whenever we make a change to the electrode voltage ratios by adjusting the voltage dividers, or if we switch from the vertical field orientation to the horizontal one. One of the first times that we performed a

calibration, we recorded the dependence of the Landau-Zener transition frequency on the amount of time that we allowed the electric field to settle after ramping up to the spectroscopy field (Fig. 5.4b). The settling time has an exponential time constant of $\tau = 4\,\mathrm{ms}$, likely determined by the low-pass effect of the voltage divider resistance and the capacitance of the wires and electrodes. For the measurements discussed in this section, this settling time did not pose an issue. Since the lattice-confined molecules are long-lived compared to this time constant, we could simply give the electric field time to settle before driving any microwave transitions. Furthermore, Förster resonance collisional shielding for NaRb does not place stringent stability requirements on the electric field (see section 5.1.3). Certain collisional shielding schemes discussed in section 5.3 do require faster bandwidths as well as low noise, so we later upgraded the electric field control system (see section 5.1.4).

It is easier to drive high efficiency microwave transfers at small electric fields than at higher ones because electric field fluctuations produce noise on the transition frequency through the DC Stark shift. In order to efficiently produce molecules in the $|1,0\rangle$ state required for Förster resonance shielding (see section 4.2), we therefore planned to transfer the molecules from $|0,0\rangle$ to $|1,0\rangle$ at a low electric field before ramping up the field to the shielding value of approximately 4.2 to 4.6 kV/cm. The transfer cannot be performed at exactly zero electric field because the target $|N = 1, m_N = 0, m_{I,\mathrm{Na}} = 3/2, m_{I,\mathrm{Rb}} = 3/2\rangle$ state has several avoided crossings with other hyperfine levels below 0.15 kV/cm (at 335 G) that we would populate when ramping to the shielding field (Fig. 5.5).

Initially, we performed a Landau-Zener sweep at 0.168 kV/cm to transfer the molecules to $|1,0\rangle$. We shape the Rabi frequency $\Omega$ and detuning $\Delta$ of the sweep

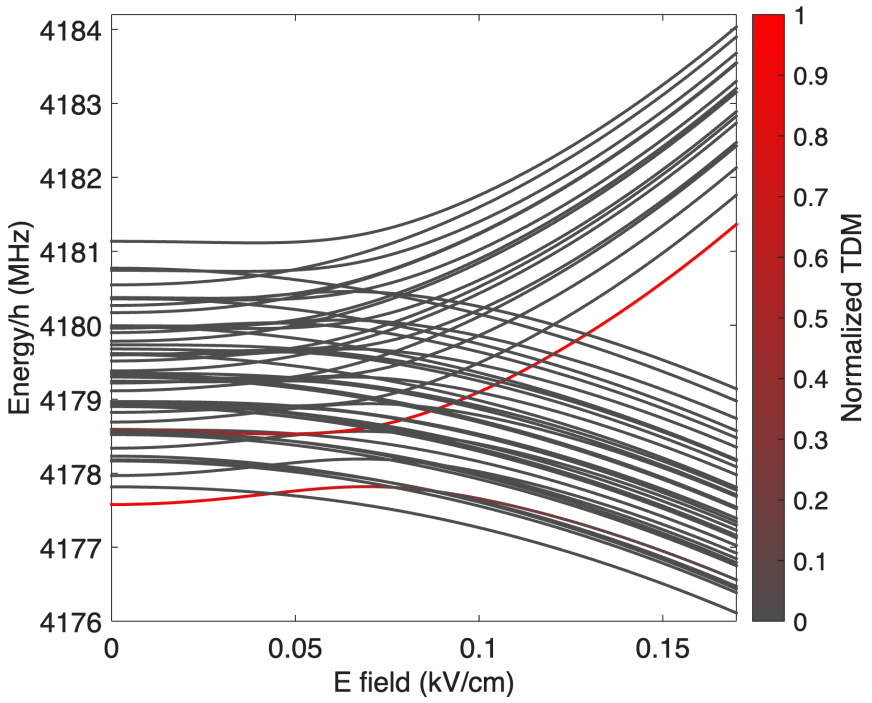


**Figure 5.5: Hyperfine crossings of the $|1,0,3/2,3/2\rangle$ state.** For low electric fields at 335 G, the $|1,0,3/2,3/2\rangle$ state has several avoided crossings with other hyperfine levels. The $|0,0,3/2,3/2\rangle$ to $|1,0,3/2,3/2\rangle$ transition dipole moment (TDM) is shown by the red shading normalized to its maximum value of $d/\sqrt{3}$, where $d$ is the permanent dipole moment.

according to

$$\begin{aligned}\Omega(t) &= \Omega_p \text{sech}\left[\frac{10}{\tau}\left(t-\frac{\tau}{2}\right)\right] \\ \Delta(t) &= \Delta_{\max}\tanh\left[\frac{10}{\tau}\left(t-\frac{\tau}{2}\right)\right]\end{aligned} \tag{5.1}$$

where $\Omega_p = 2\pi \times 110\,\text{kHz}$ is the peak Rabi frequency, $\tau = 1\,\text{ms}$ is the sweep duration, and $\Delta_{\max} = 1\,\text{MHz}$ is the maximum detuning of the sweep on either side of the center frequency (i.e. the total sweep range is $2\Delta_{\max}$). With these parameters, we measured a one-way transfer efficiency of 98%. We could then increase the electric field to the shielding value while the $|1,0\rangle$ molecules were still pinned in the optical lattice. For detection, we reverse all of these steps to place the molecules back in $|0,0\rangle$ before performing our usual dissociation and imaging procedures. However,

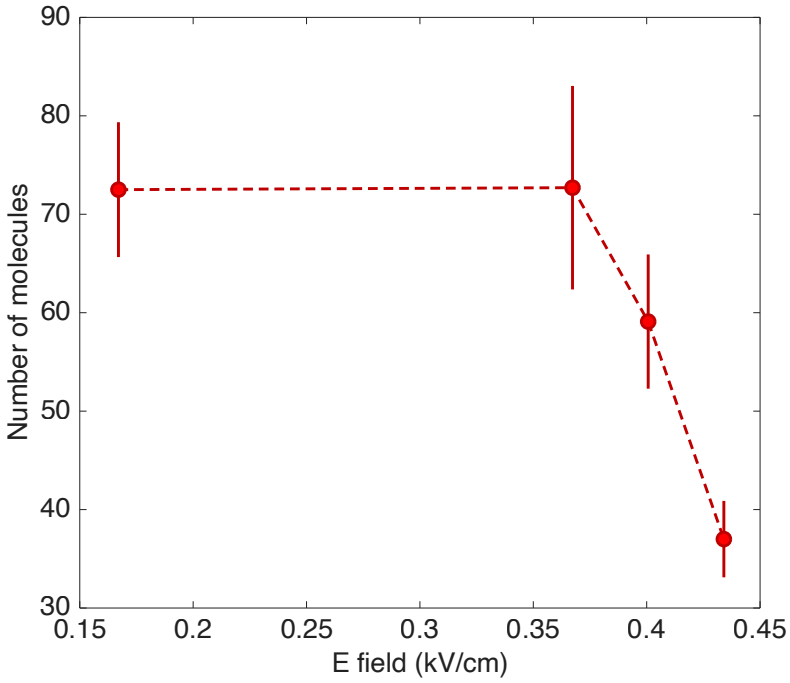


**Figure 5.6: Loss of $|1,0\rangle$ molecules.** When $|1,0\rangle$ molecules are ramped through $\sim$0.4 kV/cm, loss is observed due to a Raman process where the lattice beams transfer the molecules to $|1,\pm1\rangle$, which is dark to our detection protocol.

when we first tried the ramp to the shielding field with the $|1,0\rangle$ molecules, we observed significant loss. By tracking this loss more carefully as a function of the final value of the electric field ramp, we observed that the loss began above electric fields of $\sim$0.4 kV/cm as shown in Fig. 5.6. We realized that at this field, the energy difference between $|1,0\rangle$ and $|1,\pm1\rangle$ is approximately 30 MHz, which coincides with the frequency difference between our 2D and vertical lattice beams. This suggested that a Raman process was occurring in which the lattice beams were causing partial transfer of the $|1,0\rangle$ molecules to $|1,\pm1\rangle$, appearing as loss in our detection scheme. The solution, fortunately, was straightforward. We simply performed the Landau-Zener sweep at 0.5 kV/cm, keeping the molecules in $|0,0\rangle$ until the electric field was high enough that the splitting between $|1,0\rangle$ and $|1,\pm1\rangle$ was significantly greater than 30 MHz.

With a working microwave transfer to $|1,0\rangle$, the last step before attempting Förster resonance collisional shielding was to determine the uniformity of the electric field at the molecules and improve it if necessary. We first focused on measuring electric field gradients in the horizontal plane. In this plane, we can only correct gradients along the axis perpendicular to the rods; in the orthogonal direction we rely on the symmetry of the electrode arrangement to produce uniform electric fields. Our starting point for the voltage ratios between the rods that would produce a uniform vertical field was based on electric field simulations using Ansys Maxwell [112]. The first indication of the presence of electric field gradients came from performing a Ramsey measurement. At 0.52 kV/cm, we apply two $\pi/2$ pulses driving the $|0,0\rangle$ to $|1,0\rangle$ transition, with the pulses separated by a precession time $T$. If the electric field is uniform and constant, then all of the molecules should end up in $|1,0\rangle$ and will be dark to our detection protocol. However, a gradient of the electric field along one axis of the cloud causes molecules along that axis to experience different detunings relative to the microwave drive frequency. If a portion of the cloud accumulates a $\pi$ phase shift along the equator of the Bloch sphere during the precession time, then it will be transferred back to the $|0,0\rangle$ state by the second $\pi/2$ pulse and subsequently detected. In the image shown in Fig. 5.7, we observed two stripes of molecules with a central dark region after a $T = 70\,\mu$s precession time, indicating that the two regions had developed a $\pi$ phase shift along the equator of the Bloch sphere relative to the central region and a $2\pi$ phase shift relative to each other. A $2\pi$ phase shift accumulated over $70\,\mu$s corresponds to a relative detuning of 14.3 kHz between the stripes. Since the stripe separation is 15.7 lattice sites, where the lattice constant is 752 nm, this gives a gradient of 900 Hz/site. At 0.52 kV/cm, the slope of the transition frequency is 335.6 MHz/(kV/cm), so we can extract an electric field gradient of 36 V/cm$^2$ at this field.

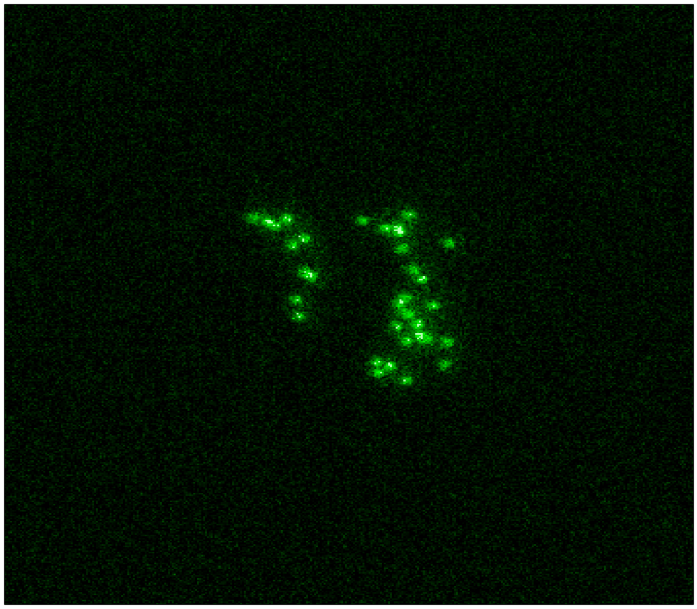

**Figure 5.7: Ramsey stripes.** Following a Ramsey sequence in the presence of an electric field gradient, stripes are visible in the molecule distribution.

Unfortunately, we found that the stripes were not very reproducible, so we adopted an alternative protocol to measure horizontal electric field gradients. Beginning with lattice-confined $|0,0\rangle$ molecules, we quickly ramped the 2D lattice off, let the molecules expand in a layer of the vertical lattice for some time $t$, and then pinned their positions by ramping the 2D lattice back on again. By comparing the position of the center of mass of the molecules at zero electric field versus a higher field, we could determine the displacement of the molecules in response to an electric field gradient. If the $x$-axis is defined perpendicular to the electrode rods, then the displacement $\Delta x$ is related to the gradient $\partial E/\partial x$ by:

$$\Delta x = \frac{t^2 d}{2m}\frac{\partial E}{\partial x}, \tag{5.2}$$

where $m$ is the molecular mass and $d$ is the induced dipole moment at a particular electric field. The same relationship can be used to determine the gradient $\partial E/\partial y$ from the displacement $\Delta y$ parallel to the rods, although we can only correct gradients

along the $x$-axis. After iterating between measuring the gradient and changing the voltage ratios of the electrodes, the final values of the horizontal electric field gradients at 1.07 kV/cm were:

$$\begin{aligned} \left|\frac{\partial E}{\partial x}\right| &= 0.27(6)\,\mathrm{V/cm^2} \\ \left|\frac{\partial E}{\partial y}\right| &= 0.80(17)\,\mathrm{V/cm^2}. \end{aligned} \tag{5.3}$$

If lower gradients along the axis of the electrodes are required in the future, a "shimming" electrode placed just outside one of the bucket windows could be used to cancel the small residual gradient.

For vertical gradients, we need to also consider the effect of gravity. It is not always necessary or desirable to cancel overall vertical gradients, particularly for experiments with molecules in isolated layers of a vertical lattice, because the energy difference between adjacent layers can prevent interlayer tunneling. For instance, we did not perform gradient nulling in the vertical direction for the experiments described in section 5.1.3, but we did implement it for the Förster resonance measurements in section 5.2. To cancel the combined vertical forces on the molecules we require an upwards force from the electric field that matches the downwards force from gravity. Since this depends on the induced dipole moment, the vertical gradient tuning is specific to a molecular state at a particular electric field. We choose to null overall (gravity and electric field) vertical gradients for $|1,0\rangle$ molecules at 4.5 kV/cm, as that is the relevant configuration for Förster resonance shielding. To measure the gradient, we begin as before with molecules confined in both a 2D lattice and a vertical lattice. We next ramp down the vertical lattice to a lower lattice depth, hold it at that value for a time $t$, and then raise it back up to its former lattice depth. A lower overall gradient in the vertical direction corresponds to enhanced molecule survival at lower vertical lattice depths. To minimize the gradient, we adjusted the voltage ratios of the

Table 5.1: **Electrode rod voltage ratios.** Final voltage ratios of electrode rods following electric field gradient minimizations for both vertical and horizontal field orientations. The voltage ratios are given relative to the output voltage of the positive amplifier $V_{\text{amp,pos}}$. The rod numbering corresponds to Fig. 5.1. The values for the vertical orientation minimize both vertical and horizontal gradients for the $|1,0\rangle$ state at 4.5 kV/cm. For the horizontal orientation, only horizontal electric field gradients were minimized.

| | Electrode rod voltage ratios relative to $V_{\text{amp,pos}}$ | | | | | | | |
|---|---|---|---|---|---|---|---|---|
| **E** | Rod 1 | Rod 2 | Rod 3 | Rod 4 | Rod 5 | Rod 6 | Rod 7 | Rod 8 |
| Vertical | –0.428 | 1.000 | 1.000 | –0.533 | 0.428 | –0.977 | –0.977 | 0.533 |
| Horizontal | 1.000 | 0.333 | –0.339 | –1.018 | 1.000 | 0.333 | –0.339 | –1.018 |

electrodes in a symmetric manner such that the horizontal gradient that we previously nulled was minimally affected (although we fine-tuned the horizontal gradient once more after nulling the vertical gradient). The final voltage ratios of the rods after the gradient minimizations are given in table 5.1.

### 5.1.3 Observation of Förster resonance shielding

As discussed in section 4.2, if NaRb molecules are prepared in the $|1,0\rangle$ state, then at ∼4.2 kV/cm the total energy of a pair of molecules equals that of one molecule in $|2,0\rangle$ and one in $|0,0\rangle$. Dipolar interactions open up an avoided crossing at this resonance for two nearby molecules. For electric fields close to but greater than this crossing, an energetic barrier exists at short intermolecular distances preventing two molecules from coming close together. This is referred to as Förster resonance collisional shielding.

Prior to implementing shielding of $|1,0\rangle$ molecules at high field, we first measured the lifetimes of $|0,0\rangle$ molecules at zero electric field as a reference. Fig. 5.8a shows the number of molecules versus hold time for $|0,0\rangle$ molecules frozen in a deep optical lattice. The 2D lattice depth is $49E_{\text{r}}$, where $E_{\text{r}} = h^2/8ma^2$ is the recoil energy for the molecules, $m$ is the molecular mass, and $a = 752\,\text{nm}$ is the lattice constant.

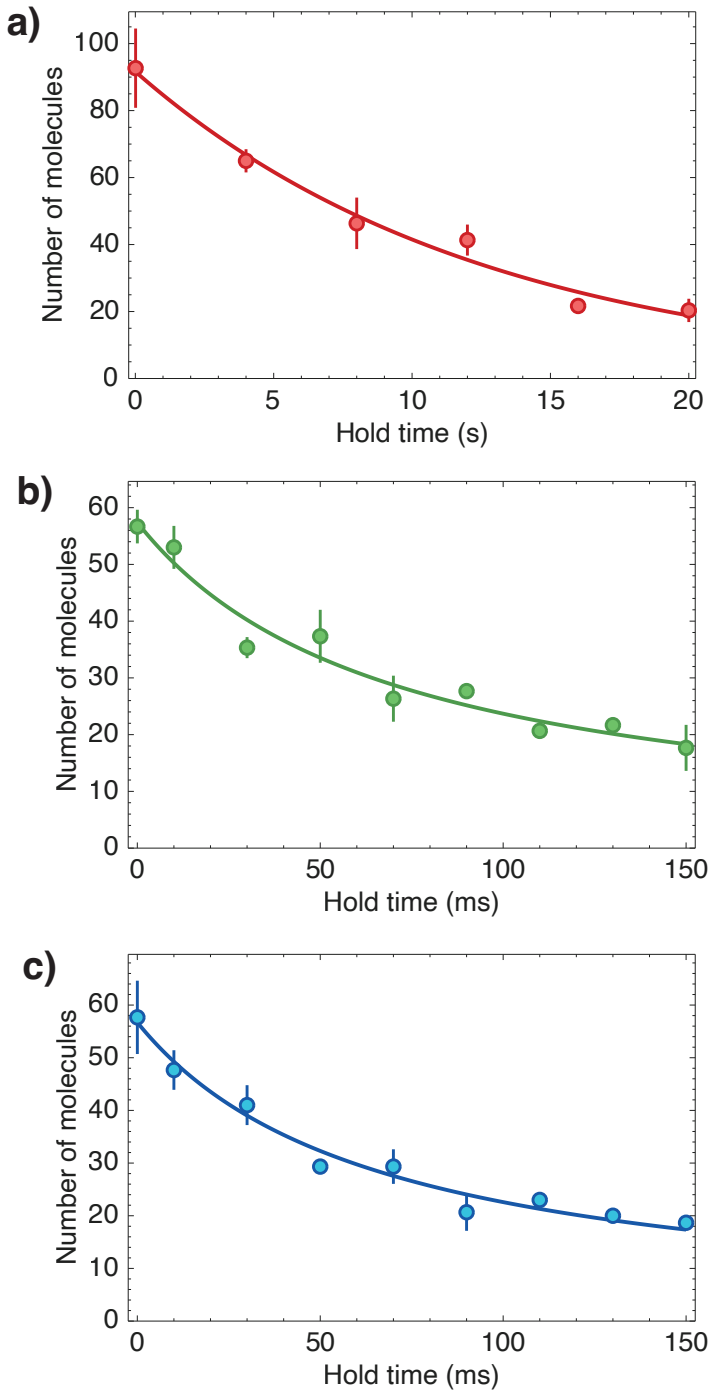


**Figure 5.8: Molecule lifetime at $E = 0\,\mathbf{kV/cm}$.** **a)** Lifetime of $|0,0\rangle$ molecules at zero electric field in a deep lattice. We extract a one-body lifetime of $\tau = 13(1)\,\mathrm{s}$. **b)** Lifetime of $|0,0\rangle$ molecules at zero electric field without a 2D lattice. Note that the $x$-axis is in milliseconds. The lifetime now fits to a two-body decay model with $\kappa = 14(2)\,\mathrm{s}^{-1}$. **c)** Lifetime of $|1,0\rangle$ molecules at zero electric field without a 2D lattice. The extracted two-body loss rate coefficient is $\kappa = 15(1)\,\mathrm{s}^{-1}$.

Confinement in the $z$ direction provided by the 3.8 $\mu$m spacing vertical lattice is $\omega_z = 2\pi \times 3.7\,\mathrm{kHz}$. We model the number decay as one-body loss:

$$\frac{\mathrm{d}N}{\mathrm{d}t} = -\frac{N}{\tau}, \tag{5.4}$$

with the solution

$$N(t) = N_0 e^{-t/\tau}. \tag{5.5}$$

Here, $N$ is the number of molecules, $N_0$ is initial number at hold time $t = 0$, and $\tau$ is the $1/e$ lifetime. From this model, we extract a lifetime of $\tau = 13(1)\,\mathrm{s}$. Since there are no collisions, the lifetime is likely limited by off-resonant scattering from the trapping potentials.

We then allow the molecules to collide in a quasi-2D geometry by turning off the 2D lattice, resulting in a significantly reduced lifetime (Fig. 5.8b). For this measurement, the 2D lattice ramps off in 20 ms, and then after a variable hold time the 2D lattice is turned back on to pin the molecular distribution. During the hold time, the optical confinement is entirely provided by the vertical lattice with $(\omega_x, \omega_y, \omega_z) = 2\pi \times (11, 17, 3.7 \times 10^3)\,\mathrm{Hz}$. The one-body loss is small for the hold times in Fig. 5.8b, so we fit the decay rate with a two-body loss model [63, 250]:

$$\frac{\mathrm{d}N}{\mathrm{d}t} = -\frac{\kappa}{N_0} N^2, \tag{5.6}$$

whose solution is given by

$$N(t) = \frac{N_0}{\kappa t + 1} \tag{5.7}$$

where $\kappa$ is the two-body number loss rate coefficient. The decay fits well to this two-body loss model, and we extract $\kappa = 14(2)\,\mathrm{s}^{-1}$. Note that the initial molecule number in Fig. 5.8b is smaller than that in Fig. 5.8a, despite these datasets having been acquired one immediately after the other. In fact, a comparison of the initial

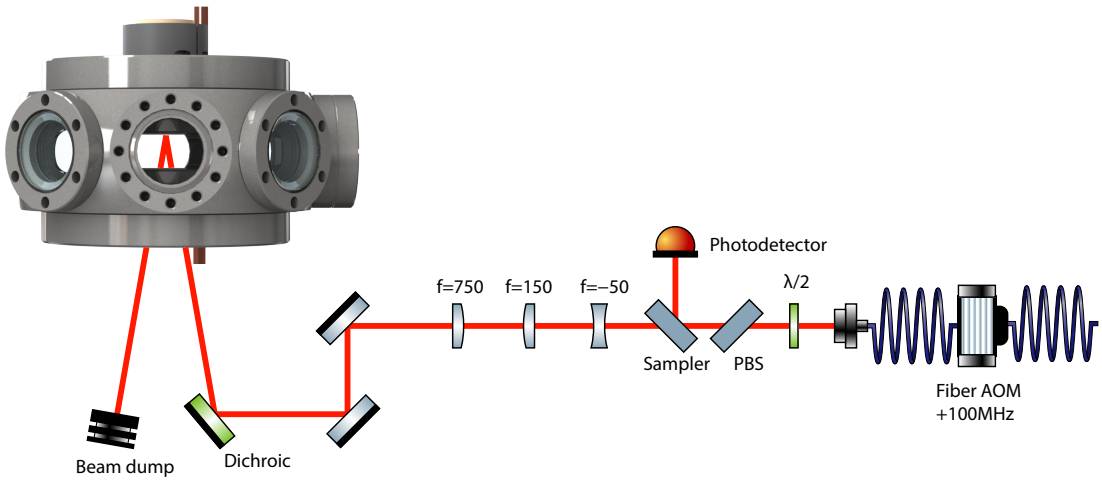


**Figure 5.9: Diagram of the vertical beam optics.** Focal lengths are in mm. All optics diagrams are made using the gwoptics ComponentLibrary created by Alexander Franzen.

peak densities shows an even larger difference. For the case in which the molecules remain confined in the 2D lattice the initial peak filling fraction is 11(1)%, while in the other dataset the $t = 0$ peak filling for the recaptured molecules is 1.6(2)%, corresponding to an initial peak density of $2.9(3) \times 10^6\,\mathrm{cm}^{-2}$. The lower numbers and densities in the second case may be partially attributed to the slow 20 ms ramp down time of the 2D lattice, during which the molecules can begin to collide. Finally, we examine the collisional lifetime for $|1,0\rangle$ molecules at zero electric field (Fig. 5.8c). Following the same protocol as for the $|0,0\rangle$ molecules, we measure the number of $|1,0\rangle$ molecules as a function of hold time in a quasi-2D trap formed by the vertical lattice. We find a similar two-body loss rate as for the $|0,0\rangle$ molecules of $\kappa = 15(1)\,\mathrm{s}^{-1}$. The initial peak density for this dataset is $3.7(4) \times 10^6\,\mathrm{cm}^{-2}$.

In the setup described so far, the vertical lattice is the only optical potential confining the molecules when the 2D lattice is turned off. This implies that in order to change the radial trap frequency, we would need to modify the vertical lattice depth. For future experiments, we wanted to be able to easily change the radial trap frequency without significantly affecting the trap frequency in the vertical direction,

so we installed a new vertically-propagating optical potential for this purpose. This vertical beam derives from the same laser as the lattice potentials, namely a 45 W fiber amplifier (Azurlight Systems) seeded by a narrow linewidth 1064 nm laser (Coherent Mephisto). We use a fiber-coupled AOM (AeroDIODE 1064AOM-1) to control the power in the vertical beam. After beam shaping and focusing lenses (see Fig. 5.9), the vertical beam is reflected upwards from underneath the science chamber by a dichroic mirror (Thorlabs DMSP900L) that transmits light from the Na and Rb 3D MOT beams. The vertical beam is then sent through the bottom bucket window of the science chamber (which is AR-coated for 1064 nm) and after passing through the position of the molecules reflects off the top bucket window (which is HR-coated for 1064 nm). To limit interference between the incident and reflected light, the beam is sent upwards at an angle of about 1° with respect to the vertical. The beam waist at the molecules was initially 125 $\mu$m, but we later changed it to 70 $\mu$m.

After setting up the vertical beam, we examined the survival of $|1,0\rangle$ molecules at high electric fields around the Förster resonance. For each electric field at which we measured a lifetime, we used the following protocol. With the molecules confined in both the 2D and vertical lattices, we first turned on the vertical beam. The 2D lattice was then ramped off in 20 ms, allowing the molecules to collide for a fixed hold time of 1 s in a quasi-2D geometry formed by the vertical lattice and the vertical beam. The overall trap frequencies during the hold time were $(\omega_x, \omega_y, \omega_z) = 2\pi \times (48, 49, 2.2 \times 10^3)$ Hz. Afterwards, the 2D lattice was ramped on, and we measured the remaining number of $|1,0\rangle$ molecules. Above 4.2 kV/cm we observed a dramatic enhancement in the survival of the molecules as shown in Fig. 5.10, representing our first demonstration of Förster resonance collisional shielding with NaRb molecules.

For a more quantitative analysis of the shielding behavior, we measured the lifetime of $|1,0\rangle$ molecules on both sides of the Förster resonance. Fig. 5.11a shows the number of molecules remaining as a function of hold time for 4.54 kV/cm (above

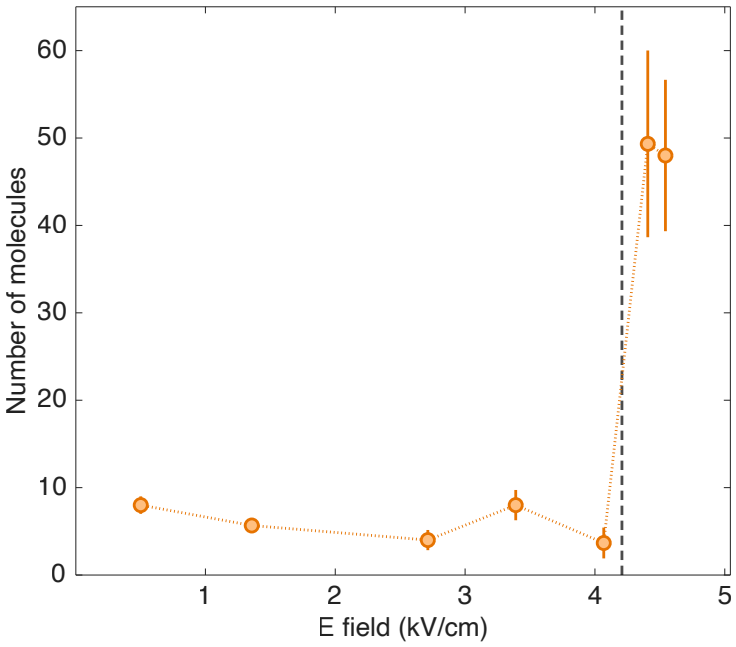


**Figure 5.10: Survival of $|1,0\rangle$ molecules versus electric field.** In our first observation of Förster resonance shielding of NaRb molecules, we measured the number of $|1,0\rangle$ molecules remaining as a function of electric field. The dashed vertical line represents the predicted Förster resonance electric field. Above the Förster resonance, we see a significant increase in the number of remaining molecules.

the resonance) and 3.39 kV/cm (below the resonance). The trap frequencies during the hold time are the same as for Fig. 5.10. At 3.39 kV/cm the data fit a two-body loss model with $\kappa = 31(6)\,\mathrm{s}^{-1}$. On the other hand, at 4.54 kV/cm shielding against two-body collisions results in a long lifetime of $\tau = 11(2)\,\mathrm{s}$, limited by one-body loss. We can compare this lifetime to that of molecules held in a 2D lattice with a modest depth of $16E_\mathrm{r}$ at the same electric field (Fig. 5.11b). In this case, we measure a slightly shorter lifetime of $\tau = 9(2)\,\mathrm{s}$. The reduced lifetime is most likely due to the higher rate of optical scattering when the 2D lattice is kept on. The fact that the molecules have a longer lifetime when held in a bulk trap than in a lattice demonstrates the efficacy of Förster resonance shielding against two-body loss. We also examine the case of $|1,0\rangle$ molecules held in a $16E_\mathrm{r}$ 2D lattice below the Förster resonance at 3.39 kV/cm, shown in Fig. 5.11c. We find an intermediate decay rate of the

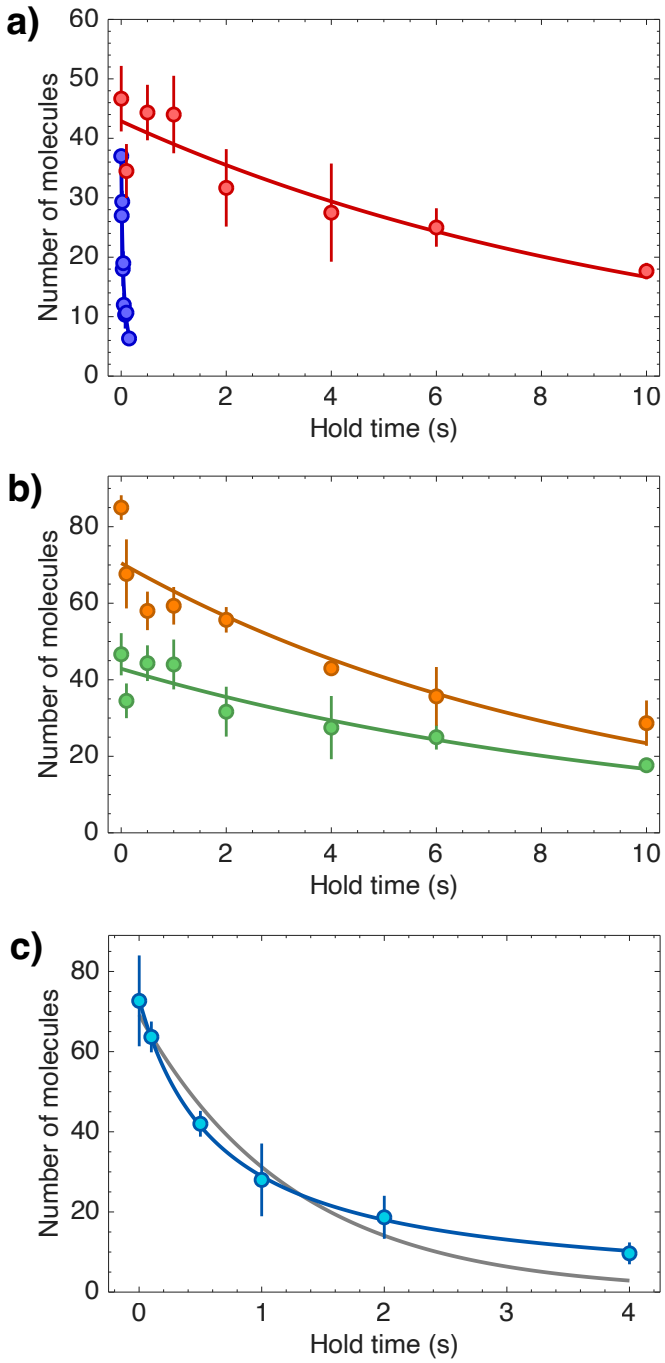


**Figure 5.11: Molecule lifetimes above and below the Förster resonance.** **a)** Lifetime of $|1,0\rangle$ molecules above the resonance (red) and below the resonance (blue) without a 2D lattice, showing a dramatically enhanced lifetime in the collisional shielding regime. **b)** Above the Förster resonance, similar lifetimes are observed with (orange) and without (green) a $16\,E_\mathrm{r}$ 2D lattice. **c)** Lifetime of $|1,0\rangle$ molecules below the resonance in a $16\,E_\mathrm{r}$ 2D lattice. The gray (blue) solid line is a one-body (two-body) fit to the data.

molecules, substantially slower than for molecules held below the resonance in a bulk trap but faster than for molecules above the Förster resonance. The molecule loss is in agreement with a two-body loss model, with a pure exponential decay showing a clear discrepancy with the data. The extracted two-body number loss rate coefficient is $\kappa = 1.53(5)\,\mathrm{s}^{-1}$. Note that although the data displayed in Fig. 5.11c is taken in a regime where the continuous quantum Zeno effect can play a role, the presence of this effect cannot be determined from these measurements alone. The continuous quantum Zeno effect describes the phenomenon in which a strong on-site loss rate can prevent two particles from tunneling onto the same site, effectively extending their lifetimes [63, 250]. This is due to the fact that such loss constitutes a measurement of the system, and repeated measurements prevent the system's state from evolving. In order to provide evidence of a quantum Zeno mechanism, we would need to show that an increased on-site loss rate at a given 2D tunneling rate decreases the number loss rate of the system. This was demonstrated for heteronuclear molecules in ref. [63]. In future work, we could accomplish this by altering the vertical lattice depth to modify the on-site loss rate while keeping the tunneling rate in the horizontal plane constant.

Having demonstrated collisional shielding of NaRb molecules, we explored the effect of adiabatically increasing the radial confinement while the shielded molecules are held in a quasi-2D geometry consisting of the vertical lattice and the vertical beam. To find the relation between the radial confinement $\omega_r$ and the peak density $n_0$ as well as between $\omega_r$ and the temperature $T$, we begin by writing the density of a thermal gas in a harmonic trap as

$$n(\mathbf{r}) = n_0 e^{-\frac{U(\mathbf{r})}{k_B T}} = n_0 e^{-\frac{m\omega_r^2 r^2}{2k_B T}}, \tag{5.8}$$

where we have assumed that the trap frequency is isotropic in the horizontal plane. The total number of particles is

$$N = \int n(\mathbf{r})\,\mathrm{d}^2\mathbf{r} = 2\pi \int_0^\infty n(r) r\,\mathrm{d}r = \frac{2\pi k_B T n_0}{m\omega_r^2}, \tag{5.9}$$

so we see that the quantity $n_0 T/\omega_r^2$ is constant for a fixed number of particles. The phase-space density (PSD) is

$$\mathrm{PSD} = n_0 \lambda_{\mathrm{th}}^2 = \frac{n_0 h^2}{2\pi m k_B T}, \tag{5.10}$$

where $\lambda_{\mathrm{th}}$ is the thermal de Broglie wavelength. Since the PSD is fixed for an adiabatic squeezing of the radial confinement, from equation 5.10 we see that $n_0 \propto T$. Combining this with the result of equation 5.9, we have the two relations:

$$\begin{aligned} n_0 &\propto \omega_r \\ T &\propto \omega_r. \end{aligned} \tag{5.11}$$

So, we see that adiabatically squeezing the trap in the radial direction will increase the density of the molecules, but this higher density comes at the expense of an increase in temperature. Care needs to be taken that the temperature increase is not so large that the thermal energy $k_B T$ becomes comparable to or greater than the vertical confinement $\hbar\omega_z$, in which case the molecules will begin to populate higher bands of the vertical lattice. This effectively sets a limit to how much of an increase in molecular density we can achieve through this method.

The protocol for this measurement is as follows. The molecules are initially confined in both the 2D and vertical lattices at the shielding field of 4.5 kV/cm. After the vertical beam is turned on, the 2D lattice is slowly ramped off in 250 ms. The molecules are then held in the vertical lattice and vertical beam for 300 ms before

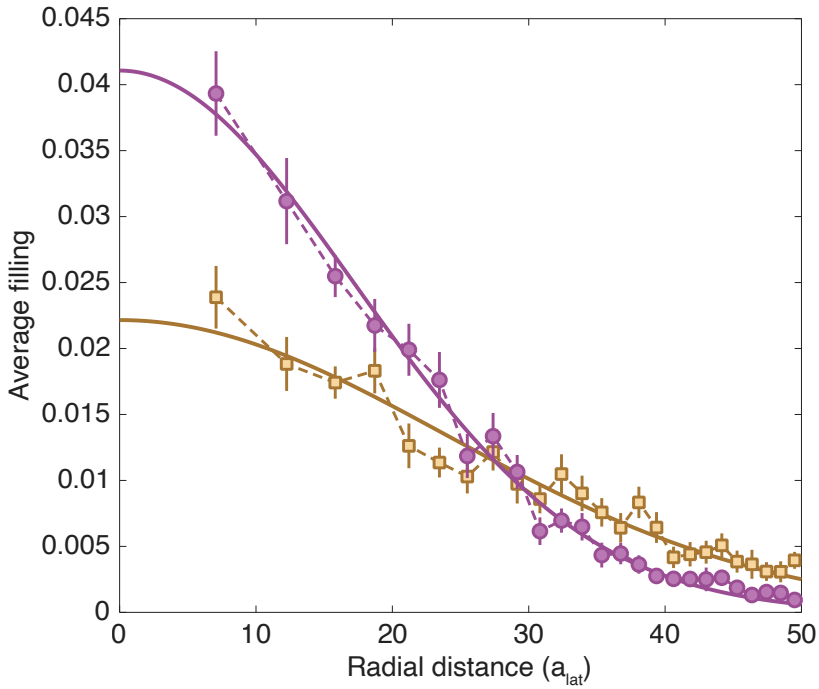


**Figure 5.12: Density profile of shielded molecules.** Azimuthally averaged density profile of collisionally shielded $|1,0\rangle$ molecules. The gold squares show the density with constant harmonic confinement. We observe an increase in the peak density after adiabatically ramping up the harmonic confinement (purple circles).

the 2D lattice turns back on in 1 ms to pin the distribution of molecules. During the hold time, we either keep the vertical beam power at a fixed value with overall trap frequencies $2\pi \times (20, 23, 3.5 \times 10^3)$ Hz or raise it over 300 ms such that the final trap frequencies are $2\pi \times (35, 38, 3.5 \times 10^3)$ Hz. For the analysis, we will treat the radial confinement as isotropic with $\overline{\omega}_r = (\omega_x \omega_y)^{1/2} = 2\pi \times 21$ Hz for the lower vertical beam power and $\overline{\omega}_r = 2\pi \times 36$ Hz for the higher power.

An azimuthally averaged density profile of the detected molecules for the two cases is shown in Fig. 5.12. The average number of molecules is similar in the two datasets, with $N = 86(3)$ for the sequence with fixed radial confinement and $N = 81(4)$ for the squeezed confinement sequence. For the case of constant $\overline{\omega}_r = 2\pi \times 21$ Hz, we measure a peak filling fraction $f_{\text{const}} = 0.022(1)$, corresponding to a peak density $n_{0,\text{const}} = 3.9(2) \times 10^6\,\text{cm}^{-2}$, and a temperature $T_{\text{const}} = 75(4)$ nK.

From equation 5.11, we expect in the squeezed dataset $f_{\mathrm{sqz,theory}} = 1.7 f_{\mathrm{const}} = 0.038$, $n_{0,\mathrm{sqz,theory}} = 6.7 \times 10^6\,\mathrm{cm}^{-2}$, and $T_{\mathrm{sqz,theory}} = 129\,\mathrm{nK}$. The measured values are $f_{\mathrm{sqz}} = 0.041(1)$, $n_{0,\mathrm{sqz}} = 7.3(2) \times 10^6\,\mathrm{cm}^{-2}$, and $T_{\mathrm{sqz}} = 114(3)\,\mathrm{nK}$. Although the results are not in exact quantitative agreement with the predicted values, we do observe the expected increase in both density and temperature for an adiabatic squeezing of the confinement. From Boltzmann statistics, the vertical lattice ground state fractions for the non-squeezed and squeezed cases are 89% and 77%, respectively. We can also verify the adiabaticity of the increase in radial confinement by comparing the PSD for the two datasets. We obtain a PSD of 0.015(1) for the lower radial confinement and a similar PSD of 0.018(1) for the higher confinement, in approximate agreement with the expected constant PSD for an adiabatic ramp.

### 5.1.4 An improved electric field control system

For future experiments with different collisional shielding methods (see section 5.3), we wanted a higher bandwidth and stability for the DC electric field. Therefore, we switched from open-loop to closed-loop control, requiring feedback electronics as well as an external circuit for accurately monitoring the output voltage of the amplifiers. A block diagram of the new system for one of the two amplifiers is shown in Fig. 5.13. The output of the high voltage amplifier, as before, is connected to a resistive divider that sets the voltage ratios between the electrode rods (which we label the "electrode divider"). Now, however, the output is also connected to another voltage divider that divides the input signal by 1000 to obtain a monitor signal between 0 V and 10 V (or 0 V and −10 V for the negative amplifier's path). We will refer to this as the "monitor divider." The monitor divider, shown in Fig. 5.14, consists of ten 10 MΩ resistors (Caddock USF370, 5ppm/°C) in series followed by a 100 kΩ resistor (Caddock USF340, 5ppm/°C). The monitor voltage is tapped off just before the final

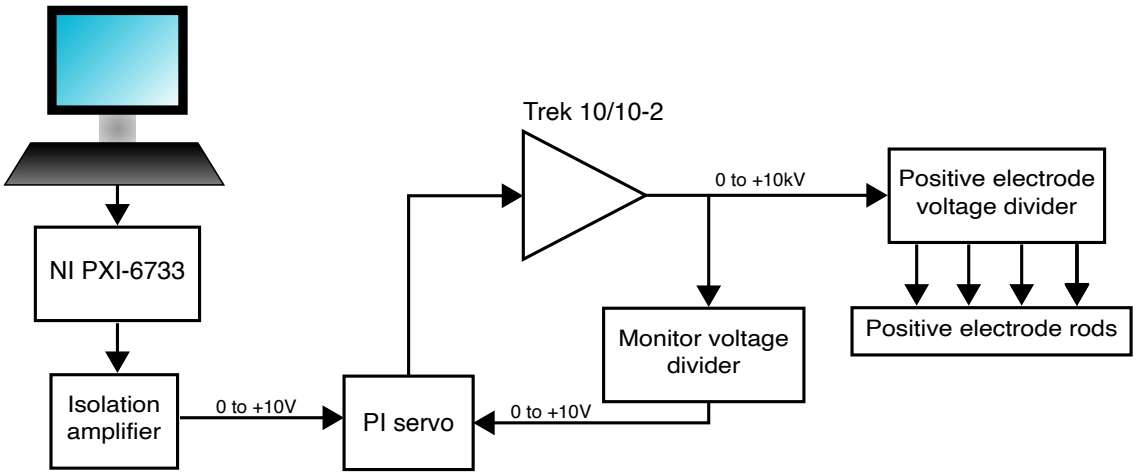


**Figure 5.13: Block diagram of the new electric field control system.** For greater stability and improved bandwidth, we now operate the high voltage system in a closed-loop configuration. Only the positive amplifier path is shown for simplicity, as the negative amplifier path is identical.

resistor. Since the output impedance is relatively high (100 kΩ), we pass the signal through a unity-gain buffer consisting of an OPA828 op amp (Texas Instruments).

This buffered monitor voltage is then combined in our servo circuit with a setpoint voltage from our computer control system to form an error signal (the circuit diagram can be found in appendix C). The servo circuit includes a 100 kHz fourth-order Bessel low-pass filter on the setpoint voltage to reduce high-frequency noise. The error signal then passes through two op amps for PI control, and the output is sent to the input of the high voltage amplifier to close the feedback loop.

When we tested this setup, we were surprised to measure only a 700 Hz bandwidth at the output of the monitor divider, despite the Trek amplifier having a stated small signal bandwidth of 25 kHz. More concerning than the bandwidth was the non-monotonic rising edge in response to a step function setpoint (Fig. 5.15a). We soon determined that neither the servo circuit nor the buffer op amp in the monitor divider was causing these issues, leaving only the resistive divider itself. Modeling the circuit in LTspice, we found that this behavior could be explained by including parasitic capacitance across each resistor and between each resistor and ground (see Fig. 5.15b,c).

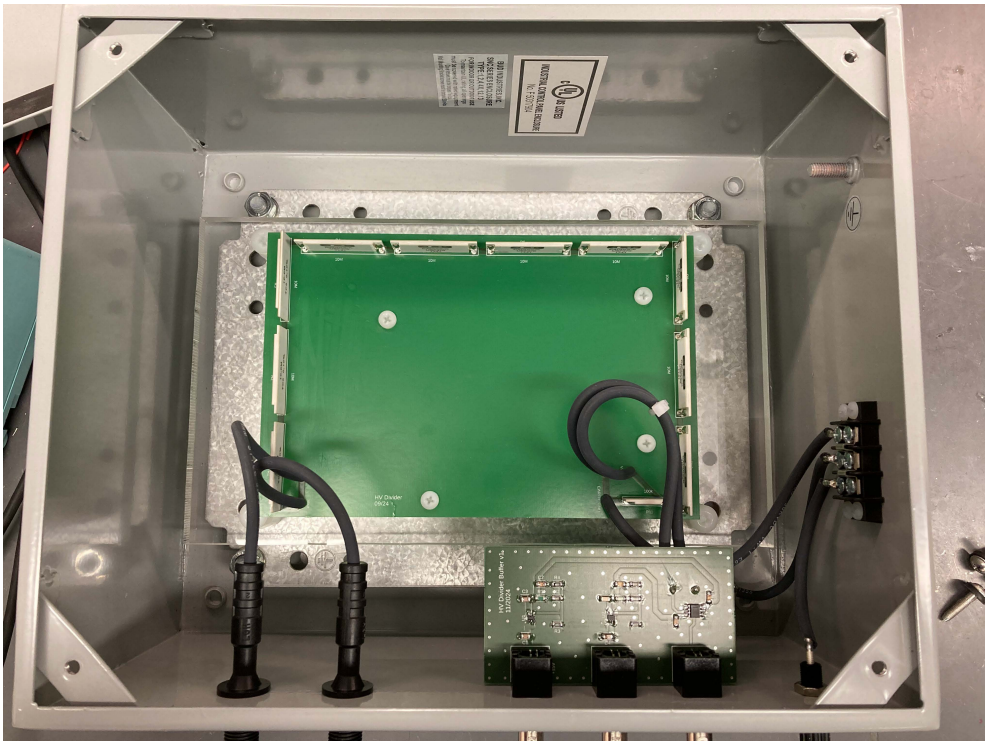

**Figure 5.14: Monitor voltage divider.** Top view of the monitor voltage divider in the improved electric field control system. The larger board consists of ten 10 MΩ resistors and a 100 kΩ resistor in series. The smaller board contains a low noise unity-gain buffer.

These capacitances are only on the order of 1 pF based on the simulation, but because of the circuit's large resistance they can have an appreciable effect on the bandwidth.

With an understanding of these parasitic effects, we designed a new version of the monitor divider. To obtain a higher bandwidth, we decreased the total resistance of the circuit from ∼100 MΩ to ∼20 MΩ using twenty 1 MΩ resistors (Caddock USF370, 5ppm/°C) followed by a 20 kΩ resistor (Caddock USF340, 5ppm/°C). The reason for the higher number of resistors is twofold. First, the maximum allowed voltage drop across each resistor must not be exceeded at the highest amplifier output of 10 kV. Second, the higher number of resistors helps minimize the power dissipated per resistor, which can lead to thermal drifts of the voltage division ratio. Since we are using the same form factor resistors, we expect that the parasitic capacitance will be similar to that of the first version of the circuit. Under this assumption, the

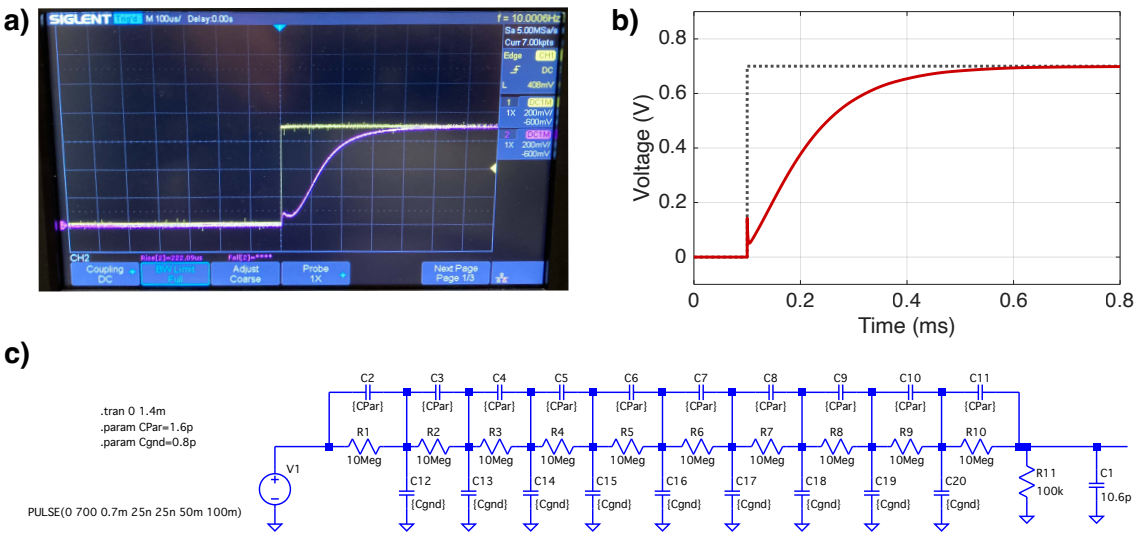


**Figure 5.15: Parasitic behavior of the monitor voltage divider.** **a)** Oscilloscope trace of the step response of the monitor voltage divider, showing a slower than expected rise time and non-monotonic behavior. **b)** This behavior can be reproduced in an LTspice simulation if parasitic capacitances are included. The circuit diagram for the simulation is shown in **c)**. The rightmost capacitor in the circuit represents the measured input capacitance of the unity-buffer circuit, likely an overestimate.

LTspice model predicts a 4 kHz bandwidth and a step response with clean rising and falling edges. Construction of the new circuit is underway as of the writing of this thesis.

In addition, the new electric field control system required the electrode divider to be redesigned. The measured capacitance of one electrode, including the long wire running from the electrode divider to the vacuum chamber, is 120 pF. Since two of the rod voltages are tapped off roughly in the middle of the electrode divider with a corresponding series resistance of tens of MΩ, the voltage on these rods is severely low-pass filtered to a bandwidth $< 100$ Hz. Indeed, we observed a time constant of $\tau = 4$ ms for the electric field to settle in Fig. 5.4b, which is consistent with a bandwidth of tens of Hz. In designing a new electrode divider, we followed the same principle as for the new monitor divider: lower total resistance and a higher number of resistors. In this case, the large combined wire and electrode capacitance forced us to use 220

surface mount 4.99 kΩ resistors (Ohmite ALX25W4K99BET). One complication is that two of the rod voltages are approximately at the amplifier's output voltage, so they have very little series resistance from the divider and consequently a much faster bandwidth than the other two rods. If the rods respond differently when the electric field is being ramped up or down then an electric field gradient could be produced at the molecules. We therefore slow down the bandwidth of these rods using two 680 kΩ, 48 kV rated resistors (RESI HVLR1529F680KK9) in series with the electrodes. The expected bandwidth of the rods is now approximately 2 kHz, almost two orders of magnitude faster than with the previous electrode divider. Note that in our new design, we have restricted ourselves to a vertical orientation of the electric fields. This greatly simplifies the divider, as we can use the fixed voltage ratios determined in table 5.1 instead of incorporating tunable resistance.

## 5.2 Increasing the number of molecules

As mentioned at the start of this chapter, our goal is to evaporate NaRb molecules to high phase-space densities as an intermediate step toward microscopy of polar molecules with near-unity lattice filling fractions. In the previous section we demonstrated the prerequisite of collisional shielding against two-body loss, but to perform an evaporation and end up with $10^2$ molecules the pre-evaporation number needs to be significantly higher. This led us to pursue a series of modifications to our experimental sequence to boost the number of molecules, ideally without compromising the current phase-space density. The changes that are described in this section still retain an optical lattice-based approach to molecule formation. Ongoing work to switch to a more conventional bulk association scheme is discussed in section 5.4.

Up to this point, we have formed molecules by overlapping dual 2D $n = 1$ Mott insulators of Rb and Na and then ramping the magnetic field across a Feshbach

resonance. This 2D approach was natural for us to implement early on because a single layer of particles is well-suited for quantum gas microscopy. However, this approach presents several difficulties. As described in section 2.3, we load a single layer of the vertical lattice by first compressing the atoms in a light sheet potential. In order to avoid loading multiple layers, we use a vertical lattice with a large spacing of 3.8 $\mu$m formed by two 1064 nm beams intersecting at a 16° angle (we refer to this lattice as the "side vertical lattice" because it enters the science chamber from one of the side viewports). The large lattice spacing comes at the cost of a low on-site interaction strength $U$, placing a stringent requirement on the temperature of the atoms in order to form near-defect-free Mott insulators [106]. In addition, as will be described in section 5.2.2, we used the same beam for the XODT as for the 752 nm spacing 2D lattice. A smaller XODT beam waist of $\sim$100 $\mu$m is helpful for limited optical power in capturing atoms from the magnetic trap and beginning the optical evaporation. On the other hand, larger beam waists are beneficial for fitting more atoms in the $n = 1$ shell of a Mott insulator. The fact that the 752 nm lattice beam waist was constrained to the XODT waist, together with the restriction to loading a single layer, made it difficult to form Mott insulators with large numbers of atoms.

We therefore decided to switch to a 3D, rather than 2D, Mott insulator approach, in which we associate molecules from dual 3D $n = 1$ Mott insulators of Rb and Na. This has the obvious advantage of larger atom numbers in the Mott insulators due to the ability to populate many layers of the vertical lattice. The molecules could ultimately be loaded into a 2D geometry following evaporation in a bulk harmonic trap, so the compatibility of this approach with our quantum gas microscope is not a fundamental concern. In addition, unlike the 2D formation which forced us to use a large spacing vertical lattice, in this approach a small spacing lattice is advantageous as more layers could be occupied. This naturally gives us a larger on-site interaction strength, reducing the sensitivity of the atomic Mott insulators to temperature. The

implementation of a 532 nm spacing vertical lattice will be described in section 5.2.1. We also decided at this point to install a new 2D lattice optical potential with a 532 nm spacing instead of a 752 nm spacing, enabling larger atom numbers in the $n = 1$ Mott shell (section 5.2.2). The 752 nm spacing lattice would still be used for microscopy as the larger spacing is helpful for high fidelity reconstruction of the lattice site occupations. Moreover, since the 532 nm 2D lattice is decoupled from the XODT, we have the freedom to adjust its beam waist to maximize the size of the $n = 1$ Mott insulators. Finally, section 5.2.3 will discuss our efforts to increase the spatial overlap of the Na and Rb Mott insulators, producing a significant increase in the number of collisionally shielded molecules.

### 5.2.1 The 532 nm spacing vertical lattice

We repurposed the non-interfering vertical beam from Fig. 5.9 to create a 532 nm vertical lattice. In our initial attempt, we simply changed the angle of the beam to be normal to the HR-coated top bucket window, forming a lattice potential at the atoms. We also increased the beam waist from 70 $\mu$m to 170 $\mu$m to help form large $n = 1$ Mott insulators. However, when loading Rb atoms into the vertical lattice we observed dramatic deformations in the shape of the cloud, with it sometimes splitting into two parts in the horizontal plane (Fig. 5.16). This splitting was previously observed by the JILA KRb experiment in ref. [251]. In our case, the unwanted interference was produced by secondary reflections from both sides of the glass making up the top and bottom bucket windows (Fig. 5.17a). Mechanical vibrations of the windows on the order of a wavelength, which can be induced by changing magnetic fields, would produce shaking in the stray interference patterns and cause the cloud shape to deform. We had deliberately introduced an angle between the top and bottom bucket windows when setting up the vacuum chamber in an attempt to avoid this issue by applying unequal torques on the vacuum bolts. However, concerns about

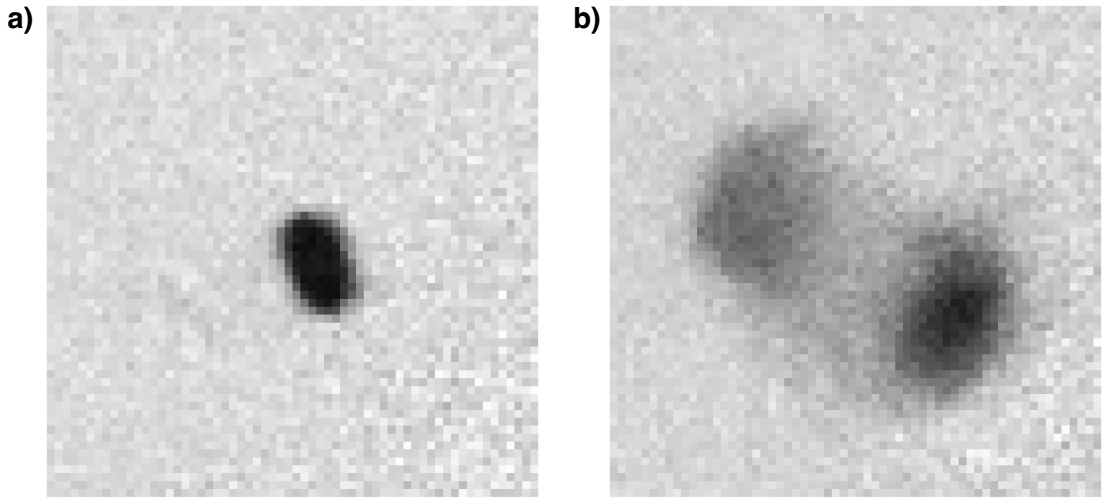


**Figure 5.16: Splitting of the Rb cloud.** **a)** The Rb atoms are initially held in the XODT. **b)** When the vertical lattice ramps on, the Rb cloud is observed to strongly deform, sometimes splitting in two as seen here.

the integrity of the vacuum seal led us to stop at a relative tilt of 0.3°, which was insufficient for this vertical lattice beam waist. In hindsight, it would have been better to have originally designed the custom bottom bucket window with an angle of a few degrees relative to the top bucket window.

This stray interference can be avoided, for example, by using a two-beam vertical lattice approach as in ref. [79, 249]. Here, as shown in Fig. 5.17b, the beams are sent into the vacuum chamber at a large enough angle to avoid interference due to secondary reflections. The lattice is formed by the interference of one beam incident directly on the particles and another beam reflected off of a mirror (in our case, that mirror would be the HR-coated top bucket window). Unfortunately, for the same beam waist and lattice depth this requires twice as much power as our previous approach. Since the power in the vertical lattice is limited by our fiber-coupled AOM to about 3 W, we decided on a different, simpler approach. We would return to the case of a single beam propagating at an angle relative to the normal of the top bucket window, as in the vertical beam of Fig. 5.9, but now the reflection off of the top bucket window would go to a mirror instead of a beam dump. The retroreflected

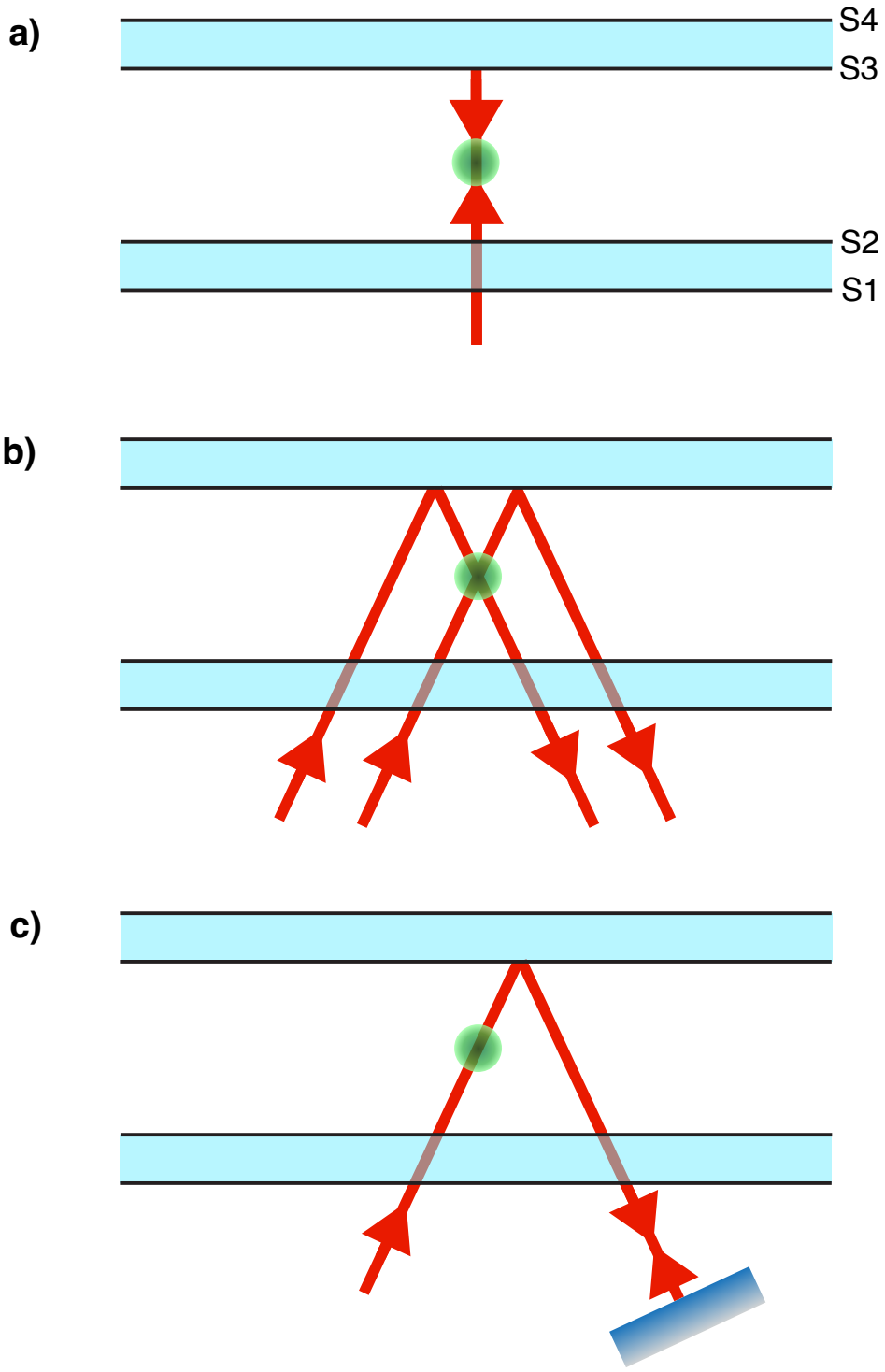


**Figure 5.17: Vertical lattice designs.** Different optical designs to generate vertical lattices as described in the main text. The green sphere represents the position of the atoms and molecules. Lattice angles are exaggerated for clarity.

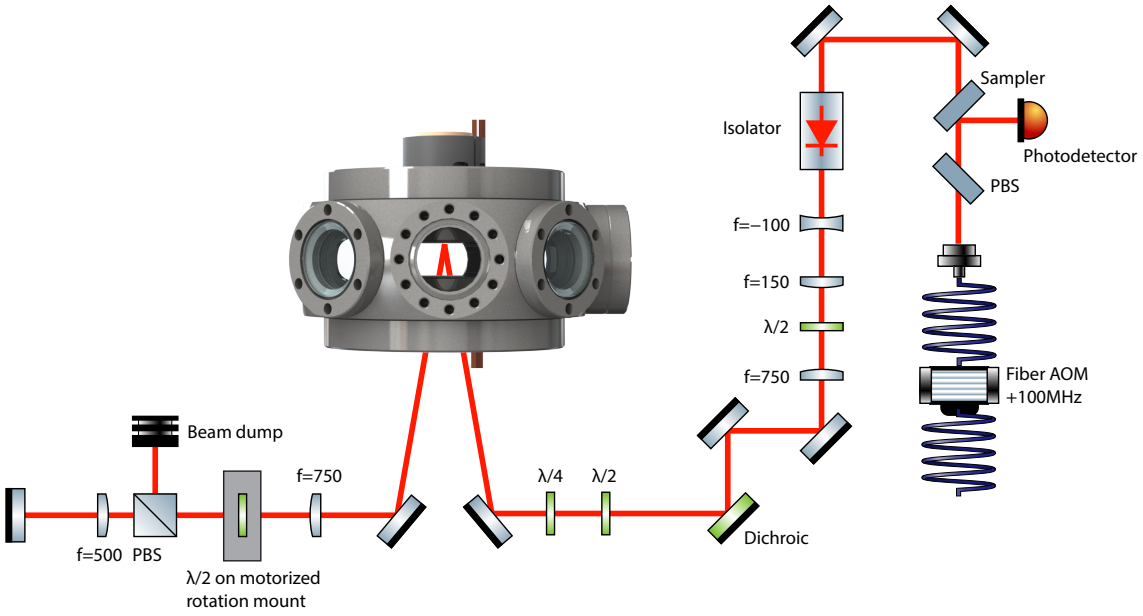


**Figure 5.18: Diagram of vertical lattice optics.** All focal lengths are in mm.

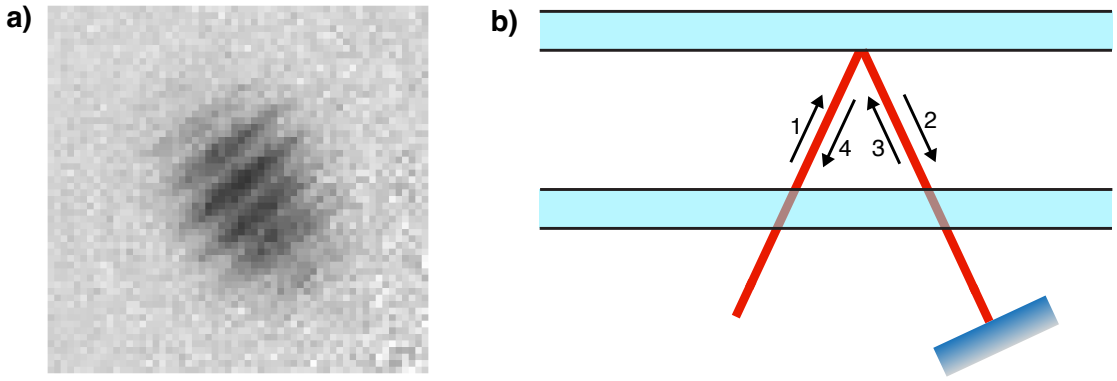


**Figure 5.19: Fringe pattern from stray interference. a)** For insufficient angular separations of the vertical lattice beams, horizontal fringes appear in the atoms. This can be explained by **b)**, where unwanted interference can occur between beams 1 and 3 or between beams 2 and 4.

beam would then interfere with the first pass at the position of the atoms forming a lattice as shown in Fig. 5.17c. Although the resulting lattice layers will not be perfectly horizontal, for small angles this is not an issue for us; a different form of vertical confinement could be used post-molecular evaporation for experiments with 2D arrays of polar molecules and for quantum gas microscopy.

The final optical layout of the vertical lattice is shown in Fig. 5.18. There are several things to note about this setup. First, if the angle $\theta$ of the beam relative to the normal of the top bucket window is too small, we observe horizontal fringes of the atoms in top absorption imaging (Fig. 5.19a). These fringes can be understood from Fig. 5.19b, in which interference between beams 1 and 3 or between beams 2 and 4 results in a series of vertical stripes with lattice spacing:

$$a_{\text{latt}} = \frac{\lambda}{2 \sin \theta}, \tag{5.12}$$

where $\lambda = 1064\,\text{nm}$ is the wavelength of the light. For example, in Fig. 5.19a the fringes are spaced by 19.3 um, which corresponds to the vertical lattice beam propagating at an angle of 1.6° with respect to the vertical. This unwanted interference was solved by increasing the angle of the vertical lattice beam. We found that an angle of about 9° was acceptable for a vertical lattice beam waist of 205 $\mu$m (shorter angles than this would likely have also worked, but we jumped directly from using a 2° angle to a 9° angle).

The optical isolator in Fig. 5.18 was originally not included in the vertical lattice path. After fixing the stray interference caused by an insufficient angle of the vertical lattice beams, we faced another issue in which the center of mass of the atoms in the vertical lattice was shifting around in the horizontal plane from shot to shot. In addition, the atomic cloud as viewed in top absorption imaging would sometimes show unusual spatial distributions instead of a clean circular shape. Initially, an optical isolator was thought not to be necessary because the output of the fiber-coupled AOM is an APC connector. This connector features a fiber tip polished at an 8° angle, so it was assumed that any reflection of the vertical lattice retroreflection beam off of the fiber tip would not make it back to the atoms. However, as shown in Fig. 5.20, the presence of the fiber collimation lens (Thorlabs A240TM-C, EFL = 8 mm) also

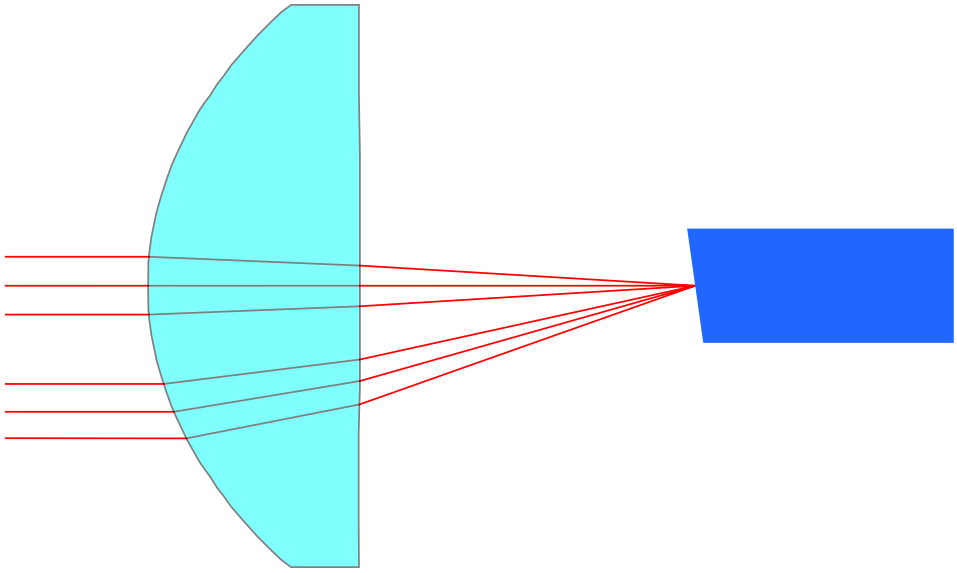

**Figure 5.20: APC fiber tip reflection.** In the absence of an optical isolator, the vertical lattice reflection comes back to the fiber tip, shown on the right. Due to the presence of the fiber collimation lens, the light that is reflected off of the fiber tip propagates parallel to but displaced from the incident beam.

collimates this stray reflection. For an 8 mm focal length lens, the reflected beam propagates parallel to the original incident beam with a separation of 2.3 mm. This parallel beam will then be refocused on the atoms by the final lens. We therefore installed an optical isolator (Thorlabs IO-3-1064-VHP), after which the atom cloud was stable in shape and position in the vertical lattice.

Another thing to note regarding the vertical lattice path relates to the dichroic mirror (Thorlabs DMSP900L) in Fig. 5.18. The purpose of this dichroic is to allow the Na and Rb imaging beams for top absorption imaging to transmit through to a mirror under the science chamber. We initially used a dichroic with a 25.4 mm diameter and a 1 mm thickness. When setting up the vertical lattice path, we noticed that the beam profile at the focus of the final lens was highly astigmatic and traced the source of the aberration to the reflection of the light off of the dichroic. The reflected wavefront error of a dichroic mirror is proportional to $D^2/s^2$, where $D$ is the diameter of the dichroic and $s$ is the thickness of the substrate [252]. By switching to

a 50.8 mm diameter, 5 mm thickness dichroic, the reflected wavefront error should be improved by a factor of six assuming similar coating parameters. Our measurements supported this prediction, as we observed minimal astigmatism of the beam profile using the new dichroic mirror.

In order to preserve a version of the non-interfering "vertical beam" of Fig. 5.9, we placed a half-wave plate in a motorized rotation mount (Thorlabs DDR25) in the vertical lattice path between the science chamber and the retroreflection mirror. A polarizing beamsplitter cube is then located after the half-wave plate so that by rotating the half-wave plate we can either dump the vertical lattice light after a single pass (the "vertical beam" configuration) or reflect it back into the science chamber (the lattice configuration).

### 5.2.2 A new 2D lattice

We next proceeded to set up a 532 nm spacing 2D lattice. This was initially believed to be quite literally as easy as a "click of a button." To see why, we can consider Fig. 5.21, which shows a simplified diagram of our 752 nm spacing 2D lattice at the time (a more complete diagram can be found in ref. [112]). When both lattice arms are vertically polarized, all four passes interfere to form a non-separable 752 nm spacing lattice (Fig. 5.22a). In principle, by changing the polarization of the second arm from vertical to horizontal, a separable 532 nm 2D lattice is produced (Fig. 5.22b). We can accomplish this polarization change using a half-wave plate in a motorized rotation mount located after the first pass of the lattice beam through the science chamber. To verify the formation of a 532 nm spacing lattice, we loaded Na atoms into the 2D lattice by ramping up the lattice depth to $8\,E_\mathrm{r}$ in 100 ms. We then released the Na atoms from the lattice for a 4 ms TOF to observe the momentum distribution. As shown in Fig. 5.23a, four peaks parallel to the original lattice vectors and four diagonal peaks are clearly visible. The former correspond to the momentum $2\hbar k_\mathrm{eff}$,

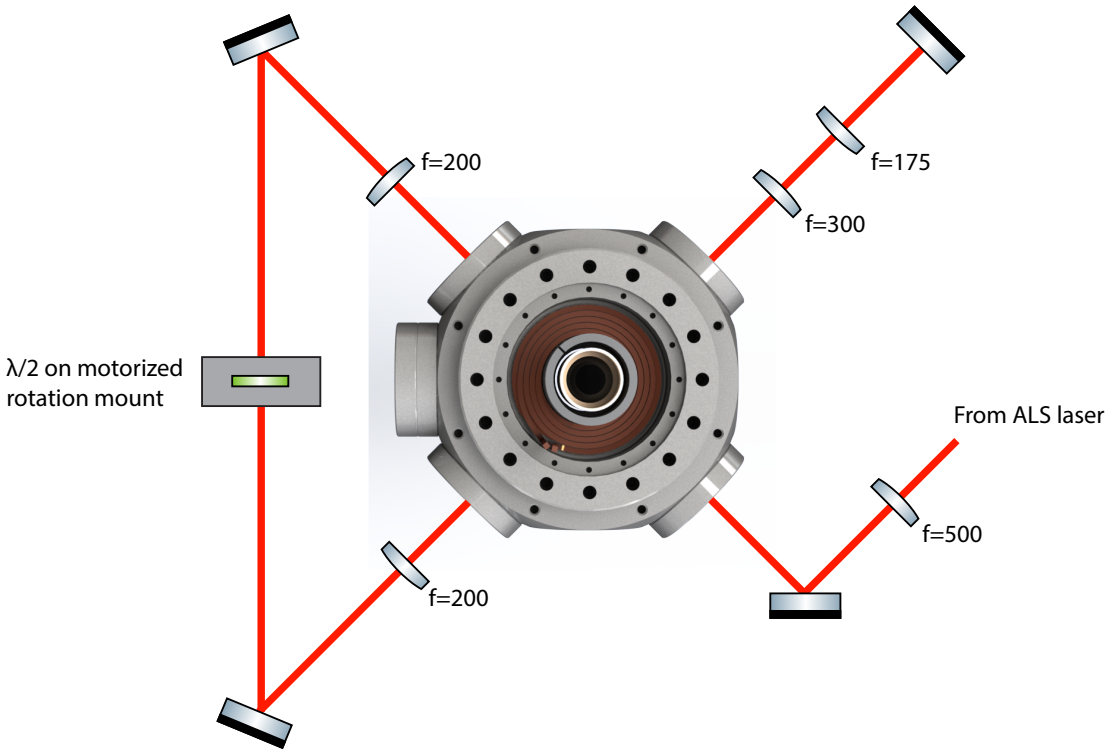


**Figure 5.21: Simplified diagram of the 752 nm spacing 2D lattice optics.** A more detailed diagram can be found in ref. [112]. All focal lengths are in mm.

where $k_{\text{eff}} = k$ for the ideal 532 nm spacing lattice and $k_{\text{eff}} = k/\sqrt{2}$ for the 752 nm lattice. We therefore expected the distance between the central peak and each of the four nearest neighbor peaks to be $d = 2\hbar k_{\text{eff}} t/m = 2ht/m\lambda = 130\,\mu$m where $t$ is the time of flight. To our initial surprise, however, the measured distance was $d = 99\,\mu$m, close to the value of $d = 92\,\mu$m predicted for a 752 nm lattice.

The explanation for this behavior is given by ref. [207], which studies a closely related single-beam 2D lattice in which both arms are horizontally polarized. They find that there are two relevant nonidealities in the implementation of the lattice optics. First, the polarization of the light could be tilted away from the intended vector. For our case, let us consider the polarization of the second arm to have a small angle $\beta$ with respect to the horizontal (with the first arm polarization remaining vertical). Both arms now have a nonzero polarization in the vertical direction, and

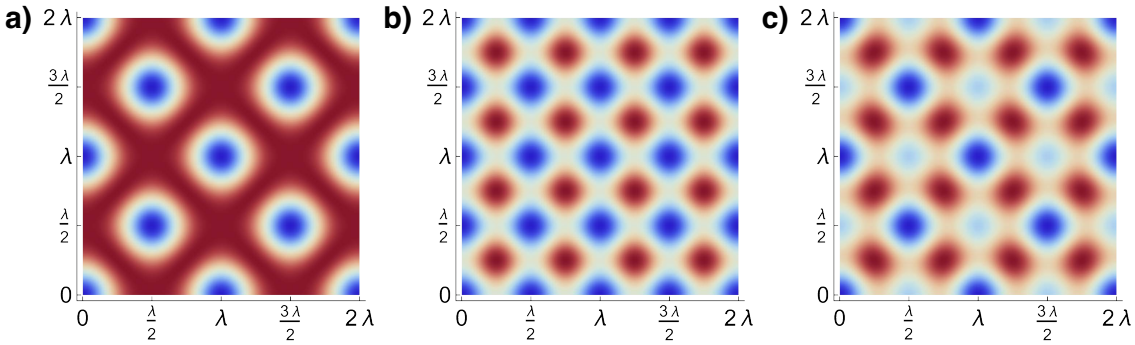


**Figure 5.22: Sensitivity of 2D lattice to alignment imperfections. a)** Lattice potential for ideal 752 nm spacing lattice. Particles sit in the blue potential wells. **b)** Lattice potential for ideal 532 nm lattice. **c)** Lattice potential for the 532 nm lattice with the polarization of the second arm tilted relative to the horizontal plane. A vastly exaggerated angle $\beta = 0.2$ is used so that the site-to-site offset is visually clear.

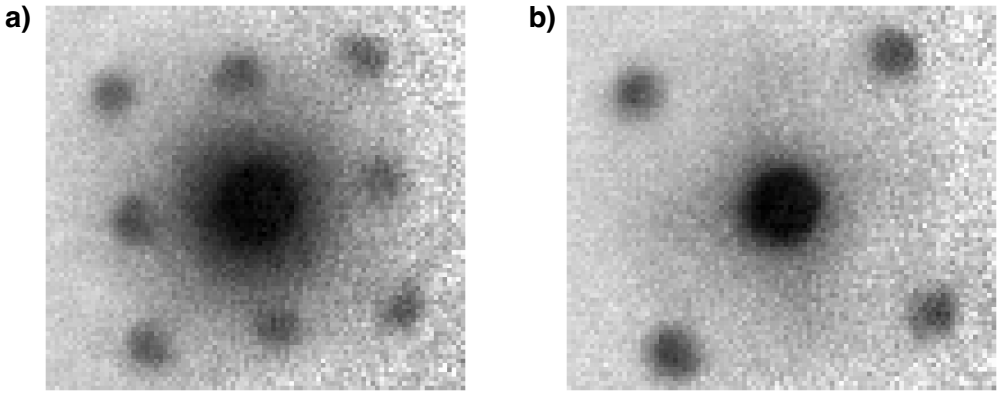


**Figure 5.23: Momentum peaks for the 2D lattice. a)** Na momentum peaks after a 100 ms ramp up of an $8\,E_{\mathrm{r}}$ 2D lattice followed by 4 ms TOF. **b)** Na momentum peaks after the 2D lattice is pulsed on for 100 $\mu$s followed by 4 ms TOF.

so there is a small admixture of a 752 nm spacing four-fold interference lattice. This results in a checkerboard pattern in the lattice potential, as shown in Fig. 5.22c, with neighboring lattice sites having an energy offset of*:

$$\Delta V = 4V_{\mathrm{latt},\beta=0} \sin\beta \approx 4V_{\mathrm{latt},\beta=0}\beta, \tag{5.13}$$

where $V_{\mathrm{latt},\beta=0}$ is the lattice depth in the ideal case of $\beta = 0$. The second lattice imperfection to consider is if the first arm of the lattice propagates at a slight angle $\epsilon$ relative to the horizontal plane. This causes its polarization vector to tilt into the direction of the second arm's polarization, again producing a checkerboard pattern lattice potential with a site-to-site offset of

$$\Delta V \approx 4V_{\mathrm{latt},\epsilon=0}\epsilon, \tag{5.14}$$

where $V_{\mathrm{latt},\epsilon=0}$ is the lattice depth in the ideal case of $\epsilon = 0$. For both imperfections, the sensitivity of the energy offset to $\beta$ and $\epsilon$ is extremely unforgiving; a $\beta$ or $\epsilon$ of $0.5°$ already results in $\Delta V/V_{\mathrm{latt}} = 0.035$.

The ground state of this checkerboard potential consists of every other site being occupied, with the occupied sites having a spacing of 752 nm. Atoms released from the lattice in time of flight, therefore, have momentum peaks with the same separation as for a "true" 752 nm lattice. Interestingly, ref. [207] pointed out that such a momentum pattern can exist even if the lattice ramp is not adiabatic with respect to the nearest-neighbor tunneling energy. All sites will then be occupied, so the momentum peaks will initially correspond to those of a 532 nm spacing 2D lattice. However, as time

*Note that our lattice has a much greater sensitivity to polarization imperfections than the in-plane lattice of ref. [207]. For a single-beam lattice constructed from two horizontally polarized arms $\Delta V \propto \beta^2$ for $\beta \ll 1$, while in our case of one horizontally polarized and one vertically polarized arm $\Delta V$ is linear in $\beta$. This is due to the fact that in their configuration both arms must have a polarization tilt to interfere, while in our setup only the second arm needs a polarization tilt for this to occur.

evolves a phase will accrue for atomic wavefunctions in the energetically offset sites, resulting in a momentum pattern that oscillates between that of the 532 nm lattice and that of the 752 nm lattice as a function of hold time. For sufficiently long times in the lattice, the oscillations damp out to a case in which both the 532 nm and 752 nm peaks are visible.

To see the underlying 532 nm spacing 2D lattice in spite of the site-to-site energy differences, we can pulse the lattice potential instead of slowly ramping it on. In this case, the atoms will diffract based on their Stark shift in the lattice light, which is relatively insensitive to small intensity offsets. Indeed, when we pulsed on the 2D lattice for 100 $\mu$s and then let the Na atoms expand for 4 ms TOF as before, we saw momentum peaks with a larger spacing of $d = 138\,\mu$m, close to the predicted $d = 130\,\mu$m for a 532 nm lattice* (Fig. 5.23b).

To avoid the extreme sensitivity of this lattice to optical imperfections, we decided to set up a new optical path for a 532 nm spacing 2D lattice consisting of two orthogonally polarized arms with a relative frequency difference of 110 MHz and beam waists of 195 $\mu$m and 145 $\mu$m. An optics diagram for this lattice is shown in Fig. 5.24. With this new setup, we once again looked at the momentum distribution of the Na atoms in time of flight. After ramping up the 2D lattice in 40 ms to 6 $E_r$, we released the atoms in a 2 ms TOF. In the resulting absorption image shown in Fig. 5.25, the first order momentum peaks are separated by $d = 70\,\mu$m from the central peak, similar to the predicted value of $d = 65\,\mu$m for a 532 nm spacing 2D lattice.

### 5.2.3 Association of molecules from 3D Mott insulators

After the installation of the new lattice potentials, we set about forming 3D Mott insulators of Na and Rb. The dual Na and Rb BECs are initially held in the XODT

*The relatively long pulse time puts us in the Bragg regime rather than the Raman-Nath regime usually used in Kapitza-Dirac measurements to calibrate lattice depths. Since we were simply using the pulse to measure the separation of the momentum peaks, the particular regime that we were in did not matter.

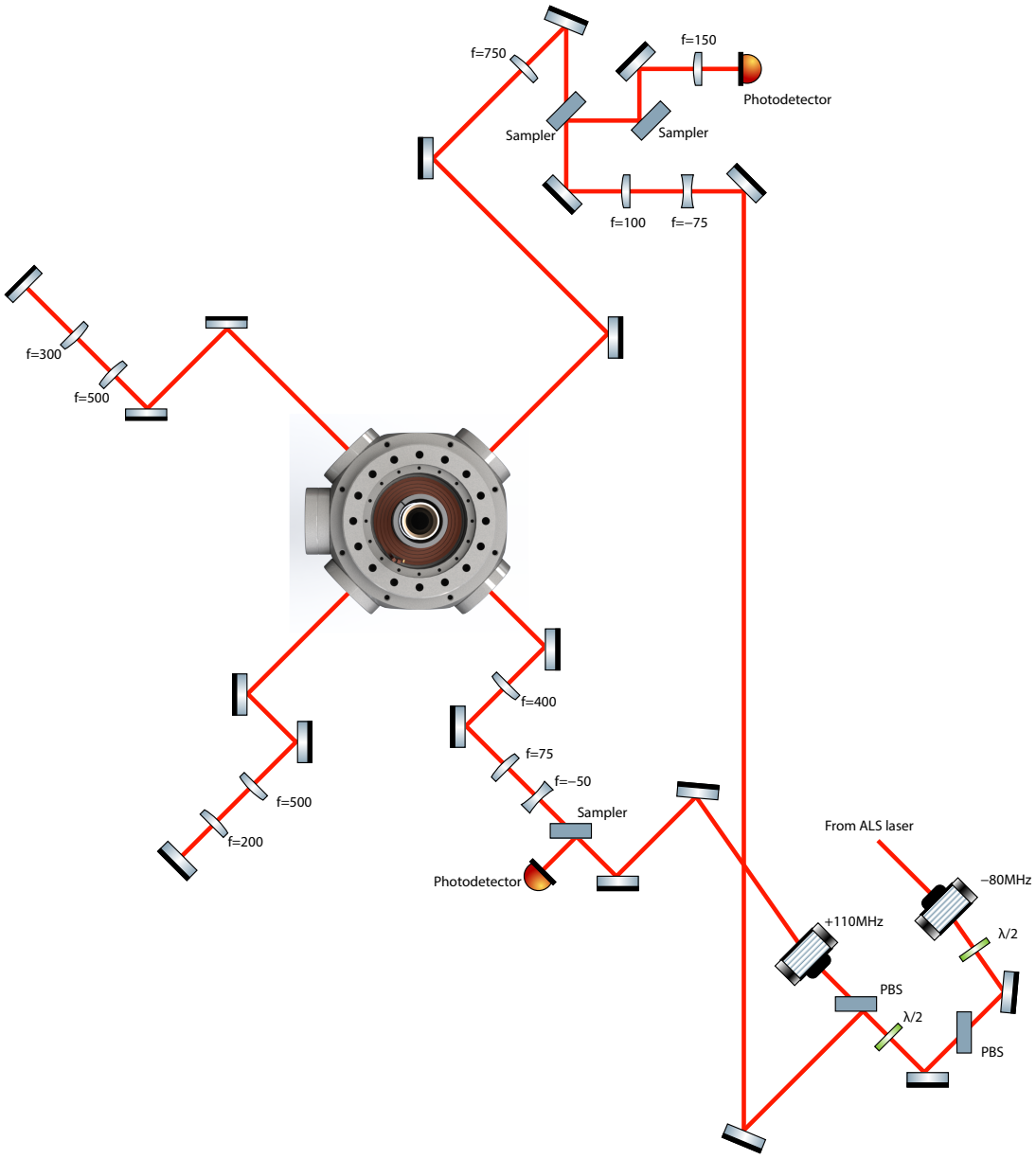


**Figure 5.24: Diagram of the 532 nm spacing 2D lattice optics.** All focal lengths are in mm.

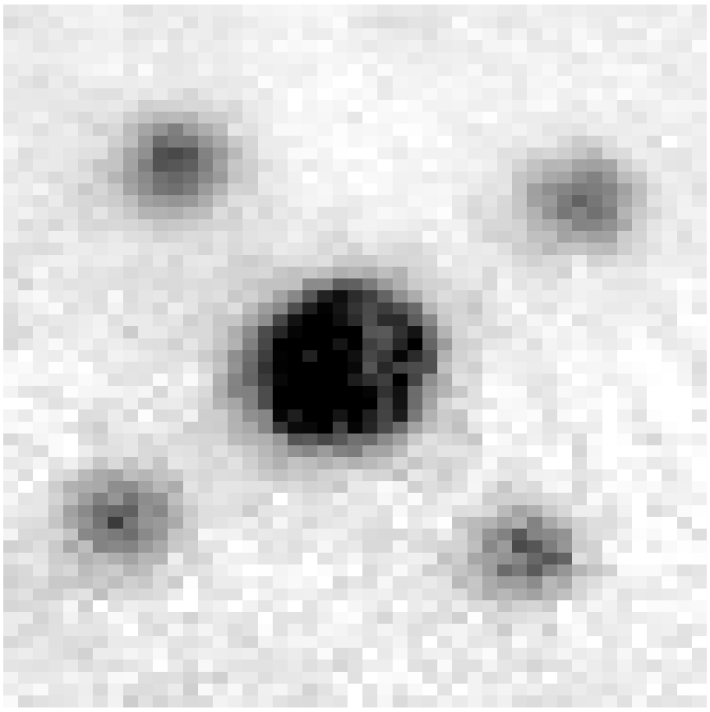

**Figure 5.25: Momentum peaks for the new 532 nm spacing 2D lattice.** Na momentum peaks after a 40 ms ramp up of the new 532 nm spacing 2D lattice to 6 $E_r$ followed by a 2 ms TOF.

at low magnetic field. In a harmonic trap, Na and Rb sit at different equilibrium positions in the vertical direction due to gravity. The differential gravitational sag $\Delta z$ is given by

$$\Delta z = g \left| \frac{1}{\omega_{\mathrm{Rb}}^2} - \frac{1}{\omega_{\mathrm{Na}}^2} \right| \tag{5.15}$$

where $\omega_{\mathrm{Rb(Na)}}$ is the vertical trapping frequency for Rb(Na), with $\omega_{\mathrm{Rb}} = 0.88\omega_{\mathrm{Na}}$ at 1064 nm. Prior to loading the atoms into the vertical lattice, we squeeze the XODT to a vertical trapping frequency of $\omega_{\mathrm{Na}} = 2\pi \times 160$ Hz, reducing the differential sag to $\Delta z = 2.8\,\mu$m in order to increase the number of lattice layers containing both Na and Rb atoms. The vertical lattice then ramps up to a depth of $V_{\mathrm{latt,Na}} = 24\,E_{\mathrm{r,Na}}$, corresponding to $V_{\mathrm{latt,Rb}} = 265\,E_{\mathrm{r,Rb}}$, in 50 ms (tunneling in the vertical direction is additionally suppressed by the layer-to-layer gravitational potential difference). Note

that in contrast to the sequence described in section 2.3, a light sheet potential was not used because we were no longer trying to load a single lattice layer. Another thing to note is that since the target atom numbers were much higher than before, the bichromatic dimple traps were no longer necessary. (At various times, we tried using them at higher powers, using them with larger beam waists, and not using them at all. Similar results were obtained in each case, although scattering became a concern for using small beam waists at high powers.)

Returning to the sequence, with the atoms pinned in the vertical direction, we quickly increased the magnetic field above the Feshbach resonance and then let it stabilize at the zero-crossing of the interspecies scattering length (approximately 352 G). Here, the Na and Rb clouds are miscible so we expect good spatial overlap within each vertical lattice layer. Since the lattice depth for Rb in units of the Rb recoil energy $V_{\mathrm{latt,Rb}}/E_{\mathrm{r,Rb}}$ is 11 times greater than $V_{\mathrm{latt,Na}}/E_{\mathrm{r,Na}}$ at 1064 nm, we proceeded to ramp up the 532 nm spacing 2D lattice in two stages. First, we raised the 2D lattice to $V_{\mathrm{latt,Rb}} = 31\,E_{\mathrm{r,Rb}}$ in 75 ms, crossing the 2D superfluid-to-Mott insulator transition within each layer for Rb. Since this corresponds to $V_{\mathrm{latt,Na}} = 3\,E_{\mathrm{r,Na}}$, Na remains a superfluid at the end of the ramp. We then increased the 2D lattice depth to $V_{\mathrm{latt,Na}} = 60\,E_{\mathrm{r,Na}}$ in an additional 75 ms, crossing the Mott insulator transition for Na. For this initial sequence, we chose to perform 2D Mott insulator transitions with many vertical layers rather than ramping up both the 2D and vertical lattices at the same time simply because of the former protocol's similarity to the sequence we had previously been using.

We then attempted to associate the atoms into molecules by ramping the magnetic field through the Feshbach resonance at 347.6 G. When we tried this, however, we saw almost no signal of Feshbach molecule formation. We first suspected spatial overlap of the atomic clouds to be the issue. We checked the overlap in the vertical direction by ramping the magnetic field to the interspecies Feshbach resonance with

the atoms pinned in the vertical lattice. The magnetic field was subsequently held at the resonance for 100 ms. If a layer only contains atoms of one species then there should be minimal loss during that hold time, while significant three-body loss should occur in layers containing both Na and Rb atoms. When we performed this test, we saw that very few atoms survived the hold time at the Feshbach resonance, while for fields a few Gauss above and below the resonance the atom numbers remained large. Therefore, we concluded that spatial overlap in the vertical direction was not the main culprit behind the lack of Feshbach molecule formation.

We next considered the spatial overlap of Na and Rb within each layer just before the 2D lattice ramp at 352 G. We used high field top absorption imaging to gain a direct characterization of the distribution of both species. Since the Na and Rb atoms are in the $|F = 1, m_F = 1\rangle$ state, we first use a microwave Landau-Zener sweep to transfer them to $|2, 2\rangle$ immediately before imaging them on the transition that corresponds to $|2, 2\rangle \rightarrow |F' = 3, m'_F = 3\rangle$ at low field. At 352 G, the excited state is in the Paschen-Back regime and is better labeled as $|J = \frac{3}{2}, m_J = \frac{3}{2}, I = \frac{3}{2}, m_I = \frac{3}{2}\rangle$. We found that although the spatial overlap between Na and Rb was not perfect, the atomic clouds were sufficiently overlapped to have expected to form a detectable number of Feshbach molecules.

This led us to consider whether the atoms were in the correct state. We could verify with Stern-Gerlach measurements that the internal state was correct, namely the $|1, 1\rangle_{\mathrm{Na}} + |1, 1\rangle_{\mathrm{Rb}}$ entrance channel of the Feshbach resonance. The atoms also need to be in the correct relative motional state in the vertical lattice. Let us consider one Na and one Rb atom in the vertical lattice. This is a quasi-2D geometry, with vertical trapping frequency $\omega_{z,\mathrm{Na}} = 2\pi \times 75\,\mathrm{kHz}$ and in-plane trapping frequency $\omega_{\perp,\mathrm{Na}} = 2\pi \times 88\,\mathrm{Hz}$ ($\omega_{\mathrm{Rb}} = 0.88\omega_{\mathrm{Na}}$). Modeling the interspecies interaction as a regularized delta function potential (i.e. a contact interaction), the Hamiltonian of

the atoms' relative motion is [208, 253, 254]:

$$H = -\frac{\hbar^2}{2\mu}\nabla^2_{\mathrm{rel}} + \frac{1}{2}\mu\omega^2_{\perp,\mathrm{rel}}\rho^2 + \frac{1}{2}\mu\omega^2_{z,\mathrm{rel}}z^2 + \frac{2\pi\hbar^2 a}{\mu}\delta(\mathbf{r})\frac{\partial}{\partial r}r. \tag{5.16}$$

Here, $\mu = m_{\mathrm{Na}}m_{\mathrm{Rb}}/(m_{\mathrm{Na}} + m_{\mathrm{Rb}})$ is the reduced mass, $\mathbf{r} = \mathbf{r}_{\mathrm{Na}} - \mathbf{r}_{\mathrm{Rb}}$ is the position in the relative coordinate system, $\rho$ is the in-plane distance between the atoms, $z$ is the vertical distance, $a$ is the s-wave scattering length, and $\omega_{\mathrm{rel}}$ is the trapping frequency in the frame of the relative motion [253]:

$$\omega_{\mathrm{rel}} = \sqrt{\frac{m_{\mathrm{Rb}}\omega^2_{\mathrm{Na}} + m_{\mathrm{Na}}\omega^2_{\mathrm{Rb}}}{m_{\mathrm{Na}} + m_{\mathrm{Rb}}}}. \tag{5.17}$$

An approximation of the eigenenergies $E$ in the quasi-2D regime can be obtained from [254]:

$$-\ln\left(\frac{2a^2_{\mathrm{2D}}\omega_{\perp,\mathrm{rel}}}{\sigma^2\omega_{z,\mathrm{rel}}}\right) = \psi\left(\frac{\omega_{z,\mathrm{rel}}}{4\omega_{\perp,\mathrm{rel}}} + \frac{1}{2} - \frac{E}{2\hbar\omega_{\perp,\mathrm{rel}}}\right) \tag{5.18}$$

where $\psi(z)$ is the digamma function, $\sigma = \sqrt{\hbar/(\mu\omega_{z,\mathrm{rel}})}$ is the vertical harmonic oscillator length, and $a_{\mathrm{2D}}$ is the 2D scattering length here defined as*:

$$a_{\mathrm{2D}} = \frac{1}{\sqrt{2}}\sigma e^{\Phi(0)/2}e^{-\sqrt{\pi}\sigma/(2a)} \tag{5.19}$$

where $\Phi(0) \approx 1.938$.

The eigenenergies are plotted in Fig. 5.26 as a function of magnetic field close to the interspecies Feshbach resonance. The inset shows the dependence of the s-wave scattering length $a$ on the magnetic field using the parameters of ref. [205]. Consider the portion of the experimental sequence in which we quickly ramp the magnetic field from below to above the Feshbach resonance with overlapped degenerate clouds of Na and Rb pinned in the vertical lattice. The speed of the magnetic field jump

*Other definitions of the 2D scattering length exist. See, for example, the more commonly used definition given in ref. [255], whose prefactor differs by $\sqrt{2}$ from that of ref. [254] used here.

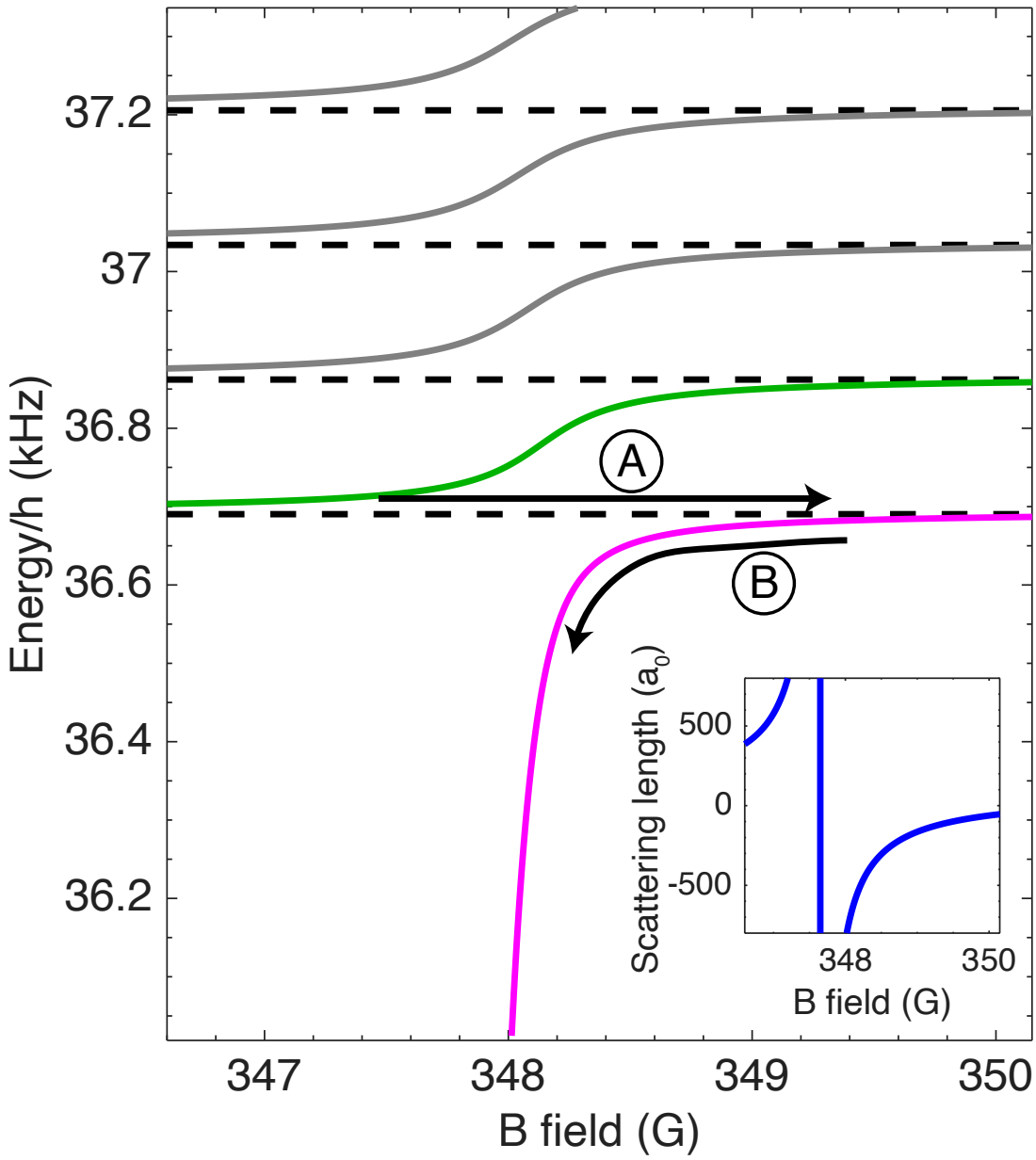


**Figure 5.26: Eigenenergies for a pair of Na and Rb in the vertical lattice around the Feshbach resonance.** As the magnetic field is ramped above the Feshbach resonance, we diabatically cross from the eigenenergy shown in green to the energy level shown in pink following the arrow labeled "A." Adiabatic ramps from above to below the Feshbach resonance to form weakly-bound molecules follow the arrow marked "B." Note that in our sequence, magnetoassociation occurs with tight confinement in all spatial directions, significantly easing the adiabatic criterion. The dashed black lines are the non-interacting harmonic oscillator energy levels. The inset shows the scattering length versus magnetic field with parameters from ref. [205].

from 335 G to 416 G is limited by eddy currents in the metal vacuum chamber. As described in section 5.4, the step response of the magnetic field can be fit to an exponential with a time constant of $\tau = 1\,\text{ms}$, so for this magnetic field jump the rate of change of the field at the Feshbach resonance (347.6 G) is 68 G/ms. At the start of the magnetic field ramp, a pair of Na and Rb atoms is initially in the ground relative motional state given by the green solid line in Fig. 5.26. Ideally, as the magnetic field passes through the resonance, the atoms diabatically transition to the relative motional state corresponding to the pink solid line. This is required for the formation of Feshbach molecules because only the ground relative motional state above the Feshbach resonance acquires a binding energy as the magnetic field is adiabatically ramped back down below the resonance. The size of the avoided crossing between the pink and green lines is approximately* $2\hbar\omega_{\perp,\text{rel}}$. In past work, we had observed the formation of Feshbach molecules using the "vertical beam" of section 5.1.3 for radial confinement during the jump to high magnetic fields (the vertical confinement was provided by the 3.8 $\mu$m spacing vertical lattice). Since the value of $\omega_{\perp,\text{rel}}$ for the vertical beam was nearly identical to that of the 532 nm spacing vertical lattice, the probability of a diabatic transfer to the ground motional state should not have significantly changed in the new setup. Moreover, the Na and Rb clouds are immiscible at magnetic fields below the Feshbach resonance [206]. This implies that the overlap of the species within each layer should be small during the fast magnetic field ramp, so most atoms should remain in the lowest motional state

*The factor of 2 in the energy difference between adjacent non-interacting harmonic oscillator states arises as follows. In the non-interacting case, the Hamiltonian for the relative motion separates into a vertical part and an in-plane part. The vertical part is simply a 1D harmonic oscillator with energies $E_z = \hbar\omega_{z,\text{rel}}(n + \frac{1}{2})$ where $n = 0, 1, 2, \ldots$ . The in-plane part is a 2D isotropic harmonic oscillator, which can be evaluated in polar coordinates to obtain the energies $E_\perp = \hbar\omega_{\perp,\text{rel}}(2k + \lambda + 1)$ where $k, \lambda = 0, 1, 2, \ldots$ . The in-plane wavefunction, up to a normalization factor, is $\psi(\rho, \phi) \sim \rho^\lambda \exp(-\mu\omega_{\perp,\text{rel}}\rho^2/(2\hbar)) L_k^\lambda(\mu\omega_{\perp,\text{rel}}\rho^2/\hbar) \exp(i\lambda\phi)$ where $L_k^\lambda(z)$ is the associated Laguerre polynomial. The $\rho^\lambda$ factor in $\psi(\rho, \phi)$ implies that only $\lambda = 0$ will be relevant to the full interacting problem with a $\delta(\mathbf{r})$ interaction, as all other values of $\lambda$ yield a vanishing wavefunction at the origin [254]. The total energy of the vertical and in-plane non-interacting Hamiltonian is therefore $E = \hbar\omega_{z,\text{rel}}(n + \frac{1}{2}) + \hbar\omega_{\perp,\text{rel}}(2k + 1)$. For $\omega_{z,\text{rel}} \gg \omega_{\perp,\text{rel}}$ the lowest energy states will have $n = 0$ and have approximate energies $E = \frac{1}{2}\hbar\omega_{z,\text{rel}} + 2\hbar\omega_{\perp,\text{rel}}k$, with $\Delta E = 2\hbar\omega_{\perp,\text{rel}}$.

of the vertical lattice. We therefore concluded that pinning the atoms in the vertical lattice as we go to high magnetic fields was unlikely to be the source of our difficulties in producing Feshbach molecules.

As it turned out, our inability to detect Feshbach molecules when initially trying the new multi-layer Mott insulator protocol arose from a combination of factors. First, only several hundred Feshbach molecules were being formed, likely limited by the spatial overlap of the atomic clouds despite our above efforts to check this. The molecules ultimately provide the best signal for optimizing the overlap, so a factor of three to four increase in Feshbach molecule number was easy to achieve once we were able to detect them. In addition, we were using absorption imaging rather than quantum gas microscopy at the time to detect the molecules (to avoid the complication of switching to our 752 nm lattice for imaging, as well as due to the presence of multiple vertical layers). Therefore, despite this being a higher number of Feshbach molecules than we had previously produced, the signal was just above the background level of the absorption imaging. In fact, it was by binning $64 \times 64$ camera pixels and averaging many experimental repetitions that we saw our first Feshbach molecule signal.

Another cause of our difficulty in observing Feshbach molecules soon became clear. While we had the capability of a fast all-optical removal of unassociated atoms when the molecules were in their ground state (see section 5.4), to remove the atoms in the presence of Feshbach molecules we were relying on a much slower process. In this protocol we used a microwave pulse to transfer the atoms from $F = 1 \rightarrow F' = 2$ and then addressed the $F' = 2$ atoms with resonant light. Due to poor Rabi frequencies at the time, we used 5–10 ms Landau-Zener sweeps for the microwave transfers and repeated the removal steps four to eight times per species. The total time from magnetoassociation to the removal of unassociated atoms was typically $\sim$65 ms. If the lifetime of the Feshbach molecules in the optical lattice were on the second-scale, as it was in

section 2.3 (see Fig. 2.14b), then this would not have been a problem. However, we measured a lifetime in the new 3D lattice of 74(24) ms (Fig. 5.27a), so about 58% of the Feshbach molecules were lost during the removal of unassociated atoms (ignoring any additional loss from the effect of the removal light on the Feshbach molecules). The reason for this shortened lifetime was the greatly increased intensity of the light in the new setup. The dependence of the lifetime $\tau$ on the intensity $I$ is given by $\tau = 1/(\mathrm{Im}(\alpha)I)$ [217], where $\alpha$ is the complex polarizability of the Feshbach molecules at 1064 nm. By fitting the highest intensity data (to ensure tunneling is negligible) from Fig. 2.14b to this function, we extract $\mathrm{Im}(\alpha) = 5.9 \times 10^{-11}\,\mathrm{MHz}/(\mathrm{W/cm^2})$ (Fig. 5.27b). For a 3D lattice intensity of $120\,\mathrm{kW/cm^2}$, this would predict a lifetime of $\tau = 140$ ms, within a factor of two of the measured lifetime. Once we were aware of the short Feshbach molecule lifetime, the solution was straightforward. Following the removal of Na atoms, we could greatly reduce the lattice depths while still preventing unassociated Rb and Feshbach molecules from tunneling. This is particularly effective in the case of fast all-optical removal of Na, which we performed after transferring the Feshbach molecules to the ground state. After implementing this solution and optimizing the spatial overlap of the atomic clouds, we detected $10^3$ Feshbach molecules formed from $2 \times 10^4$ atoms of each species.

This represented an order of magnitude improvement in the number of Feshbach molecules compared to our previous single-layer Mott insulator approach, but the conversion efficiency was only ∼5% and the number was still much lower than we desired. We therefore tried an alternative approach in which we cross a 3D superfluid-to-Mott insulator transition by ramping up the vertical and 2D lattices simultaneously. This approach necessitated a number of changes, both in terms of the experimental sequence as well as in the optical potentials that we employed. We still desired to cross the Mott insulator transition at the zero-crossing of the interspecies scattering length at 352 G. This meant that we needed an optical potential to take the part of

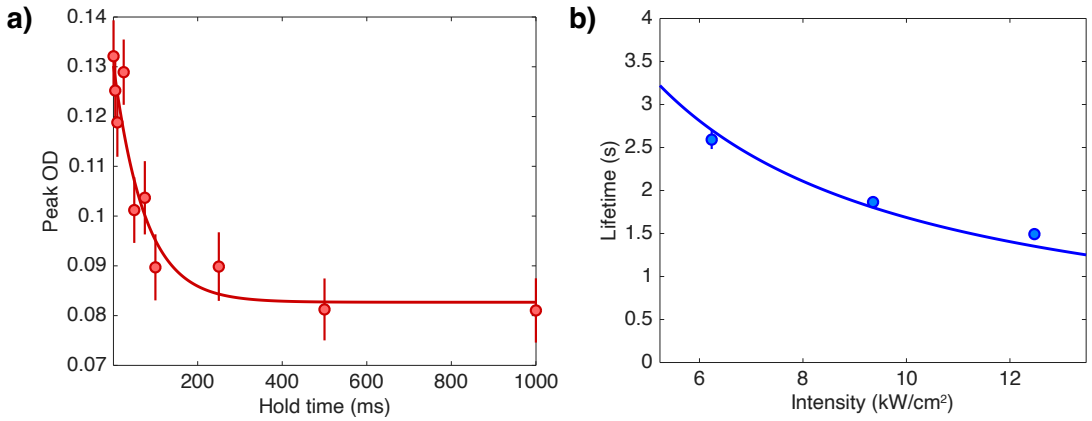


**Figure 5.27: Feshbach molecule lifetime in the 3D lattice.** **a)** We measure an optical scattering-limited lifetime of $\tau = 74(24)$ ms for Feshbach molecules in the 3D lattice. Note that the constant nonzero background is due to incomplete removal of unassociated Rb atoms in this dataset. These atoms show up in our detection protocol but do not affect the decay rate of the molecules. **b)** By fitting the lifetime versus intensity data for the highest lattice depths in Fig. 2.14b, we can extract the imaginary polarizability of the Feshbach molecules at 1064 nm. For the 3D lattice intensity used in **a)**, the predicted lifetime from this imaginary polarizability is within a factor of two of the measured lifetime.

the vertical lattice in holding the atoms as we ramped the magnetic field above the Feshbach resonance to the miscible regime. The logical choice was to use the XODT, as it was already used to trap the atoms prior to loading the vertical lattice at low field in the former sequence. However, the beam waist of the XODT is only 105 $\mu$m. If we were to hold the atoms in the XODT as the 3D lattice ramps on, then the extra harmonic confinement of the XODT would limit the maximum size of the $n = 1$ Mott insulators we could produce. As mentioned earlier, we wanted to keep the small waist of the XODT for the early parts of the experimental sequence in which we use it to capture atoms from the magnetic trap and evaporate them to degeneracy. Consequently, we decided to dynamically increase its beam waist after the evaporation but before ramping on the 3D lattice.

One complication for this scheme is that our XODT actually contains a weak lattice arising from stray interference. The XODT consists of the same optical path

as our 752 nm spacing 2D lattice (Fig. 5.21), except that the retroreflection used to form the 2D lattice is blocked when using the path for the XODT. Ideally, the first arm is vertically polarized and propagates in the horizontal plane orthogonal to the horizontally polarized second arm. For the same reasons outlined in section 5.2.2, a small tilt of the second arm's polarization or of the first arm's **k** vector out of the horizontal plane will cause unwanted interference (the two arms are at identical frequencies unlike those in the new 532 nm spacing 2D lattice). We can generally tolerate this interference when using the XODT to optically evaporate the atoms to degeneracy. However, if the XODT is on while the 3D lattice is ramping up to form a Mott insulator, then the stray interference would hinder our ability to produce a uniformly filled lattice. To avoid this issue, we set up a mirror on a motorized flip mount (Thorlabs MFF101) to block the second pass of the XODT midway through the sequence (the atoms are held in a different optical potential during this time so they do not experience the sudden change in the XODT). The resulting single-pass ODT does not have any stray interference issues, but it also does not provide significant harmonic confinement along its axial direction. To hold the atoms along the propagation axis of the ODT, we make use of our ability to dynamically block the retroreflection of the vertical lattice using a waveplate on a motorized rotation mount (see section 5.2.1). The non-interfering 205 $\mu$m waist "vertical beam" can then be used to provide radial confinement of the atoms, including along the axial direction of the ODT. When it comes time to turn on the vertical lattice in the sequence, we simply program a rotation of the waveplate to smoothly ramp up the vertical interference pattern.

Due to the need to hold the atoms against gravity combined with constraints on the available optical power, we opted to keep the same vertical ODT waist but dynamically increase the horizontal waist. This was accomplished by dithering the frequency of the AOM (Gooch & Housego 3110-197) controlling the ODT. To deter-

mine the required modulation rate, we consider the following. The 3D Mott insulator ramp proceeds in two stages: an initial ramp of the 3D lattice to $V_{\mathrm{latt,Rb}} = 30\,E_{\mathrm{r,Rb}}$ to pin the Rb atoms, immediately followed by a ramp to our maximum vertical lattice depth of $V_{\mathrm{latt,Na}} = 24\,E_{\mathrm{r,Na}}$ with the 2D lattice continuing to rise to $V_{\mathrm{latt,Na}} = 60\,E_{\mathrm{r,Na}}$. For a 532 nm spacing lattice, $V_{\mathrm{latt,Na}} = 24\,E_{\mathrm{r,Na}}$ corresponds to an on-site harmonic confinement of $2\pi \times 75$ kHz for Na and $2\pi \times 66$ kHz for Rb. The maximum modulation rate of our AOM is ∼1 MHz, which is thirteen times the Na on-site harmonic oscillator frequency. We anticipate needing to modulate close to the upper frequency modulation bandwidth of the AOM in order to avoid heating of the atoms (1 MHz modulation is only 6.5 times the parametric driving frequency of $2\omega_{\mathrm{on-site}}$) [256]. Modulating fast compared to the final 2D lattice depth of $V_{\mathrm{latt,Na}} = 60\,E_{\mathrm{r,Na}}$ is likely not possible ($\omega_{\mathrm{on-site}} \approx 120$ kHz), so the ODT needs to be turned off prior to ramping the 2D lattice from $V_{\mathrm{latt,Na}} = 24\,E_{\mathrm{r,Na}}$ to $V_{\mathrm{latt,Na}} = 60\,E_{\mathrm{r,Na}}$.

In the absence of nonlinearities, a triangular frequency modulation waveform will produce a clean "box-shaped" ODT potential in the horizontal plane. We aimed to increase the in-plane waist by a factor of four from 105 $\mu$m to 420 $\mu$m, corresponding to modulating the frequency of the AOM by ±8.5 MHz about the 110 MHz center frequency. We used a Keysight 33621A arbitrary waveform generator (AWG) as the frequency source for the AOM, and analyzed the beam shape using a DataRay WinCamD-UCD23 beam profiling camera. We performed initial testing at a lower modulation frequency of 500 kHz. Programming the AWG with a triangular modulation waveform, we recorded the beam profile shown in Fig. 5.28a (note that the profile is rotated by 90° so that the horizontal plane appears vertical in the image). The profile is stretched in the horizontal plane as desired, but the intensity has a substantial gradient and large ripples are present. To smooth out the profile, we implemented a two-stage optimization. The triangular modulation waveform's rising edge was divided into 15 optimization points that could be fed into a nonlinear

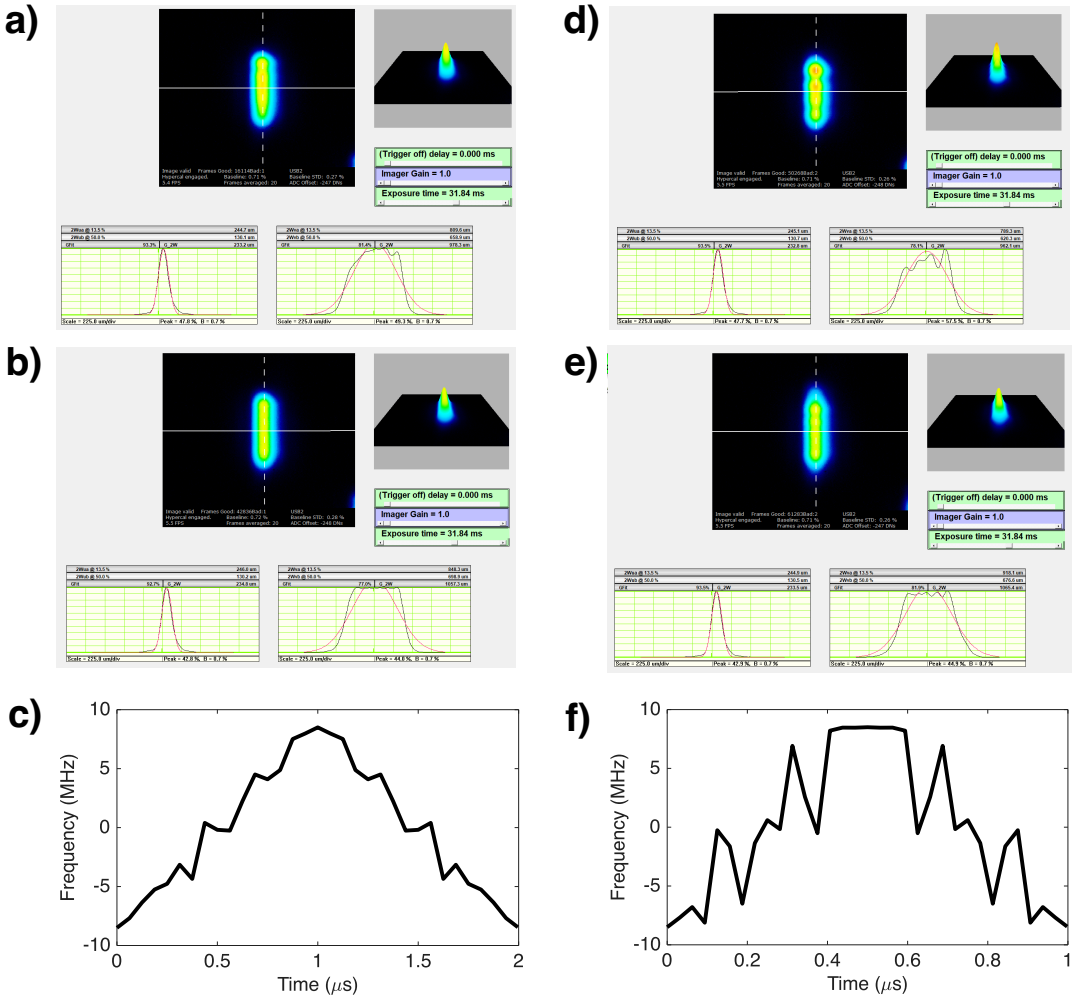


**Figure 5.28: Dithering the ODT. a), b), c)** show the results of dithering the ODT with a modulation frequency of 500 kHz. **d), e), f)** are with a 1 MHz modulation frequency. **a)** and **d)** show the beam profile with a triangular modulation waveform prior to optimization. **b)** and **e)** show the final beam profile after optimization for intensity uniformity. **c)** and **f)** are the optimized modulation waveforms corresponding to **b)** and **e)**.

least-squares solver in MATLAB. The falling edge was set to mirror the rising edge. A linear interpolation was then used to construct a modulation waveform with 512 samples. In the first round of optimization, the derivative of the beam profile's horizontal cross-section within a region of interest was minimized. We found that the optimized profile after this first round had most of its intensity ripples removed but preserved a small overall gradient. A second round of optimization in which the error was defined as the difference in the central region between each intensity data point and the mean value helped to flatten the beam shape. The resulting beam profile and optimized AWG modulation waveform are shown in Fig. 5.28b,c. We next performed the optimization of the beam profile at the full 1 MHz modulation frequency. Although the beam profile was substantially improved by the optimization procedure, at this high modulation frequency the final beam profile retained ripples of 5% of the peak intensity (Fig. 5.28d,e,f).

Since these intensity ripples in the dithered ODT beam posed a concern for the uniformity of the $n = 1$ Mott insulators, we set up a new static optical potential with the desired elliptical beam profile. Fig. 5.29 shows the optics diagram for this "elliptical beam," which is derived from the main XODT optical path. As the two beams are not needed simultaneously, we used a combination of motorized flip mounts as well as a waveplate on a motorized rotation stage to transition between the two potentials during the sequence. As before with the intended dithered ODT, the elliptical beam only passes through the science chamber a single time with axial confinement provided by the non-interfering "vertical beam." The measured beam waists for the elliptical beam are 77 $\mu$m in the vertical direction and 390 $\mu$m in the horizontal.

After empirically optimizing the experimental sequence based on the number of molecules produced, we settled on the following protocol. We begin with dual BECs of approximately $1.5 \times 10^4$ Na atoms and $1 \times 10^4$ Rb atoms held at 9 G in a combination

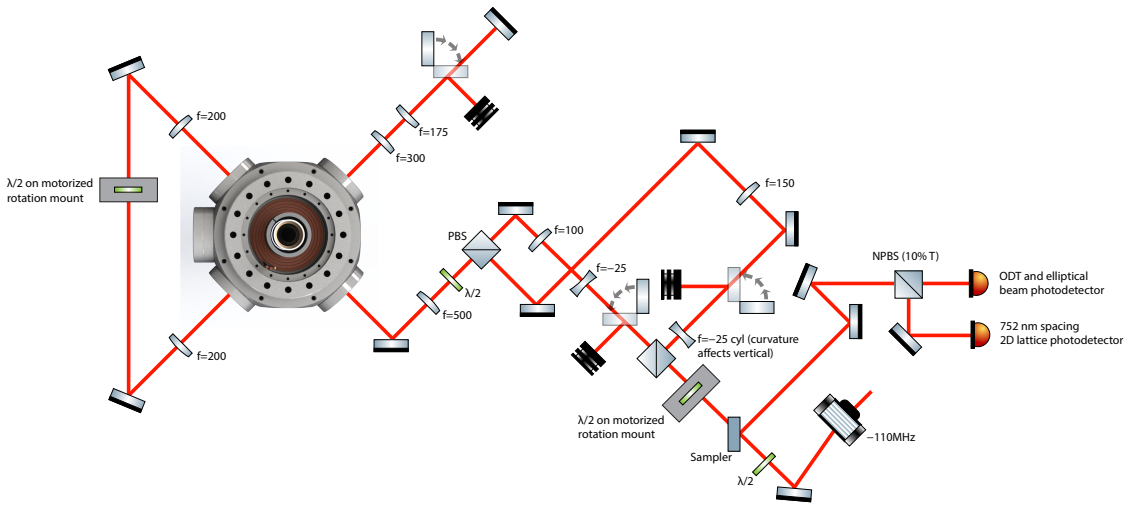


**Figure 5.29: Diagram of the elliptical beam, XODT, and new 752 nm spacing 2D lattice optics.** All focal lengths are in mm.

of the elliptical beam ($\omega_{\mathrm{Na}} = 2\pi \times (27, 0, 136)\,\mathrm{Hz}$, $\omega_{\mathrm{Rb}} = 0.88\omega_{\mathrm{Na}}$) and the non-interfering vertical beam (radial confinement $\omega_{r,\mathrm{Na}} = 2\pi \times 27\,\mathrm{Hz}$). The magnetic field is then ramped to 335 G in 50 ms, at which point the field jumps above the Feshbach resonance to 416 G. At this field, the Na and Rb atoms are still immiscible, so we then ramp the magnetic field into the miscible regime in 50 ms, ending at 354 G. At this point, the confinement from the vertical beam is reduced to $\omega_{r,\mathrm{Na}} = 2\pi \times 16\,\mathrm{Hz}$ in order to form larger $n = 1$ Mott insulators. The magnetic field is subsequently decreased to 352 G, which is the zero-crossing of the interspecies Feshbach resonance. We then proceed to ramp up the 3D lattice over 150 ms, crossing the Rb superfluid-to-Mott insulator transition. In this step, the final depth of the 532 nm spacing 2D lattice is $V_{\mathrm{latt,Rb}} = 31\,E_{\mathrm{r,Rb}}$ ($V_{\mathrm{latt,Na}} = 3\,E_{\mathrm{r,Na}}$). Simultaneously, the waveplate controlling the retroreflection of the vertical beam/lattice is smoothly rotated such that the vertical lattice reaches a final depth of $V_{\mathrm{latt,Rb}} = 45\,E_{\mathrm{r,Rb}}$ ($V_{\mathrm{latt,Na}} = 4\,E_{\mathrm{r,Na}}$). We can then take advantage of the fact that Rb is pinned in the lattice while Na is superfluid in order to maximize the vertical overlap of the Na and Rb clouds. Na experiences less gravitational sag than Rb, so the elliptical beam confinement is

reduced to $\omega_{\mathrm{Na}} = 2\pi \times (22, 0, 109)$ Hz in order to match the Na vertical position to that of the pinned Rb. Finally, in 75 ms the lattices are raised to depths of $V_{\mathrm{latt,Na}} = 27.5\, E_{\mathrm{r,Na}}$ and $V_{\mathrm{latt,Na}} = 24\, E_{\mathrm{r,Na}}$ for the 2D lattice and vertical lattice, respectively, crossing the Na superfluid-to-Mott insulator transition. The elliptical beam is then be ramped off, and magnetoassociation and STIRAP proceed as before.

With this sequence, we detected up to $1.6 \times 10^3$ ground state molecules. In contrast to the $> 90\%$ one-way STIRAP efficiency that we measured previously in section 3.2, for these experiments we only achieved a one-way efficiency of 79%. The reduced STIRAP efficiency is believed to be due to the larger size of the molecular cloud. We need to use a small STIRAP up-leg beam waist of 45 $\mu$m to maximize the Rabi frequency given the limited available power of $\sim$25 mW, so at the edges of large clouds the intensity of the up-leg beam is reduced (see section 3.2 for more details). Taking into account the STIRAP efficiency, our detected ground state number of $1.6 \times 10^3$ molecules corresponds to $2.0 \times 10^3$ ground state molecules produced out of $2.6 \times 10^3$ Feshbach molecules. Following the all-optical removal of unassociated atoms (see section 5.4), the lattice depths are reduced to $V_{\mathrm{latt,mol}} = 68\, E_{\mathrm{r,mol}}$ (equivalent of $V_{\mathrm{latt,Rb}} = 57\, E_{\mathrm{r,Rb}}$) for the 2D lattice and $V_{\mathrm{latt,mol}} = 81\, E_{\mathrm{r,mol}}$ for the vertical lattice to limit one-body loss from off-resonant scattering. At these depths, we measure a ground state lifetime of 7(2) s (Fig. 5.30). In addition, by preparing the molecules in the $|1, 0\rangle$ rotational state and turning on the electric field to 4.54 kV/cm, we could examine Förster resonance collisional shielding with the new experimental sequence. We slowly ramped off the 2D lattice at this field so that the molecules were only held in the vertical lattice. After a variable amount of hold time, we then pinned the molecules with the 2D lattice. We fit the data to a one-body loss model and extracted a lifetime of $\tau = 4.3(6)$ s (Fig. 5.31). Note that initial loss during the ramp down of the 2D lattice as the molecules begin to tunnel is not captured by this measurement.

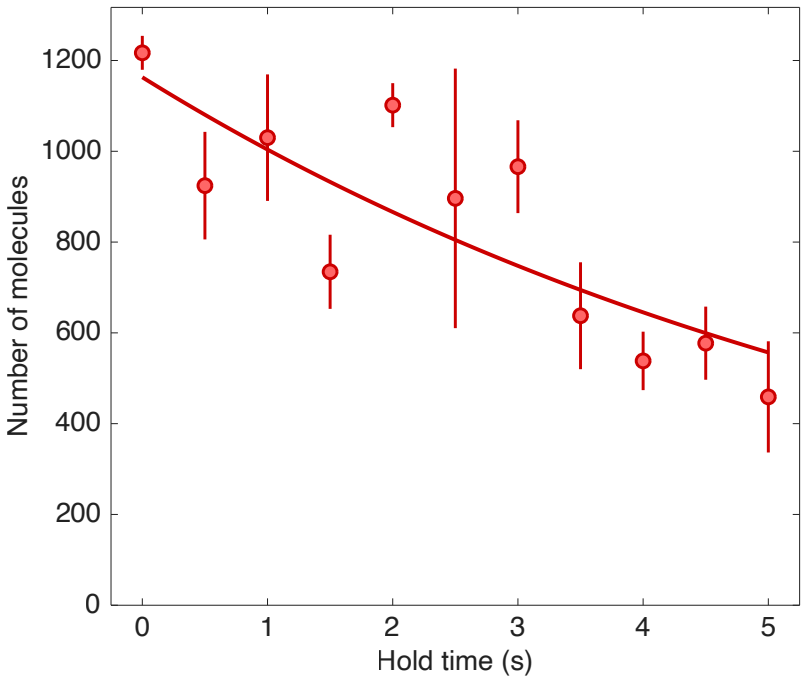


**Figure 5.30: Ground state molecule lifetime in the 3D lattice.** For a 2D lattice depth of $V_{\mathrm{latt,mol}} = 68\, E_{\mathrm{r,mol}}$ and a vertical lattice depth of $V_{\mathrm{latt,mol}} = 81\, E_{\mathrm{r,mol}}$, we measure a ground state lifetime of 7(2) s.

To further boost the conversion efficiency of atoms into molecules, we made several additional changes to the experiment. These changes were motivated by the work of ref. [33], in which RbCs Feshbach molecules were produced by combining dual 3D Mott insulators, achieving a molecular lattice filling fraction greater than 30%. In that work, Cs atoms cross the Mott insulator transition while they are spatially separated from the (still-superfluid) Rb atoms. A tunable-position optical dipole trap is then used to move the Rb atoms to the Cs position at the zero-crossing of the interspecies scattering length, at which point the lattice continues to ramp up to form dual $n = 1$ Mott insulators. Such a protocol, applied to our case, has several possible benefits. First, we had previously observed that the purity of the Rb BEC was reduced following the magnetic field ramp above the Feshbach resonance, particularly in the presence of Na, which may have limited the filling of the Rb Mott insulator. By initially keeping the Rb and Na atoms separate, we would be able to form a Rb Mott

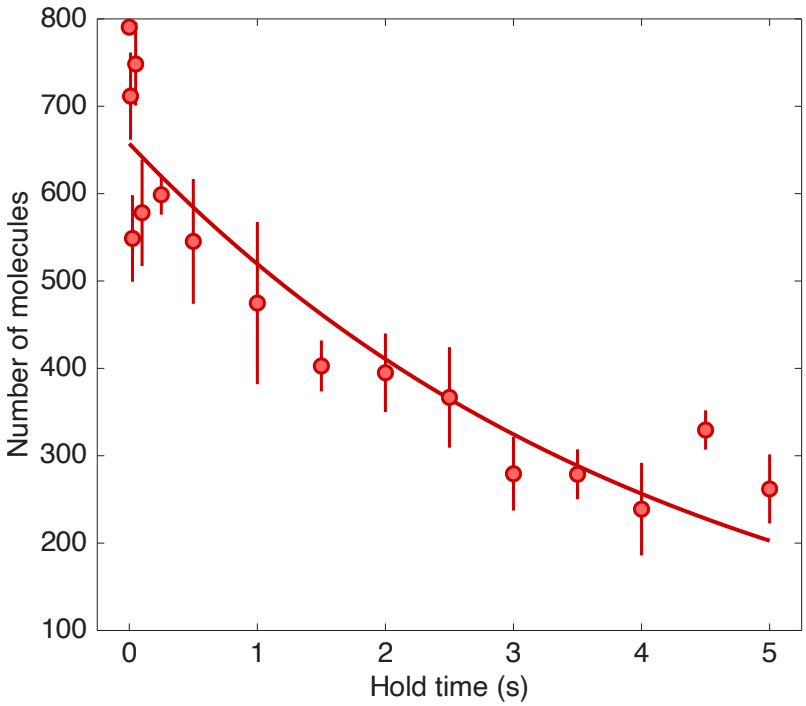


**Figure 5.31: Collisional shielding lifetime of $|1,0\rangle$ molecules with the 3D Mott insulator sequence.** At 4.54 kV/cm (above the Förster resonance), we observe a one-body limited lifetime for the $|1,0\rangle$ molecules of $\tau = 4.3(6)$ s.

insulator at low magnetic field. The atomic species would then continue to be kept separate until the magnetic field was ramped to the zero-crossing of the interspecies scattering length (the fast jump above the interspecies Feshbach resonance would no longer be required since the atomic clouds would be spatially isolated). This would also remove the possibility of inducing excitations in the atomic mixture during an immiscible-to-miscible transition, as was observed in ref. [257]. Moreover, the use of a species-specific optical dipole trap to separate and later recombine the atoms would provide us with the ability to finely tune the vertical overlap of the two species, which was still a concern despite efforts to maximize overlap by modifying the confinement of the elliptical beam prior to the Na Mott insulator transition.

The species-specific optical dipole trap is generated by a 638 nm laser diode (Thorlabs L638P200) with an output power of 190 mW (Fig. 5.32). This wavelength is attractive for Na and repulsive for Rb, with a dipole potential ratio of

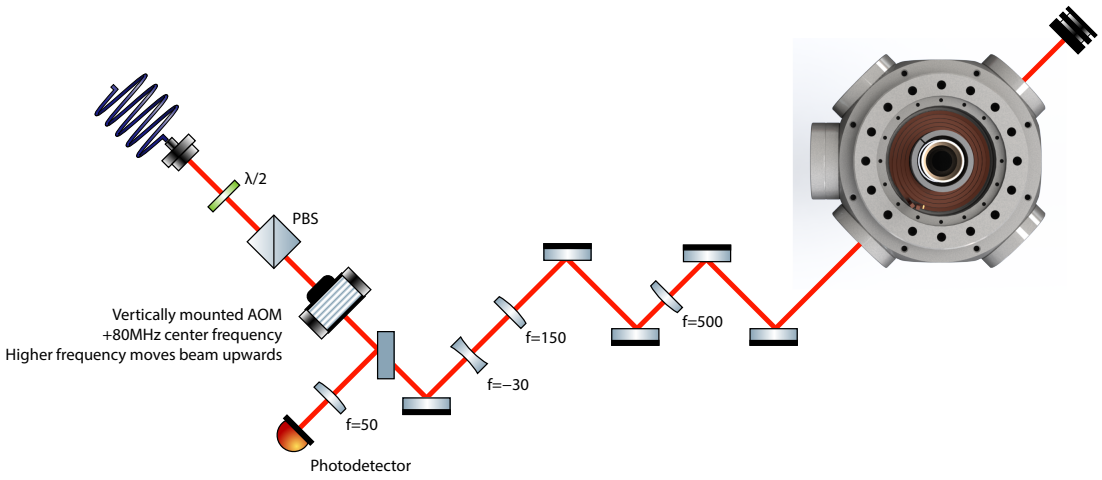


**Figure 5.32: Diagram of the 638 nm beam optics.** All focal lengths are in mm.

$V_{\mathrm{dip,Na}} = -1.8 V_{\mathrm{dip,Rb}}$. The 638 nm beam, which propagates in the horizontal plane, passes through a vertically oriented AOM so that by changing the frequency of the AOM we can alter the vertical position of the beam at the center of the science chamber. We measure a vertical displacement of 17 $\mu$m/MHz at the atoms (80 MHz center frequency), with a beam waist of 45 $\mu$m.

In the experimental sequence, both species are initially held at 9 G in a combination of the non-interfering vertical beam (radial confinement $\omega_{r,\mathrm{Na}} = 2\pi \times 37$ Hz) and the XODT ($\omega_{\mathrm{Na}} = 2\pi \times (91, 91, 129)$ Hz). The 638 nm beam is then ramped on in 75 ms to $\omega_{\mathrm{Na}} = 2\pi \times 293$ Hz, corresponding to a combined vertical potential well depth (XODT, 638 nm beam, and gravity) of 6.4 $\mu$K for Na and 2.3 $\mu$K for Rb. The vertical position of the 638 nm beam is subsequently moved by $\Delta z = +200\,\mu$m in 100 ms to transport the Na atoms upwards, while the Rb atoms remain at the original position. The horizontal confinement of the Na atoms along the axis of the 638 nm beam continues to be provided by the vertical beam. At this point in the sequence, shortly before ramping on the 3D lattice to pin the Rb atoms, we apply a vertical magnetic field gradient of 27 G/cm to partially levitate the $|1, 1\rangle$ Rb atoms. By adjusting the strength of the gradient, we can ultimately control the vertical spatial

overlap of the Rb and Na Mott insulators. Note that despite having a species-specific optical potential in the 638 nm beam, we cannot use it to directly match the Rb and Na vertical positions; due to its small waist, the 638 nm beam must be turned off prior to pinning the Na atoms in order to avoid severely limiting the size of the Na $n = 1$ Mott insulator. The Na vertical position is therefore determined by its gravitational sag in the 1064 nm optical potentials prior to crossing the Mott insulator transition.

Once the Rb is partially levitated, it no longer requires as deep of an optical potential to hold it against gravity. We therefore transfer the Rb to a weaker vertical confinement trap consisting of a single-pass 1064 nm optical potential ($\omega_{\mathrm{Rb}} = 2\pi \times 75\,\mathrm{Hz}$), and we also decrease the radial confinement of the vertical beam to $\omega_{\mathrm{Rb}} = 2\pi \times 22\,\mathrm{Hz}$ during this time. To weaken the radial confinement from the single-pass ODT, we simultaneously turn off the ODT and turn on a weak 2D lattice over 200 ms before ramping up a 3D lattice in 150 ms to cross the Rb superfluid-to-Mott insulator transition. The final lattice depths are $V_{\mathrm{latt,Rb}} = 61\,E_{\mathrm{r,Rb}}$ in the horizontal plane and $V_{\mathrm{latt,Rb}} = 88\,E_{\mathrm{r,Rb}}$ along the vertical axis. With the Rb pinned, the magnetic gradient is turned off and a uniform magnetic field along the $z$-axis is ramped to the zero-crossing of the interspecies scattering length at 352 G. We temporarily reduce the vertical lattice depth to $V_{\mathrm{latt,Na}} = 4\,E_{\mathrm{r,Na}}$ ($V_{\mathrm{latt,Rb}} = 48\,E_{\mathrm{r,Rb}}$) before transporting the Na downwards in 100 ms to the Rb position by adjusting the height of the 638 nm beam. As discussed in ref. [33], the rate at which the Na is transported through the weak vertical lattice must be below a critical velocity. If the 638 nm beam moves downwards too quickly, then the Na will not be able to follow it and will instead stay at the same vertical position. The depth of the 2D lattice that the Na experiences increases as it moves down toward the center of the beam, where $V_{\mathrm{latt,Na}} = 5.5\,E_{\mathrm{r,Na}}$ ($V_{\mathrm{latt,Na}} = 4\,E_{\mathrm{r,Na}}$ for the vertical lattice). The ratio of on-site interaction to tunneling ($U/J$) is therefore highest near the conclusion of the ramp. As the critical velocity

for the Na to follow the 638 nm beam is given by [33, 258]:

$$\begin{aligned} v_c &= \left.\frac{\partial E}{\partial q}\right|_{q_c} \\ q_c &= \frac{\hbar k}{\pi}\mathrm{Re}\left[2(\,1-\frac{(U/J)}{(U/J)_c}\,)\right], \end{aligned} \tag{5.20}$$

the most stringent condition on the rate of movement is obtained by using the lattice depths at the end of the transport. Here, $q$ is the quasimomentum, $E$ is the energy of the ground band, and $(U/J)_c$ is the interaction-to-tunneling ratio at the superfluid-to-Mott insulator transition, which is approximately 34.8 in three dimensions. In our case, we obtain $v_c = 4 \times 10^3\,\mu$m/s, twice the rate at which we transport Na.

With the Na atoms approximately at the Rb vertical position, the vertical lattice depth is increased to $V_{\mathrm{latt,Na}} = 8\,E_{\mathrm{r,Na}}$ and the 2D lattice depth to $V_{\mathrm{latt,Na}} = 9\,E_{\mathrm{r,Na}}$, following which the 638 nm beam is ramped off in 200 ms. Finally, the 3D lattice is raised to a horizontal depth of $V_{\mathrm{latt,Na}} = 24\,E_{\mathrm{r,Na}}$ and a vertical depth of $V_{\mathrm{latt,Na}} = 26\,E_{\mathrm{r,Na}}$, forming a Na Mott insulator.

To characterize the lattice filling fractions, we can approximate the column density of the Rb and Na Mott insulators in absorption imaging as a Thomas-Fermi profile with radii $R_x, R_y, R_z$, resulting in a peak filling fraction $f_0$ of [32, 259]:

$$f_0 = \frac{15Na^3}{8\pi R_x R_y R_z}, \tag{5.21}$$

where $N$ is the number of atoms and $a$ is the lattice spacing. Therefore, by taking an absorption image from the side and another from the top, we can fit the column densities to parabolas to extract the Thomas-Fermi radii (as well as the particle number), giving us an estimation of the peak filling of the atomic Mott insulators. In our setup, the Thomas-Fermi radii were expected to be within the range of 10 to 30 $\mu$m along all three axes. Accurately measuring the horizontal radii $R_x$ and $R_y$ was not an issue thanks to the resolution afforded by the high numerical aperture

objective from our quantum gas microscope (full-width half maximum of the point spread function is 1010(15) nm as shown in Fig. 2.12). However, the lower end of that range for the vertical radius was difficult to resolve with our existing diagnostic side imaging. One issue with this imaging system was that several one inch diameter optics limited the numerical aperture to NA = 0.05. The corresponding resolution for Rb imaging is 10 $\mu$m, potentially leading to an overestimation of the vertical radius for small cloud sizes. The maximum numerical aperture along that imaging axis is limited by the Macor electrode holder (see section 5.1.1) to NA = 0.065 (Rb resolution 7 $\mu$m), so the external optics were limiting the resolution rather than the geometry of the science chamber. In addition, our side imaging system had a magnification of 1/2.6 to enable a large field of view (this was helpful for imaging the atomic MOTs as well as performing long time of flights). Since the side imaging camera (Allied Vision Guppy F-080) has a pixel size of 4.65 $\mu$m, the vertical Thomas-Fermi radius would only occupy 1 to 3 pixels.

To improve our vertical resolution while preserving the large field of view of our existing setup, we split our side imaging system into two paths as shown in Fig. 5.33. A 2 inch diameter non-polarizing plate beamsplitter (Thorlabs BSW27) divides the light into a high-resolution (small field of view) and a low-resolution (large field of view) path. The latter uses the same camera as before and preserves the 1/2.6 magnification. For the high-resolution path, we use a camera (Allied Vision Alvium 1800 U-501m NIR) with a smaller pixel size of 2.2 $\mu$m and a magnification of 1.1. The light collection optics are designed to be compatible with the full numerical aperture of 0.065.

With this new side imaging system installed, we proceeded to measure the atomic Mott insulator fillings. After optimizing the alignments, timings, Rb levitation gradient, and atom numbers we measured Na and Rb Thomas-Fermi radii of $R_{x,y,z;\,\mathrm{Na}} = (23(1), 16.9(9), 24.5(5))\,\mu$m and $R_{x,y,z;\,\mathrm{Rb}} = (17.0(5), 14.8(4), 28.6(4))\,\mu$m. The corre-

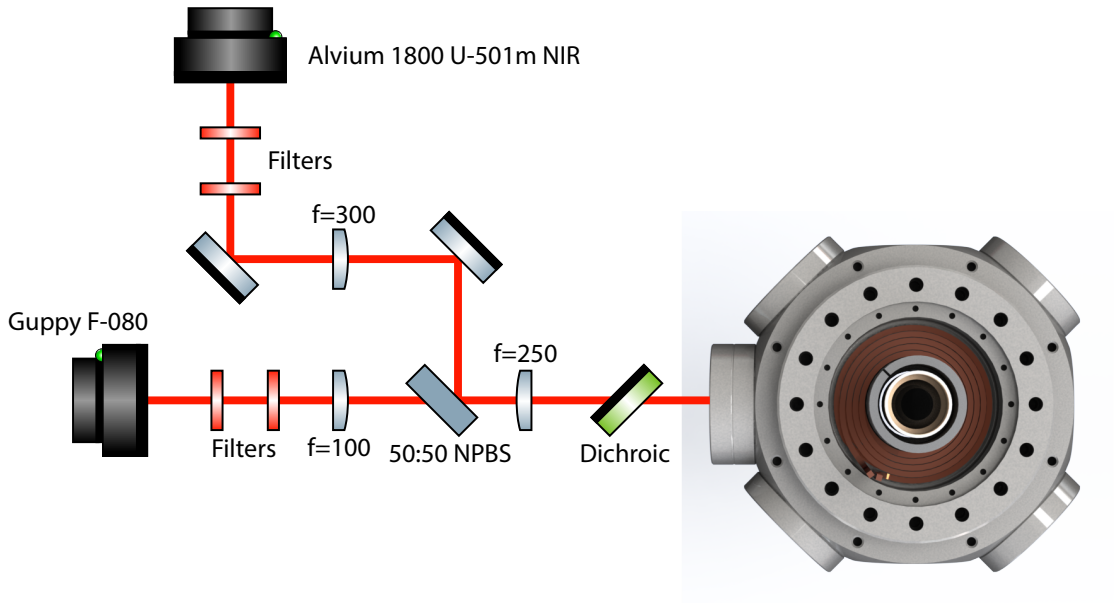


**Figure 5.33: Diagram of the new side imaging system.** All focal lengths are in mm.

sponding atom numbers were $N_{\mathrm{Na}} = 4.6(2) \times 10^4$ and $N_{\mathrm{Rb}} = 8.8(4) \times 10^4$. From equation 5.21, we obtain a peak lattice filling fraction of 0.43(4) for Na and 1.10(7) for Rb. Following magnetoassociation, the same technique yields Thomas-Fermi radii of $(18.9(4), 15.2(4), 28.6(6))\,\mu$m for the Feshbach molecules. Along a given axis, the Feshbach molecule radius should be less than or equal to the smaller of the two atomic radii. The fact that this is not true in our measurement is likely the result of a slight adjustment to the levitation gradient between the atomic and molecular datasets to improve the spatial overlap; the atomic radii were not remeasured following this change. At a molecule number of $3.5(1) \times 10^3$, the molecular Thomas-Fermi radii correspond to a peak Feshbach molecule filling of 0.038(2). Interestingly, we measured a similar number of Feshbach molecules for an improved Na lattice filling of 1.02(4) (corresponding to $8.4(2) \times 10^4$ atoms with radii $(27.4(5), 17.5(3), 15.4(3))\,\mu$m), perhaps indicating that spatial overlap of the two species remains an issue. It should be noted that by further increasing the atom numbers beyond what is expected to form $n = 1$ Mott insulators, we could form up to $8.8(2) \times 10^3$ Feshbach molecules;

however, as expected, this came at the cost of a lower Feshbach molecule peak filling of 0.021(1).

## 5.3 Toward microwave shielding

We became concerned about the prospect of using Förster resonance collisional shielding for the production of high phase-space density polar molecules following the publication of ref. [154] (see section 4.4). In particular, it was shown that the intermolecular potential for two $|1,0\rangle$ NaRb molecules supports a bound state for shielding electric fields corresponding to a positive scattering length. This bound state can lead to significant three-body loss at high densities, which has been observed to prevent the evaporation of bosonic polar molecules to degeneracy [16, 240]. Although microwave collisional shielding as originally envisioned is also susceptible to loss from three-body recombination, a technique has been developed using a combination of $\pi$ and $\sigma^+$ polarized microwaves to get rid of the bound state in the intermolecular potential [16, 142]. This "double microwave shielding" mitigates both two-body and three-body loss and has enabled the formation of a BEC of NaCs molecules [16]. We therefore decided to adopt this proven approach, switching from Förster resonance collisional shielding to microwave shielding. (As it turns out, a combination of the two techniques may be best suited for our apparatus, as will be discussed at the end of this section.)

There are several requirements for implementing effective microwave shielding. First, a large Rabi frequency is required. A previous demonstration of NaRb microwave shielding by the Wang group, for example, used a Rabi frequency of $\Omega = 2\pi \times 9.8\,\mathrm{MHz}$ [141]. This corresponds to an electric field at the molecules of $E =$

11 V/cm, using the relation for the $|0,0\rangle \rightarrow |1,1\rangle$ transition:

$$\Omega = \frac{dE}{\sqrt{3}\hbar}, \tag{5.22}$$

where $d = 3.2\,\mathrm{D}$ is the permanent electric dipole moment. Second, the microwaves need to be circularly polarized. Shielding is ineffective for $\pi$ polarization, and numerical simulations indicate that elliptical polarization must be at least 90% circular [135]. This level of polarization purity can be difficult to achieve in practice, as reflections from nearby metal objects tend to scramble the polarization. Third, phase noise in the microwaves can lead to one-body loss by driving transitions to unshielded collision channels [260]. Specifically, the phase noise of interest is at an offset relative to the carrier frequency of $\sqrt{\Omega^2 + \Delta^2}$ where $\Delta$ is the detuning (typically, microwave shielding is implemented with $\Omega \sim \Delta$). Although the ultralow phase noise needed for long one-body lifetimes was once challenging to achieve, requiring top-of-the-line frequency sources*, the use of high Q factor bandpass cavity filters (with bandwidths $\lesssim 10\,\mathrm{MHz}$) has significantly eased the technical requirements [141].

For our implementation of microwave shielding, we chose to implement the cloverleaf antenna design of ref. [261]. An early version of our antenna array is shown in Fig. 5.34a. In this design, four independent loop antennas are used, each of which ideally produces a linearly polarized electric field. By simultaneously driving all of the antennas with tunable relative phases and amplitudes, one can compensate for nonidealities in the electric field at the molecules to produce nearly circular polarization. This tunability proved especially important for our apparatus due to the presence of the eight electrode rods. As will be discussed later in this section, at the microwave shielding frequency the electrodes strongly attenuate the component of the electric field parallel to their symmetry axis, necessitating strongly imbalanced microwave

*For example, several groups have used the Rohde & Schwarz SMA100B signal generator [140, 242].

powers among the four loops. Another advantage of this design is that it provides good optical access via the central hole in the mount. This optical access is important because in order to obtain large Rabi frequencies, the antenna array must be located as close to the molecules as possible. We place the cloverleaf antenna just below the bottom bucket window of our science chamber with the plane of the loops vertically separated by ∼20 mm from the molecules (Fig. 5.34b). The vertical MOT arms, $z$ absorption imaging beams, and vertical lattice beam pass unobstructed through the center of the cloverleaf antenna.

The frequency of the $|N, m_N, m_{I,\mathrm{Na}}, m_{I,\mathrm{Rb}}\rangle = |0, 0, 3/2, 3/2\rangle \rightarrow |1, 1, 3/2, 3/2\rangle$ transition at 345.9 G is 4.179 GHz. For a detuning of +10 MHz, similar to the detuning used for NaRb in ref. [141], the $\sigma^+$ microwave frequency is 4.189 GHz, corresponding to a vacuum wavelength of $\lambda = 72$ mm. The path length of each loop is designed to be approximately one wavelength, so that antinodes of the voltage are located at opposite ends of the loop, 90° from the feed point. For the version shown in Fig. 5.34a the length is slightly smaller at 65 mm. The loops in the cloverleaf antenna are oriented such that one pair of opposite loops ideally produces an electric field polarized parallel to the symmetry axis of the rods while the other pair produces an electric field perpendicular to that axis (Fig. 5.34c). We construct the loops out of 18 AWG bare copper wire and install them in a custom 3D-printed PLA plastic mount. The ends of the wires are soldered to SMA connectors (Molex 0732512123). The central optical access hole has a diameter of 25.4 mm. In addition, we use a metal reflector made of 250 $\mu$m thickness copper located 4 mm below the loops in order to increase the electric field strength at the molecules (Fig. 5.34d).

We tried several versions of these 3D-printed cloverleaf antenna mounts, iterating the design based on experimental data and EM simulations using Ansys HFSS. In our initial Rabi frequency measurements of the antenna array, we did not need to use a high power amplifier as we could simply extrapolate the measured Rabi frequencies to

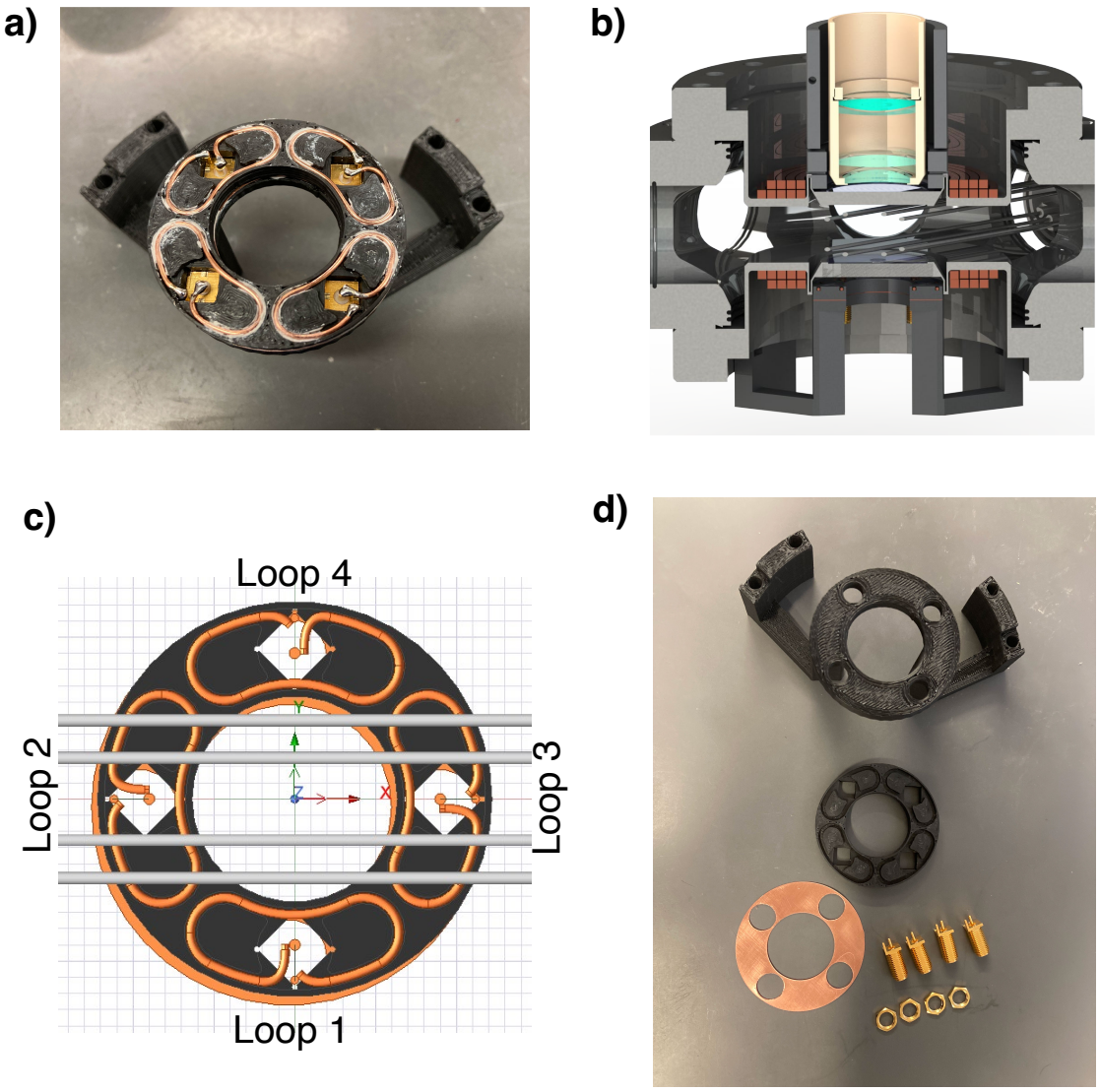


**Figure 5.34: Cloverleaf antenna. a)** In this early version of our cloverleaf antenna, four wire loops are attached to a 3D printed mount. **b)** The cloverleaf antenna mount screws into the science chamber, keeping the antennas within a few mm of the bottom bucket window. **c)** The loop antenna numbering convention used in the main text. Loops 1 and 4 ideally produce an electric field parallel to the electrode rods, while loops 2 and 3 ideally produce a field perpendicular to the rods. **d)** Cloverleaf antenna during assembly, with the copper reflector visible.

what they would be at higher input powers. In fact, low powers are desirable for these measurements in order to address a single molecular transition. We use an Agilent E8257C (option UNR) analog signal generator as our microwave source. Phase noise is irrelevant for the Rabi frequency measurements so no bandpass filters were installed, although it should be noted that the signal generator already has a very good phase noise of $< -150\,\mathrm{dBc/Hz}$ for 4.2 GHz at a 10 MHz offset. The signal is then sent to an RF switch (Mini-Circuits ZASWA-2-50DRA+) before being divided into four paths by a power splitter (Mini-Circuits ZN4PD1-63LW-S+) corresponding to the four loop antennas. One signal path goes directly to one of the loop antennas, while the other three signal paths pass through programmable phase shifters (Vaunix LPS-802) before going to their respective loops. LMR-240 coaxial cables (Times Microwave Systems) are used throughout the system for their low loss at the shielding frequency.

We impedance match each loop antenna to maximize the accepted power. The RF signal path prior to the antennas has a characteristic impedance of $50\,\Omega$. On the other hand, the impedance of each loop is in general complex with a real part that can be well in excess of $100\,\Omega$ depending on the exact loop geometry and surrounding materials. Following ref. [261], we use open-circuit stub tuning to match the impedances. As depicted in Fig. 5.35, we can write the load impedance (i.e. the loop impedance) as $Z_L$ and the characteristic impedance of the RF system as $Z_0 = 50\,\Omega$. A coaxial tee connector is inserted in the transmission line to connect a coaxial stub of length $\ell_s$ and impedance $Z_s$ in parallel with the antenna load. If the length of coaxial cable between the stub and the antenna is $\ell_{sL}$ and the wavenumber in the transmission line is $\beta$ (which is *not* equal to the vacuum wavenumber), then the input impedance just after the stub is given by the lossless transmission line impedance [262]:

$$Z_{\mathrm{in},sL}(\ell_{sL}) = Z_0 \frac{Z_L + iZ_0 \tan(\beta \ell_{sL})}{Z_0 + iZ_L \tan(\beta \ell_{sL})}. \tag{5.23}$$

The stub impedance obeys the same equation, but with a load impedance of $\infty$. Therefore,

$$Z_s(\ell_s) = -iZ_0 \cot(\beta \ell_s). \tag{5.24}$$

The total input impedance is the parallel combination of $Z_{\text{in},sL}(\ell_{sL})$ and $Z_s(\ell_s)$. The effect of stub tuning is clearest if we work in terms of admittance instead of impedance:

$$Y_{\text{in,tot}}(\ell_{sL}, \ell_s) = \frac{1}{Z_{\text{in,tot}}(\ell_{sL}, \ell_s)} = Y_{\text{in},sL}(\ell_{sL}) + Y_s(\ell_s). \tag{5.25}$$

Since from equation 5.24 the stub input admittance is pure imaginary, it can only affect the imaginary part of $Y_{\text{in,tot}}$. We must therefore vary $\ell_{sL}$ to set the real part of $Y_{\text{in,tot}}$ to $1/(50\,\Omega)$. The remaining imaginary part can then be canceled by tuning the stub length $\ell_s$.

In practice, we use a handheld vector network analyzer (LiteVNA-64) to measure the $S_{11}$ parameter, which quantifies how much of an input signal is reflected by a load. $S_{11}$, in decibels, is related to $Z_{\text{in,tot}}$ by [262]:

$$S_{11} = 20 \log_{10}(|\Gamma|), \tag{5.26}$$

where the reflection coefficient $\Gamma$ can be written as

$$\Gamma = \frac{Z_{\text{in,tot}} - Z_0}{Z_{\text{in,tot}} + Z_0}. \tag{5.27}$$

We use combinations of SMA adapters to adjust $\ell_{sL}$. For each value of $\ell_{sL}$ that we try, the coaxial cable forming the stub is clipped progressively shorter while monitoring the vector network analyzer until the optimal $S_{11}$ for that $\ell_{sL}$ is found. We typically adjust $S_{11}$ to be $< -7\,\text{dB}$ over the frequency range of interest. Better values of $S_{11}$ at a single frequency can be obtained relatively easily, but for performing spectroscopy on multiple transitions ($\sigma^+$, $\pi$, and $\sigma^-$) we prefer to have a flatter frequency response.

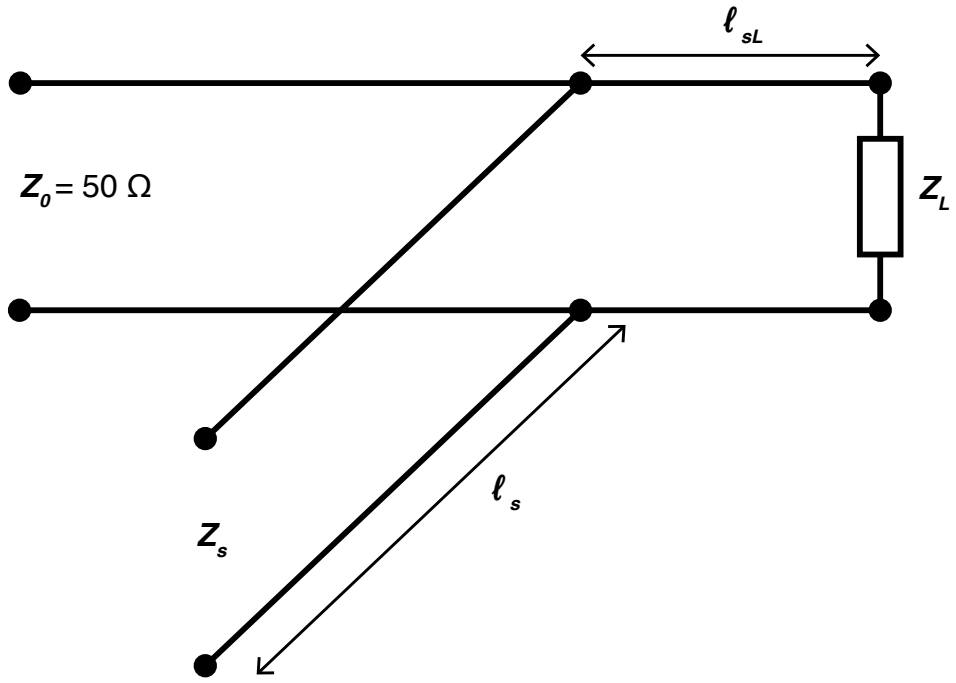


**Figure 5.35: Open-circuit stub tuning.** Schematic of open-circuit stub tuning used to match the impedance of the loop antennas to the 50 Ω characteristic impedance of the RF system. See main text for definitions of the symbols.

We begin our testing of the cloverleaf antenna by identifying the relevant $N = 0 \rightarrow 1$ rotational transitions. A coarse scan is first performed using a single loop antenna. We apply 50 kHz Landau-Zener sweeps in 100 kHz steps and look for loss of molecules, since the reverse STIRAP used for detection is rotational-state selective (Fig. 5.36a). Several strong loss features are visible corresponding to both $\pi$ and $\sigma^{\pm}$ transitions, implying that the loop antenna's polarization is not completely in the plane perpendicular to the quantization axis. We then more carefully find the resonance frequencies of the two starred transitions in the figure by measuring Rabi frequencies at various detunings and fitting them to $\sqrt{\Omega_0^2 + \Delta^2}$ where $\Omega_0$ is the Rabi frequency at $\Delta = 0$ (an example plot for the $\sigma^-$ transition is shown in Fig. 5.36b).

Driving two adjacent loops of the cloverleaf antenna, ideally radiating orthogonal linearly polarized microwaves in the horizontal plane, is the minimal configuration

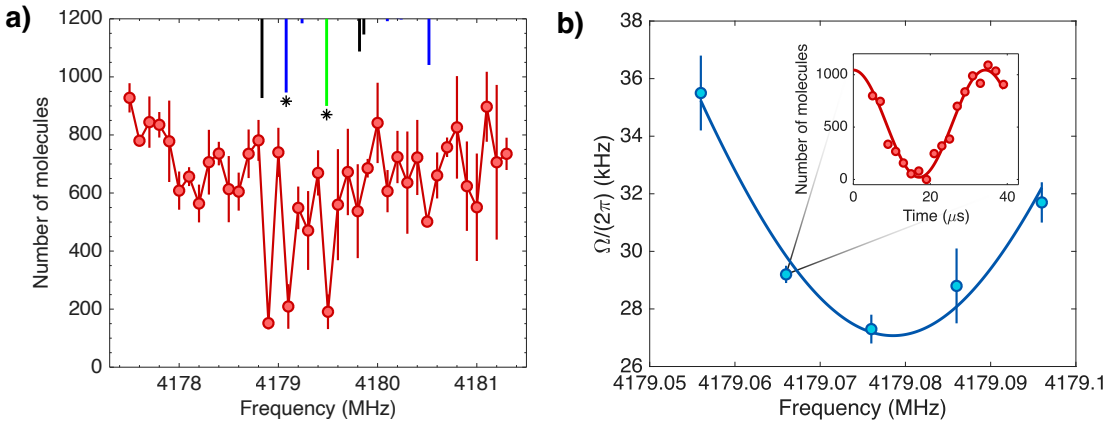


**Figure 5.36: Rotational state microwave spectroscopy. a)** We drive the $N = 0 \rightarrow 1$ rotational transition at 345.9 G with the cloverleaf antenna. The upper lines are the predicted transition frequencies based on the molecular parameters of ref. [27]. The heights are scaled by the transition dipole moment, and the colors correspond to the polarization ($\pi$ is black, $\sigma^+$ is green, and $\sigma^-$ is blue). Large loss signals are observed for the three strongest transitions. The starred transitions represent the $\sigma^+$ and $\sigma^-$ transitions used for the remainder of the Rabi frequency measurements. **b)** Measurement of the generalized Rabi frequency $\sqrt{\Omega_0^2 + \Delta^2}$ for the $\sigma^-$ transition. We extract a resonance frequency of 4179.079(1) MHz. The inset shows an example Rabi frequency measurement for the data point at 4179.066 MHz.

expected to be able to produce clean circular polarization. We therefore attempt to find the power and relative phase of the microwave signals going to these loops, which we label loops 1 and 2, that drive pure $\sigma^+$ transitions (see Fig. 5.34c). First, we drive each loop separately and measure the Rabi frequencies for the $\sigma^+$ transition. We then place fixed RF attenuators on the loop with the greater Rabi frequency (loop 2) to equalize the $\sigma^+$ component of the electric fields produced by the two loops at the location of the molecules. Next, loops 1 and 2 are driven simultaneously, with $\sigma^+$ Rabi frequency measurements performed for different relative phases $\phi$ set by a programmable phase shifter. The $\sigma^+$ Rabi frequency $\Omega_{1+2}$ as a function of the relative phase $\phi$ can be approximated as

$$\Omega_{1+2}(\phi) = \Omega_1 \sqrt{2 - 2\sin(\phi - \phi_0)}, \tag{5.28}$$

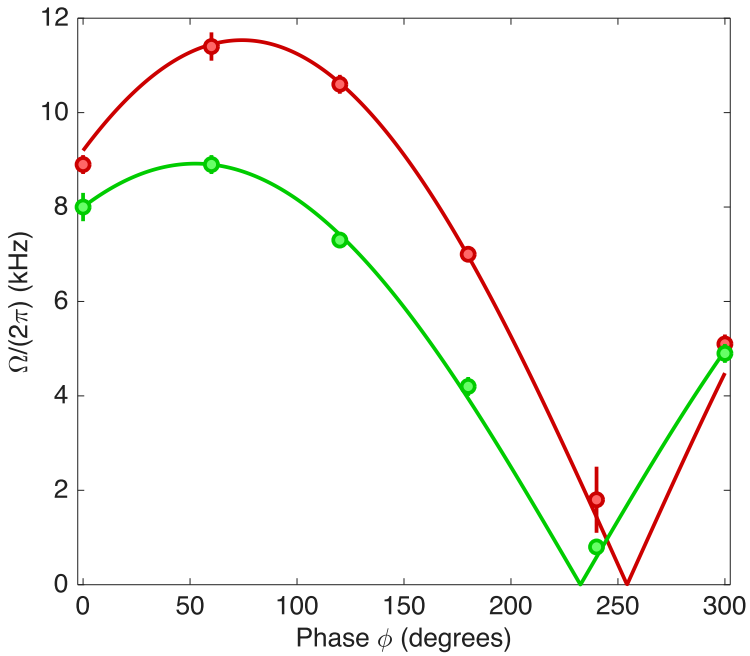


**Figure 5.37: Combined Rabi frequency of two loop antennas.** The Rabi frequency for loops 1 and 2 being driven simultaneously is plotted as a function of their relative phase shift. The phase corresponding to the maximum $\sigma^+$ Rabi frequency (red) is only 21° different from that of the maximum $\sigma^-$ Rabi frequency (green).

where $\Omega_1 = \Omega_2$ is the $\sigma^+$ Rabi frequency of an individual loop and $\phi_0$ is an offset in the relative phase. In Fig. 5.37, we fit the data to this equation with $\Omega_1$ and $\phi_0$ as fitting parameters. The $\sigma^+$ Rabi frequency has a maximum at $\phi_{\max,\sigma^+} = 74(3)°$. One would expect that this relative phase corresponds to a minimum, or at least is close to the minimum, of the orthogonal $\sigma^-$ Rabi frequency. However, when we repeat this procedure driving the $\sigma^-$ transition, we find that the $\sigma^-$ Rabi frequency of loops 1 and 2 is maximized at $\phi_{\max,\sigma^-} = 53(2)°$, only 21° different from $\phi_{\max,\sigma^+}$. Measurements on loops 3 and 4 similarly showed poor antenna performance.

EM simulations in Ansys HFSS revealed the likely explanation for why the electric fields produced by the loop antennas were so far from the ideal. The eight electrodes in our science chamber attenuate the component of the microwave electric field parallel to the rods by more than a factor of 10 at 4.2 GHz. This has the effect of "cleaning

up" the polarization of loops 2 and 3 in Fig. 5.34c, enabling large amplitude linear electric fields perpendicular to the rods at modest microwave powers. The parallel component of the electric field from loops 1 and 4, on the other hand, is strongly attenuated, accentuating any imperfections in the electric field polarization produced by the loops. We initially did not expect the electrodes to pose a significant problem as the Munich NaK experiment has successfully implemented microwave shielding in conjunction with four in-vacuum electrode rods [260]. The difference in our setup as compared to theirs is likely twofold. First, we use a longer wavelength to address the $N = 0 \rightarrow 1$ NaRb rotational transition, operating at 4.2 GHz ($\lambda = 71$ mm) versus 5.6 GHz ($\lambda = 54$ mm) for NaK. In addition, our rods are spaced closer together. The NaK experiment has a horizontal rod spacing of $d = 28$ mm [247], while in our apparatus the bottom two rods are separated by $d = 10$ mm. Moreover, the pair of rods on the lower left and the pair on the lower right of Fig. 5.1 have a separation of only $d = 5$ mm.

This situation of radiation incident on parallel rods with separation $d \ll \lambda$ is reminiscent of a wire-grid linear polarizer. It can be shown that the fractional electric field strength of normally incident radiation transmitted through a wire-grid polarizer with polarization parallel to the wires is [263]:

$$t \equiv \frac{|E_{\text{trans}}|}{|E_{\text{inc}}|} = \frac{|Ckd|}{\sqrt{1 + C^2k^2d^2}}, \tag{5.29}$$

where

$$C = \frac{1}{\pi} \ln\left(\frac{2\pi a}{d}\right). \tag{5.30}$$

Here, $d$ is the wire spacing, $a$ is the wire radius, and $k = 2\pi/\lambda$. The dependence of $t$ on frequency and wire spacing can be seen in Fig. 5.38. For a fixed wire spacing $d = 10$ mm and wire radius $a = 0.75$ mm, the plot reveals that $t$ is approximately linear for frequencies through 10 GHz. If we instead fix the frequency to 4.2 GHz and vary

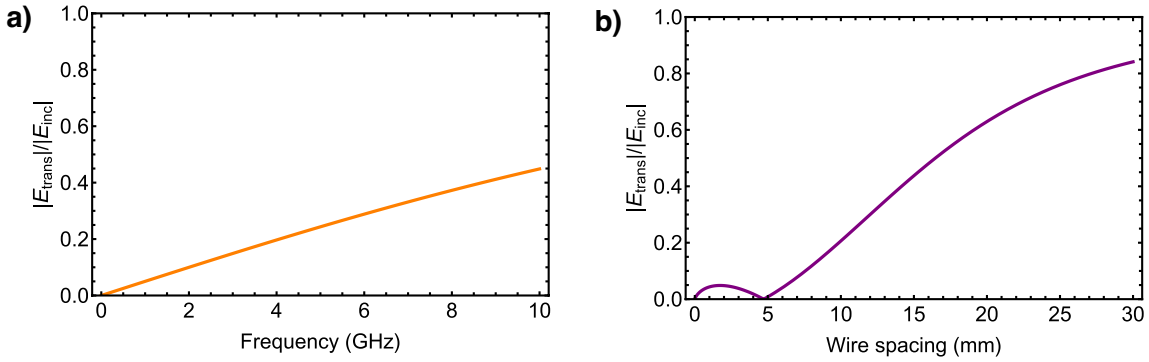


**Figure 5.38: Electric field transmission through a wire-grid polarizer.** Fraction of electric field strength transmitted for normally incident radiation on a wire-grid polarizer with polarization parallel to the wires. **a)** Shows $t = |E_{\text{trans}}|/|E_{\text{inc}}|$ as a function of frequency for fixed wire spacing $d = 10\,\text{mm}$ and wire radius $a = 0.75\,\text{mm}$. **b)** Shows $t$ as a function of wire spacing for fixed frequency $f = 4.2\,\text{GHz}$ and wire radius $a = 0.75\,\text{mm}$.

$d$, then we see that the polarizer almost completely blocks the transmitted electric field at a wire spacing of 5 mm, following which the transmission fraction quickly rises to greater than $t = 0.5$ by $d = 17\,\text{mm}$. For our apparatus (using $d = 10\,\text{mm}$ and $f = 4.2\,\text{GHz}$), the electric field transmission for electric fields polarized parallel to the rods is $t = 0.2$. By contrast, in the NaK setup with $a = 1\,\text{mm}$, $d = 28\,\text{mm}$, and $f = 5.6\,\text{GHz}$ the transmission is $t = 0.8$ (although $d \ll \lambda$ begins to break down for these parameters). We emphasize that this is simply a qualitative picture for intuition on why our electrodes strongly attenuate one of the microwave polarizations; the rods do not form an extended periodic array in a single plane and the radiation is not at normal incidence. Quantitative simulations can be performed using Ansys HFSS. However, it does show that seemingly small changes in the electrode geometry and frequency can have a significant impact on the electric field strength at the molecules (note that a factor of 16 increase in microwave power is required to compensate a factor of four reduction in electric field transmission).

To experimentally verify the attenuation of the parallel component of the microwave electric field as well as to aid the design of future antennas, we created a test

setup following ref. [260] to directly measure the antenna electric field without the use of molecules. 3D printed versions of our electrode holders together with stainless steel rods identical to those in the vacuum chamber were used to replicate our in-vacuum electrode geometry (Fig. 5.39a). The cloverleaf antenna was placed below the rods at the same relative position as when it is installed outside the bottom bucket window of our science chamber. To measure the electric field, we use a compact dipole probe antenna modeled on refs. [260, 264] (Fig. 5.39b). The dipole arms consist of two PCB traces with an end-to-end length of 14 mm ($\lambda/5$) and a width of 0.8 mm, designed to fit within the octagon formed by the eight electrode rods. An RF Schottky diode (Infineon BAT15-03W) rectifies the signal, which is then low-pass filtered ($f_c = 1.7$ kHz) using two 47 kΩ resistors and a 1 nF capacitor (Fig. 5.39c). Two carbon traces painted onto the PCB (MG Chemicals 838AR-P) connect the signal after the low-pass filter to an SMA connector ∼200 mm away. The high resistivity of the carbon traces (end-to-end resistance of each trace is ∼100 kΩ) reduces unwanted electric field pickup in this portion of the probe PCB. The PCB is placed in a rotation mount so that we can easily record the electric field strength along axes both perpendicular to and parallel to the rods. The output voltage is measured using a Keysight 34465A multimeter. We found that fluctuations in the voltage could be greatly reduced by surrounding the setup with RF absorbing foam (The EMC Shop PU-RAM-P200) as was used in ref. [260]. To relate the measured voltage to an electric field strength, we perform a calibration using a well-behaved microwave source, namely a horn antenna (Fairview Microwave FMWAN187-10SF). The voltage from the probe antenna is recorded at several different distances from the aperture of the horn antenna and compared to Ansys HFSS simulations of the horn antenna's electric field to obtain a voltage to electric field conversion.

After calibrating the probe antenna, we could use it to measure the electric field produced by the cloverleaf antenna in our test setup. We first measured the electric

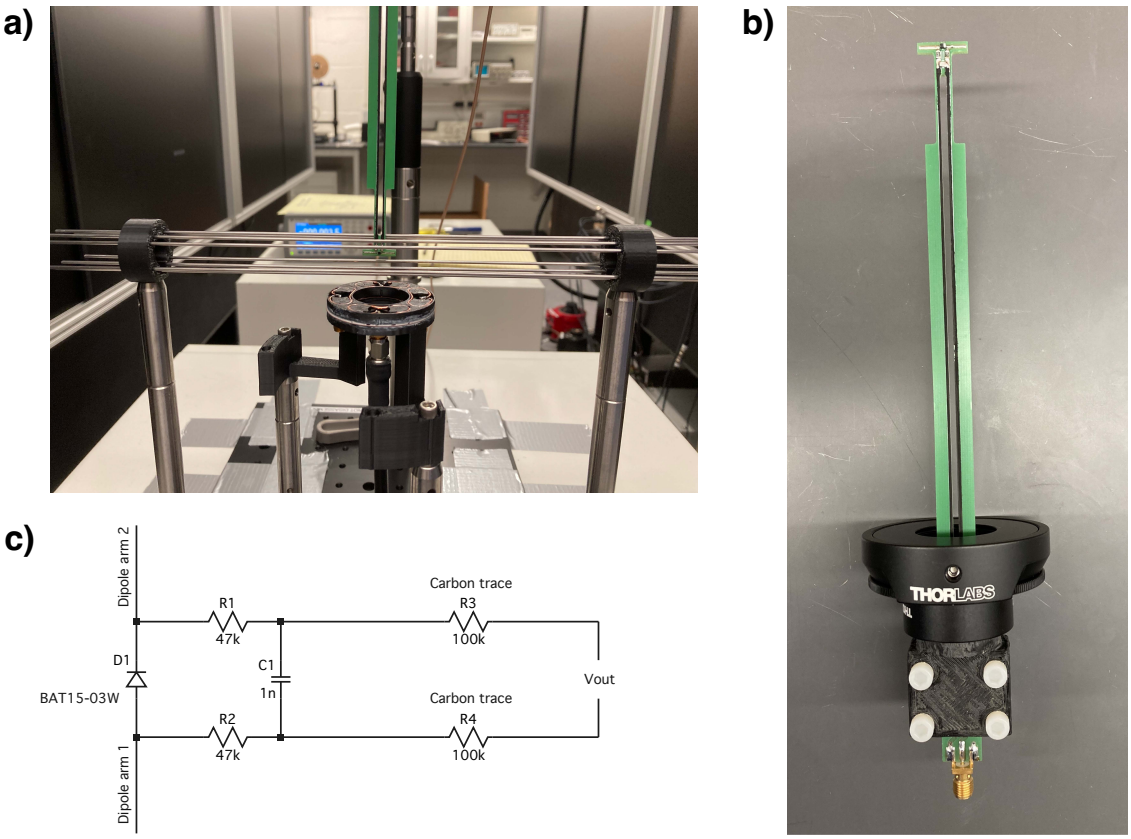


**Figure 5.39: Dipole probe antenna. a)** Test setup to measure the antenna electric field using a dipole probe antenna. **b)** Top view of the dipole probe antenna, showing the 200 mm carbon traces. **c)** Circuit diagram of the probe antenna.

field components of the four loops (driven one at a time) in the absence of the electrode rods. The electric fields were normalized to the accepted power of each loop, which was calculated based on the measured $S_{11}$ parameter. We found that the four loops produced similar electric fields along their dominant axis, with the field strengths all being within 5% of the mean. We then repeated these measurements with the electrode rods in place. For loops 2 and 3 (which ideally produce an electric field perpendicular to the rods), we did not observe significant attenuation of the electric field. In fact, the field strength of loop 3 was enhanced by 20%. However, the component of the electric field parallel to the rods was attenuated by a factor of 12 for loop 1 and by a factor of 19 for loop 4, confirming that the electrode rods were

severely limiting our ability to produce electric fields along this axis. Moreover, the electric field component perpendicular to the rods produced by loops 1 and 4 was found to be similar in strength to the parallel component, which helps explain the unexpected behavior of Fig. 5.37.

We decided following these results to switch from our current antenna construction with copper wires to a PCB-based cloverleaf antenna. This had several benefits. First, the geometry of the loops could be more precisely modeled in our EM simulations, enabling improved optimization of the electric field strengths at the location of the molecules. In addition, we hoped that this would reduce asymmetries in the loop performance, such as the disparity between the parallel field strengths of loops 1 and 4 measured in our test setup in the presence of the electrodes. The PCB cloverleaf antenna would also have the advantage of being easier to assemble, avoiding hand-winding and epoxying of the wire loop antennas. Following modeling in Ansys HFSS, our redesigned PCB antenna is shown in Fig. 5.40. Each loop is rectangular with length $\ell = 20.7\,\text{mm}$ and width $w = 5.1\,\text{mm}$ for loops 1 and 4 and $\ell = 27.5\,\text{mm}$, $w = 3.6\,\text{mm}$ for loops 2 and 3. The emphasis of our optimization was on maximizing the electric field parallel to the rods produced by loops 1 and 4, which led to the different dimensions for those loops as compared to those of loops 2 and 3. The trace width for all loops is 0.5 mm. The PCB substrate is 1.52 mm thickness Rogers 4350, chosen for its low loss tangent and well-characterized dielectric constant at high frequencies. We again make use of a copper reflector below the antennas, this time consisting of a separate PCB with a copper pour. The reflector is separated from the loops by 4 mm, with that distance maintained by PTFE washers around the four SMA connectors. The assembly is mounted on a PA 12 3D-printed structure that can be attached to the bottom of the science chamber with nylon screws. Unfortunately, with this setup we continued to have unacceptably weak microwave electric fields parallel to the rods.

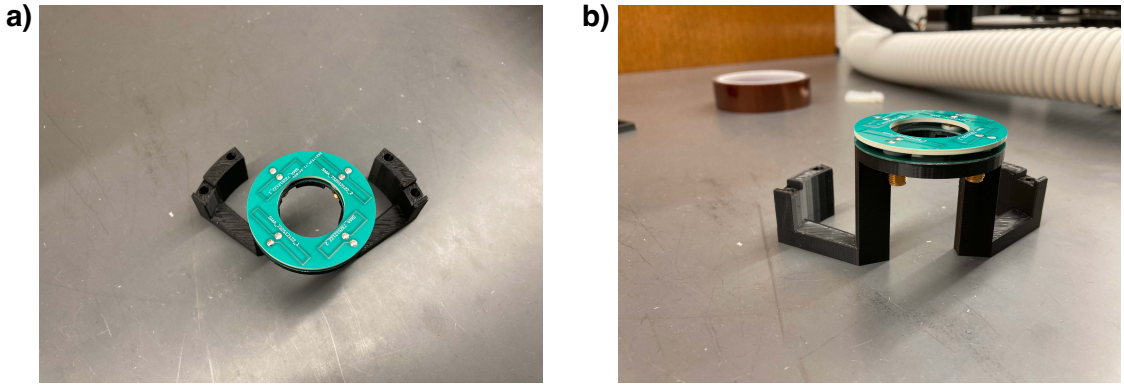


**Figure 5.40: PCB cloverleaf antenna. a)** Top view of the PCB cloverleaf antenna, showing the precise loop geometry possible with the circuit board construction. **b)** Side view of the PCB antenna, in which the edge of the copper reflector circuit board is visible beneath the main loop PCB.

Meanwhile, we looked into the design of a separate antenna for producing $\pi$ polarized microwaves required for double microwave shielding. As discussed in section 4.4, a combination of both $\pi$ and $\sigma^+$ polarizations can be used to shield molecules against both two- and three-body loss [16, 142]. We first examined whether our in-vacuum electrodes would serve as effective antennas due to their proximity to the molecules. Since at the time we had stopped using the rods to generate DC electric fields, a high voltage bias tee such as that used in ref. [230] would not be needed. We performed initial testing with just a single electrode rod, soldering the center conductor of a coaxial cable close to the vacuum feedthrough. For an input power of 100 mW and $S_{11} < -7$ dB, we measured a $\pi$ Rabi frequency of $2\pi \times 33$ kHz. Even if several electrodes were used to drive the transition, this would require kW-scale input powers to reach $\Omega = 2\pi \times 10$ MHz assuming similar performance from each rod. The rod length is much larger than the wavelength of the microwaves, so there are multiple nodes and antinodes of the electric field as a function of distance along the rod. It appears that the molecules are located close to one of the nodes. The distance from the end of each rod to the molecules was not a major consideration in the construction of the apparatus since they were primarily to be used for DC electric fields (and

indeed this distance varies slightly from rod to rod). In addition, there are likely significant losses arising from the coaxial cable-to-rod transition as we do not have coaxial vacuum feedthroughs. We also tried using an external loop antenna close to a side viewport of the science chamber (with the center of the loop coaxial with the symmetry axis of the rods), but we observed low Rabi frequencies and poor $\pi$ polarization purity with this design.

Faced with these difficulties in producing large $\sigma^+$ and $\pi$ Rabi frequencies, with the former severely affected by the attenuation of 4.2 GHz electric fields parallel to the rods, we decided to draw on our experience with Förster resonance shielding and combine it with microwaves. The idea of using both static and microwave frequency electric fields for collisional shielding of molecules, discussed in section 4.4, is not new [133,144,145]. However, the details of our scheme differ from previously proposed methods in order to address our problems achieving large Rabi frequencies at 4.2 GHz. In our approach, we propose to prepare the molecules in the $|1,0\rangle$ rotational state and work at DC electric fields above the Förster resonance of $\sim$4.2 kV/cm where we have previously demonstrated shielding against two-body loss. To eliminate the bound state in the intermolecular potential, we will also address the molecules with $\sigma^+$ microwaves on the $N = 1 \rightarrow 2$ transition. Since the circularly polarized microwaves induce a rotating dipole moment orthogonal to that of the static electric field, the combination can reduce or eliminate the dipolar attraction between two colliding molecules and therefore decrease the depth of the potential well until it can no longer support a bound state [144]. The benefit for our experiment of this approach as compared to double microwave shielding is that the microwave frequency to address the $N = 1 \rightarrow 2$ transition at the shielding electric field is much higher at $\sim$7.5 GHz. We have seen from our simplified model of the electrode rods as a wire-grid linear polarizer that the transmission of the electric field component parallel to the rods increases for higher frequencies. Simulations in Ansys HFSS suggest that we should

be able to achieve electric fields approximately three times higher than before along the rod direction. This outweighs the slight decrease in transition dipole moment from from $d/\sqrt{3}$ to $d/\sqrt{5}$ for the $|1,0\rangle \rightarrow |2,1\rangle$ transition, and should enable us to reach $2\pi \times 10\,\mathrm{MHz}$ Rabi frequencies at microwave powers of $< 20\,\mathrm{W}$ per each of the two parallel polarization loops (as before, the loops producing electric fields perpendicular to the rods require substantially lower powers to achieve the same Rabi frequency). Preliminary simulations performed by graduate student Jongheum Jung indicate that an elastic-to-inelastic collision ratio greater than $10^3$ should be achievable, and work is ongoing on the design and implementation of this scheme.

## 5.4 Bulk association

In addition to implementing the combined microwave and Förster resonance shielding, efforts are currently underway to switch from lattice-based formation of molecules to a bulk association approach. As we saw by the end of section 5.2, our 3D Mott insulator scheme involved a complex sequence requiring the careful alignment of many different optical potentials. Nevertheless, the conversion efficiency of atoms into molecules was comparable to what has been achieved in bosonic molecule experiments by simply ramping the magnetic field through the interspecies Feshbach resonance with the atoms held in a bulk harmonic trap. In the interest of simplicity and reliable day-to-day operation of the experiment, we are therefore adopting this more conventional approach.

We had briefly attempted bulk association of atoms into molecules in 2023 prior to adopting the 3D Mott insulator approach. One of the first issues that we had to face was the difference of timescales between bulk and lattice methods. Previously, atom-molecule and molecule-molecule collisions did not occur in the deep lattice used during the formation of molecules, so the molecular lifetime was only limited by one-body

loss due to off-resonant scattering from the lattice light. As we have seen, depending on the intensity of the lattice light the lifetime of both Feshbach and ground state molecules could be on the second-scale. By contrast, Feshbach molecules formed in a bulk trap are rapidly lost due to collisions with atoms and other molecules. Ground state molecules suffer a similarly short lifetime in the presence of unassociated atoms, although molecule-molecule collisions can be suppressed through shielding mechanisms. Two changes to the apparatus were therefore required. First, we needed to perform STIRAP as soon as possible after the Feshbach association, and second, we needed to rapidly remove the residual atoms once ground state molecules were formed.

In prior work, the magnetic field ramped down to 335 G over several milliseconds following magnetoassociation and stayed at that value for tens of milliseconds as we performed a slow series of Landau-Zener sweeps and resonant light pulses to remove unassociated atoms. The magnetic field had consequently completely settled at 335 G by the time we applied STIRAP pulses to transfer the Feshbach molecules to their ground state. Continuing to use the lattice association method for initial testing, we first examined how the STIRAP efficiency was affected by applying the STIRAP pulses at 346.9 G (0.75 G below the Feshbach resonance) with a minimal amount of hold time at this field. Specifically, we ramped the magnetic field across the Feshbach resonance at a rate of $-2.2$ G/ms following ref. [265] and performed STIRAP immediately after the magnetic field setpoint reached 346.9 G. When we tried this sequence, however, no ground state molecules were produced. We soon realized that the magnetic field had not yet settled by the time of the STIRAP transfer to the ground state but that it had settled for the reverse STIRAP used for detection. Since the forward and reverse STIRAP transfers had the same up leg and down leg frequencies but occurred at different magnetic fields, at most one of the STIRAP pulse sequences could be on-resonance. By adding a hold time before the first STIRAP

transfer for the magnetic field to settle and varying its duration, we determined that $\sim$5 ms of settling time were needed to recover full STIRAP efficiency.

We suspected that the long settling time of the magnetic field was due to eddy currents induced in the metal science chamber. To solve this issue, we tried to implement a feedforward technique initially developed in ref. [266] to enable fast changes in the magnetic field in the presence of eddy currents, which was also later successfully used by ref. [267]. Briefly, we consider flowing a current $I_1$ through the magnetic field coils, which couples to an effective eddy current circuit through the mutual inductance $M_{12}$ producing an eddy current $I_2$. The eddy current circuit has resistance $R_2$ and inductance $L_2$ with RL time constant $\tau = L_2/R_2$. For magnetic fields $B_1 = C_1 I_1$ and $B_2 = C_2 I_2$ with proportionality constants $C_1$ and $C_2$, and taking positive $B_1$ and $B_2$ to point in the same direction, it can be shown that [266]:

$$\frac{dB_2}{dt} = -\frac{1}{\tau}B_2 - \eta\frac{dB_1}{dt}, \tag{5.31}$$

where $\eta = \frac{C_2 M_{12}}{C_1 L_2}$. To find $\eta$ and $\tau$ for our system, we perform a linear ramp of the magnetic field $B_1$ from $B_1(t_0)$ at time $t_0$ to $B_1(t_1)$ at time $t_1$. If the magnetic field has been constant prior to $t = t_0$, then the eddy current $B_2(t_0) = 0$ and from equation 5.31 we have:

$$B_2(t_1) = \eta\tau\frac{B_1(t_1) - B_1(t_0)}{t_1 - t_0}\left(e^{-(t_1 - t_0)/\tau} - 1\right). \tag{5.32}$$

After $t = t_1$, we keep the magnetic field $B_1$ fixed such that $dB_1/dt = 0$. At time $t > t_1$,

$$B_2(t) = B_2(t_1)e^{-(t - t_1)/\tau}. \tag{5.33}$$

The total magnetic field $B_{\text{tot}}$ that the molecules experience is the sum of the magnetic field from the coils and the magnetic field from the eddy current. Since $B_1$ is constant

for $t > t_1$, we can perform spectroscopy on the molecules for different times following the coil magnetic field ramp and fit the measured values of $B_{\text{tot}}$ to

$$B_{\text{tot}}(t) = B_2(t_1)e^{-(t-t_1)/\tau} + B_1(t_1) \tag{5.34}$$

to determine $B_2(t_1)$ and $\tau$. With knowledge of the magnetic field ramp parameters $t_0, t_1, B_1(t_0), B_1(t_1)$, we can then use equation 5.32 to find $\eta$.

Fig. 5.41a presents the results of this measurement. The magnetic field was linearly ramped down by $\Delta B_1 = -4.4\,\text{G}$ over 2.24 ms and was then kept constant starting at $t = 0$. The data points were obtained by recording the down leg frequency at the STIRAP two-photon resonance for a given hold time after the magnetic field ramp.* The down leg frequencies could then be compared to a separate measurement of the resonant down leg frequency versus magnetic field in which the magnetic field was allowed to stabilize in order to determine the total magnetic field at each of the hold times. From the fit, we extract $\tau = 0.98\,\text{ms}$ and $\eta = 0.34$.

By substituting $\eta$ and $\tau$ into equation 5.31, we can now predict the eddy current response to an arbitrary coil magnetic field ramp. Ref. [266] demonstrated that this allows one to feed forward on the coil magnetic field to compensate for the eddy current, producing the desired waveform for the total magnetic field. At the time, our plan was to ramp the magnetic field at $-2.2\,\text{G/ms}$ from 350 G to 347.4 G to cross the Feshbach resonance and then quickly ramp the field in 100 $\mu$s to 346 G to increase the closed channel fraction of the Feshbach molecules for STIRAP. Fig. 5.41b shows a numerical simulation of how the total magnetic field would respond to this waveform, illustrating the damping effect of the eddy current. We can then perform a simulation in Fig. 5.41c using feedforward on the main coil magnetic field to generate the target piecewise ramp of the total field. In reality, the current in our main coils has a finite

*An additional 400 ms hold time was included in the sequence following the STIRAP transfer to the ground state so that a different down leg frequency could be programmed for the reverse STIRAP sequence, which occurred at a stabilized magnetic field.

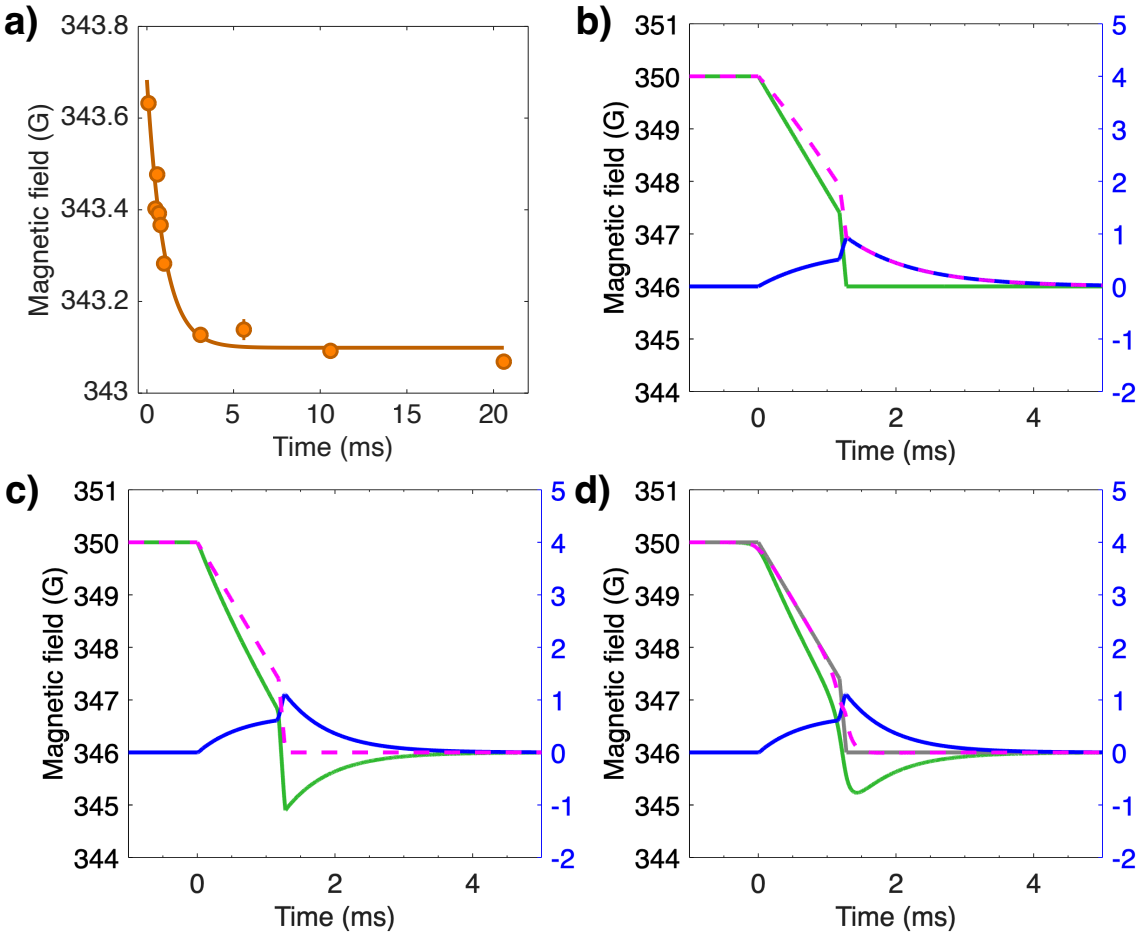


**Figure 5.41: Magnetic field feedforward. a)** Total magnetic field (including the eddy field) following a linear ramp of the coil current, as determined by measuring the STIRAP two-photon resonance. From the fit we can determine the values of $\eta$ and $\tau$ in equation 5.31. **b)** Numerical simulation of the effect of eddy fields on the total magnetic field at the center of the science chamber. The presence of an eddy field (solid blue line, with its magnetic field in Gauss shown on the right y-axis) slows down the response of the total field (dashed magenta line) to a fast coil magnetic field ramp (solid green line). **c)** By using feedforward as described in the main text, the coil magnetic field can be programmed to compensate for the effect of the eddy current, producing the desired ramp of the total magnetic field. **d)** Our magnetic field coils have a finite 1.8 kHz bandwidth, which limits how well we can follow the feedforward waveform of **c)**. Here, we simulate programming the feedforward waveform, which is distorted by the low-pass effect of the coil bandwidth. We see that the total field no longer exactly follows the target magnetic field ramp (gray solid line).

bandwidth of 1.8 kHz which limits how well we can compensate the eddy current. If we were to program the main coil field to follow the waveform in Fig. 5.41c, this low-pass filter effect would result in the total magnetic field of Fig. 5.41d, which no longer exactly matches the target magnetic field ramp. Nevertheless, the magnetic field settles considerably faster than without the use of feedforward.

While this method would have likely been successful in allowing us to shorten the duration between magnetoassociation and STIRAP, we decided for simplicity to use a compromise solution in our initial attempt at bulk association. Namely, we performed the first STIRAP transfer on a magnetic field slope, following which we could quickly remove unassociated atoms using the all-optical protocol to be described next. With the atoms removed, the molecule lifetime is longer [204] so we are able to ramp the magnetic field to a new value prior to the reverse STIRAP pulse sequence. This value is empirically tuned until the reverse STIRAP is on resonance, indicating that we have matched the magnetic field of the first STIRAP pulse sequence.

The all-optical removal of unassociated atoms alluded to above is a dramatic improvement on our earlier removal protocol. Previously, for each species we first performed a Landau-Zener sweep to transfer the atoms from $F = 1$ to $F = 2$. Once they were in the $F = 2$ state, we could apply resonant light to eject the atoms from the trap. Due to the poor Rabi frequencies of our atomic spin flips, the Landau-Zener sweeps took up to 10 ms each and needed to be repeated multiple times to achieve high efficiency removal. In total, the process could take 60 ms. In the lattice-based association approach, we had the luxury of long molecular lifetimes so improving the rate of unassociated atom removal was not a priority. However, this was not usable for bulk association as all of the molecules would be lost long before the atoms were removed.

Motivated by ref. [268], we replaced the Landau-Zener sweeps by an optical removal beam that pumps the atoms into the $F = 2$ state. This is only possible once

the molecules have been transferred to their ground state, as the weakly-bound Feshbach molecules are ejected from the trap by light addressing $F = 1$. For both Na and Rb at 346 G, this beam primarily addresses the $|J = \frac{1}{2}, m_J = -\frac{1}{2}, I = \frac{3}{2}, m_I = \frac{3}{2}\rangle \rightarrow |\frac{3}{2}, -\frac{1}{2}, \frac{3}{2}, \frac{3}{2}\rangle$ transition between the $S_{\frac{1}{2}}$ and $P_{\frac{3}{2}}$ manifolds, although in the case of Rb it is $> 100$ MHz detuned. We combine this beam with the light addressing the high field $F = 2 \rightarrow F' = 3$ transition discussed in section 5.2.3 and see complete removal of Na and Rb from a bulk trap in less than 150 $\mu$s.

We modeled our bulk association sequence on that of ref. [204]. Namely, we performed an optical evaporation of the atoms at 364 G in the XODT where the two species are miscible. At the end of the evaporation, we had $2 \times 10^5$ Na atoms and $1 \times 10^5$ Rb atoms at $\sim$700 nK. The magnetic field was then quickly ramped to 350 G, followed by a 5 ms hold time. The XODT trap frequency during these steps was $\omega_{\mathrm{Na}} = 2\pi \times (127, 117, 173)$ Hz, with $\omega_{\mathrm{Rb}} = 0.88\omega_{\mathrm{Na}}$. The magnetic field was then ramped through the Feshbach resonance at a rate of $-2.2$ G/ms, followed by STIRAP at 346 G and all-optical removal of unassociated atoms. With this protocol, we measured approximately $10^3$ ground state molecules at a low peak density of $n_0 = 9 \times 10^9\,\mathrm{cm}^{-3}$.

When we tried this in 2023, we were having technical issues with the apparatus preventing us from reliably producing cold, dense atomic clouds with large atom numbers. This is partly why we went back to our lattice-based approach, with which we could produce higher molecular densities for the same initial atomic parameters. Nevertheless, it was useful in pointing to two areas of improvement for future attempts at bulk association. First, our Na optical molasses is mostly ineffective, which limits the starting phase-space density for evaporation in the magnetic quadrupole trap (this also affects the post-evaporation phase-space density of the Rb atoms since the Rb is sympathetically cooled by the Na). In our apparatus, the optical molasses (and the MOT) consists of three retroreflected beams. A working optical molasses

requires that the beams from all directions have balanced intensities, so we attempt to compensate for the retroreflection beams' lower powers by slightly focusing them on the atoms (there are losses both from the light passing through the atomic cloud as well as from the retroreflection optics). This alignment is difficult in practice and the optimal conditions can change depending on the atomic numbers and densities, leading to our struggles in implementing an effective optical molasses. In the future, by switching to a 5-beam rather than 3-beam MOT and optical molasses configuration (the vertical beam would remain retroreflected) we should have significantly higher initial phase-space densities for evaporation in the quadrupole trap.

An important parameter for evaporative cooling is the collision rate of the atoms, which dictates how fast they can rethermalize as the most energetic atoms are removed from the trap [269]. The elastic collision rate at the center of the trap is given by $\Gamma_{\text{el}} = n_0 \sigma \bar{v}$ where $n_0$ is the peak density, $\sigma = 8\pi a^2$ is the collisional cross-section (for bosons) with $a$ being the s-wave scattering length, and $\bar{v} = 4\sqrt{k_B T/(m\pi)}$ is the average relative velocity between two atoms of mass $m$ and temperature $T$ [270, 271]. Over the whole cloud in a quadrupole trap, the average collision rate is $\bar{\Gamma}_{\text{el}} = \Gamma_{\text{el}}/8$. For the quadrupole field $\mathbf{B} = (-\frac{B'_z}{2}x, -\frac{B'_z}{2}y, B'_z z)$ and ignoring the small effect of gravity, the average collision rate is

$$\bar{\Gamma}_{\text{el}} = \frac{N a^2 (\mu_B g_F m_F B'_z)^3}{8\sqrt{m\pi}(k_B T)^{5/2}}. \tag{5.35}$$

Here, $N$ is the total number of atoms, $\mu_B$ is the Bohr magneton, and $g_F = -1/2$ for Na in the low field-seeking state $|F, m_F\rangle = |1, -1\rangle$. From this equation, we see that the collision rate is proportional to $T^{-5/2}$, so achieving lower temperatures through an effective optical molasses would also improve the initial collision rate in the quadrupole trap.

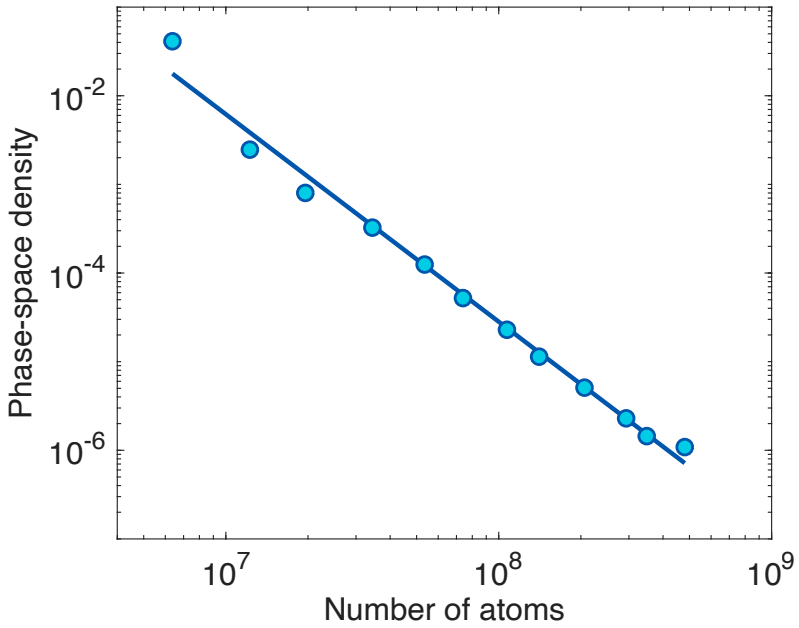


**Figure 5.42: Na evaporation in the quadrupole trap.** Phase-space density versus Na atom number during the 20 s evaporation in the quadrupole trap. The evaporation efficiency is $-d\ln(\mathrm{PSD})/d\ln(N) = 2.3$.

Another way of boosting the collision rate is by adiabatically increasing the gradient of the quadrupole trap, which is the second area that we have identified for improving bulk association in our apparatus. The temperature in equation 5.35 is itself a function of the gradient. Since the peak density $n_0 \propto (B'_z/T)^3$, the constant phase-space density condition for an adiabatic compression implies that $T \propto (B'_z)^{2/3}$. Therefore, the collision rate scales as $(B'_z)^{4/3}$ for an adiabatic change in the magnetic field gradient.

Currently, we use a fixed magnetic field gradient of 186.4 G/cm both for catching the atoms in the quadrupole trap and for the subsequent RF knife evaporation. Typical Na parameters in the quadrupole trap prior to evaporation are $4 \times 10^8$ atoms at 150 $\mu$K to 250 $\mu$K (the quality of the atomic MOTs and their alignment to the quadrupole trap tend to drift over time leading to this range of temperatures). These values correspond to an average Na collision rate $\bar{\Gamma}_{\mathrm{el}}$ of 1 Hz to 4 Hz. The slow initial collision rate leads to a long 20 s evaporation in the quadrupole trap, a significant

fraction of the 30 s Na vacuum lifetime*. The phase-space density (PSD) of the Na atoms as a function of atom number during the 20 s evaporation is shown in Fig. 5.42, with an evaporation efficiency of $-d\ln(\mathrm{PSD})/d\ln(N) = 2.3$. In order to boost the initial collision rate and speed up the evaporation relative to the vacuum lifetime, we plan to perform an adiabatic compression of the magnetic field gradient. We were previously using the maximum 220 A current that our power supply (Delta Elektronika SM18-220, high speed programming option) could source for the quadrupole trap, so we have recently acquired a larger power supply (Delta Elektronika SM70-CP-450) with a maximum current of 450 A (details on our magnetic field control system can be found in appendix A). If we adiabatically double the magnetic field gradient from its current value to 372.8 G/cm, then the collision rate at the start of the evaporation will increase by a factor of $2^{4/3}$ to between 3 Hz and 10 Hz. Together with an improved Na optical molasses, we anticipate producing degenerate or near-degenerate† gases of Na and Rb with larger atom numbers than before, providing an excellent starting condition for bulk association into molecules.

*After using by one count four different helium leak checkers during the construction of our apparatus to fix issues with the vacuum chamber, we were quite happy to achieve this somewhat limited lifetime.

†Several groups have found that better molecule production can be obtained by stopping the atomic evaporation for one or both species just prior to condensation. See, for example, refs. [204, 272].

# Chapter 6

# Conclusion

Over the past seven years in which the work of this thesis has taken place, the field of ultracold molecules has seen remarkable progress. For example, optical tweezer arrays of diatomic [41] and polyatomic [43] ultracold molecules have been created, dipolar spin-exchange has been observed in tweezer [13, 64–66] and lattice [35, 67] experiments, rotational coherence times have been pushed out to the second scale [13], collisional shielding has been demonstrated [132,136,138,140,141,150,151], degenerate quantum gases of fermionic [14, 15] and bosonic [16] molecules have been produced, and, as described in this thesis, a quantum gas microscope of polar molecules has been realized [35]. Nevertheless, many outstanding goals remain, among them the achievement of a high filling fraction lattice of polar molecules. With the recent demonstration of a BEC of polar molecules in the Will group [16], this is poised to change in the coming years, and our development of a molecular quantum gas microscope is ideally suited to probe the many-body dynamics of these high filling systems.

One of the most exciting prospects is the formation of dipolar spin liquids of polar molecules [273]. Quantum spin liquids are highly entangled states lacking spin order down to zero temperature due to the presence of magnetic frustration [274,275].

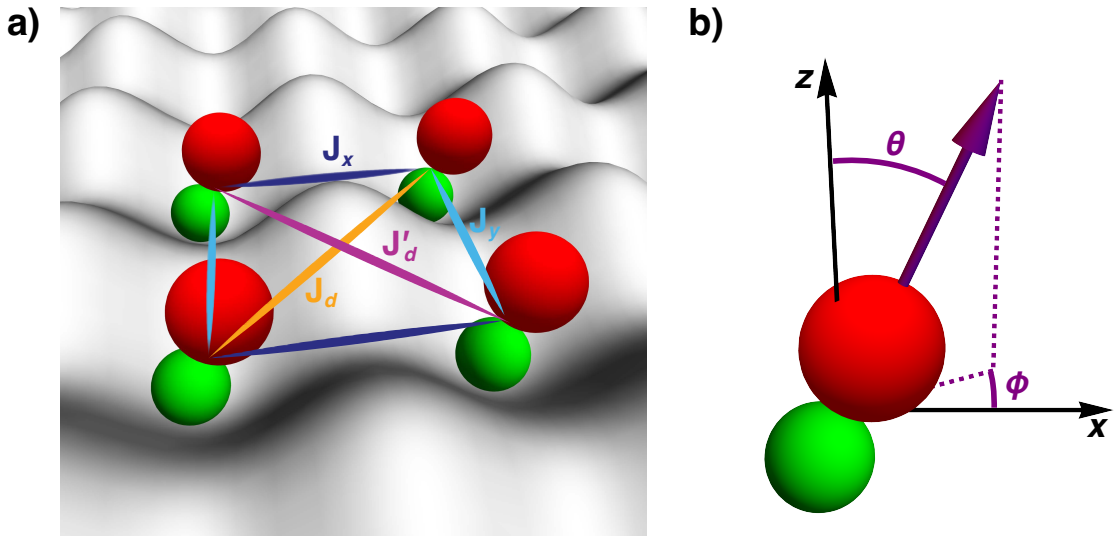


**Figure 6.1: Dipolar frustration.** **a)** For certain quantization axes (as defined in **b)**) there is competition between the dipolar couplings $J_x, J_y, J_d, J'_d$ on a square plaquette. Adapted from ref. [276].

Intriguingly, rather than relying on the geometric frustration of kagome and triangular lattices, it has been proposed that the anisotropic interactions of polar molecules can be used to engineer frustration on a square lattice [276]. We can understand the source of this magnetic frustration by considering the interactions on a single square plaquette under a dipolar $XXZ$ Hamiltonian. In this case, there are four possible dipolar couplings characterized by $J_x, J_y, J_d, J'_d$ as shown in Fig. 6.1. The relative strength and sign of these terms can be varied by rotating the quantization axis of the molecules. For certain angles, the couplings are all antiferromagnetic and similar in strength, thereby realizing competition between the spin-exchange interactions.

Since the experimental observation of quantum spin liquids can be challenging in practice [277], other advances in the study of dipolar many-body systems with ultracold molecules may be easier to achieve in the short-term. The dipolar $XXZ$ model was proposed in ref. [278] to realize spin squeezing. This has recently been confirmed in Rydberg [85] and magnetic atom [279] platforms using dipolar $XY$ Hamiltonians, but the generation of spin squeezing has yet to be demonstrated with

polar molecules. In addition, by allowing the molecules to tunnel in a lattice, an extended Bose-Hubbard model can be engineered [69]. Site-resolved measurements, such as those demonstrated in this thesis, may then reveal the presence of fractional Mott insulators as have been observed with magnetic atoms [101]. The creation of high filling lattices of polar molecules will also allow the exploration of equilibrium phases of the dipolar $t$-$J$ model [61]. Moreover, itinerant dynamics can be realized without physical lattice tunneling by using the rotational structure of molecules as a synthetic dimension, opening the door to studying lattice physics with polar molecules in optical tweezer arrays [10, 280].

It therefore appears that the past twenty years of effort to gain control over the structure of ultracold molecules are now paying rich dividends, and the next five years, let alone twenty, are bound to contain many more landmark achievements in the use of molecules to probe the physics of dipolar systems.

# Appendix A

# Magnetic field control system

## A.1 Main coils for the quadrupole trap and Feshbach fields

We use one pair of coils to generate both uniform magnetic fields along the vertical direction of up to 560 G (the "Feshbach configuration") and magnetic field gradients of up to 190 G/cm (the "quadrupole configuration") for our maximum drive current of 220 A. Each coil in the pair consists of water-cooled hollow copper wire (3.18 mm $\times$ 3.18 mm) wound in two layers with five turns per layer. Details on the construction and geometry of these coils can be found in ref. [112]. Here, we focus on the control electronics used to drive current through the coils.

We use a Delta Elektronika SM18-220 power supply (with the high speed programming option) as our current source. To switch between uniform fields and quadrupole fields using the same pair of coils (as well as to switch the current on and off), we rely on an H-bridge topology, shown in Fig. A.1a. L1 represents the upper coil (above the science chamber) and L2 represents the lower coil (below the science chamber). Q1 through Q4 are insulated-gate bipolar transistors (IGBTs), which act as voltage-controlled switches. We use two half-bridge IGBT modules (Infineon FF600R12ME4)

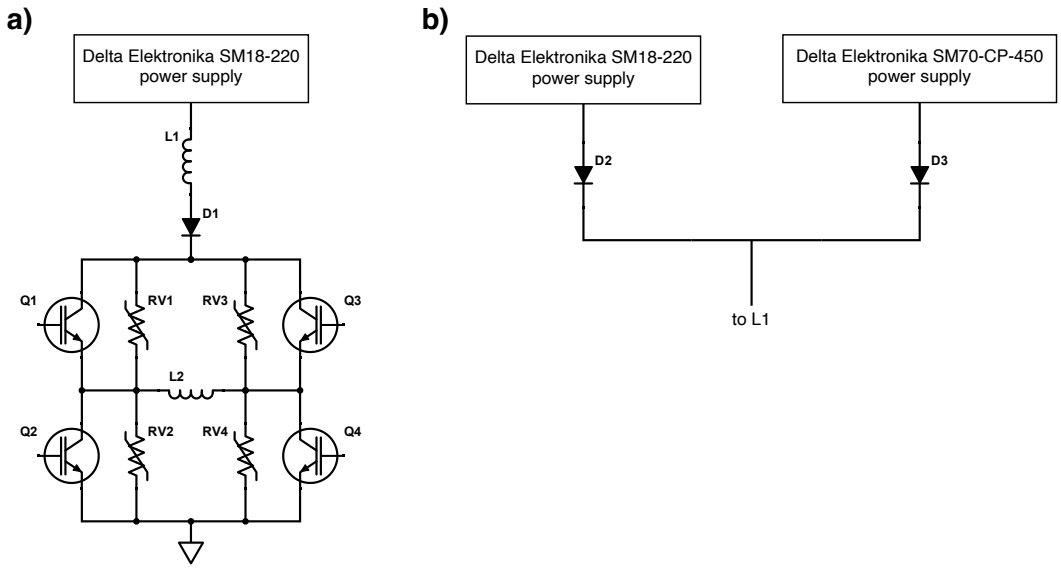


**Figure A.1: Main coil current control circuits. a)** An H-bridge circuit enables the use of one pair of coils for both Helmholtz and anti-Helmholtz configurations. L1 and L2 are the two magnetic field coils, Q1 through Q4 are IGBTs, RV1 through RV4 are varistors, and D1 is a high current diode. The gate driver circuits for the IGBTs are not shown. **b)** A two-diode circuit enables the use of the lower bandwidth but higher current Delta Elektronika SM70-CP-450 power supply for the quadrupole trap and the higher bandwidth but lower current Delta Elektronika SM18-220 power supply for the remainder of the experimental sequence.

in our implementation such that Q1 and Q2 are in one module and Q3 and Q4 are in the other module. Gate drivers (Power Integrations 2SP0115T2A0-FF600R12ME4) are used to interface between the IGBTs and digital programming signals.

By turning all of the IGBTs off, we can block current flow through the coils. If we turn Q1 and Q4 on while leaving Q2 and Q3 off, then the current through the lower coil flows from left to right in the circuit diagram. On the other hand, if we turn Q2 and Q3 on but leave Q1 and Q4 off, then current through the lower coil flows from right to left. The current through the upper coil L1 flows in the same direction in both cases. When the current flows in the same direction through both coils, we realize an approximately Helmholtz configuration and obtain nearly uniform magnetic fields at the center of the science chamber. If the current flows in opposite directions, then we

realize an approximately anti-Helmholtz configuration resulting in a magnetic field gradient. To protect against inductive voltage spikes when switching the IGBTs on and off, we employ varistors (Littelfuse V321DA40; labeled RV1 through RV4 in the circuit diagram) across each IGBT as well as the diode D1 (Vishay VS-400UR120D). This diode as well as the IGBTs are mounted on water cooling plates (Ohmite CP4A-114A-108E) to aid in heat dissipation.

We use closed-loop feedback control to stabilize and reduce noise on the magnetic fields. The output current of the power supply is measured using a fluxgate current transducer (Danisense DS200ID). This produces a proportional current in a 500:1 ratio that is passed through a 10 Ω resistor (Vishay Y169010R0000T9L) to obtain a corresponding voltage. The voltage signal is then sent (along with an analog setpoint voltage) to a PI servo, the output of which is connected to the voltage programming input of the power supply to close the feedback loop.

As discussed at the end of chapter 5, we are now using higher currents for the quadrupole trap in order to improve the initial collision rate of Na atoms. These currents are produced by a 450 A power supply (Delta Elektronika SM70-CP-450) and necessitate a few modifications to the above setup to increase the components' current handling capabilities. In particular, the diode D1 has been replaced by an Infineon DZ600N18KHPSA1, the fluxgate current transducer is a Danisense DS400ID, and the sense resistor for the fluxgate transducer's output is a 25 Ω Vishay Y169025R0000T9L resistor.

We found that the bandwidth of the new power supply is almost an order of magnitude lower than that of the 220 A power supply. Since higher bandwidths are more important for the portions of the experimental sequence involved with molecule formation close to the Feshbach resonance than for the quadrupole trap, we decided to combine both power supplies using the configuration of Fig. A.1b. Here, two additional diodes (Infineon DZ600N18KHPSA1) enable smooth changes between the

power supplies such that the 450 A power supply can be used for the quadrupole trap while the 220 A power supply can be used for the remainder of the experimental sequence. The higher bandwidth (and consequently faster rise time) 220 A power supply can also be used for the initial catch of the atoms in the magnetic trap.

## A.2 Bias coils

Throughout the experimental sequence, it is often necessary to shim the magnetic field along one or more spatial dimensions. We accomplish this using three pairs of bias coils oriented along the $x$, $y$, and $z$ axes that are capable of producing magnetic fields of $\sim$7 G at $\sim$6 A. Each coil consists of ten turns of 22 AWG copper wire wrapped around the edges of the science chamber.

Originally, the current control systems for all three pairs of bias coils were identical, and our $x$ and $y$ bias coils are still driven using the following setup. For each coil pair, an Acopian YL010MC700 power supply (10 V, 7 A) produces a current that is sent to an H-bridge circuit similar to that of Fig. A.1a for the main coils. Here, instead of switching between a Helmholtz versus anti-Helmholtz configuration, the H-bridge allows us to reverse the orientation of a uniform field without the need for a bipolar power supply. This is done by placing both coils at the location of L2 in the circuit diagram. Due to the much lower currents, we use different components for the bias coil H-bridge than for the main coil H-bridge. Q1 through Q4 are power MOSFETs (IXYS IXFN64N50P) controlled using half-bridge gate drivers (Analog Devices LT1158). The varistors (Bourns MOV-20D180KTR) and diode D1 (onsemi MBR40250G) have also been changed to lower power components. Finally, instead of a fluxgate current transducer to measure the current for closed-loop control, we use a precision current shunt (Texas Instruments INA250EVM).

At one point during our initial exploration of bulk association of atoms into molecules (see section 5.4), we desired to have higher bandwidth current control for the $z$ bias coil. Consequently, we replaced the Acopian power supply for that coil with a water-cooled high current op amp (Texas Instruments OPA549) powered by a GW Instek GPR-1820HD. The bandwidth of the current control with this setup was 3.2 kHz. In order to further increase the bandwidth, we added five 0.47 Ω resistors (TE Connectivity SQPW10R47J) in series with the coils. This decreased the RL time constant of the circuit, resulting in a bandwidth of 7.9 kHz.

# Appendix B

# Mains voltage zero-crossing detection circuit

For synchronizing the experimental sequence to the 60 Hz mains voltage, we employ the circuit shown in Fig. B.1 based on ref. [281]. This circuit produces a 3.3 V logic signal whose rising edge corresponds to the falling edge of the mains voltage. The logic signal can then be used to trigger our experimental control software (Cicero Word Generator) to advance to the next steps in the sequence.

The circuit's operation is as follows. The 120 $V_{rms}$ mains voltage is divided by resistors R1 through R3 and diodes D1 and D2 into a $\sim$1 $V_{pp}$ signal. The use of diodes as part of the voltage divider increases the slew rate at the zero-crossing to speed up the response time of the logic output. R4 and C1 form a 16 kHz low pass filter to suppress false triggers from noise on the mains voltage. A comparator (Texas Instruments LM311) is then used to produce a logic signal based on the polarity of the mains voltage. Negative outputs of the comparator are clamped close to 0 V by the Schottky diode D3. For safety, an optocoupler (Broadcom HCPL-2400) is used to divide the high voltage and low voltage sides of the circuit. Finally, a Schmitt-trigger

inverter (Texas Instruments SN74HC14) is used to translate the logic level to 3.3 V for compatibility with our experimental sequence control hardware.

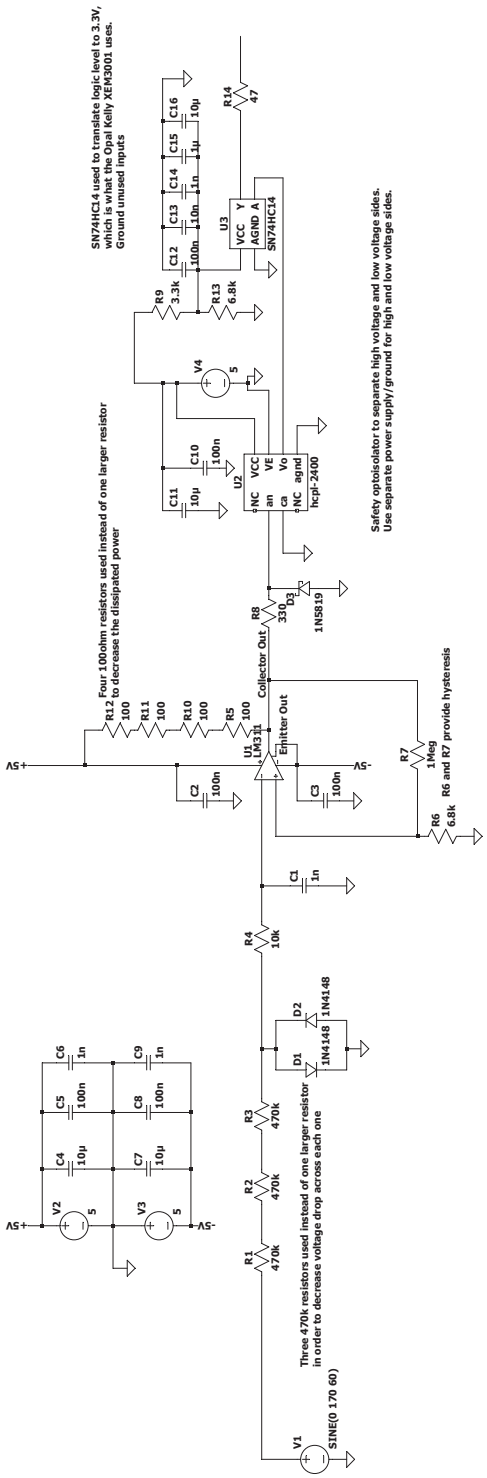


**Figure B.1: Circuit diagram of the mains voltage zero-crossing detector.** This circuit is based on ref. [281].

# Appendix C

# High voltage servo circuit

The circuit for our high voltage servo is shown in Fig. C.1. We consider here only the servo for our positive high voltage amplifier path; the negative servo circuit is nearly identical. The setpoint voltage is buffered by the op amp U3 and then passed through a 100 kHz fourth order Bessel low pass filter consisting of U4 and U5. We found that the noise on our setpoint voltage is independent of the amplitude of the setpoint, so the highest signal-to-noise ratio is obtained at the setpoint's 10 V maximum. If a 10 V setpoint were directly used to form the error signal with the monitor divider's output voltage (see section 5.1.4), then the high voltage amplifier output would be at 10 kV. Such a high voltage is not needed for our current experiments, so to maximize the signal-to-noise ratio we multiply the setpoint by a factor of 0.75 using U5 and U7. U7 also buffers the signal from the monitor divider. An instrumentation amplifier U6 (Analog Devices AD8429) is then used to produce the error signal. Finally, U8 and U9 form a PI control circuit with tunable proportional and integral gain. To avoid integrator windup, U10 and U11 allow for the integration capacitors to be shorted based on an enable logic signal. We use two op amp models throughout the circuit: Analog Devices AD8597/AD8599 (single/dual op amp package) and Texas Instruments OPA828. The choice of which model to use throughout the circuit is dictated

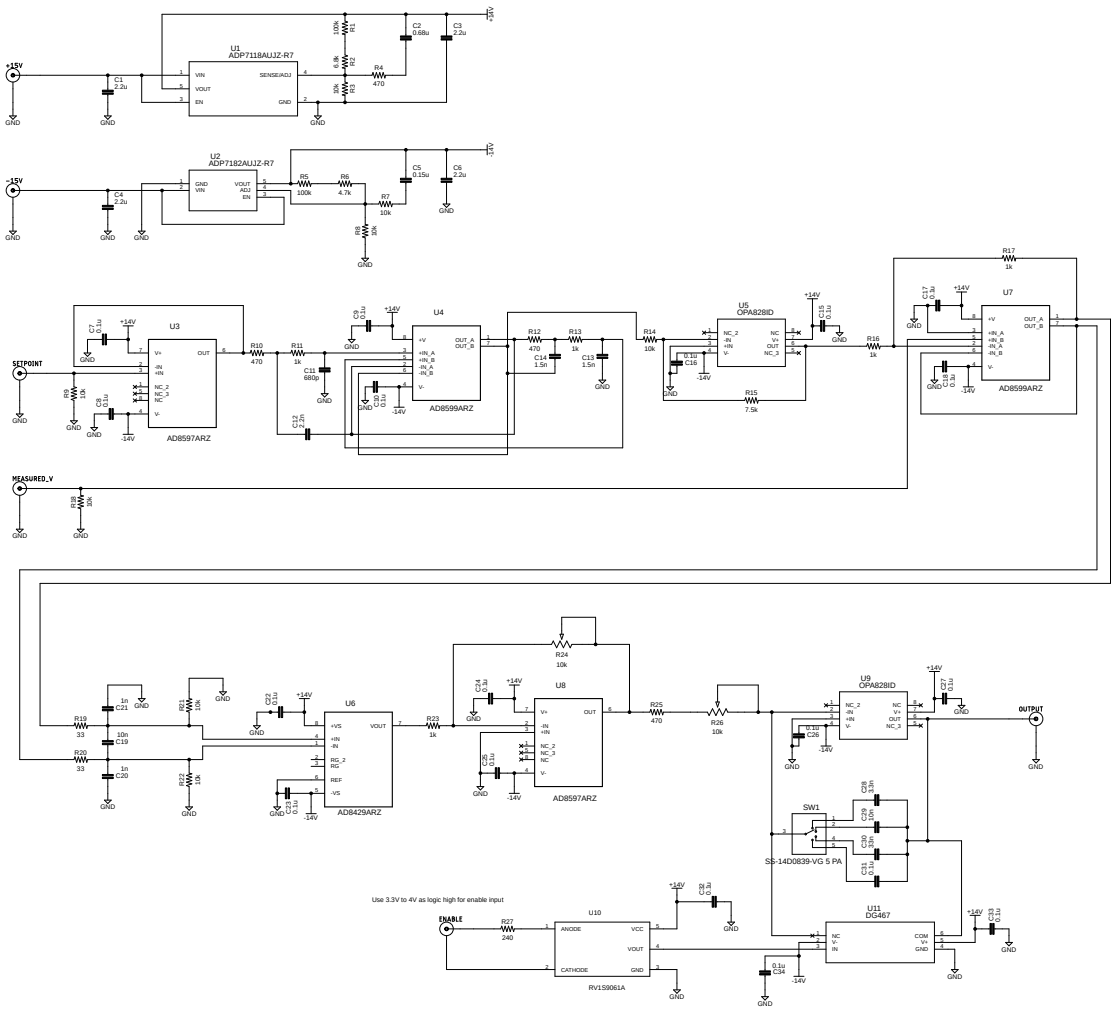


**Figure C.1: Circuit diagram of the high voltage servo.**

by noise considerations. For high source impedances, the JFET-input OPA828 has superior noise characteristics, while for lower source impedances the AD8597/AD8599 performs better.

# Bibliography


[1] Anderson, P. W. More Is Different. *Science* **177**, 393–396 (1972).

[2] DeMille, D., Hutzler, N. R., Rey, A. M. & Zelevinsky, T. Quantum sensing and metrology for fundamental physics with molecules. *Nat. Phys.* **20**, 741–749 (2024).

[3] Krems, R. V. Cold controlled chemistry. *Phys. Chem. Chem. Phys.* **10**, 4079–4092 (2008).

[4] Quéméner, G. & Julienne, P. S. Ultracold Molecules under Control! *Chem. Rev.* **112**, 4949–5011 (2012).

[5] Bohn, J. L., Rey, A. M. & Ye, J. Cold molecules: Progress in quantum engineering of chemistry and quantum matter. *Science* **357**, 1002–1010 (2017).

[6] Liu, Y. & Ni, K.-K. Bimolecular Chemistry in the Ultracold Regime. *Annu. Rev. Phys. Chem.* **73**, 73–96 (2022).

[7] Karman, T., Tomza, M. & Pérez-Ríos, J. Ultracold chemistry as a testbed for few-body physics. *Nat. Phys.* **20**, 722–729 (2024).

[8] Baranov, M. A., Dalmonte, M., Pupillo, G. & Zoller, P. Condensed Matter Theory of Dipolar Quantum Gases. *Chem. Rev.* **112**, 5012–5061 (2012).

[9] Gadway, B. & Yan, B. Strongly interacting ultracold polar molecules. *J. Phys. B* **49**, 152002 (2016).

[10] Cornish, S. L., Tarbutt, M. R. & Hazzard, K. R. A. Quantum computation and quantum simulation with ultracold molecules. *Nat. Phys.* **20**, 730–740 (2024).

[11] Ni, K.-K. *et al.* A High Phase-Space-Density Gas of Polar Molecules. *Science* **322**, 231–235 (2008).

[12] Liu, Y.-X. *et al.* Quantum interference in atom-exchange reactions. *Science* **384**, 1117–1121 (2024).

[13] Ruttley, D. K., Hepworth, T. R., Guttridge, A. & Cornish, S. L. Long-lived entanglement of molecules in magic-wavelength optical tweezers. *Nature* **637**, 827–832 (2025).

[14] De Marco, L. *et al.* A degenerate Fermi gas of polar molecules. *Science* **363**, 853–856 (2019).

[15] Duda, M. *et al.* Transition from a polaronic condensate to a degenerate Fermi gas of heteronuclear molecules. *Nat. Phys.* **19**, 720–725 (2023).

[16] Bigagli, N. *et al.* Observation of Bose–Einstein condensation of dipolar molecules. *Nature* **631**, 289–293 (2024).

[17] Langen, T., Valtolina, G., Wang, D. & Ye, J. Quantum state manipulation and cooling of ultracold molecules. *Nat. Phys.* **20**, 702–712 (2024).

[18] Moses, S. A., Covey, J. P., Miecnikowski, M. T., Jin, D. S. & Ye, J. New frontiers for quantum gases of polar molecules. *Nat. Phys.* **13**, 13–20 (2017).

[19] McCarron, D. Laser cooling and trapping molecules. *J. Phys. B* **51**, 212001 (2018).

[20] Tarbutt, M. R. Laser cooling of molecules. *Contemp. Phys.* **59**, 356–376 (2018).

[21] Köhler, T., Góral, K. & Julienne, P. S. Production of cold molecules via magnetically tunable Feshbach resonances. *Rev. Mod. Phys.* **78**, 1311–1361 (2006).

[22] Chin, C., Grimm, R., Julienne, P. & Tiesinga, E. Feshbach resonances in ultracold gases. *Rev. Mod. Phys.* **82**, 1225–1286 (2010).

[23] Vitanov, N. V., Rangelov, A. A., Shore, B. W. & Bergmann, K. Stimulated Raman adiabatic passage in physics, chemistry, and beyond. *Rev. Mod. Phys.* **89**, 015006 (2017).

[24] Ospelkaus, S. *et al.* Controlling the Hyperfine State of Rovibronic Ground-State Polar Molecules. *Phys. Rev. Lett.* **104**, 030402 (2010).

[25] Will, S. A., Park, J. W., Yan, Z. Z., Loh, H. & Zwierlein, M. W. Coherent Microwave Control of Ultracold $^{23}$Na$^{40}$K Molecules. *Phys. Rev. Lett.* **116**, 225306 (2016).

[26] Gregory, P. D., Aldegunde, J., Hutson, J. M. & Cornish, S. L. Controlling the rotational and hyperfine state of ultracold $^{87}$Rb$^{133}$Cs molecules. *Phys. Rev. A* **94**, 041403 (2016).

[27] Guo, M., Ye, X., He, J., Quéméner, G. & Wang, D. High-resolution internal state control of ultracold $^{23}$Na$^{87}$Rb molecules. *Phys. Rev. A* **97**, 020501 (2018).

[28] Liu, L. R. *et al.* Building one molecule from a reservoir of two atoms. *Science* **360**, 900–903 (2018).

[29] Zhang, J. T. *et al.* Forming a Single Molecule by Magnetoassociation in an Optical Tweezer. *Phys. Rev. Lett.* **124**, 253401 (2020).

[30] Cairncross, W. B. *et al.* Assembly of a Rovibrational Ground State Molecule in an Optical Tweezer. *Phys. Rev. Lett.* **126**, 123402 (2021).

[31] Ruttley, D. K. *et al.* Formation of Ultracold Molecules by Merging Optical Tweezers. *Phys. Rev. Lett.* **130**, 223401 (2023).

[32] Moses, S. A. *et al.* Creation of a low-entropy quantum gas of polar molecules in an optical lattice. *Science* **350**, 659–662 (2015).

[33] Reichsöllner, L., Schindewolf, A., Takekoshi, T., Grimm, R. & Nägerl, H.-C. Quantum Engineering of a Low-Entropy Gas of Heteronuclear Bosonic Molecules in an Optical Lattice. *Phys. Rev. Lett.* **118**, 073201 (2017).

[34] Rosenberg, J. S., Christakis, L., Guardado-Sanchez, E., Yan, Z. Z. & Bakr, W. S. Observation of the Hanbury Brown–Twiss effect with ultracold molecules. *Nat. Phys.* **18**, 1062–1066 (2022).

[35] Christakis, L. *et al.* Probing site-resolved correlations in a spin system of ultracold molecules. *Nature* **614**, 64–69 (2023).

[36] Barry, J. F., McCarron, D. J., Norrgard, E. B., Steinecker, M. H. & DeMille, D. Magneto-optical trapping of a diatomic molecule. *Nature* **512**, 286–289 (2014).

[37] Anderegg, L. *et al.* Radio Frequency Magneto-Optical Trapping of CaF with High Density. *Phys. Rev. Lett.* **119**, 103201 (2017).

[38] Truppe, S. *et al.* Molecules cooled below the Doppler limit. *Nat. Phys.* **13**, 1173–1176 (2017).

[39] Collopy, A. L. *et al.* 3D Magneto-Optical Trap of Yttrium Monoxide. *Phys. Rev. Lett.* **121**, 213201 (2018).

[40] Di Rosa, M. D. Laser-cooling molecules. *Eur. Phys. J. D* **31**, 395–402 (2004).

[41] Anderegg, L. *et al.* An optical tweezer array of ultracold molecules. *Science* **365**, 1156–1158 (2019).

[42] Holland, C. M., Lu, Y. & Cheuk, L. W. Bichromatic Imaging of Single Molecules in an Optical Tweezer Array. *Phys. Rev. Lett.* **131**, 053202 (2023).

[43] Vilas, N. B. *et al.* An optical tweezer array of ultracold polyatomic molecules. *Nature* **628**, 282–286 (2024).

[44] Lu, Y., Li, S. J., Holland, C. M. & Cheuk, L. W. Raman sideband cooling of molecules in an optical tweezer array. *Nat. Phys.* **20**, 389–394 (2024).

[45] Bao, Y. *et al.* Raman Sideband Cooling of Molecules in an Optical Tweezer Array to the 3D Motional Ground State. *Phys. Rev. X* **14**, 031002 (2024).

[46] Wang, D. *et al.* Direct absorption imaging of ultracold polar molecules. *Phys. Rev. A* **81**, 061404 (2010).

[47] Kozyryev, I. *et al.* Sisyphus Laser Cooling of a Polyatomic Molecule. *Phys. Rev. Lett.* **118**, 173201 (2017).

[48] Vilas, N. B. *et al.* Magneto-optical trapping and sub-Doppler cooling of a polyatomic molecule. *Nature* **606**, 70–74 (2022).

[49] Augenbraun, B. L. *et al.* Direct laser cooling of polyatomic molecules. In DiMauro, L. F., Perrin, H. & Yelin, S. F. (eds.) *Advances in Atomic, Molecular, and Optical Physics*, vol. 72, 89–182 (Academic Press, 2023).

[50] Feynman, R. P. Simulating physics with computers. *Int. J. Theor. Phys.* **21**, 467–488 (1982).

[51] Georgescu, I. M., Ashhab, S. & Nori, F. Quantum simulation. *Rev. Mod. Phys.* **86**, 153–185 (2014).

[52] Altman, E. *et al.* Quantum Simulators: Architectures and Opportunities. *PRX Quantum* **2**, 017003 (2021).

[53] Daley, A. J. *et al.* Practical quantum advantage in quantum simulation. *Nature* **607**, 667–676 (2022).

[54] Bloch, I., Dalibard, J. & Nascimbène, S. Quantum simulations with ultracold quantum gases. *Nat. Phys.* **8**, 267–276 (2012).

[55] Gross, C. & Bloch, I. Quantum simulations with ultracold atoms in optical lattices. *Science* **357**, 995–1001 (2017).

[56] Browaeys, A. & Lahaye, T. Many-body physics with individually controlled Rydberg atoms. *Nat. Phys.* **16**, 132–142 (2020).

[57] Houck, A. A., Türeci, H. E. & Koch, J. On-chip quantum simulation with superconducting circuits. *Nat. Phys.* **8**, 292–299 (2012).

[58] Aspuru-Guzik, A. & Walther, P. Photonic quantum simulators. *Nat. Phys.* **8**, 285–291 (2012).

[59] Blatt, R. & Roos, C. F. Quantum simulations with trapped ions. *Nat. Phys.* **8**, 277–284 (2012).

[60] Foss-Feig, M., Pagano, G., Potter, A. C. & Yao, N. Y. Progress in Trapped-Ion Quantum Simulation. *Annu. Rev. Condens. Matter Phys.* **16**, 145–172 (2025).

[61] Gorshkov, A. V. *et al.* Tunable Superfluidity and Quantum Magnetism with Ultracold Polar Molecules. *Phys. Rev. Lett.* **107**, 115301 (2011).

[62] Gorshkov, A. V. *et al.* Quantum magnetism with polar alkali-metal dimers. *Phys. Rev. A* **84**, 033619 (2011).

[63] Yan, B. *et al.* Observation of dipolar spin-exchange interactions with lattice-confined polar molecules. *Nature* **501**, 521–525 (2013).

[64] Holland, C. M., Lu, Y. & Cheuk, L. W. On-demand entanglement of molecules in a reconfigurable optical tweezer array. *Science* **382**, 1143–1147 (2023).

[65] Bao, Y. *et al.* Dipolar spin-exchange and entanglement between molecules in an optical tweezer array. *Science* **382**, 1138–1143 (2023).

[66] Picard, L. R. B. *et al.* Entanglement and iSWAP gate between molecular qubits. *Nature* **637**, 821–826 (2025).

[67] Miller, C. *et al.* Two-axis twisting using Floquet-engineered XYZ spin models with polar molecules. *Nature* **633**, 332–337 (2024).

[68] Carroll, A. N. *et al.* Observation of Generalized t-J Spin Dynamics with Tunable Dipolar Interactions (2024). Preprint at https://doi.org/10.48550/arXiv.2404.18916.

[69] Capogrosso-Sansone, B., Trefzger, C., Lewenstein, M., Zoller, P. & Pupillo, G. Quantum Phases of Cold Polar Molecules in 2D Optical Lattices. *Phys. Rev. Lett.* **104**, 125301 (2010).

[70] Gregory, P. D. *et al.* Second-scale rotational coherence and dipolar interactions in a gas of ultracold polar molecules. *Nat. Phys.* **20**, 415–421 (2024).

[71] Park, J. W., Yan, Z. Z., Loh, H., Will, S. A. & Zwierlein, M. W. Second-scale nuclear spin coherence time of ultracold $^{23}$Na$^{40}$K molecules. *Science* **357**, 372–375 (2017).

[72] Gregory, P. D., Blackmore, J. A., Bromley, S. L., Hutson, J. M. & Cornish, S. L. Robust storage qubits in ultracold polar molecules. *Nat. Phys.* **17**, 1149–1153 (2021).

[73] Lin, J., He, J., Jin, M., Chen, G. & Wang, D. Seconds-Scale Coherence on Nuclear Spin Transitions of Ultracold Polar Molecules in 3D Optical Lattices. *Phys. Rev. Lett.* **128**, 223201 (2022).

[74] Burchesky, S. *et al.* Rotational Coherence Times of Polar Molecules in Optical Tweezers. *Phys. Rev. Lett.* **127**, 123202 (2021).

[75] Kotochigova, S. & DeMille, D. Electric-field-dependent dynamic polarizability and state-insensitive conditions for optical trapping of diatomic polar molecules. *Phys. Rev. A* **82**, 063421 (2010).

[76] Neyenhuis, B. *et al.* Anisotropic Polarizability of Ultracold Polar $^{40}$K$^{87}$Rb Molecules. *Phys. Rev. Lett.* **109**, 230403 (2012).

[77] Gregory, P. D., Blackmore, J. A., Aldegunde, J., Hutson, J. M. & Cornish, S. L. ac Stark effect in ultracold polar $^{87}$Rb$^{133}$Cs molecules. *Phys. Rev. A* **96**, 021402 (2017).

[78] Lin, J., He, J., Ye, X. & Wang, D. Anisotropic polarizability of ultracold ground-state $^{23}$Na$^{87}$Rb molecules. *Phys. Rev. A* **103**, 023332 (2021).

[79] Tobias, W. G. *et al.* Reactions between layer-resolved molecules mediated by dipolar spin exchange. *Science* **375**, 1299–1303 (2022).

[80] Park, A. J. *et al.* Extended Rotational Coherence of Polar Molecules in an Elliptically Polarized Trap. *Phys. Rev. Lett.* **131**, 183401 (2023).

[81] Seeßelberg, F. *et al.* Extending Rotational Coherence of Interacting Polar Molecules in a Spin-Decoupled Magic Trap. *Phys. Rev. Lett.* **121**, 253401 (2018).

[82] Li, J.-R. *et al.* Tunable itinerant spin dynamics with polar molecules. *Nature* **614**, 70–74 (2023).

[83] de Léséleuc, S. *et al.* Observation of a symmetry-protected topological phase of interacting bosons with Rydberg atoms. *Science* **365**, 775–780 (2019).

[84] Chen, C. *et al.* Continuous symmetry breaking in a two-dimensional Rydberg array. *Nature* **616**, 691–695 (2023).

[85] Bornet, G. *et al.* Scalable spin squeezing in a dipolar Rydberg atom array. *Nature* **621**, 728–733 (2023).

[86] Scholl, P. *et al.* Microwave Engineering of Programmable $XXZ$ Hamiltonians in Arrays of Rydberg Atoms. *PRX Quantum* **3**, 020303 (2022).

[87] Qiao, M. *et al.* Realization of a doped quantum antiferromagnet with dipolar tunnelings in a Rydberg tweezer array (2025). Preprint at https://doi.org/10.48550/arXiv.2501.08233.

[88] Nguyen, T. L. *et al.* Towards Quantum Simulation with Circular Rydberg Atoms. *Phys. Rev. X* **8**, 011032 (2018).

[89] Cantat-Moltrecht, T. *et al.* Long-lived circular Rydberg states of laser-cooled rubidium atoms in a cryostat. *Phys. Rev. Res.* **2**, 022032 (2020).

[90] Cohen, S. R. & Thompson, J. D. Quantum Computing with Circular Rydberg Atoms. *PRX Quantum* **2**, 030322 (2021).

[91] Ravon, B. *et al.* Array of Individual Circular Rydberg Atoms Trapped in Optical Tweezers. *Phys. Rev. Lett.* **131**, 093401 (2023).

[92] Hölzl, C., Götzelmann, A., Pultinevicius, E., Wirth, M. & Meinert, F. Long-Lived Circular Rydberg Qubits of Alkaline-Earth Atoms in Optical Tweezers. *Phys. Rev. X* **14**, 021024 (2024).

[93] Zeiher, J. *et al.* Coherent Many-Body Spin Dynamics in a Long-Range Interacting Ising Chain. *Phys. Rev. X* **7**, 041063 (2017).

[94] Guardado-Sanchez, E. *et al.* Quench Dynamics of a Fermi Gas with Strong Nonlocal Interactions. *Phys. Rev. X* **11**, 021036 (2021).

[95] Weckesser, P. *et al.* Realization of a Rydberg-dressed extended Bose Hubbard model (2024). Preprint at https://doi.org/10.48550/arXiv.2405.20128.

[96] Schymik, K.-N. *et al.* Single Atoms with 6000-Second Trapping Lifetimes in Optical-Tweezer Arrays at Cryogenic Temperatures. *Phys. Rev. Appl.* **16**, 034013 (2021).

[97] Zhang, Z. *et al.* A high optical access cryogenic system for Rydberg atom arrays with a 3000-second trap lifetime (2024). Preprint at https://doi.org/10.48550/arXiv.2412.09780.

[98] de Paz, A. *et al.* Nonequilibrium Quantum Magnetism in a Dipolar Lattice Gas. *Phys. Rev. Lett.* **111**, 185305 (2013).

[99] Patscheider, A. *et al.* Controlling dipolar exchange interactions in a dense three-dimensional array of large-spin fermions. *Phys. Rev. Res.* **2**, 023050 (2020).

[100] Baier, S. *et al.* Extended Bose-Hubbard models with ultracold magnetic atoms. *Science* **352**, 201–205 (2016).

[101] Su, L. *et al.* Dipolar quantum solids emerging in a Hubbard quantum simulator. *Nature* **622**, 724–729 (2023).

[102] Kaufman, A. M. & Ni, K.-K. Quantum science with optical tweezer arrays of ultracold atoms and molecules. *Nat. Phys.* **17**, 1324–1333 (2021).

[103] Bakr, W. S., Gillen, J. I., Peng, A., Fölling, S. & Greiner, M. A quantum gas microscope for detecting single atoms in a Hubbard-regime optical lattice. *Nature* **462**, 74–77 (2009).

[104] Sherson, J. F. *et al.* Single-atom-resolved fluorescence imaging of an atomic Mott insulator. *Nature* **467**, 68–72 (2010).

[105] Gross, C. & Bakr, W. S. Quantum gas microscopy for single atom and spin detection. *Nat. Phys.* **17**, 1316–1323 (2021).

[106] Bakr, W. S. *et al.* Probing the Superfluid–to–Mott Insulator Transition at the Single-Atom Level. *Science* **329**, 547–550 (2010).

[107] Cheuk, L. W. *et al.* Observation of spatial charge and spin correlations in the 2D Fermi-Hubbard model. *Science* **353**, 1260–1264 (2016).

[108] Parsons, M. F. *et al.* Site-resolved measurement of the spin-correlation function in the Fermi-Hubbard model. *Science* **353**, 1253–1256 (2016).

[109] Boll, M. *et al.* Spin- and density-resolved microscopy of antiferromagnetic correlations in Fermi-Hubbard chains. *Science* **353**, 1257–1260 (2016).

[110] Brown, P. T. *et al.* Spin-imbalance in a 2D Fermi-Hubbard system. *Science* **357**, 1385–1388 (2017).

[111] Wei, D. *et al.* Quantum gas microscopy of Kardar-Parisi-Zhang superdiffusion. *Science* **376**, 716–720 (2022).

[112] Christakis, L. *Microscopy of quantum correlations in an ultracold molecular gas*. Ph.D. thesis, Princeton University (2023).

[113] Guo, M. *et al.* Creation of an Ultracold Gas of Ground-State Dipolar $^{23}Na^{87}Rb$ Molecules. *Phys. Rev. Lett.* **116**, 205303 (2016).

[114] Ospelkaus, S. *et al.* Quantum-State Controlled Chemical Reactions of Ultracold Potassium-Rubidium Molecules. *Science* **327**, 853–857 (2010).

[115] Julienne, P. S., Hanna, T. M. & Idziaszek, Z. Universal ultracold collision rates for polar molecules of two alkali-metal atoms. *Phys. Chem. Chem. Phys.* **13**, 19114–19124 (2011).

[116] Żuchowski, P. S. & Hutson, J. M. Reactions of ultracold alkali-metal dimers. *Phys. Rev. A* **81**, 060703 (2010).

[117] Takekoshi, T. *et al.* Ultracold Dense Samples of Dipolar RbCs Molecules in the Rovibrational and Hyperfine Ground State. *Phys. Rev. Lett.* **113**, 205301 (2014).

[118] Park, J. W., Will, S. A. & Zwierlein, M. W. Ultracold Dipolar Gas of Fermionic $^{23}Na^{40}K$ Molecules in Their Absolute Ground State. *Phys. Rev. Lett.* **114**, 205302 (2015).

[119] Ye, X., Guo, M., González-Martínez, M. L., Quéméner, G. & Wang, D. Collisions of ultracold $^{23}Na^{87}Rb$ molecules with controlled chemical reactivities. *Sci. Adv.* **4**, eaaq0083 (2018).

[120] Gregory, P. D. *et al.* Sticky collisions of ultracold RbCs molecules. *Nat. Commun.* **10**, 3104 (2019).

[121] Christianen, A., Zwierlein, M. W., Groenenboom, G. C. & Karman, T. Photoinduced Two-Body Loss of Ultracold Molecules. *Phys. Rev. Lett.* **123**, 123402 (2019).

[122] Mayle, M., Ruzic, B. P. & Bohn, J. L. Statistical aspects of ultracold resonant scattering. *Phys. Rev. A* **85**, 062712 (2012).

[123] Mayle, M., Quéméner, G., Ruzic, B. P. & Bohn, J. L. Scattering of ultracold molecules in the highly resonant regime. *Phys. Rev. A* **87**, 012709 (2013).

[124] Bause, R., Christianen, A., Schindewolf, A., Bloch, I. & Luo, X.-Y. Ultracold Sticky Collisions: Theoretical and Experimental Status. *J. Phys. Chem. A* **127**, 729–741 (2023).

[125] Gregory, P. D., Blackmore, J. A., Bromley, S. L. & Cornish, S. L. Loss of Ultracold $^{87}$Rb$^{133}$Cs Molecules via Optical Excitation of Long-Lived Two-Body Collision Complexes. *Phys. Rev. Lett.* **124**, 163402 (2020).

[126] Bause, R. *et al.* Collisions of ultracold molecules in bright and dark optical dipole traps. *Phys. Rev. Res.* **3**, 033013 (2021).

[127] Gersema, P. *et al.* Probing Photoinduced Two-Body Loss of Ultracold Nonreactive Bosonic $^{23}$Na$^{87}$Rb and $^{23}$Na$^{39}$K Molecules. *Phys. Rev. Lett.* **127**, 163401 (2021).

[128] Büchler, H. P. *et al.* Strongly Correlated 2D Quantum Phases with Cold Polar Molecules: Controlling the Shape of the Interaction Potential. *Phys. Rev. Lett.* **98**, 060404 (2007).

[129] Micheli, A. *et al.* Universal Rates for Reactive Ultracold Polar Molecules in Reduced Dimensions. *Phys. Rev. Lett.* **105**, 073202 (2010).

[130] Quéméner, G. & Bohn, J. L. Dynamics of ultracold molecules in confined geometry and electric field. *Phys. Rev. A* **83**, 012705 (2011).

[131] Zhu, B., Quéméner, G., Rey, A. M. & Holland, M. J. Evaporative cooling of reactive polar molecules confined in a two-dimensional geometry. *Phys. Rev. A* **88**, 063405 (2013).

[132] Valtolina, G. *et al.* Dipolar evaporation of reactive molecules to below the Fermi temperature. *Nature* **588**, 239–243 (2020).

[133] Karman, T. & Hutson, J. M. Microwave Shielding of Ultracold Polar Molecules. *Phys. Rev. Lett.* **121**, 163401 (2018).

[134] Lassablière, L. & Quéméner, G. Controlling the Scattering Length of Ultracold Dipolar Molecules. *Phys. Rev. Lett.* **121**, 163402 (2018).

[135] Karman, T. & Hutson, J. M. Microwave shielding of ultracold polar molecules with imperfectly circular polarization. *Phys. Rev. A* **100**, 052704 (2019).

[136] Anderegg, L. *et al.* Observation of microwave shielding of ultracold molecules. *Science* **373**, 779–782 (2021).

[137] Karman, T., Yan, Z. Z. & Zwierlein, M. Resonant and first-order dipolar interactions between ultracold $^1\Sigma$ molecules in static and microwave electric fields. *Phys. Rev. A* **105**, 013321 (2022).

[138] Schindewolf, A. *et al.* Evaporation of microwave-shielded polar molecules to quantum degeneracy. *Nature* **607**, 677–681 (2022).

[139] Deng, F. *et al.* Effective potential and superfluidity of microwave-shielded polar molecules. *Phys. Rev. Lett.* **130**, 183001 (2023).

[140] Bigagli, N. *et al.* Collisionally stable gas of bosonic dipolar ground-state molecules. *Nat. Phys.* **19**, 1579–1584 (2023).

[141] Lin, J. *et al.* Microwave Shielding of Bosonic NaRb Molecules. *Phys. Rev. X* **13**, 031032 (2023).

[142] Karman, T. *et al.* Double Microwave Shielding (2025). Preprint at https://doi.org/10.48550/arXiv.2501.08095.

[143] Dutta, J., Mukherjee, B. & Hutson, J. M. Universality in the microwave shielding of ultracold polar molecules (2025). Preprint at https://doi.org/10.48550/arXiv.2501.03170.

[144] Gorshkov, A. V. *et al.* Suppression of Inelastic Collisions Between Polar Molecules With a Repulsive Shield. *Phys. Rev. Lett.* **101**, 073201 (2008).

[145] Karman, T. Microwave shielding with far-from-circular polarization. *Phys. Rev. A* **101**, 042702 (2020).

[146] Avdeenkov, A. V., Kajita, M. & Bohn, J. L. Suppression of inelastic collisions of polar $^1\Sigma$ state molecules in an electrostatic field. *Phys. Rev. A* **73**, 022707 (2006).

[147] Wang, G. & Quéméner, G. Tuning ultracold collisions of excited rotational dipolar molecules. *New Journal of Physics* **17**, 035015 (2015).

[148] Quéméner, G. & Bohn, J. L. Shielding $^2\Sigma$ ultracold dipolar molecular collisions with electric fields. *Phys. Rev. A* **93**, 012704 (2016).

[149] González-Martínez, M. L., Bohn, J. L. & Quéméner, G. Adimensional theory of shielding in ultracold collisions of dipolar rotors. *Phys. Rev. A* **96**, 032718 (2017).

[150] Matsuda, K. *et al.* Resonant collisional shielding of reactive molecules using electric fields. *Science* **370**, 1324–1327 (2020).

[151] Li, J.-R. *et al.* Tuning of dipolar interactions and evaporative cooling in a three-dimensional molecular quantum gas. *Nat. Phys.* **17**, 1144–1148 (2021).

[152] Lassablière, L. & Quéméner, G. Model for two-body collisions between ultracold dipolar molecules around a Förster resonance in an electric field. *Phys. Rev. A* **106**, 033311 (2022).

[153] Mukherjee, B., Frye, M. D., Le Sueur, C. R., Tarbutt, M. R. & Hutson, J. M. Shielding collisions of ultracold CaF molecules with static electric fields. *Phys. Rev. Res.* **5**, 033097 (2023).

[154] Mukherjee, B. & Hutson, J. M. Controlling collisional loss and scattering lengths of ultracold dipolar molecules with static electric fields. *Phys. Rev. Res.* **6**, 013145 (2024).

[155] Rosenberg, J. S., Christakis, L., Guardado-Sanchez, E., Yan, Z. & Bakr, W. S. Observation of the Hanbury Brown and Twiss Effect with Ultracold Molecules (2022). DAMOP.

[156] Brown, R. H. & Twiss, R. A New Type of Interferometer for Use in Radio Astronomy. *Philos. Mag.* **45**, 663–682 (1954).

[157] Hanbury Brown, R. & Twiss, R. Q. Correlation between Photons in two Coherent Beams of Light. *Nature* **177**, 27–29 (1956).

[158] Hanbury Brown, R. & Twiss, R. Q. A Test of a New Type of Stellar Interferometer on Sirius. *Nature* **178**, 1046–1048 (1956).

[159] Glauber, R. J. The Quantum Theory of Optical Coherence. *Phys. Rev.* **130**, 2529–2539 (1963).

[160] Fox, M. *Quantum Optics* (Oxford University Press, 2006).

[161] Aspect, A. Hanbury Brown and Twiss, Hong Ou and Mandel effects and other landmarks in quantum optics: from photons to atoms. In Browaeys, A. *et al.* (eds.) *Current Trends in Atomic Physics*, 428–449 (Oxford University Press, 2019).

[162] Henny, M. *et al.* The Fermionic Hanbury Brown and Twiss Experiment. *Science* **284**, 296–298 (1999).

[163] Oliver, W. D., Kim, J., Liu, R. C. & Yamamoto, Y. Hanbury Brown and Twiss-Type Experiment with Electrons. *Science* **284**, 299–301 (1999).

[164] Iannuzzi, M., Orecchini, A., Sacchetti, F., Facchi, P. & Pascazio, S. Direct Experimental Evidence of Free-Fermion Antibunching. *Phys. Rev. Lett.* **96**, 080402 (2006).

[165] Cohen, J. D. *et al.* Phonon counting and intensity interferometry of a nanomechanical resonator. *Nature* **520**, 522–525 (2015).

[166] Riedinger, R. *et al.* Non-classical correlations between single photons and phonons from a mechanical oscillator. *Nature* **530**, 313–316 (2016).

[167] Yasuda, M. & Shimizu, F. Observation of Two-Atom Correlation of an Ultracold Neon Atomic Beam. *Phys. Rev. Lett.* **77**, 3090–3093 (1996).

[168] Fölling, S. *et al.* Spatial quantum noise interferometry in expanding ultracold atom clouds. *Nature* **434**, 481–484 (2005).

[169] Öttl, A., Ritter, S., Köhl, M. & Esslinger, T. Correlations and Counting Statistics of an Atom Laser. *Phys. Rev. Lett.* **95**, 090404 (2005).

[170] Schellekens, M. *et al.* Hanbury Brown Twiss Effect for Ultracold Quantum Gases. *Science* **310**, 648–651 (2005).

[171] Rom, T. *et al.* Free fermion antibunching in a degenerate atomic Fermi gas released from an optical lattice. *Nature* **444**, 733–736 (2006).

[172] Jeltes, T. *et al.* Comparison of the Hanbury Brown–Twiss effect for bosons and fermions. *Nature* **445**, 402–405 (2007).

[173] Hodgman, S. S., Dall, R. G., Manning, A. G., Baldwin, K. G. H. & Truscott, A. G. Direct Measurement of Long-Range Third-Order Coherence in Bose-Einstein Condensates. *Science* **331**, 1046–1049 (2011).

[174] Perrin, A. *et al.* Hanbury Brown and Twiss correlations across the Bose-Einstein condensation threshold. *Nat. Phys.* **8**, 195–198 (2012).

[175] Dall, R. G. *et al.* Ideal n-body correlations with massive particles. *Nat. Phys.* **9**, 341–344 (2013).

[176] Carcy, C. *et al.* Momentum-Space Atom Correlations in a Mott Insulator. *Phys. Rev. X* **9**, 041028 (2019).

[177] Preiss, P. M. *et al.* High-Contrast Interference of Ultracold Fermions. *Phys. Rev. Lett.* **122**, 143602 (2019).

[178] Tenart, A., Hercé, G., Bureik, J.-P., Dareau, A. & Clément, D. Observation of pairs of atoms at opposite momenta in an equilibrium interacting Bose gas. *Nat. Phys.* **17**, 1364–1368 (2021).

[179] Baym, G. The physics of Hanbury Brown–Twiss intensity interferometry: from stars to nuclear collisions. *Acta Phys. Pol. B* **29**, 1839–1884 (1998).

[180] Lisa, M. A., Pratt, S., Soltz, R. & Wiedemann, U. FEMTOSCOPY IN RELATIVISTIC HEAVY ION COLLISIONS: Two Decades of Progress. *Annual Review of Nuclear and Particle Science* **55**, 357–402 (2005).

[181] Brown, R. H. *The Intensity Interferometer* (Taylor & Francis, 1974).

[182] Pease, F. G. Interferometer Methods in Astronomy. *Ergeb. Exact. Naturwiss.* **10**, 84–96 (1931).

[183] Born, M. & Wolf, E. *Principles of Optics* (Cambridge University Press, 1999).

[184] Hanbury Brown, R., Jennison, R. C. & Das Gupta, M. K. Apparent Angular Sizes of Discrete Radio Sources: Observations at Jodrell Bank, Manchester. *Nature* **170**, 1061–1063 (1952).

[185] Brannen, E. & Ferguson, H. I. S. The Question of Correlation between Photons in Coherent Light Rays. *Nature* **178**, 481–482 (1956).

[186] Hanbury Brown, R. & Twiss, R. Q. Interferometry of the intensity fluctuations in light. II. An experimental test of the theory for partially coherent light. *Proc. R. Soc. Lond. A* **243**, 291–319 (1958).

[187] Armstrong, J. T., Hutter, D. J., Johnston, K. J. & Mozurkewich, D. Stellar Optical Interferometry in the 1990s. *Physics Today* **48**, 42–49 (1995).

[188] Mandel, L. & Wolf, E. *Optical coherence and quantum optics* (Cambridge University Press, 1995).

[189] Glauber, R. J. Photon Correlations. *Phys. Rev. Lett.* **10**, 84–86 (1963).

[190] Paul, H. Photon antibunching. *Rev. Mod. Phys.* **54**, 1061–1102 (1982).

[191] Zou, X. T. & Mandel, L. Photon-antibunching and sub-Poissonian photon statistics. *Phys. Rev. A* **41**, 475–476 (1990).

[192] Singh, S. Antibunching, sub-Poissonian photon statistics and finite bandwidth effects in resonance fluorescence. *Opt. Commun.* **44**, 254–258 (1983).

[193] Kimble, H. J., Dagenais, M. & Mandel, L. Photon Antibunching in Resonance Fluorescence. *Phys. Rev. Lett.* **39**, 691–695 (1977).

[194] Fano, U. Quantum Theory of Interference Effects in the Mixing of Light from Phase-Independent Sources. *Am. J. Phys.* **29**, 539–545 (1961).

[195] Altman, E., Demler, E. & Lukin, M. D. Probing many-body states of ultracold atoms via noise correlations. *Phys. Rev. A* **70**, 013603 (2004).

[196] Spielman, I. B., Phillips, W. D. & Porto, J. V. Mott-Insulator Transition in a Two-Dimensional Atomic Bose Gas. *Phys. Rev. Lett.* **98**, 080404 (2007).

[197] Simon, J. *et al.* Quantum simulation of antiferromagnetic spin chains in an optical lattice. *Nature* **472**, 307–312 (2011).

[198] Fölling, S. Quantum Noise Correlation Experiments with Ultracold Atoms. In Törmä, P. & Sengstock, K. (eds.) *Quantum Gas Experiments*, chap. 8, 145–177 (Imperial College Press, 2015).

[199] Greiner, M., Mandel, O., Esslinger, T., Hänsch, T. W. & Bloch, I. Quantum phase transition from a superfluid to a Mott insulator in a gas of ultracold atoms. *Nature* **415**, 39–44 (2002).

[200] Fölling, S. *Probing Strongly Correlated States of Ultracold Atoms in Optical Lattices*. Ph.D. thesis, Johannes Gutenberg-Universität (2008).

[201] Gerbier, F. *et al.* Expansion of a Quantum Gas Released from an Optical Lattice. *Phys. Rev. Lett.* **101**, 155303 (2008).

[202] Peng, A. W.-C. *Quantum Gas Microscope With Optical Lattice*. Ph.D. thesis, Harvard University (2010).

[203] Wang, F., Xiong, D., Li, X., Wang, D. & Tiemann, E. Observation of Feshbach resonances between ultracold Na and Rb atoms. *Phys. Rev. A* **87**, 050702 (2013).

[204] Wang, F. *et al.* Formation of ultracold NaRb Feshbach molecules. *New J. Phys.* **17**, 035003 (2015).

[205] Guo, Z. *et al.* Improved characterization of Feshbach resonances and interaction potentials between $^{23}$Na and $^{87}$Rb atoms. *Phys. Rev. A* **105**, 023313 (2022).

[206] Wang, F., Li, X., Xiong, D. & Wang, D. A double species $^{23}$Na and $^{87}$Rb Bose–Einstein condensate with tunable miscibility via an interspecies Feshbach resonance. *J. Phys. B* **49**, 015302 (2015).

[207] Sebby-Strabley, J., Anderlini, M., Jessen, P. S. & Porto, J. V. Lattice of double wells for manipulating pairs of cold atoms. *Phys. Rev. A* **73**, 033605 (2006).

[208] Busch, T., Englert, B.-G., Rzażewski, K. & Wilkens, M. Two Cold Atoms in a Harmonic Trap. *Found. Phys.* **28**, 549–559 (1998).

[209] Tiesinga, E., Williams, C. J., Mies, F. H. & Julienne, P. S. Interacting atoms under strong quantum confinement. *Phys. Rev. A* **61**, 063416 (2000).

[210] Stöferle, T., Moritz, H., Günter, K., Köhl, M. & Esslinger, T. Molecules of Fermionic Atoms in an Optical Lattice. *Phys. Rev. Lett.* **96**, 030401 (2006).

[211] Ospelkaus, C. *et al.* Ultracold Heteronuclear Molecules in a 3D Optical Lattice. *Phys. Rev. Lett.* **97**, 120402 (2006).

[212] Fuhrmanek, A., Bourgain, R., Sortais, Y. R. P. & Browaeys, A. Light-assisted collisions between a few cold atoms in a microscopic dipole trap. *Phys. Rev. A* **85**, 062708 (2012).

[213] Marinescu, M. & Dalgarno, A. Dispersion forces and long-range electronic transition dipole moments of alkali-metal dimer excited states. *Phys. Rev. A* **52**, 311–328 (1995).

[214] Marinescu, M. & Sadeghpour, H. R. Long-range potentials for two-species alkali-metal atoms. *Phys. Rev. A* **59**, 390–404 (1999).

[215] Hutson, J. M. & Le Sueur, C. R. BOUND and FIELD: Programs for calculating bound states of interacting pairs of atoms and molecules. *Comput. Phys. Commun.* **241**, 1–8 (2019).

[216] Danzl, J. G. *et al.* Deeply bound ultracold molecules in an optical lattice. *New J. Phys.* **11**, 055036 (2009).

[217] Chotia, A. *et al.* Long-Lived Dipolar Molecules and Feshbach Molecules in a 3D Optical Lattice. *Phys. Rev. Lett.* **108**, 080405 (2012).

[218] Pyzh, M., Krönke, S., Weitenberg, C. & Schmelcher, P. Quantum point spread function for imaging trapped few-body systems with a quantum gas microscope. *New J. Phys.* **21**, 053013 (2019).

[219] Christakis, L. *et al.* Quantum gas microscopy of polar molecules (2022). DAMOP.

[220] Bakr, W. S. Measuring quantum correlations in a many-body system of polar molecules (2023). DAMOP.

[221] Bransden, B. H. & Joachain, C. J. *Physics of Atoms and Molecules* (Prentice Hall, 2003).

[222] Bacskay, G. B., Reimers, J. R. & Nordholm, S. The Mechanism of Covalent Bonding. *J. Chem. Educ.* **74**, 1494 (1997).

[223] Guo, M. *An Ultracold Dipolar Gas of Ground-state $^{23}Na^{87}Rb$ Molecules.* Ph.D. thesis, The Chinese University of Hong Kong (2017).

[224] Guo, M. *et al.* High-resolution molecular spectroscopy for producing ultracold absolute-ground-state $^{23}$Na$^{87}$Rb molecules. *Phys. Rev. A* **96**, 052505 (2017).

[225] Brown, J. & Carrington, A. *Rotational Spectroscopy of Diatomic Molecules* (Cambridge University Press, 2003).

[226] Ni, K.-K. *A Quantum Gas of Polar Molecules.* Ph.D. thesis, University of Colorado, Boulder (2009).

[227] Docenko, O. *et al.* Deperturbation treatment of the $A\,^1\Sigma^+ - b\,^3\Pi$ complex of NaRb and prospects for ultracold molecule formation in $X\,^1\Sigma^+(v = 0; J = 0)$. *Phys. Rev. A* **75**, 042503 (2007).

[228] Borsalino, D. *et al.* Prospects for the formation of ultracold polar ground state KCs molecules via an optical process. *J Phys. B* **49**, 055301 (2016).

[229] Demtröder, W. *Atoms, Molecules and Photons* (Springer, 2018).

[230] Covey, J. P. *Enhanced optical and electric manipulation of a quantum gas of KRb molecules.* Ph.D. thesis, University of Colorado, Boulder (2017).

[231] Willner, K., Dulieu, O. & Masnou-Seeuws, F. Mapped grid methods for long-range molecules and cold collisions. *J. Chem. Phys.* **120**, 548–561 (2004).

[232] Kokoouline, V., Dulieu, O., Kosloff, R. & Masnou-Seeuws, F. Mapped Fourier methods for long-range molecules: Application to perturbations in the Rb2(0u+) photoassociation spectrum. *J. Chem. Phys.* **110**, 9865–9876 (1999).

[233] Wall, M. L. & Carr, L. D. Hyperfine molecular Hubbard Hamiltonian. *Phys. Rev. A* **82**, 013611 (2010).

[234] Bryce, D. L. & Wasylishen, R. E. Microwave Spectroscopy and Nuclear Magnetic Resonance Spectroscopy–What Is the Connection? *Acc. Chem. Res* **36**, 327–334 (2003).

[235] Hazzard, K. R. A. *et al.* Many-Body Dynamics of Dipolar Molecules in an Optical Lattice. *Phys. Rev. Lett.* **113**, 195302 (2014).

[236] Blackmore, J. A. *et al.* Ultracold molecules for quantum simulation: rotational coherences in CaF and RbCs. *Quantum Sci. Technol.* **4**, 014010 (2018).

[237] Zeiher, J. *et al.* Many-body interferometry of a Rydberg-dressed spin lattice. *Nat. Phys.* **12**, 1095–1099 (2016).

[238] Choi, J. *et al.* Robust Dynamic Hamiltonian Engineering of Many-Body Spin Systems. *Phys. Rev. X* **10**, 031002 (2020).

[239] Geier, S. *et al.* Floquet Hamiltonian engineering of an isolated many-body spin system. *Science* **374**, 1149–1152 (2021).

[240] Stevenson, I. *et al.* Three-Body Recombination of Ultracold Microwave-Shielded Polar Molecules. *Phys. Rev. Lett.* **133**, 263402 (2024).

[241] Chen, X.-Y. *et al.* Ultracold field-linked tetratomic molecules. *Nature* **626**, 283–287 (2024).

[242] Chen, X.-Y. *et al.* Field-linked resonances of polar molecules. *Nature* **614**, 59–63 (2023).

[243] Büchler, H. P., Micheli, A. & Zoller, P. Three-body interactions with cold polar molecules. *Nat. Phys.* **3**, 726–731 (2007).

[244] Deng, F., Hu, X., Jin, W.-J., Yi, S. & Shi, T. Two- and many-body physics of ultracold molecules dressed by dual microwave fields (2025). Preprint at https://doi.org/10.48550/arXiv.2501.05210.

[245] Rosenberg, J. S. *et al.* Collisional shielding of a bosonic gas of polar molecules (2023). DAMOP.

[246] Rosenberg, J. S., Keshava, S. K., Alaoui, Y. A. & Bakr, W. S. Toward microscopy of a high filling optical lattice of polar molecules (2024). DAMOP.

[247] Seeßelberg, F. *Interacting gases of ultracold polar molecules.* Ph.D. thesis, Ludwig–Maximilians–Universität München (2019).

[248] Keshet, A. & Ketterle, W. A distributed, graphical user interface based, computer control system for atomic physics experiments. *Rev. Sci. Instrum.* **84**, 015105 (2013).

[249] Tobias, W. G. *Degenerate Polar Molecules with Controlled Interactions and Reactivity*. Ph.D. thesis, University of Colorado, Boulder (2022).

[250] Syassen, N. *et al.* Strong Dissipation Inhibits Losses and Induces Correlations in Cold Molecular Gases. *Science* **320**, 1329–1331 (2008).

[251] Moses, S. A. *A quantum gas of polar molecules in an optical lattice*. Ph.D. thesis, University of Colorado, Boulder (2016).

[252] Erdogan, T. Optical Filters: Flatness. Technical Report, Semrock, A Unit of IDEX Corporation (2011). URL https://www.idex-hs.com/docs/default-source/resources/flatness.pdf.

[253] Deuretzbacher, F. *et al.* Heteronuclear molecules in an optical lattice: Theory and experiment. *Phys. Rev. A* **77**, 032726 (2008).

[254] Idziaszek, Z. & Calarco, T. Analytical solutions for the dynamics of two trapped interacting ultracold atoms. *Phys. Rev. A* **74**, 022712 (2006).

[255] Bloch, I., Dalibard, J. & Zwerger, W. Many-body physics with ultracold gases. *Rev. Mod. Phys.* **80**, 885–964 (2008).

[256] Yan, Z. Z. *et al.* Two-Dimensional Programmable Tweezer Arrays of Fermions. *Phys. Rev. Lett.* **129**, 123201 (2022).

[257] Wang, F. *Studies of an Ultracold Bose-Bose Mixture with Tunable Interspecies Interactions*. Ph.D. thesis, The Chinese University of Hong Kong (2016).

[258] Altman, E., Polkovnikov, A., Demler, E., Halperin, B. I. & Lukin, M. D. Superfluid-Insulator Transition in a Moving System of Interacting Bosons. *Phys. Rev. Lett.* **95**, 020402 (2005).

[259] DeMarco, B., Lannert, C., Vishveshwara, S. & Wei, T.-C. Structure and stability of Mott-insulator shells of bosons trapped in an optical lattice. *Phys. Rev. A* **71**, 063601 (2005).

[260] Chen, X.-Y. *Microwave-shielded ultracold polar molecules*. Ph.D. thesis, Ludwig–Maximilians–Universität München (2023).

[261] Yuan, W. *et al.* A planar cloverleaf antenna for circularly polarized microwave fields in atomic and molecular physics experiments. *Rev. Sci. Instrum.* **94**, 123201 (2023).

[262] Pozar, D. M. *Microwave Engineering* (John Wiley & Sons, Inc., 2012).

[263] McDonald, K. T. Wire Polarizers (2012). http://kirkmcd.princeton.edu/examples/polarizer.pdf.

[264] Živković, Z., Senić, D., Šarolić, A. & Vučić, A. Design and testing of a diode-based electric field probe prototype. In *SoftCOM 2011, 19th International Conference on Software, Telecommunications and Computer Networks* (2011).

[265] Ye, X. *Studies of Ultracold Collisions of Ground-state $^{23}Na^{87}Rb$ Polar Molecules*. Ph.D. thesis, The Chinese University of Hong Kong (2019).

[266] Olsen, M. L. *Experiments with Feshbach molecules in a Bose-Fermi mixture*. Ph.D. thesis, University of Colorado, Boulder (2008).

[267] Bause, R. *et al.* Efficient conversion of closed-channel-dominated Feshbach molecules of $^{23}Na^{40}K$ to their absolute ground state. *Phys. Rev. A* **104**, 043321 (2021).

[268] Lam, A. Z. H. *Ultracold dipolar gases of NaCs ground state molecules*. Ph.D. thesis, Columbia University (2022).

[269] Ketterle, W., Durfee, D. S. & Stamper-Kurn, D. M. Making, probing and understanding Bose-Einstein condensates. In Inguscio, M., Stringari, S. & Wieman, C. E. (eds.) *Proceedings of the International School of Physics "Enrico Fermi"*, 67–176 (IOS Press, 1999).

[270] Ketterle, W. & Druten, N. J. V. Evaporative Cooling of Trapped Atoms. *Adv. At., Mol., Opt. Phys.* **37**, 181–236 (1996).

[271] Dalibard, J. Collisional dynamics of ultra-cold atomic gases. In Inguscio, M., Stringari, S. & Wieman, C. E. (eds.) *Proceedings of the International School of Physics "Enrico Fermi"*, 321–349 (IOS Press, 1999).

[272] Bigagli, N. *Reaching the Bose-Einstein Condensation of Dipolar Molecules: a Journey from Ultracold Atoms to Molecular Quantum Control*. Ph.D. thesis, Columbia University (2024).

[273] Yao, N. Y., Zaletel, M. P., Stamper-Kurn, D. M. & Vishwanath, A. A quantum dipolar spin liquid. *Nat. Phys.* **14**, 405–410 (2018).

[274] Norman, M. R. Colloquium: Herbertsmithite and the search for the quantum spin liquid. *Rev. Mod. Phys.* **88**, 041002 (2016).

[275] Broholm, C. *et al.* Quantum spin liquids. *Science* **367**, eaay0668 (2020).

[276] Zou, H., Zhao, E. & Liu, W. V. Frustrated Magnetism of Dipolar Molecules on a Square Optical Lattice: Prediction of a Quantum Paramagnetic Ground State. *Phys. Rev. Lett.* **119**, 050401 (2017).

[277] Semeghini, G. *et al.* Probing topological spin liquids on a programmable quantum simulator. *Science* **374**, 1242–1247 (2021).

[278] Perlin, M. A., Qu, C. & Rey, A. M. Spin Squeezing with Short-Range Spin-Exchange Interactions. *Phys. Rev. Lett.* **125**, 223401 (2020).

[279] Douglas, A. *et al.* Spin Squeezing with Magnetic Dipoles (2024). Preprint at https://doi.org/10.48550/arXiv.2411.07219.

[280] Sundar, B., Gadway, B. & Hazzard, K. R. A. Synthetic dimensions in ultracold polar molecules. *Sci. Rep.* **8**, 3422 (2018).

[281] Cummins, S. Isolated Zero-Cross Detection Circuit. Application Brief SBAA542, Texas Instruments (2022). URL https://www.ti.com/lit/ab/sbaa542/sbaa542.pdf.